To the Graduate Council:

I am submitting herewith a dissertation written by *Seong Soo Park* entitled "Structural Studies of Microwave Heated Vitreous Silica." I have examined the final copy of this dissertation for form and content and recommend that it be accepted in partial fulfillment of the requirements for the degree of Doctor of Philosophy, with a major in Metallurgical Engineering.

Thomas T. Meek, Major Professor

We have read this dissertation
and recommend its acceptance:

Accepted for the Council:

Associate Vice Chancellor
and Dean of the Graduate School

Structural Studies of
Microwave Heated Vitreous Silica

A Dissertation

Presented for the

Doctor of Philosophy

Degree

The University of Tennessee, Knoxville

Seong Soo Park

December 1993

To my parents

Acknowledgments

For assistance with this doctoral dissertation, the author would like to express his deep gratitude to his major professor, Dr. Thomas T. Meek, who directed the work with shining encouragement and whose wise, inspirational guidance enabled him to enjoy all the process and complete it with great satisfaction. Appreciation is also expressed to the contribution of his committee members, Dr. R. A. Buchanan, Dr. R. S. Benson, and Dr. B. Wunderlich, for their advice and guidance. He would like to thank Dr. A. J. Pedraza for his expertise and support.

The author would like to warmly thank High Temperature Materials Lab in Oak Ridge National Lab for the use of their equipment. Dr. C. R. Hubbard's and Mr. O. B. Cavin's help should be particularly appreciated. The financial supports from Thomas J. Watson Research Center of IBM, Lindberg/General Signal Co., D. M. Steward Mfg. Co., and The University of Arizona during the course of this work are gratefully acknowledged.

The author owes a debt of gratitude to his parents and parents-in-law for their unconditional trust and support. All his family members, friends, and professors in Korea should know how deeply thankful he is for their constant belief in him. Special thanks must go to his wife, Bong Eun Kim, for her undying support, infinite tolerance and proofreading of this thesis. His sons, Minshik and Youngshik Park, were the primary sources of his rest, fresh inspiration and motivation. Finally and most truly, He thanks God who has always listened to his prayers.

Seong Soo Park
The University of Tennessee, December 1993

Abstract

Microwave technology is a rapidly expending field in the processing of ceramics and glass materials. Many researchers proposed a number of different theories for loss mechanisms of glass materials at microwave frequencies, but there was no comprehensive analysis available which would describe how glass materials interact with microwave radiation. If the explanation of the basic nature of the microwave interactions with glass materials is available, it will be of a great use. Therefore, the structural analysis of a microwave melted vitreous silica can be a very useful tool for characterizing the microwave heating process and understanding glass-microwave interaction.

In this investigation, the structural difference of the microwave melted vitreous silica and the conventionally melted vitreous silica was examined using the X-ray diffraction method. To get accurate intensity data, CuK_α radiation was applied at lower k values, and MoK_α radiation with Zr-Y balanced filter was applied at higher k values. The different X-ray patterns between the microwave sample and the conventional sample were analyzed in terms of pair function distribution and distance distribution function. These analyses provided the structural differences between the microwave sample and the conventional sample. Data on bond distance distributions and bond angle distributions yielded information on the structural units which made up the random network model.

The microwave treated vitreous silica experienced an increase in non-bridging oxygens, resulting in a change in the random network,

which, in tern, resulted in a shift of Si-O-Si bond angle distributions and in a broader distance distributions of Si-O, O-O, and Si-Si pairs. The coupling of the microwave radiation to vitreous silica is enhanced due to the increase in concentration of broken Si-O bonds.

Table of Contents

List of Figures

List of Tables

Chapter I.

Introduction

Materials processing using microwave radiation is a rapidly expanding technology. In particular, the processing of ceramics, glasses and composite materials by this technology offers the potential for increased productivity, reduced cost and improved material performance. The microwave energy has been used in sintering, joining and melting of ceramics by a number of researchers for over 50 years.[1] Ceramics including alumina[2-4], zirconia[5,6], alumina-zirconia composite[7,8], ferrite[9,10], silicon carbide[11,12] and silicates[13-15] are among the materials that have been successfully processed.

In the conventional thermal process, higher energy photons are converted to phonons at the material surface and then diffused through the bulk. It means that this processing depends upon conducting heat from the surface into the center and is completely dependent on the heat transfer characteristics of the material. In the microwave heating process when microwaves penetrate and propagate through the material, producing a uniform flux of microwave photons throughout which are readily converted to phonons. The internal electric fields generated within the affected volume induce translational motion of free or bound charge complexes such as dipoles. This induced motion causes energy losses and attenuates the electric field. It means that the penetrating action of microwave energy into the material results in uniform internal heating of large cross sections in a relatively short period of time. This is particularly important because

microwave energy continuously couples to the material without being limited by the thermal phonon diffusion process and results in the ability to heat to any desired temperature quickly.

As a result of different heating mechanisms, the major advantages of the microwave heating process[16-19] over the conventional thermal process can be summarized as follows: 1) high heating rates can be obtained, 2) thermal energy can be rapidly deposited or removed from the material, 3) the heating type affects the total volume rather than being based on surface heat-transfer, 4) heating can be more uniform, and 5) high energy transfer efficiency can be obtained by localized energy deposition.

Recently, many researchers[13-15] applied microwave energy to fabricate glass materials. Although several physical properties of microwave heated silicate glasses were measured, no one examined the effect on the glass structure. A number of different theories[20-23] have been put forward to account for the dielectric loss of glass materials at microwave frequencies, but there is no comprehensive analysis available that will describe how materials interact with microwave radiation. If an explanation of the basic nature of the microwave interactions with glass materials were available, it would be of great use. Hence, the structural analysis of microwave heated glass can be a very useful tool for characterizing the microwave heating process and understanding of glass-microwave interaction.

Since vitreous silica is the simplest of the silicate glasses, the study of its molecular structure has long been fundamental to understanding the structure of other silicates. Various techniques[24-27] have been employed to

obtain accurate structural information on amorphous materials. In the 1950's, a more exact treatment which makes no assumptions regarding the scattering factor curves was pioneered by Finbak[28] and further developed by Warren.[29] This was called the pair function distribution or Warren's exact method. Mozzi and Warren[30] applied this method to the structural analysis of vitreous silica. They were able to measure accurate intensity data to high values of k (= $4\pi \sin\theta / \lambda$) by means of the Warren-Mavel X-ray fluorescence technique[31] and were able to obtain a well-resolved pair function distribution of vitreous silica.

To obtain the information about the structural change of vitreous silica in the microwave heating process and the conventional thermal process, Warren's exact diffraction theory was applied. To get the unmodified X-ray intensity in the high k region, CuK_α radiation and MoK_α radiation with a Zr-Y balance filter were employed to measure accurate coherent intensity for vitreous silica out to $k_m \approx 17.11$. The soft programs were developed to correct the measured X-ray intensity vs. 2θ data and to analyze pair function distribution and distance distribution function.

A comparison of X-ray intensity data obtained on the microwave melted sample and the conventionally melted sample indicated different short-range order. The pair function distribution was able to exactly identify what the differences were between the two fabrication methods for vitreous silica. In addition, the distance distribution functions, which were related to the statistical description of the structure, gave a precise quantitative statistical description of the structural change of vitreous silica. Therefore, the results of structural analysis could explain how silica glass interacted with 2.45 GHz microwave radiation.

Chapter II.

Microwave Heating

Microwave processing has been shown by several researchers to be a suitable technique to heat ceramic materials. When the ceramic material is subjected to an electromagnetic field, direct production of thermal energy inside the ceramic material can be achieved by many different loss mechanisms at microwave frequency. In order to better understand the heating of any specific material by microwave energy, it is necessary to discuss some general concepts of microwave heating of the material. In addition, the knowledge of loss mechanisms is useful to understanding the interactions between the electric field and the material for microwave heating. However, until recently loss mechanisms in the ceramic materials at microwave frequency have been poorly understood near room temperature and at elevated temperature. The purpose of this chapter is to review the progress of microwave heating in the ceramic materials and to examine the fundamental interaction mechanisms between microwaves and ceramic materials.

A. Progress of Microwave Heating in Ceramic Materials

One of the first to work in the area of microwave processing of ceramics was Von Hipple[32] in the late 1940's. He studied how oxide materials interact with microwave radiation and how the loss characteristics of these vary as a function of microwave frequency. Much of

his theory and some data provided a valuable background for microwave heating until now.

In the mid 1960's, Tinga together with Voss[33-36] have continued to lead much of the activity involving microwave heating technology. They investigated how certain oxides were heated in 915 MHz and 2.45 GHz microwave fields and developed reaction cavities that caused oxides to be uniformly heated. They tabulated dielectric permittivity data for various materials as a function of frequency, temperature, and moisture contents.

Berteaud and Badot[37] sintered refractory materials at high temperature in a single mode cavity with a 2.45 GHz microwave field. They used 400 W for initial heating and only 100 W to maintain the sintering temperature; the continual application of 400 W caused refractory material to be melted. The process seemed to be a local melting by thermal runaway. However, Schurbring[38] demonstrated that an alumina spark plug could be sintered at 1600 °C in a 2.45 GHz microwave oven and thermal runaway could be prevented by feedback control of the microwave power. His study was the first commercial application in microwave heating of ceramic materials. He reported that the microwave energy required per spark plug for the complete firing cycle was about 50% of the energy required in the conventional manufacturing process.

McGill[39] determined the effect of power level on the microwave heating characteristics of a variety of reagent-grade chemicals and minerals. In his investigation, heating rates increased as input power increased except that very low-lossy materials had negligible changes with increased power. Haas[40] demonstrated that UO_2 and U_3O_8 materials coupled very well with microwave radiation so that these samples could be

heated to their melting points in a 600 W home microwave oven. Holcombe[41,42] screened several different materials for coupling with microwave energy in a 2.45 GHz microwave system. He found that boron carbide, zirconia, UO_2, U_3O_8, and SiC could be used as a coupling agent during microwave sintering.

Microwave sintering research[43-49] at Los Alamos National Laboratory involved the use of 2.45 GHz and a 60 GHz, 200 kW gyrotron source. They proposed first going to higher frequency than 2.45 GHz because the loss tangent was higher for many ceramics and consequently, initial heating was easier. They have observed what appeared to be the enhanced material transport, rapid sintering and different microstructure for various multi-component, composite and glassy materials. To sinter low-lossy ceramics at 2.45 GHz microwave radiation, they suggested the use of various materials to act as both a microwave susceptor material and a second or primary phase material which would act as a crack inhibitor upon sintering. Several researchers,[50-52] following the work of Meek and Blake,[44] have demonstrated that high quality joints could be produced in alumina, mullite, and silicon nitride by microwave heating of the ends of two rods butted together. They used a specially designed single-mode cavity to maximize the electric field and to maximize heating in the area to be joined.

Work at Oak Ridge National Laboratory[53-57] involved a 28 GHz, 200 kW gyrotron source and a large untuned cavity for sintering and annealing of ceramics. They reported that alumina, which was difficult to be heated at 2.45 GHz, could be easily sintered in a uniform microwave field without dead spots by raising the frequency in the large cavity from the 2.45 GHz to

28 GHz and changing the ratio of the wavelength of the microwaves to the size of a 0.56 m^3 cavity from 1:3 to 1:100. They reported that the activation energy for microwave sintering was about one-third of that for conventional sintering. Since their temperature measurement was based on measurement with a thermocouple, it remains to be seen whether such a change in activation energy has taken place or not. The apparent lower activation energy for microwave heating may be explained by the formation of liquid phase since the activation energy of liquid phase sintering is generally lower than that of solid state sintering. Meek[58] suggested the possibility that the microwave sintered samples could have undergone transient liquid phase sintering during a portion of microwave heating because the existence of a surface amorphous layer by TEM analysis was found in the microwave sintered sample.

Roy[59] reported that controlled microwave heating and melting of silica, alumina, and aluminosilicate gels could be achieved in a 600 W domestic type microwave oven. He believed that the heating behavior was dependent on the chemistry, structure, and mass of gels. However, he did not speculate on the precise relaxation mechanism for the microwave absorption by these gels since there was no information on the dielectric properties of gels. In his study, the X-ray diffraction analysis of the alumina, mullite, and silica gels heated to 1500 °C revealed the crystallization of corundum and mullite in the former two while silica remained amorphous. It means that microwave radiation may prohibit silica gels from crystallization. Therefore, the microwave heating process can easily fabricate silica glass. Pope[15] fabricated a prototype furnace by using a novel microwave suscepting ceramic composite for the heat

treatment and by sintering glasses and ceramics which were non-microwave susceptable at ambient temperature. Using this indirect method, porous silica gels were sintered into dense glass rods in 10 minutes. However, Pope did not investigate whether this dense glass rod was the amorphous phase or not. Hassler and Johansen[60] introduced microwave heating in the fabrication process of high quality quartz fibers for telecommunication. He found the loss factor of quartz to be strongly dependent on the temperature below 1000 °C and less dependent above. In his work, the preheating to approximately 1000 °C was required to increase the microwave absorption of the ultra-pure quartz to enable microwave heating to take over as the heat source and then this quartz was heated up to 2000 °C. It means that microwave coupler must be used to fabricate pure silica glass.

B. A Proposed Model for Microwave Heating

The purpose of this section is to present a model for heating of dielectric materials in an electromagnetic field. Modeling of microwave heating is found in many places in the literature.[61-64] The heating model proposed by Meek[61] in an electromagnetic field describes how the electromagnetic field behaves at an interface between two dielectric media. The model of microwave heating can also be used to predict and improve temperature profiles in the material being heated.

In discussing the model of microwave heating, it is useful to describe the losses in terms of the dielectric properties as follows:

(II-1) $\mathbf{E} = V/t$

(II-2) $\mathbf{D} = \varepsilon_0 \mathbf{E} + \mathbf{P} = \varepsilon \mathbf{E}$

(II-3) $\mathbf{P} = \varepsilon \mathbf{E} - \varepsilon_0 \mathbf{E} = \varepsilon_0 (\kappa^* - 1) \mathbf{E}$

where V (volt) is the applied electric potential, t (m) is the distance across which the voltage V is dropped or dissipated, **E** (volt/m) is the vector electric field intensity, **P** (coul/m^2) is the vector electric polarization, **D** (coul/m^2) is the vector electric flux density, ε_0 (8.854 x 10^{-12} farad/m) is the permittivity of free space, ε (farad/m) is the dielectric permittivity of the material, and κ^* ($=\varepsilon/\varepsilon_0$) is the relative dielectric permittivity of the material.

The electric field and the resulting electric flux density of the microwave are given:

(II-4) $\mathbf{E} = \mathbf{E}_0 e^{i\omega t}$

(II-5) $\mathbf{D} = \mathbf{D}_0 e^{i(\omega t - \delta)}$

where $\mathbf{E}_0$ and $\mathbf{D}_0$ is the amplitude of the electric field and the electric flux density, ω is the angular frequency, t is the time lag in the polarizing the material, and δ is the phase angle associated with the time lag in polarizing the material.

The total relative permittivity can be expressed in terms of a complex as $\kappa^* = \kappa' - i\,\kappa''$. The total complex permittivity can also be written as $\varepsilon^* = \varepsilon' - i\,\varepsilon''$. The - i indicates a 90^0 phase shift between the real and imaginary part. From the equation (II-2), (II-3) and (II-4), it also can be expressed as:

$$(II\text{-}6) \qquad \kappa^* = \frac{\varepsilon^*}{\varepsilon_0} = \frac{\mathbf{D}}{\varepsilon_0 \mathbf{E}} = \frac{\mathbf{D}_0 e^{-i\delta}}{\varepsilon_0 \mathbf{E}_0} = \frac{\mathbf{D}_0}{\varepsilon_0 \mathbf{E}_0} (\cos \delta - i \sin \delta)$$

And then, from the equation (II-6), the real part (κ') and the imaginary part (κ'') of the relative permittivity are

$$(II\text{-}7) \qquad \kappa' = \frac{\varepsilon'}{\varepsilon_0} = \frac{\mathbf{D}_0}{\varepsilon_0 \mathbf{E}_0} \cos \delta \quad \text{and} \quad \kappa'' = \frac{\varepsilon''}{\varepsilon_0} = \frac{\mathbf{D}_0}{\varepsilon_0 \mathbf{E}_0} \sin \delta$$

where ε' is the dielectric permittivity and ε'' is the dielectric loss factor of the material. The loss tangent ($\tan \delta$) is defined as the ratio of the real part to the imaginary part of the permittivity:

$$(II\text{-}8) \qquad \tan \delta = \frac{\kappa''}{\kappa'} = \frac{\varepsilon''}{\varepsilon'}$$

Especially, the relative dielectric permittivity and the loss tangent are widely used and measured parameters that describe the behavior of a dielectric material under the influence of an electromagnetic field.

Let the relative dielectric permittivity κ'_1 of region 1 be greater than the relative dielectric permittivity κ'_2 of region 2 in the material body. As pointed out by Meek[58], the electric field intensity (Volts/cm) is described by:

$$(II\text{-}9) \qquad \mathbf{E}_2 = \mathbf{E}_1 [\cos^2\alpha_1 + (\kappa'_1 / \kappa'_2)^2 \sin^2\alpha_1]^{1/2}$$

where α_1 is the angle between the electric field direction and the material surface. For the case where $\alpha_1=90^o$, the equation (II-9) is simplified as $\mathbf{E}_2 = \mathbf{E}_1 (\kappa'_1/\kappa'_2)$. It indicates that the electromagnetic field is largest in regions

of small permittivity and the location of this energy will vary as the material is heated.

The power density (watts/cm^3) is described by the well known relation

(II-10) $$P = \frac{1}{2} E^2 \omega \kappa' \tan \delta$$

where P is the power absorbed per unit volume and ω is the angular frequency of the incident electromagnetic radiation. This expression indicates that the power absorbed in the material is directly proportional to the angular frequency, the square of the electric field, the dielectric permittivity and the loss tangent. In addition, ω, κ', tan δ, and E are all interdependent. E is dependent on the size, geometry and location of the material within a microwave cavity and on the design and volume of the cavity. Moreover, the expression (II-9) and expression (II-10) show that more power is deposited into the lower dielectric permittivity region (lower density region) than into the higher dielectric permittivity region (fully dense region). It is beneficial to characterize how a ceramic will heat in an electromagnetic field.

The half-power depth is defined as that distance into a material, in a specified configuration, where the power is reduced to one half that at the surface. Thus, the half-power penetration depth (cm) is described as:

(II-11) $$H = 3 \lambda_0 / [\, 8.686 \pi (\kappa')^{1/2} \tan \delta \,]$$

where H is the half-power depth, and λ_0 is the characteristic wavelength of the incident microwave radiation. This expression shows that the half-

power penetration depth into the lower dielectric permittivity region is larger than into the fully dense region.

The temperature rise (ΔT) can be expressed as:

$$\Delta T = \frac{P\ \Delta t}{\rho\ C_p} \qquad \text{(II-12)}$$

where P is the power absorbed, Δt is the time of exposure to the microwaves, ρ is the density of the material, and C_p is the heat capacity of the material. From the equation (II-10) and (II-12), the heating rate (dT/dt) is described as:

$$dT/dt \approx \pi\ f\ E^2\ \kappa'\ \tan\delta\ /\ (\rho\ C_p) \qquad \text{(II-13)}$$

where $\omega = 2\pi f$ and f is the frequency. It indicates that the heating rate is directly proportional to the frequency, the square of the electric field, the dielectric permittivity and the loss tangent. This temperature rise is only an approximate increase in temperature resulting from the absorption of microwave energy because it does not include heat loss due to conduction, convection, radiation, or change of state. Also, this heating rate is only an average heating rate since the lower density regions will heat faster in an electromagnetic field than the already sintered regions.

C. Microwave-Material Interactions

As microwaves penetrate and propagate through a dielectric material, the affected volume of the material is polarized by an external field. In the process, the internal electric fields reorder the molecules in

the material by adding potential energy to the state of each molecule. If the external field is suddenly removed, these molecules will try to return to their random orientation. To achieve this, the stored potential energy converts into random energy which causes molecules to collide and give up their extra energy in the form of heat. This loss of externally applied energy within the material is commonly referred to as relaxation. The relaxation time lag between the applied field and the resultant polarization implies an irreversible degradation of energy, which is energy loss.

1. Polarization Mechanisms[65]

There are various possible mechanisms for polarization in a dielectric material as shown in Figure 1. One process common to all materials is an electron polarization: upon the application of an external electric field the center of gravity of the negative electron cloud is shifted in relation to the positive atom nucleus.

A second mechanism is an atomic (or ionic) polarization: when atoms of different types form molecules, this polarization arises from the displacement of ions of opposite sign, from their regular sites under the influence of an applied field, and also from the deformation of the electronic shells resulting from the relative displacement of the ions.

A third mechanism is an orientation (or dipole) polarization: the asymmetric charge distribution between unlike partners of a molecule gives rise to permanent dipole moments which exist also in the absence of an external field. When an electric field is applied, such moments tend to line up with the electric dipoles in the direction of the electric field.

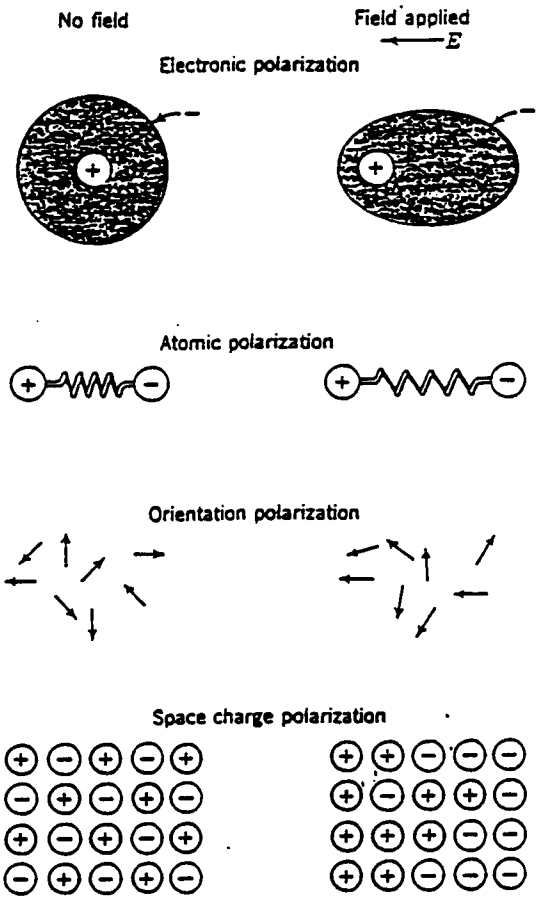

Figure 1. Schematic representation of mechanisms of polarization. From A. R. Von Hipple, regference 32.

A final source of mechanism is a space charge (or interfacial) polarization: charge carriers, which usually exist, can migrate for some distance through the dielectric material. When such carriers are impeded in their motion, either because they are trapped in the material or on interfaces or because they exist in an electric field, a macroscopic field distortion follows.

2. Possible Loss Mechanisms for Glass Materials

Electromagnetic energy can be deposited in glass materials through several loss mechanisms, which result from electronic polarization, ion vibration, ion jump relaxation, conduction, or interfacial polarization.

Electronic polarization losses and ion vibration losses are a kind of resonance phenomenon: electronic polarization may alter the energy barrier to be overcome by the jumping ion, and ionic vibration may alter the frequency of attempted jumps. It means that the application of resonance theory is not possible for any reasonable damping force since the microwave and the ion jump frequency differ by three or four orders of magnitude; microwave frequency is in the range of 10^9 to 10^{10} Hz, the ion jump frequency is of the order of the Debye frequency (10^{13} Hz), and the electronic polarization is occurred in the visible spectrum range. Kenkre[23] reported that resonance mechanisms were unable to provide an explanation of the source of microwave interactions in dielectric ceramics. Since electronic polarization and ion jump occur at higher frequencies than the ionic vibration, these loss mechanisms are not also thought to be operable at microwave frequency in glass materials.

Katz and Blake[66] suggested that the loss mechanisms of relaxation type were thought to be operable during microwave heating of dielectric ceramics to explain the enhanced diffusion during microwave heating of ceramic materials. They explained that the ion jump relaxation in a crystalline ceramic occurred when an aliovalent ion and vacancy formed an associated pair. The vacancy was thought to jump around the aliovalent ion to align its dipole moment with the applied electric field. MacDowell[67] took a look at the structure of a nepheline since a wide variation in microwave absorption values could occur within the same composition range. In his study, he examined the microwave heating characteristics of nepheline glass-ceramics containing K_2O, CaO, and Li_2O substitutions for Na_2O. The remarkably high susceptibility of pure sodium nepheline was ascribed to a "loose fit" for sodium ions in interstitial sites designed to accommodate large potassium ions. Dramatic reduction in absorption of microwave energy was recorded for K_2O and for Li_2O. The effect of Li_2O was explained on the basis of a slightly expanding unit cell and Na^+/Li^+ skewed "ion pairs" fitting snugly into one half of the large K sites. Calcium substitution seemed to have little effect upon microwave heat-up and was believed to exchange directly for Na^+ in the smaller interstitial cavities. It means that the energy losses in glass materials show an intimate relationship with the glass structure and composition; the nature of the modifying cations has a significant effect on the energy losses since localized motion of the alkali ion in silicate cages can lead to strong absorption in the microwave range. Ion jump relaxation losses are thought to be operable during microwave heating in glass material when two or more equivalent positions for an ion are present.

Katz and Blake[66] suggested that interfacial polarization losses occurred at a structural inhomogeneity such as a grain boundary, dislocation, or vacancy cluster. In an ionic lattice there will be a localized disruption in electroneutrality at such a structural inhomogeneity with a net dipole moment which will align itself with the applied electric field. The interfacial polarization losses are thought to be operable during microwave heating of glass material.

According to Berteaud and Bardot[37], when temperature of ceramic material increases, the conduction losses increase at a faster rate than any other relaxation losses. The total electromagnetic losses increase rapidly with temperature causing auto-acceleration of the heating rate and thermal runaway. Therefore, conduction losses are very important in dielectric ceramics. These losses are directly related to the dc conductivity of the dielectric ceramics. Such conductivity gives rise to currents which in an ac field are in phase with the applied voltage and hence cause dielectric losses which are independent of any other loss mechanisms. The loss factor can be written in terms of the electrical conductivity;

$$\text{(II-14)} \qquad \sigma = \omega \varepsilon'' = \tan \delta \quad \text{or} \quad \tan \delta = \frac{\sigma}{2 \pi f \kappa' \varepsilon_0}$$

where σ is the electronic conductivity. The loss tangent is expected to increase exponentially with temperature because conductivity effects increase exponentially with temperature. For example, these conduction losses are small at microwave frequency at room temperature for silicate glasses, but they become increasingly more important at elevated

temperatures. A significant part of increase in loss tangent of the soda-lime-silicate glasses[65] indicated in Figure 2 corresponds to conduction losses.

Navias and Green[68] proposed a qualitative explanation of the mechanisms producing energy absorption and energy losses in the microwave range. In their work, these mechanisms were explained by the nature of the bonds joining atoms and ions in the randomly oriented atomic networks of glasses; the continuous glassy networks of SiO_2 and B_2O_3 do not absorb appreciable energy in the microwave range because the rigid atomic structure does not oscillate readily without setting the atoms into motion. Addition of network-modifying oxides yields glasses of greater energy absorption owing to the oscillation of the interstitial ions introduced. Alkali ions being weakly held in the interstices on the network produce high losses because these alkali ions are easily set into motion under the influence of microwaves. This results from the modification of the continuous atomic networks of glass-formers by these additional oxides: some rigid bonds are broken, the alkali ions-O bond is relatively weak, and the oxygen atoms adjacent to each alkali ion are essentially single bonded. The divalent ions of alkaline earths do not contribute as much to losses as alkalis because their divalent charges and large ionic diameters secure them more firmly than the alkali ions to the adjacent atoms, causing them to be less mobile. Glasses containing combinations of alkali or dissimilar interstitial ions show lower losses than the equivalent compositions with only one component. The unlike sets of oscillating ions may possibly have different vibration frequencies so that they are not moving together and might restrict the motion of either or both.

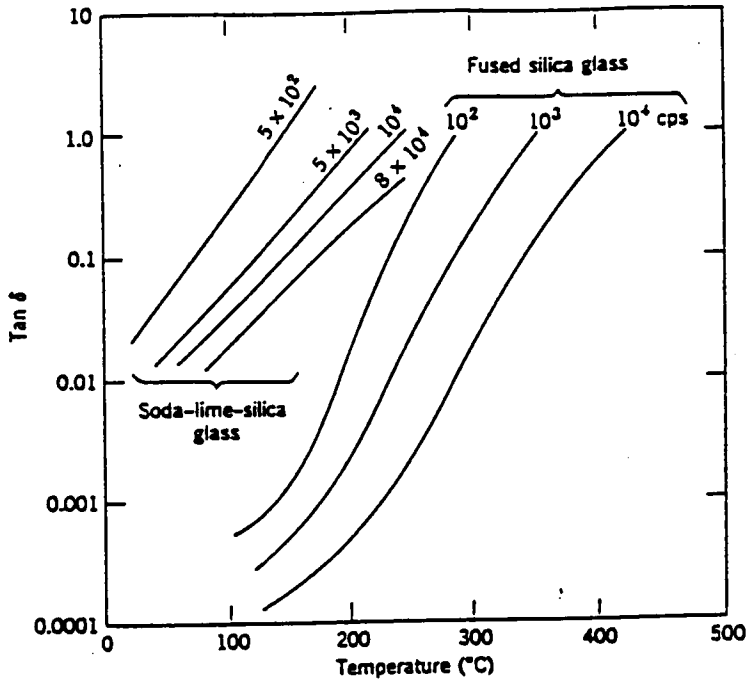

Figure 2. Loss tangent with increasing temperature for a fused-silica glass and for a soda-lime-silica glass. From W. D. Kingery, reference 65.

Chapter III.

The Structure of Vitreous Silica

The determination of the structure of glasses has been established by means of X-ray, neutron[69-73], and electron scattering[74-75] with spectroscopic methods.[76-78] In diffraction methods, the main efforts have been directed towards improvement of the resolution of the method by extending the range of k (real space) measured experimentally. Such investigations provided results about fundamental structural units as well as about their connection to a three-dimension network by yielding data on distributions of bond lengths and bond angles. Therefore, the short-range order of glasses has been well obtained up to 8 Å in most cases by the results of diffraction methods.

The alternative way of obtaining information on the structure of glasses is to use spectroscopic methods which analyze the various individual atomic sites. Infrared[76], Raman[77], and NMR (nuclear magnetic resonance)[78-79] are used most frequently. They have permitted the determination of the symmetry of some particular atomic sites or the number of neighbors surrounding a given atomic species.

The above experimental methods contain a serious limitation as a three-dimensional disordered structure is insufficiently defined. Thus, the interpretation of the results of either diffraction or spectroscopic methods inevitably requires the adoption of a structural model to compare the calculated results with those given by experiment. Random network models[80-83] have been constructed employing Si-O-Si bond angle

distributions similar to those derived from X-ray and neutron diffraction studies. Random network models were generally categorized according to their ring statistics.[84] Today the use of high speed computers has permitted the refinement of mechanically built models.[85]

The historical progress of the X-ray diffraction method that can be employed to obtain structural information for amorphous solids is discussed in the following section.

A. Historical Progress in X-ray Diffraction Method

Under the assumptions that non-crystalline substances can produce an X-ray pattern, Debye and Scherrer[86] found the first X-ray diffraction pattern of glass in 1916. No notable progress was made towards deriving structural information from the X-ray diffraction pattern of glass until the early 1930's. The systematic study of the structure of vitreous silica was started by Randall et al.[87] They observed that the broad maxima of the vitreous silica pattern were located at the same positions as sharp reflections in crystalline silica. Since it was known at that time that small crystallite sizes made X-ray diffraction broaden, they proposed the crystallite theory for amorphous silica: vitreous silica is composed of an aggregate of very small crystals. Valenkov and Poray-Koshitz[88] supported crystallite theory because they assumed that vitreous silica consisted of crystallites of the order of 10 - 15 Å with comparatively small distortions, bound by regions of much greater distortion.

The major step in our understanding of the atomic arrangements within amorphous solids was taken by Zachariasen.[89] He stated that amorphous materials were made up of extended three dimensional

networks which lacked periodicity but had an internal energy and a structure both of which were not significantly different from that of the corresponding crystal. His statement was called random network model. According to this model, he predicted that vitreous silica consisted of SiO_4 tetrahedra joined at the corners with relatively few additional structural constraints resulting in a continuous but random set of polyhedral linkage. The random-network model, based largely on the arguments advanced by Warren[90], has been generally accepted as the best description of the structure of non-crystalline solids until now.

In early 1930's, Warren, Krutter and Morningstar[91] were the first to analyze the X-ray pattern of vitreous silica by using an approximate Fourier analysis method. From this X-ray diffraction pattern, they could calculate a radial distribution giving the average number of atoms about an average atom, as a function of interatomic separation. This method was the so called radial distribution function analysis. By using the radial distribution function method, Warren[90] confirmed that the structure of vitreous silica consisted not of an aggregate of small crystals, but of a continuous random network of SiO_4 tetrahetra; SiO_2 was found to consist of oxygen atoms situated at the vertices of a tetrahedron enclosing a central silicon atom, each vertex being shared by two tetrahedra. As a result of Warren's effort, X-ray diffraction studies with the approximate Fourier analysis could be applied widely to determine the interatomic distances and coordination numbers of amorphous materials. Hartlief[92] undertook an X-ray diffraction study of the structure of vitreous silica with using ionization chambers, which were to record the diffracted intensity.

In the late of 1930's, the X-ray diffraction analysis on vitreous silica was only as approximate as one had to assume that the scattering factor of silicon and oxygen were proportional to one another in order to successfully carry out the Fourier analysis of the diffraction data of vitreous silica. This approximation was introduced in the work of Warren et al.[91] It means that different atoms in a unit of composition have the atomic scattering factor curves that are constant multiples of each other. This approximation in diffraction theory was not justifiable in analyzing the improved X-ray intensity data.

In the 1950's, a more exact treatment which made no assumptions regarding the scattering factor curves was pioneered by Finbak.[28] This exact treatment for analyzing X-ray scattering from vitreous silica with more than one kind of atom was further developed and applied by Warren.[29] Warren used the concept of pair functions and then analyzed X-ray diffraction data with eliminating the above assumption. It means that the Warren's exact treatment takes into account the fact that the atomic scattering factors of the constituent atoms in amorphous material need not to be proportional to one another.

Mozzi and Warren[30] carried out the first structure investigation of vitreous silica using the pair function distribution (PFD), which was Warren's exact treatment. By means of Warren-Mavel X-ray fluorescence technique[31], Mozzi and Warren were able to measure accurate intensity data to high values of k and obtain a well-resolved pair function distribution of vitreous silica. In terms of distance distribution function which were related to the statistical description of the structure of vitreous silica, they were able to give a precise quantitative description of the variation of the Si-

O-Si bond angle as well as the variation of the orientation of SiO_4 tetrahedra about Si-O bond directions: each silicon atom was tetrahedrally surrounded by four oxygen atoms with a Si-O bond of 1.62 Å, a O-O bond of 2.65 Å, and a Si-Si bond of 3.12 Å. The angular distribution function V(α) showed a variation in the Si-O-Si bond angle (α) of 120° to 180° with a maximum frequency at 144°. In addition, they fitted their data to a crystobalite-like structure. Wicks[93] reinterpreted the data of Mozzi and Warren because he determined a Si-O bond length of 1.625 Å, a O-O bond of 2.66 Å, and a Si-O-Si angle (α) of 130° to 180° with a maximum at 143°. Coombs et al.[94] confirmed the result of Mozzi and Warren (144°) by analyzing the shape of the distribution curve of the angle Si-O-Si proceeding from the most accurate value of the Si-O distance (1.62 Å).

Gokularathnam[95] studied the effect of heat treatment, water content, and fast neutron irradiation on the structure of vitreous silica by using the Warren-Marvel X-ray fluorescence technique.[31] His analysis of the effect of fast neutron irradiation for vitreous silica showed a broader distribution of the interatomic distances and a decrease in the Si-O-Si bond angle such as; 1) the mean Si-1st O distance was increased from 1.62 Å to 1.67 Å, 2) the tetrahedral units were preserved even after heavy neutron irradiation and 3) the Si-1st Si distances tended to be distributed over a wide range of r values with a concomitant shift in the distribution of the Si-O-Si bond angles towards lower values. Therefore, he suggested that the deformation of the SiO_4 tetrahedra themselves would be slight, but greater deformations of these tetrahedra configurations with respect to one another could occur due to the collision process during the neutron bombardment. This seems to

occur in such a way as to make the structure more compact with respect to the SiO_4 tetrahedra to compensate for the increased Si-1st O distances.

For better resolution and detail of the radial distribution functions of the glasses, it is necessary to go out to as a large k ($=4\pi\sin\theta/\lambda$) value as the diffraction equipment will allow. Using X-ray diffraction method, good resolution of intensity can be obtained up to about 20 $Å^{-1}$. Therefore, Keating[96] suggested that a combination of neutron and X-ray diffraction methods could be used to interpret the structural details of a liquid-like glass. Henninger[97] used both X-ray diffraction and neutron diffraction methods along with approximate Fourier analysis method to obtain an atomic radial distribution functions on vitreous silica. He did not find a new information, but only confirmed the results derived from X-ray diffraction.

Finally, the results of the structure of vitreous silica done by various investigators are summarized in Table 1. It should be noted that most of the investigators have reported mainly the interatomic distances in vitreous silica, while Mozzi and Warren[30] have reported a function $V(\alpha)$ which gives a precise quantitative description of the variation of the Si-O-Si bond angles.

B. Methods Used to Eliminate Compton Scattering

To obtain higher resolution and desired accuracy for radial distribution function or pair function distribution, the X-ray intensity must be measured out to as high angle as possible and then it must be Fourier analyzed. For glass materials of low atomic number, the contribution of incoherent scattering can outweigh the coherent radiation by almost as much as an order of magnitude in high angle regions. This is a direct

Table 1. Interatomic distances and bond angle in vitreous silica.

	Warren[27] (1936)	Hartlief[92] (1938)	Breen[69] (1957)	Henninger[97] (1967)	Mozzi[100] (1969)	Wicks[93] (1975)
Si - O	1.62 Å	1.7 Å	1.6 Å	1.59 Å	1.62 Å	1.62 Å
O -1st O	2.65 Å	2.7 Å	2.6 Å	2.62 Å	2.65 Å	2.66 Å
Si - 1st Si	3.20 Å	3.1 Å	3.3 Å	3.22 Å	3.12 Å	3.12 Å
Si - 2nd O	4.2 Å	4.1 Å	3.9 Å	4.09 Å	4.15 Å	4.15 Å
O - 2nd O	4.5 Å	--	4.5 Å	--	5.1 Å	5.15 Å
Si - 2nd Si	5.2 Å	5.3 Å	5.1 Å	5.03 Å	5.1 Å	5.15 Å
Si - 3rd O	--	--	--	--	6.4 Å	6.35 Å
Si - O - Si Bond Angle (Maximum)					120° - 180° (144°)	130° - 180° (143.3°)
Method	x-ray	x-ray	neutron	neutron	x-ray	x-ray

consequence of the relatively weak bonding of electrons to atoms in the glass structure. The subtraction of the theoretical contribution of incoherent scattering from the experimental X-ray intensity produces serious errors in the coherent scattering obtained and hence in the Fourier transform. Therefore, it is desirable that the Compton modified scattering should be removed as effectively as possible in experimental measurements.

Short[98] used monochromatic CuK_α radiation, provided by nickel-cobalt balanced filters placed in the primary X-ray beam, to determine the fraction of incoherent scattering present in the total X-ray scattering from non-crystalline materials. In his experiment, the incoherent scattering from a carbon black between 55° and 160° 2θ was measured in good agreement with that predicted by theory. Ruland[99] reported that the possibility of separating coherent and incoherent Compton X-ray scattering in a theoretical and experimental study depended on the profile of the Compton line as well as on the resolution of the monochromator. He proposed that since the correction for the remaining incoherent scattering at smaller angles involved information on the Compton profile, it would often be preferable to use the combination of Ross filters and pulse-height discrimination. This combination can choose the incoherent scattering which is not affected by the monochromatization.

Warren-Mavel fluorescence technique[31] represented a significant contribution to the X-ray study of glasses by experimentally eliminating the incoherent scattering. Warren and Mavel reported that experimental elimination of the modified scattering in amorphous scattering could be done by use of fluorescence excitation in the detector circuit: the monochromated RhK_α (λ = 0.615 Å) by a singly bent LiF crystal fell upon the

amorphous sample, and then unmodified and modified scattering fell upon a thin sheet of Mo (λK_{edge} = 0.620 Å). This fluorescence radiation, which was received in a Kr filled counter placed near Mo sheet, was closely a measure of the unmodified scattering since the unmodified scattering was well suited to excite fluorescence and most of the modified scattering is incapable of exciting fluorescence. With these combinations, a clean unmodified intensity was measured. They suggested another combination which was $AgK_{\alpha 1}$ with Ru sheet: the unmodified $AgK_{\alpha 1}$ excites fluorescence RuK radiation since the wavelength of $AgK_{\alpha 1}$ (λ = 0.5594 Å) is so close to the K absorption edge of Ru (λ = 0.5605 Å), that any excitation by modified $AgK_{\alpha 1}$ is completely negligible. The counter reading can be strictly proportional to the intensity of unmodified $AgK_{\alpha 1}$ even down to small scattering angles. Henninger[97] applied a method of eliminating incoherent component by a selective fluorescence technique with AgK_{α} radiation in his experiment, but imperfect monochromatization of the AgK_{α} line forced his method abandon. To get unmodified intensity, he measured the total intensity by a scinitillation detector with MoK_{α} radiation, the modified intensity calculated from Hartree-Fock wave functions was then subtracted from the measured intensity.

Mozzi and Warren[30] applied the Warren-Mavel X-ray fluorescence technique to obtain accurate information for the structure of vitreous silica. Mozzi[100] reported that he was able to eliminate most of the Compton scattering that took place at high k. Mozzi's experimental set-up consisted of directing a primary beam of crystal-monochromated RhK_{α} radiation upon the sample of vitreous silica. The scattered radiation, consisting of both the unmodified and modified, then fell upon a sheet of molybdenum

foil which was oriented 45° to the beam. The molybdenum fluorescence K radiation was detected by a kryptron filled counter at 90° to the diffracted X-ray beam. Since the wavelength of RhK_α was 0.615 Å and the wavelength of MoK_{edge} was 0.620 Å, most of Compton scattering could not excite fluorescence radiation. It was apparent that Compton component of the scattered radiation would be effectively eliminated at high k values. Unfortunately, the efficiency of this process was approximately 0.5%. However, Mozzi reported that intensities were sufficient to yield very good results.

Strong and Kaplow[101] reported that bent and ground LiF crystal monochromators, placed after the specimen in X-ray diffraction experiments could remove nearly all of the $CuK_{\alpha 2}$ component of the source and the incoherent component with CuK_α or longer wavelengths. Also, these monochromators could reduced approximately 50% of $MoK_{\alpha 2}$ component of the source and a large portion of the incoherent component with MoK_α or shorter radiation. The efficiency of about 25% for MoK_α and 20% for CuK_α radiation were readily attainable, allowing high geometrical resolution to the diffuse intensity analyses with polystyrene and B_2O_3 of low atomic number. This experimental arrangement was approximately six times as efficient as the Warren-Mavel X-ray fluorescence technique with comparable diffraction geometry.

Ergun et al[102] suggested the use of LiF crystal monochromated AgK_α radiation with balanced Rh-Ru filters to eliminate experimentally and to determine the Compton component in diffuse scattering. The balanced Rh-Ru filters were placed away from the detector slit in order to diminish the effects of the fluorescence from the Ru filter. They found that no

measurable background was obtained and an excellent balance was achieved. Since the K absorption edge of Ru (λ = 0.5605 Å) was located very close to the wavelength of $AgK_{\alpha 1}$ (λ = 0.5594 Å), the Compton scattering involving shifts larger than the differences between the two wavelengths (0.0011 Å) would be more effectively removed. Therefore, the intensity obtained using balanced Rh-Ru filters at scattering angles $2\theta > 20°$ was essentially the unmodified scattering. At the lower angles, $2\theta < 20°$, the correction of the Compton scattering was desirable for more precise values of unmodified intensities. This correction was accomplished by using intensities obtained with the Rh filter and the Rh-Ru difference intensity. Ennas et al.[103] empirically approached through the examination of five independent MoK_{α} diffraction measurements taken on the sample of amorphous silica. They concluded that MoK_{α} diffraction measurement was reliable and was predictor for the various structural hypotheses.

Alternatively, many researchers[104-106] used high-resolution energy-dispersive diffractometry to eliminate experimentally Compton scattering in the amorphous material. This energy-dispersive diffractometry was achieved by an energy dispersive detector and multi-channel pulse-height analyzer combination with a X-ray goniometer. It is assumed that the Compton scattering occurs within a range of energy lower than that of the incident X-ray radiation. Hence, they found that the half-profile on the higher-energy side of the peak maxima of the incident X-ray beam could be taken to represent the coherent intensity because the Compton contribution was negligibly small compared with the strong coherent intensity. They reported that results were in good agreement with the carefully examined results of using a crystal monochromator in the diffracted X-ray beam.

Chapter IV.

X-Ray Diffraction Theory

Knowledge of the structural arrangement of atoms of amorphous solids is an essential prerequisite to a detailed understanding of other physical or chemical properties. In the case of a crystal the arrangement of atoms is periodic, so the description of its structure is complete once the dimensions and content of the unit cell are specified. The position of all the atoms is then determined by translation of this unit cell. In case of amorphous solids only short-order is present and the unit cell can no longer be defined. Hence this structure is described statistically by means of distribution functions expressing the probability of finding an atom at a certain distance from another atom.

This technique involves the use of mathematical modeling using experimentally obtained data to describe the structure of non-crystalline solids. The most widely used functions are the radial distribution function (RDF) and pair function distribution (PFD), which are important since they can be obtained directly from X-ray diffraction method.

A. Radial Distribution Function

Whether a liquid or an amorphous solid is considered, there is no directional order present. However, the existence of short-range order in the amorphous solid makes it possible to describe the atomic array in terms of an average density function of atoms per unit volume ρ_0 and an actual density function $\rho(r)$ which measures the number of atoms per unit volume

a distance r away from an atom placed at the origin. It is convenient to think about the number of atoms per unit volume contained in a spherical shell of thickness dr surrounding the origin atom since the radial density of atoms surrounding any atom is spherically symmetric. The radial distribution function (RDF) is defined as the number of atoms lying at distances between r and r+dr from the center of an arbitrary origin atom. This can be written as $4\pi r^2\rho(r)$ dr. The foregoing mathematical procedure was first developed by Zernike and Prins[107] in 1927. Debye and Menke[108] first applied it to determine the RDF of liquid mercury in 1930.

Without considering the procedure in detail, the structural information is extracted by means of the Fourier transform to interpret the experimental curve of the X-ray scattering. The RDF takes on a final form as shown in Figure 3. In this representation, the RDF is plotted as a function of the radial distance. The RDF exhibits oscillations about the average density parabola given by the curve $4\pi r^2\rho_0$ since $\rho(r)$ for an amorphous solid exhibits an oscillatory behavior with the peaks in the probability function representing average interatomic separations; after the first few maxima, $\rho(r)$ approaches ρ_0 due to the lack of long range order. The maxima at low r values indicate high density differences or short range ordering. Compared with crystal data and atomic radii, the positions of these peaks serve to indicate mean interatomic distances, and the area under the peaks indicates the number of atoms situated about that mean distance of separation. Consequently, the short range structure of the vitreous solid can be defined.

The preceding method, which contains the fundamental approximation of effective electron number, has been widely employed up to

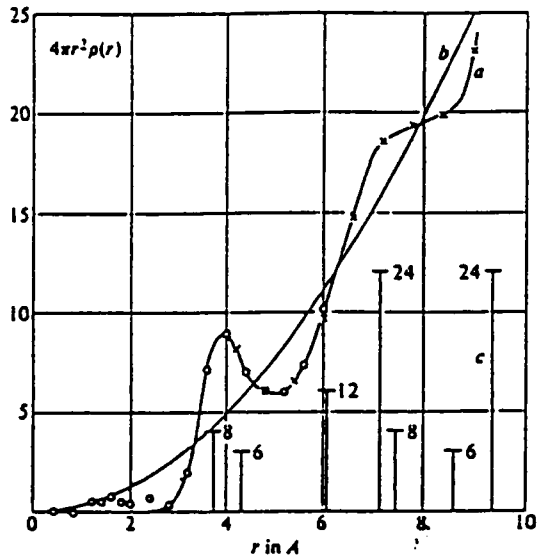

Figure 3. (a) The radial distribution function $4\pi r^2\rho(r)$ for liquid sodium. (b) The average density curve $4\pi r^2\rho_0$. (c) The distribution of neighbors in crystalline sodium. From B. E. Warren, reference 29.

recent years. This approximation involves assuming no angular dependence of the various scattering factors for the different atom-atom combinations. It means that the effective electron number is treated as a constant for each kind of atom. In practice a three dimensional covalently bonded network is not composed of spherical free atoms or ions. This is particularly important for elements of low atomic number where a significant fraction of the electrons are involved in the bonding process. The validity of this assumption is tested in Figure 4 for vitreous silica. It is clear that this assumption is not correct for more than one kind of atom. By the use of pair functions which express directly the pair interactions between an i th and j th atom, this approximation can be eliminated. Therefore, Warren's exact treatment[24] will be further discussed and developed in the subsequent section.

B. Exact Treatment for Scattering by Amorphous Solids

A more exact treatment for analyzing X-ray scattering from an amorphous solid with more than one kind of atom was pioneered by Finbak as well as by Waser and Schomaker.[28] Credit goes again to Warren[24] for calling attention to this method and applying it to the case of glasses. The development given here follows primarily Warren's exact treatment.

In the case of X-ray scattering by an amorphous sample, it is assumed that there is a random orientation and any number of different kinds of atoms in the sample. Let a vector $\mathbf{r}_m$ and $\mathbf{r}_n$ be the instantaneous position of each atom of type m and n. Expressed in electron units, the intensity scattered from the sample containing atoms of type m and type n is obtained by summing the amplitude scattered by each atom multiplied by

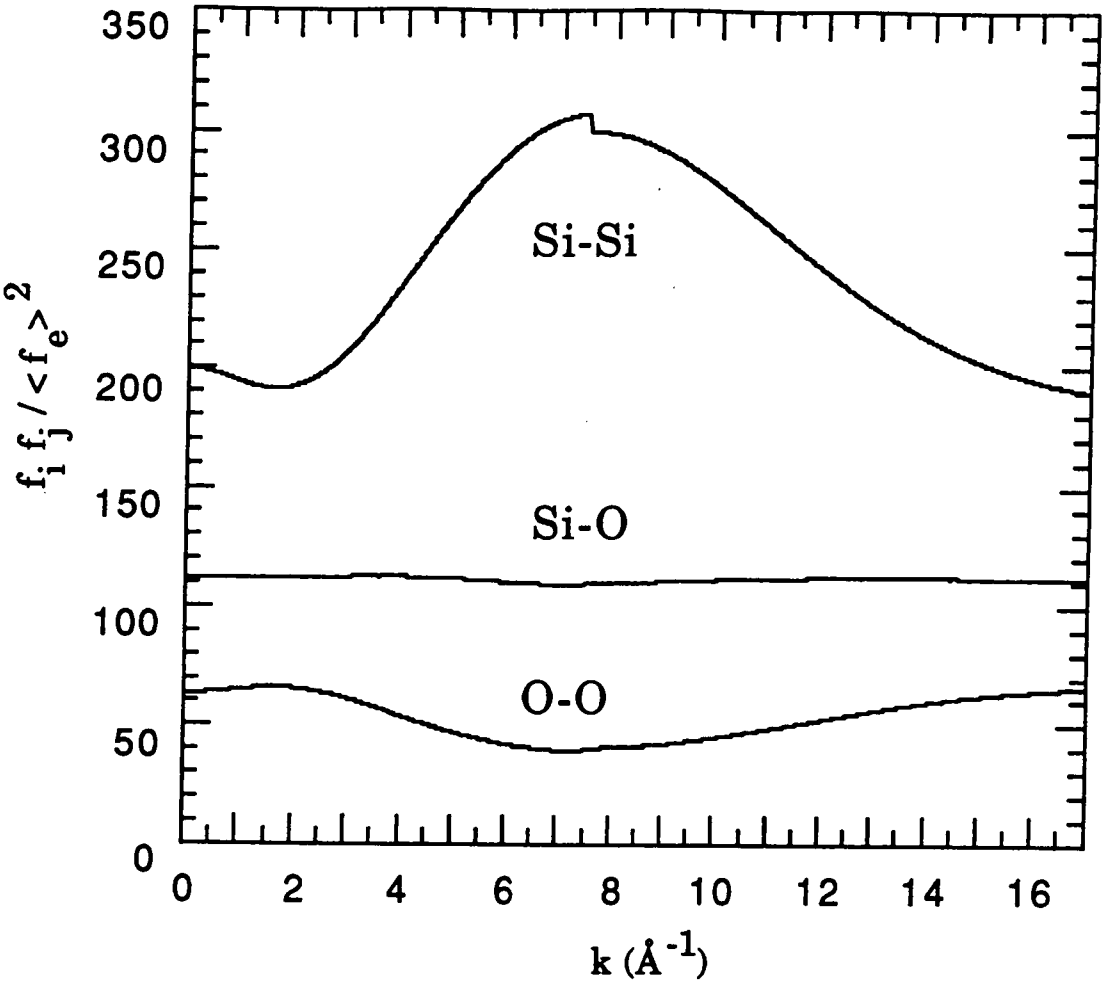

Figure 4. Proportionality of scattering factors for Si-Si, Si-O, and O-O in CuK_α and MoK_α radiation.

the conjugate quantity:

$$(IV\text{-}1) \qquad I_{eu} = \sum_m f_m \, e^{(2\pi i/\lambda)(\mathbf{s} - \mathbf{s}_0)\cdot \mathbf{r}_m} \sum_n f_n \, e^{-(2\pi i/\lambda)(\mathbf{s} - \mathbf{s}_0)\cdot \mathbf{r}_n}$$

where I_{eu} is the intensity expressed in electron units, i.e., the ratio of sample intensity divided by the scattered intensity per electron, f_m and f_n are the scattering factors of the *m* th atom and the *n* th atom, λ is the X-ray wavelength, and $\mathbf{s}$ and $\mathbf{s}_0$ are unit vector in the relative directions of the incident and scattered X-ray beams. Introducing the difference vector $\mathbf{r}_{mn} = \mathbf{r}_m - \mathbf{r}_n$ relative to the pairs, expression (IV-1) can be written as:

$$(IV\text{-}2) \qquad I_{eu} = \sum_m \sum_n f_m f_n \, e^{(2\pi i/\lambda)(\mathbf{s} - \mathbf{s}_0)\cdot \mathbf{r}_{mn}}$$

From assuming a random orientation of the sample, it is allowed to take with equal probability all orientations in space. The exponential term in expression (IV-2) may then be replaced by its average value when the vector $\mathbf{r}_{mn}$ take all orientations with equal probability relative to the diffraction vector $\mathbf{s} - \mathbf{s}_0$. In this case, the average of the exponential term in equation (IV-2) is given by:

$$(IV\text{-}3) \qquad \langle e^{(2\pi i/\lambda)(\mathbf{s} - \mathbf{s}_0) \cdot \mathbf{r}_{mn}} \rangle = \frac{\sin k r_{mn}}{k r_{mn}}$$

where $k = 4\pi \sin\theta / \lambda$. k takes the value for elastic scattering. With substituting equation (IV-3) in equation (IV-2) for the exponential term, expression (IV-2) can be simplified as:

$$(IV\text{-}4) \qquad I_{eu} = \sum_m \sum_n f_m f_n \frac{\sin kr_{mn}}{kr_{mn}}$$

Equation (IV-4) is known as the Debye equation for a random array of scattering atoms. It represents the average unmodified intensity from an array of atoms which takes all orientations with equal probability. It should be noticed that this equation involves only the magnitudes of the distances r_{mn} of each atom from every other atom. The derivation of this relationship is discussed in more detail in Appendix I.

To proceed further, one must take into account the type of atoms within the sample. When a unit of composition (uc) is defined for silica, it would consist of one silicon atom and two oxygen atoms. Let $\sum_{uc}$ be a sum over all the units of composition, N the number of units of composition in the sample, V the irradiated volume of the sample, and N/V the number of units of composition per unit volume.

From expression (IV-2) with separating terms for which n = m and n $\neq$ m, the intensity is given by:

$$(IV\text{-}5) \qquad I_{eu} = \sum_m f_m^2 + \sum_m f_m \sum_{n \neq m} f_n \, e^{(2\pi i/\lambda)(\mathbf{s} - \mathbf{s}_o)\cdot \mathbf{r}_{nm}}$$

If $\rho_m(\mathbf{r}_{nm})\, dV_n$ is the number of atoms in the volume element dV_n at the position $\mathbf{r}_{nm}$ relative to atom type m, the summation over atom type n can be replaced by the integral over the sample volume and spherical symmetry:

$$(IV\text{-}6) \qquad I_{eu} = \sum_m f_m^2 + \sum_m f_m \int_s \rho_m(\mathbf{r}_{nm})\, e^{(2\pi i/\lambda)(\mathbf{s} - \mathbf{s}_o)\cdot\mathbf{r}_{nm}}\, dV_n$$

where the integral is taken of the entire volume of the sample. Designating the kind of atom by j, the average value of $\rho_m(\mathbf{r}_{nm})\, dV_n$ can be expressed by the relation:

$$(IV\text{-}7) \qquad < \rho_m(\mathbf{r}_{nm})\, dV_n > = \frac{N}{V} \sum_{uc} f_j\, dV_n$$

Then, adding and subtracting a term to be involved, this average yields:

$$(IV\text{-}8) \qquad I_{eu} = \sum_m f_m^2 + \sum_m f_m \int_s [\rho_m(\mathbf{r}_{nm}) - \frac{N}{V}\sum_{uc} f_j\,]\, e^{(2\pi i/\lambda)(\mathbf{s} - \mathbf{s}_o)\cdot\mathbf{r}_{nm}}\, dV_n$$

$$+ \sum_m f_m \int_s \frac{N}{V} \sum_{uc} f_j\, e^{(2\pi i/\lambda)(\mathbf{s} - \mathbf{s}_o)\cdot\mathbf{r}_{nm}}\, dV_n$$

Amorphous solids possess no long-range order, and an equivalent way of expressing this is to note that the density function $\rho_m(\mathbf{r}_{nm})$ tends to be $<\rho_m(\mathbf{r}_{nm})>$ at large r. The quantity $[\rho_m(\mathbf{r}_{nm}) - N/V\sum f_j\,]$ tends to zero for distances greater than a few primary atom separations, and hence the integral in the second term of expression (IV-8) is dominated by scattering predominantly from the close scattering centers. The last term of expression (IV-8) involves interactions between distant points in the sample. Warren[29] showed that this last term represents small angle scattering due to the finite sample size, which is generally limited to scattering vectors $k < 2\pi / R$ where R is the specimen size.

Using the average of expression (IV-4) and dropping the last term of expression (IV-8), expression (IV-8) can be simplified:

$$(IV\text{-}9) \qquad I_{eu} = \sum_m f_m^2 + \sum_m f_m \int_s [\rho_m(\mathbf{r}_{nm}) - \frac{N}{V} \sum_{uc} f_j] \frac{\sin kr_{nm}}{kr_{nm}} dV_n$$

With replacing integral by the original sum over n due to $\rho_m(\mathbf{r}_{nm})$ only to be able to justify the average of exp $\{ (2\pi i/\lambda) (\mathbf{s} - \mathbf{s}_o)\cdot\mathbf{r}_{nm} \}$, equation (IV-9) becomes:

$$(IV\text{-}10) \qquad I_{eu} = \sum_m f_m^2 + \sum_m f_m \sum_{n \neq m} f_n \frac{\sin kr_{nm}}{kr_{nm}}$$

$$- \sum_m f_m \int_s \frac{N}{V} \sum_{uc} f_j \frac{\sin kr_{nm}}{kr_{nm}} dV_n$$

Instead of summing over m, it is worthwhile to consider atom centers located in spherical shells at distances of r_{ij} from an atom type j. Let r_{ij} be the distance from an atom j to an atom in the *i* th shell of surrounding atoms and N_{ij} be the average number of atoms in shell i at a distance r_{ij} from an atom type j. Summations may be performed over the individual shells. Also, let $q_m(r)$ be the fraction within the sample that lies on a sphere of radius r centered on atom m. Extending the integral from zero to infinity since $q_m(r)$ goes to zero for large r and equals 1 for r = 0, equation (IV-10) becomes:

$$(IV\text{-}11) \qquad I_{eu} = N \sum_{uc} f_j^2 + N \sum_{uc} f_j \sum_i N_{ij} f_i \frac{\sin kr_{ij}}{kr_{ij}}$$

$$- \frac{N}{V} \sum_{uc} f_i \sum_m f_m \int_0^\infty \frac{\sin kr_{nm}}{kr_{nm}} 4\pi r^2 q_m(r) dr$$

Replacing $q_m(r)$ by its average value q(r), multiplying by k, equation (IV-11) can be rearranged:

$$\text{(IV-12)} \qquad k\left(\frac{I_{eu}}{N} - \sum_{uc} f_j^2\right) = \sum_{uc} f_j \sum_{i} f_i \frac{N_{ij}}{r_{ij}} \sin kr_{ij} - \frac{N}{V}\left(\sum_{uc} f_j\right)^2 4\pi \int_0^\infty rq(r) \sin kr \, dr$$

Introducing the abbreviations as below:

$$\text{(IV-13)} \qquad i(k) = \left\{\frac{I_{eu}}{N} - \sum_{uc} f_j^2\right\} / g^2(k) \quad \text{and} \quad Y(k) = 4\pi \int_0^\infty rq(r) \sin kr \, dr$$

where i(k) expresses the relative difference between the total scattering intensity and the independent intensity. Expression (IV-13) can be simplified:

$$\text{(IV-14)} \qquad k\, i(k) = \sum_{uc} f_j \sum_{i} f_i \frac{N_{ij}}{r_{ij}} \frac{1}{g^2(k)} \sin kr_{ij} - \frac{N}{V}\left(\sum_{uc} f_j\right)^2 \frac{1}{g^2(k)} Y(k)$$

Now it is necessary to introduce a convergence factor $e^{-\alpha^2 k^2}$ and sharpening factor $1/g^2(k)$ to k i(k) before performing the Fourier inversion because k i(k) may display very large peaks and dips at k_m, a maximum value in k. The convergence factor will be used for damping intensity data by reducing termination satellites and weighting down the inaccurate measurements at high values of k. For example, an adjustable constant α^2 in a convergence factor $e^{-\alpha^2 k^2}$ can be set as $1/ k_m^2$. With dividing by a sharpening factor, where g(k) decreases with increasing k and has the value g(k) = 1.0 at k = 0, the picks and dips at high values of k is sharpened.

For example, the sharpening factor g(k) can be set as the average electron scattering factor. Also, any other suitable function can be used.

Multiplying by the convergence factor and sin kr, dividing by the sharpening factor, and then integrating from k = 0 to k = k_m, expression (IV-14) becomes:

$$\text{(IV-15)} \qquad \int_0^{k_m} ki(k)\, e^{-\alpha^2 k^2} \sin kr\, dk = \sum_{uc} \sum_i \frac{N_{ij}}{r_{ij}} \int_0^{k_m} \frac{f_j f_i}{g^2(k)} e^{-\alpha^2 k^2} \sin kr_{ij} \sin kr\, dk$$

$$- \frac{N}{V} \int_0^{k_m} \left(\sum_{uc} f_j\right)^2 \frac{e^{-\alpha^2 k^2}}{g^2(k)}\, Y(k) \sin kr\, dk$$

and

$$g^2(k) = \left(\sum_{uc} f_e\right)^2 = \left(\sum_{uc} f_j\right)^2 / \left(\sum_{uc} Z_j\right)^2$$

where f_e is the average scattering factor per electron, f_j is the atomic scattering factor of the *j* th kind of atom and Z_j is the atomic number of the *j* th kind of atom. For example, $f_e = (f_{si} + 2f_o) / (14 + 2 \times 8)$ in vitreous silica. The last term of equation (IV-15) with a term having all of its slowly varying quantities can be replaced by their values at k = 0. Y(k) is negligible except at small values of k because it decreases rapidly with increasing values of k. Hence, it is possible to let the integral expand to infinity. The last term of equation (IV-15) becomes:

$$\text{(IV-16)} \qquad \frac{N}{V} \int_0^{k_m} \left(\sum_{uc} f_j\right)^2 \frac{e^{-\alpha^2 k^2}}{g^2(k)}\, Y(k) \sin kr\, dk = \frac{N}{V} \left(\sum_{uc} Z_j\right)^2 \int_0^{\infty} Y(k) \sin kr\, dk$$

From the definition of Y(k), it can be inverted by using the inversion relations for the Fourier integral. If $\phi(k)$ is the Fourier transform of f(r), then f(r) is given as the Fourier transform of $\phi(k)$. With constants appropriate to Y(k), the relations are defined by the expression:

$$\phi(k) = 4\pi \int_0^\infty f(r) \sin kr \, dr$$

and

$$f(r) = \frac{1}{2\pi^2} \int_0^\infty \phi(k) \sin kr \, dk$$

Identifying $\phi(k)$ with Y(k) and f(r) with rq(r), the Fourier transform of Y(k) becomes:

$$2\pi^2 \, rq(r) = \int_0^\infty Y(k) \sin kr \, dk$$

With a little rearrangement, the right hand side of equation (IV-16) can be simplified by:

$$2\pi^2 \, rq(r) \frac{N}{V} \left(\sum_{uc} Z_j\right)^2 = 2\pi^2 \, r\rho_e \sum_{uc} Z_j \qquad \text{(IV-17)}$$

where $\rho_e = (N/V) \sum_{uc} Z_j$, ρ_e is the average electron density, and q(r) = 1.0 for the small r. Inserting equation (IV-16) and (IV-17) into equation (IV-15),

$$\text{(IV-18)} \qquad \sum_{uc}\sum_{i} \frac{N_{ij}}{r_{ij}} \int_0^{k_m} \frac{f_j f_i}{g^2(k)} e^{-\alpha^2 k^2} \sin kr_{ij} \sin kr \, dk$$

$$= 2\pi^2 r\rho_e \sum_{uc} Z_j + \int_0^{k_m} k\, i(k)\, e^{-\alpha^2 k^2} \sin kr \, dk$$

The use of the pair functions in an exact treatise of amorphous scattering was pointed out by Waser and Schomaker.[28] They indicated that the number of interatomic interactions at a given distance could be found by the Fourier transform of the suitably modified interatomic part of the intensity function multiplied by r. More precisely, a set of the pair functions $P_{ij}(r)$ introduced by Warren[29] is defined:

$$\text{(IV-19)} \qquad P_{ij}(r) = \int_0^{k_m} \frac{f_j f_i}{g^2(k)} e^{-\alpha^2 k^2} \sin kr_{ij} \sin kr \, dk$$

A set of the pair functions $P_{ij}(r)$ can be solved by means of the auxiliary functions $Q_{ij}(r)$. There will be one auxiliary function for each type of atom pair. The variation of electron density versus distances for each atom pair will be described by an independent auxiliary function. For example, SiO_2 will have $Q_{Si\text{-}Si}$, $Q_{Si\text{-}O}$, and $Q_{O\text{-}O}$. Each Q-function consists of symmetric peak centered at $x\ (= r - r_{ij}) = 0$. Let the auxiliary pair function Q_{ij} be as:

$$\text{(IV-20)} \qquad Q_{ij}(x) = \frac{1}{2} \int_0^{k_m} \frac{f_j f_i}{g^2(k)} e^{-\alpha^2 k^2} \cos kx \, dk$$

Using of the auxiliary functions $Q_{ij}(x)$ can simplify a set of the pair

functions $P_{ij}(r)$. By using the relationships of the trigonometric functions, $\sin kr_{ij} \sin kr = \{\cos k (r - r_{ij}) - \cos k (r + r_{ij})\} / 2$, a set of the pair functions can be written as:

$$P_{ij}(r) = Q_{ij}(r - r_{ij}) - Q_{ij}(r + r_{ij}) \qquad \text{(IV-21)}$$

Since $Q_{ij}(r + r_{ij})$ is usually small enough to neglect, equation (IV-21) with inserting equation (IV-19) becomes:

$$P_{ij}(r) \approx Q_{ij}(x) = \frac{1}{2} \int_0^{k_m} \frac{f_j f_i}{g^2(k)} e^{-\alpha^2 k^2} \cos kx \, dk \qquad \text{(IV-22)}$$

where $x = r - r_{ij}$.

In terms of the pair functions, equation (IV-18) can be simplified:

$$\sum_{uc} \sum_{i} \frac{N_{ij}}{r_{ij}} P_{ij}(r) = 2\pi^2 r\rho_e \sum_{uc} Z_j + \int_0^{k_m} ki(k) e^{-\alpha^2 k^2} \sin kr \, dk \qquad \text{(IV-23)}$$

Equation (IV-23) is the Warren's final expression in an exact treatment which is used in structure determination of an amorphous solid. It is certain that the exact method presents a considerable advantage relative to the traditional methods and should be more widely employed. It ends the criticism relative to the effective electron number and permits an increase in the resolution in extending the limit k_m without risk of introducing artificial peaks into the PFD.

The right hand side of equation (IV-23) is an experimentally determined term. The ρ_e is obtained from a measure of the sample density in the absence of porosity. The k i(k), a quantity previously defined in

equation (IV-14), is determined from the initially observed coherent intensity which is normalized after making several corrections discussed in Chapter VI. By choosing suitable sharpening factor and convergence factor, the right hand side of equation (IV-23) can be evaluated and plotted as a function of r. The first few peaks represent the various interatomic distances r_{ij} between the relative atoms. With known atomic sizes and interatomic distances in the crystalline solids, it is possible to identify the kinds of atoms associated with r_{ij} of each peak for an amorphous sample. However, this task is difficult at higher values of r_{ij} due to the peak overlapping and the greater variety of possible interatomic combinations.

The left hand side of equation (IV-23) is used to develop a proposed theoretical model. Applying the same convergence factor and sharpening factor, the pair functions $P_{ij}(r)$ can be evaluated for each r_{ij} by using equation (IV-22). Given some proposed model of the structure, through trial and error, each coordination number N_{ij} for each r_{ij} can be derived by best matching the summation of the ordinates of all these peaks in $P_{ij}(r)$ and the experimental curve. At the case of the best fit, the peaks of the right hand side of equation (IV-23) may be a little broader and lower due to variations in each r_{ij}. Although this procedure does not seem to be a unique method, it is possible to describe well the atomic structure of the amorphous solids in a more precise manner than with the radial distribution function.

C. Application of Pair Function Distribution in Vitreous Silica

Mozzi and Warren[30] applied the pair function distribution (PFD) to analyze the structure of vitreous silica. Using CuK_α radiation and RhK_α

radiation with the Warren-Mavel X-ray fluorescence technique[31], they measured reliable intensity to k = 20. The PFD curve, measured and calculated by Mozzi and Warren[30], are shown in Figure 5. The solid curve is the experimental PFD and dashed curve is the calculated PFD.

In crystalline silicates, it is found that each silicon atom is tetrahedrally surrounded by four oxygen atoms with the Si-O distance of 1.62 Å and the O-^{1st} O distance of 2.65 Å. In comparison of this information with Figure 5, the first peak on the distribution curve of Figure 5 corresponds to the Si-O distance of 1.62 Å, and the second peak corresponds to the O-^{1st} O distance of 2.65 Å. The widths of these peaks are consistent with a tetrahedral distribution of oxygen atoms around each silicon atom, as shown by the calculated peaks in Figure 5. The third peak, which is at 3.12 Å, is the Si-^{1st} Si contribution, and is much broader than the other two peaks due to the angular variation of Si-O-Si bond. The fourth peak, which is at 4.15 Å, is the Si-^{2nd} O contribution. The fifth peak, which is at about 5.1 Å, is a combination of the O-^{2nd} O and Si-^{2nd} Si peaks. The sixth peak, which is at about 6.4 Å, may result from the Si-^{3rd} O contribution.

After having determined several peaks of the PFD, the next step is to represent the variation of interatomic distances with a distance distribution function (DDF). This DDF can theoretically be calculated by deconvoluting each of the peaks of the PFD. In principle, the number of neighbors about an atom can be obtained by comparing the peak area on the experimental curve to the area of the PFD. This procedure is not practical due to serious overlapping of the PFD peaks. So, it is practical method that the values of N_{ij} and the distribution of r_{ij}, which must be assumed to bring the sum of the computed pair functions, are chosen by trial and error to give the best fit

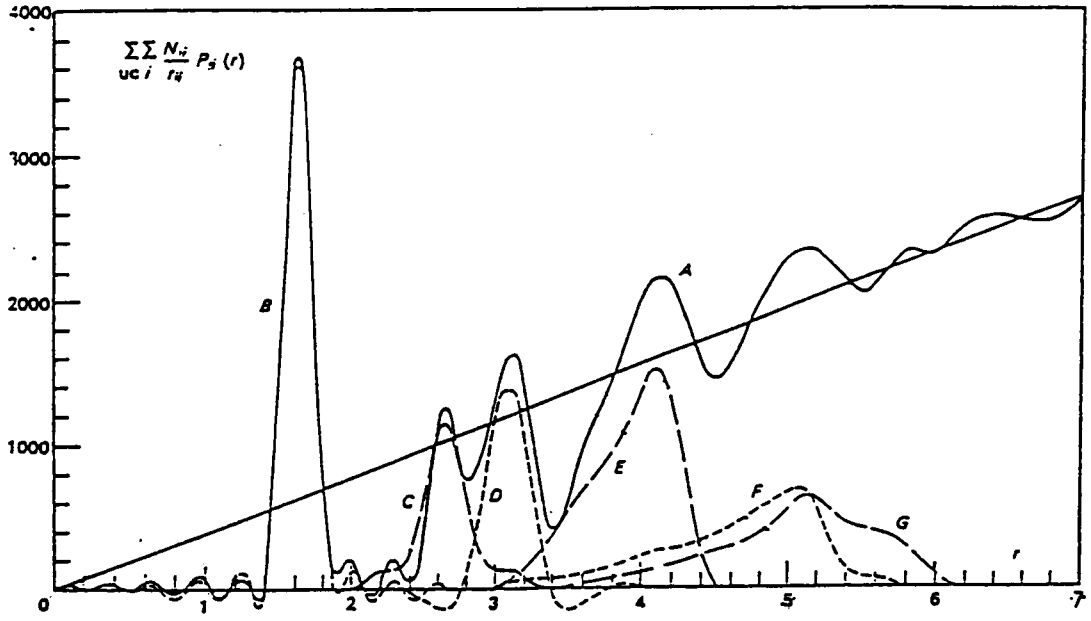

Figure 5. The pair function distribution curves for vitreous silica. A is the experimental curve. The calculated contributions are given by: B, Si-O; C, O-^{1st} O; D, Si-^{1st} Si; E, Si-^{2nd} O; F, O-^{2nd} O; G, Si-^{2nd} Si. From Mozzi and Warren, reference 30.

for the experimental curve of Figure 5. A best fit could be obtained only up to the fourth peak of the PFD. When a set of DDF giving a calculated PFD in close agreement with the experimental PFD is obtained, the structure of vitreous silica can be described quantitatively.

A typical vitreous silica DDF obtained by Mozzi and Warren[30] is shown in Figure 6. The distance distribution of Si-^{1st} Si is shown in Figure (6a) and the angular distribution of Si-O-Si is shown in Figure (6b). The ratio of the O-1^{st} O to the Si-1^{st} O distance is equal to $2.65/1.62 = \sqrt{8}/3$ and is exactly what would be expected for tetrahedral bonding. The angular distribution function $V(\alpha)$ shows a variation in the Si-O-Si bond angle of 120° to 180° with a maximum at 144°. As shown in Figure 7, the unit structure of vitreous silica can be taken as a SiO_4 tetrahedron, consisting of silicon at the center and four oxygen at the corners of the tetrahedron with a maximum at Si-O-Si bond angle $\alpha = 144°$.

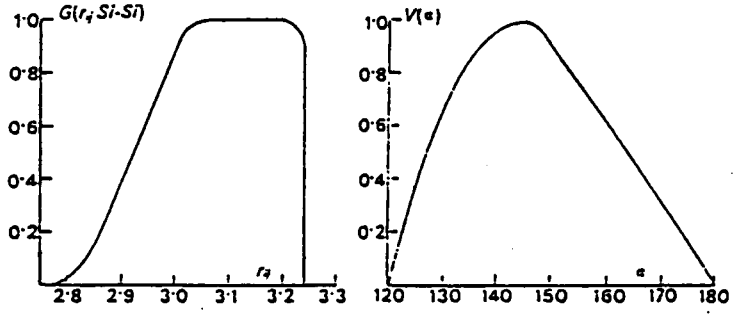

Figure 6. (a) The distribution function for the Si-Si distance of vitreous silica. (b) The distribution function with the Si-O-Si bond angle of vitreous silica. From Mozzi and Warren, reference 30.

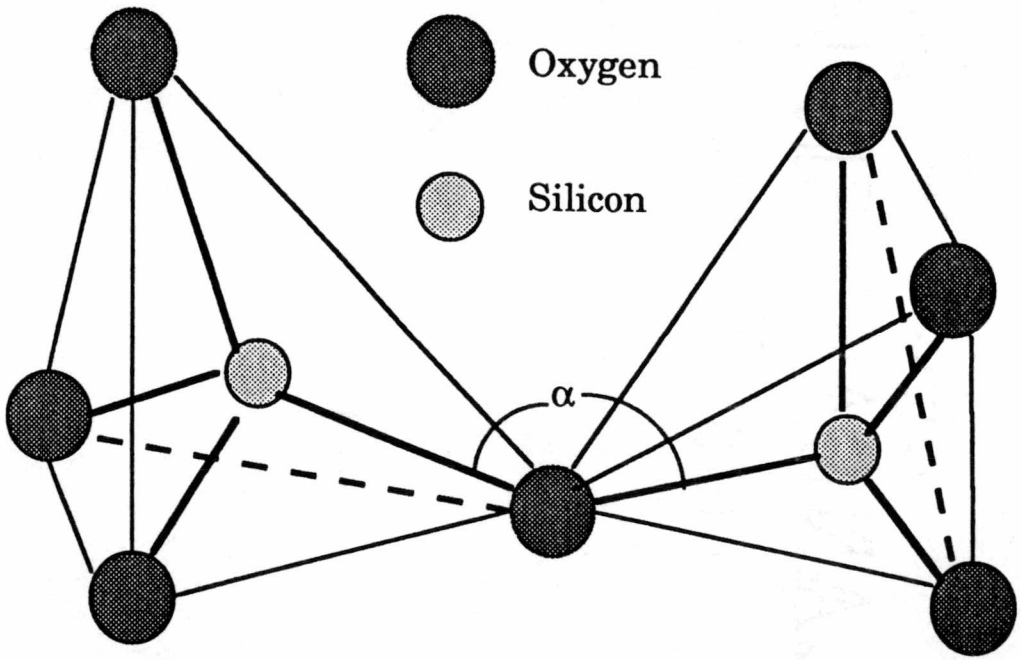

Figure 7. Schematic representation of adjacent tetrahedra in vitreous silica.

Chapter V.

Experimental Procedure

A. Microwave Heating of Sample

The 99.9% pure fused silica which was purchased from Aldrich Chemical Company, Inc. of Wisconsin and the silica sand which was supplied by the Oak Ridge National Laboratory were used as starting materials. The concentration of impurities in the as-received materials was scanned by ICP Spectrometry in the Oak Ridge National Laboratory.

These silica samples were heated in the Model S6F Cober microwave oven which operated at 2.45 GHz. The samples were inserted at the region of the highest electric field intensity in a microwave cavity. To melt the samples in this investigation, the microwave power of 1 kW for the silica sand and 2 kW for the pure fused silica was supplied. The output of the IR-pyrometer was recored to monitor the instaneous surface temperature of the sample. Zero time was marked by the instant the microwave power was turned on. Before any experiments were started, the single-stub tuner with aid of the forward and reflected power measurement was controlled to match the impedance between the source and the load to optimize heating. The heated samples were held at their melting point for a short period of time and then air quenched to room temperature. Although an automatic controller was readily available for this work, all the experiments and data recordings were performed manually due to the short processing time.

The silica sand was heated effectively although a susceptor was not used to couple with microwave radiation. The reason was that the silica sand

contained about 3% impurities. Since the 99.9% pure fused silica, a low-loss material, was transparent to 2.45 GHz microwave radiation, it could not be effectively heated to its melting point in a current microwave cavity. To accomplish efficient coupling of the sample to the microwave radiation, a zirconia substrate, a high-loss material, was used as a microwave coupler. The microwave coupler (the zirconia plate) initially absorbed the 2.45 GHz microwave energy. Above a critical temperature, the increase in the loss tangent of pure fused silica sample caused the pure fused silica sample to couple with the microwave energy, and then the pure fused silica sample could be heated continuously up to its melting point. Alternatively, microwave hybrid heating could be used instead of the microwave coupler. The only difference between microwave hybrid heating and microwave coupler heating was the kind of heat source used.

B. Microwave Heating System

The microwave heating system used was the Cober Model S6F industrial microwave system. In this system, microwave power was supplied to the microwave cavity through a waveguide by a 6 kW variable-power microwave generator operating at 2.45 GHz. The generator was housed in a cabinet. The complete assembly measured 163 cm high, 91 cm wide and 46 cm deep. Air, to cool the cabinet, was brought in through a heat exchanger mounted on the top of the cabinet and a portion of the air was exhausted through the waveguide to the applicator.

Two of the major components, the magnetron tube and the circulator, were directly water cooled. Components included in the waveguide sections were a protective circulating water load and a single-

stub tuner used to match impedance between the source and the load. The applicator was mounted to a waveguide flange such that the load was along the geometric center line of incident microwave irradiation. A multi-mode resonant cavity served as an applicator that was coupled to the power source using WR-284 waveguide sections. This cavity was covered with low-loss thermal insulation.

A block diagram of the microwave heating system used in conducting the various experiments is shown in Figure 8. A detailed description of how each individual component fits into the system is presented in the following section.

1. Microwave Generator

The microwave generator, a key element in the microwave system, is available with continuous output power ranges from 1 kW to 6 kW at 2.45 GHz. The microwave generator has a single variac power level control and a pair of meters which indicates forward and reflecting power flow into and out of the waveguide. The amount of available microwave power from the generator is varied by changing the anode current of the magnetron tube. This magnetron tube, source of the microwave power, is commonly water cooled at power levels in excess of 1 kW.

The reflected power meter is a useful tool in this tuning system which is referred to as impedance matching. Instantaneous changes in the input admittance of the applicator can be monitored by the reflected power meter. The optimal match between source and load is established when the reflected power is at a minimum for any given forward power

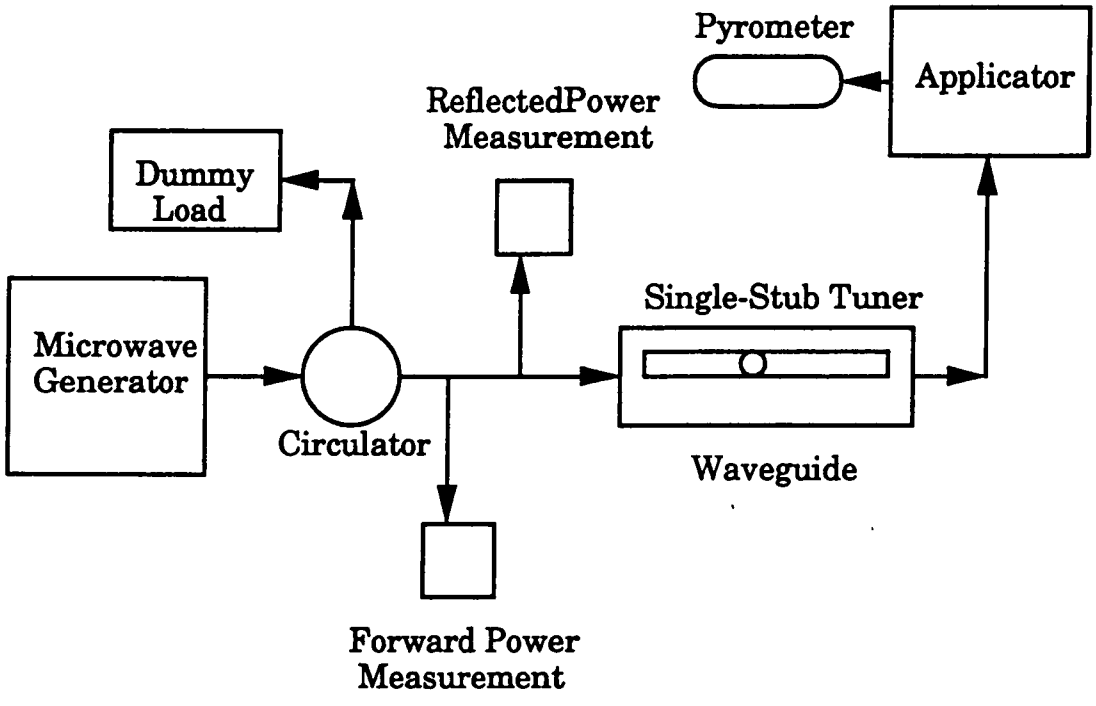

Figure 8. Schematic representation of the microwave heating system.

setting. The actual absorbed power into the sample is simply the difference between the forward power and the reflected power.

2. Circulator

The protective devices in a microwave generator are a 3-port circulator and a dummy load. The 3-port circulator is a tube protection device which prevents reflected microwave energy from reaching and possibly damaging the magnetron tube because the circulator diverts the reflected microwave energy from the applicator to its third port where a dummy load is mounted. The dummy load connects to the 3-port circulator, is normally a water load in higher power configurations. As a result, the magnetron in the microwave generator is protected from possible damages which follows an excessive feedback of microwave energy from the load.

3. Waveguide

The waveguide in a microwave heating system is simply used as a conduit for the transmission of microwave energy from the source to the applicator. In this study, a WR-284 brass waveguide was used. This waveguide can be configured with any assortment of straight sections and bends. The most important waveguide component is a tuning section. The single-stub tuner is the device which is used to impedance match the load to the source. Since the single-stub tuner helps to minimize the amount of net-reflection of microwave power by the whole applicator structure when it is properly positioned, the load can be placed in a high-electric field intensity region.

4. Applicator

The applicator used is a multi-mode resonant cavity which is the most common applicator in a microwave heating system. The applicator is a rectangular box made from stainless steel that has been seam welded to prevent arcing. The internal dimensions of the stainless-steel cavity (24" wide, 25.5" deep and 27" high) are multiples of a half wavelength of the 2.45 GHz microwave frequency to heat large irregular samples uniformly. The microwave power density in the applicator may be made uniformly with a very large number of cavity modes by allowing the microwave energy to reflect on and off of the cavity walls many times. The small reaction cavity (9.5" wide, 9.5" deep and 9.75" high) inside the metal shielded cavity has an area 54 cm^3 surrounded by Babcock-Wilcox 17C alumina insulation which serves as a heat shield and withstand up to 3000 °F.

The insulation, transparent to microwaves but opaque to infrared radiation, forms an infrared cavity to trap whatever heat energy the load converts from the microwave irradiation. In practice, some heat is conducted through the less than perfect insulation and is lost as radiation to the ambient environment. The door on the cavity has an absorbent material to prevent microwave leakage. The absorbent material used is "ECOSORB", which is a ferrite filled rubber composition.

5. Temperature Measurement

Temperature measurement in a microwave field is not always a simple matter. In spite of many efforts[109-113] to measure accurate temperature in a microwave field, there is no adequate method in use.

However, shielded thermocouples have been commonly used to acquire temperature by many researchers. Johnson[114] reported that the presence of metallic structure concentrated the electric field and produced unwanted hot spots during his experiment. The shield may perturb the microwave field around the thermocouple region. This field perturbation may affect the electromagnetic field distribution around sample and also affect measuring the temperature of the sample. Unshielded thermocouple elements will act as an antenna and channel microwave energy out of the microwave oven cavity. Therefore, direct temperature measurement using a thermocouple is extremely difficult in the electromagnetic field due to its interference with the field which induces an extra voltage in the thermocouple wires.

As an alternative method, an infrared pyrometer is an adequate technique because it neither perturbs the electromagnetic field nor causes hot spots. With the use of the infrared pyrometer, the measured temperature corresponds to the surface temperature of the sample, which is lower than the internal temperature of the sample due to convection loss. It indicates that neither the infrared pyrometer nor the thermocouple yields the absolute value of temperature relative to the explanation of physical phenomena such as sintering activation energy and enhanced diffusion. It is because no temperature comparison is possible with conventional heating where the temperature gradient is inverted as suggested by Berteaud & Badot.[37] When the infrared pyrometer is a part of control system, the absolute value of temperature is not necessary because the objective of a system is to maintain the relative surface temperature constant at a desired value. Consequently, the infrared pyrometer will be a

suitable tool for the surface temperature feedback control system due to the measurement of the instantaneous changing in temperature.

In this investigation, temperature was measured by the Mikron model 210s infrared pyrometer. The manufacture's manual states that its accuracy is within 1.0% up to 2000 °C. Since Mikron infrared pyrometer has a silicon photo voltaic detector, it only detects the thermal radiation between 0.6 μm and 1.0 μm among the thermal radiation from the sample surface being measured. The setting of the emittance knob on the infrared pyrometer is important when infrared pyrometer is used to measure accurate temperature, but is not important when instrument is used as a control system. The objective of temperature measurement was to maintain the relative surface temperature constant at a desired value. Therefore, the emittance knob was usually set to the value of 1.0.

C. Sample Preparation in the X-ray Diffraction

The microwave samples, which were 99.9 % pure fused silica and silica sand, were prepared in a 2.45 GHz microwave system. The conventional pure fused silica was purchased from Aldrich Chemical Company, Inc. of Wisconsin and the conventional silica sand was supplied by the Oak Ridge National Laboratory. To prepare powder sample for X-ray diffraction experiment, the microwave sample and conventional sample were pulverized in an alumina crucible and then passed through a 325 mesh per square inch screen. After that, powder samples were compressed into a 0.25" thick rectangular cavity having a 25 x 25 mm dimension.

D. Balanced Filters Preparation in the X-ray Diffraction

The Zr-Y balanced filter was constructed to isolate the MoK_{α} doublet and the Compton modified scattering using a transmission of about 33% for filter of Y-foil at the line interest. The optimum thickness[115] of yttrium foil for molybdenum radiation was about 25 μ. The zirconium foil of 0.1 mm thickness was required to balance 25 μ yttrium-foil. Since the Zr-foil and Y-foil were available commercially, they were purchased from Alpha Inorganics, Inc. A check of the balance could be made by using an analyzing crystal placed in place of the sample on the X-ray diffractometer. When the balanced Zr-Y filter away from the detector slit is placed, evidently diminished the effects of the fluorescence from the Y-filter can be evidently diminished. Therefore, the balanced Zr-Y filters were placed in front of the receiving slit of the diffracted X-ray beam.

E. X-ray Diffraction Scans

A Scintag PADV X-rays generator, high frequency and ultra-stabilized 4.0 kilowatt generator, was used to drive Cu and Mo AEG X-ray tubes under full-wave rectification and high stability through solid-state circuitry. Focusing conditions for a flat powder sample were maintained by driving the detector at twice the sample rotation rate so that the sample always coincided with the diffraction vector $\mathbf{s} - \mathbf{s}_0$. Thus, the detector recorded the measured intensity as a function of the angle (usually given as 2θ). Since the dimensions of the sample irradiated by X-ray beams would be changed continuously as the diffraction angle varies, it was necessary to select a slit of an angular aperture appropriate for the measuring angle range. In addition, the solar slit was used to minimize the angle of

inclination as less as possible. It was composed of metal foil piled up leaving some space between each layer in parallel with the focusing circle plane. The space between each layers of metal foil was designed to make the angular aperture of X-ray beams become 5°. The standard diffraction geometry as shown in Figure 9 was used for the CuK_α and MoK_α diffraction scans. By selecting targets and appropriate focusing geometry, CuK_α and MoK_α lines of X-rays could be produced.

The technique used to record CuK_α and MoK_α diffraction runs was by step scanning a horizontal goniometer in increments of 0.1° 2θ. Since the intensity of the sample was very low, a rate meter time-constant of 40 seconds was used. The intensity of the sample was determined by the Sintag Germanium detector after it passed through a pulse height analyzer whose baseline and window were calibrated in accordance with the radiation used. No graphite monochromator was required to resolve K_α and K_β radiation because Sintag solid-state detector inherently discriminated between X-rays of differing energies. Scintag solid-state detector did not require to use monochromator, thereby allowing the full intensity of the diffracted beam to be measured. Another benefit was the intrinsically low background of the solid-state detector, which operated near liquid nitrogen temperatures, resulting in better peak-to-background ratios and greater sensitivity. A permanent record of the intensity was stored at MicroVAX 32-bit computer on a data file listing angle, total count, normalized count, and scan condition. The procedure was fully automated and presented the raw intensity data in a form that was readily adaptable for any computer processing.

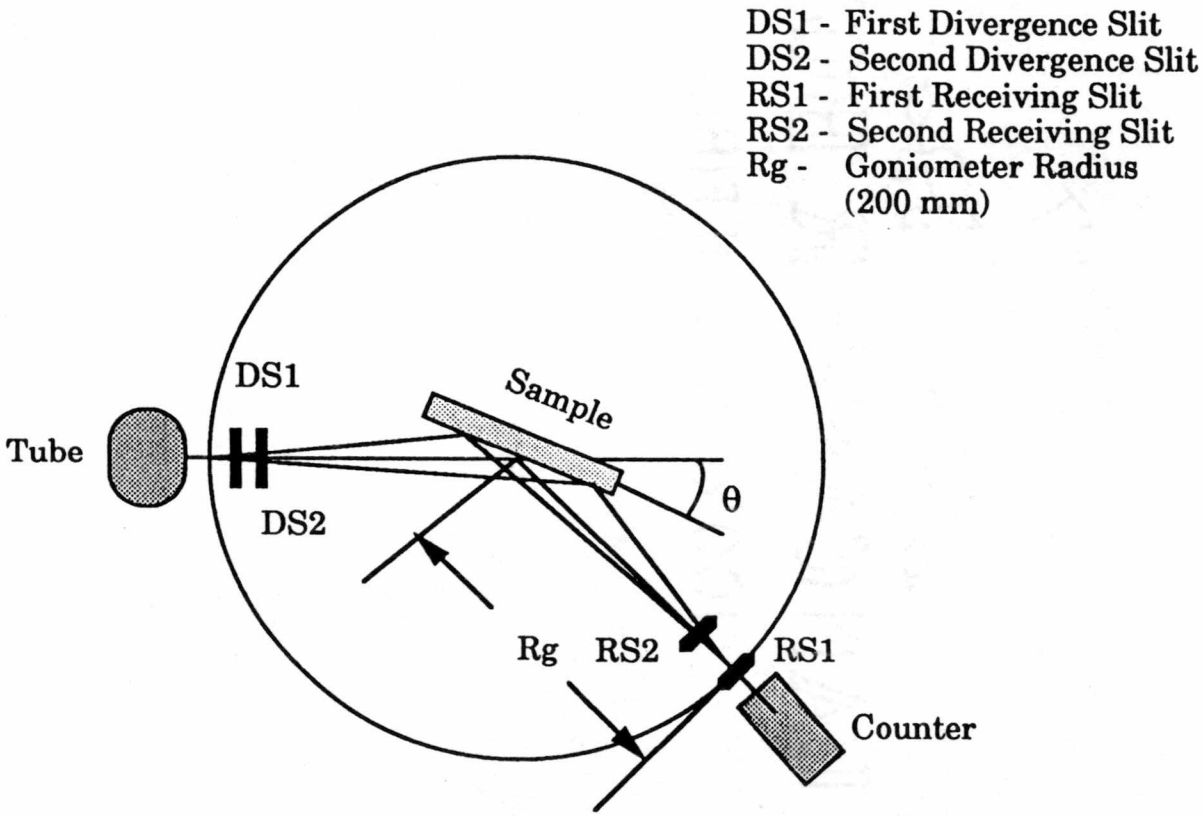

Figure 9. Schematic diagram of X-ray diffractometer assembly.

Prior to each diffraction scan, background scan of air scattering was obtained by running with the absence of the sample under the standard condition that would be identical to subsequent diffraction run. Also, background level of instrument was recorded with X-rays and electronics operating under standard condition with the X-ray port closed. Since repeated CuK_α scans were practically identical, a smooth curve drawn through two scan was used for the final result. In the case of MoK_α scan, a smooth curve drawn through a superposition of three MoK_α scans was used for the final results. In addition, diffraction patterns were measured using direct chart plotting and continuous scanning at a count speed of 0.5° per minute. Since intensities of sample were very low, a rate meter time-constant of 40 seconds is used to smooth intensity fluctuations by choosing the scan speed to be 1/32 2θ/min. The slowly varying patterns could be not distorted by this relatively long time constant.

1. X-ray Diffractometer Alignment

First, the height and inclination of the goniometer were adjusted so that the focus of X-rays and the slit system were on the same height, and the slit system was on the same plane. Next, a fine rotation adjustment of the sample axis was carried out so that the surface of the powder sample was on the same plane. Hence, after the 2θ is set to 0.00°, the X-ray generator was set to the working condition with a divergence slit of 0.05 mm, a receiving slit of 0.05 mm, and two alumina absorber plates. As the direct X-ray beams entered the counter, the tube voltage and tube current should have been set to less than 9 KV and 1 mA. With the adjustment at the position where the X-ray intensity reached the maximum, the mutual

relations between the slit system and the focus of X-rays could be adjusted correctly.

The scanning speed of the goniometer was set to 1/4° per minute, and the scanning speed of the chart paper to 20 mm/min. The installed computer program was made to perform an automatic recording of the X-ray intensity by in a range of 0.5° ~ - 0.5°. After the center point of the half width maximum intensity in the X-ray intensity distribution on the computer monitor was taken, the difference between this point and the 0° position of the angle mark were measured. This alignment procedure was repeated until the difference was less than 1/100°.

2. CuK_α Radiation

The Cu X-ray tube was operated at 45 kV and 40 mA. The diffraction scans were conducted over a range of 2θ extending from 7° to 151°. Time constant of rate meter was 40 seconds. The intensity was later extrapolated to 0° so that the scope of the diffraction scan was from k = 0 to k = 7.80 $Å^{-1}$. The slit system was composed of an adjustable first divergence slit of 0.3 mm, an adjustable second divergence slit of 0.5 mm, an adjustable first receiving slit of 0.5 mm, and an adjustable second receiving slit of 0.2 mm. Although Cuk_α $\lambda/2$ was excited at the operating voltages, the half wavelength contribution was entirely negligible for this study.

3. MoK_α Radiation

The Mo X-ray tube was usually operated at 50 kV and 40 mA. Since powder sample was glass material of low atomic number, the measured intensity was very low. Hence, a rate meter time constant of 40 seconds was

used to get higher intensity and to smooth intensity fluctuation This slowly varying patterns was not distorted by this relatively long time constant. The step scans covered the range from 7° to 151° 2θ or the interval of k = 1.08 to k = 17.11 $Å^{-1}$. The slit system was composed of an adjustable first divergence slit of 0.3 mm, an adjustable second divergence slit of 0.5 mm, an adjustable first receiving slit of 0.5 mm, and an adjustable second receiving slit of 0.2 mm. The Zr-Y balanced filters were inserted in the position of the first adjustable receiving slit to effectively eliminate the Compton modified scattering.

Chapter VI.

Experimental Data Reduction and Processing

To obtain the best intensity data possible, several corrections had to be handled on the raw intensity data before the intensity data could be analyzed and the pair function distributions obtained. Therefore, careful data reduction is explained in detail in this chapter.

The intensity in electron units per unit of composition (I_{eu}/N) was obtained by correcting the measured X-ray diffraction intensity (I_m) for background (B), polarization (P), absorption (A), multiple scattering (M.S.), Compton modified scattering (C.M.), and normalization (n). In general, I_{eu}/N is formulated as:

$$\frac{I_{eu}}{N} = \frac{n\,(I_m - B)}{P\,A} - C.M. - M.S. \qquad \text{(VI-1)}$$

Corrections and analyses were performed using an Macintosh IIsi computer with the my own programs written in FORTRAN 77 and the commercialized plotting programs.

A. Correction for Anomalous Dispersion Scattering

It is assumed that the X-ray wavelength is much smaller than any of the absorption edge wavelengths in the atom and that electron distribution in the atom takes on spherical symmetry. Since this assumption did not hold in this investigation, it was necessary to employ the anomalous

dispersion correction. Therefore, the corrected scattering factor is expressed by:

$$(VI\text{-}2) \qquad f_j = f_j^0 + \Delta f_j' + i \Delta f_j''$$

where f_j^0 is the uncorrected scattering factor for radiation with frequency much higher than any absorption edge. $\Delta f_j'$ and $\Delta f_j''$ are the real and imaginary dispersion corrections which depend on the X-ray wavelength. Angular dependence of $\Delta f_j'$ and $\Delta f_j''$ is small compared to f_j^0. Here $\Delta f_j''$ represents a small shift in phase of the scattered radiation.

The values of f_j^0 as a function of k is computed from self-consistent field relativistic Dirac-Slater wave functions by Cromer and Weber.[116] These Dirac-Slater wave functions are given by:

$$(VI\text{-}3) \qquad f_j^0 = \sum_{i=1}^{n} a_i \exp(-b_i k^2) + c$$

with n = 4. The coefficients a_i, b_i and c, which fit f_j^0 of silicon and oxygen, are listed in Table 2. This analytical function is a precise means of representing the f_j^0 curves over the entire range. It is also a convenient means for entering the f_j^0 curves into a computer. From equation (VI-2) and (VI-3), the independent coherent scattering, $\sum_{uc} f_j^2$, is computed from using Dirac-Slater scattering factors including the anomalous dispersion corrections for silicon[117] and oxygen[118] listed in Table 3.

B. Correction for Background Noise and Instrumental Background

Table 2. Coefficient for nine parameter of Dirac-Slater scattering factors.

	a_1	a_2	a_3	a_4	b_1	b_2	b_3	b_4	c
Si	6.0755	3.2815	2.1670	1.3197	2.3497	29.1900	0.7060	84.8342	1.1533
O	2.8604	2.5212	1.5296	0.8135	12.7907	5.4279	0.3282	34.9406	0.2742

Table 3. Anomalous dispersion corrections.

	$\Delta f_j'$ ($CuK\alpha$)	$\Delta f_j''$ ($CuK\alpha$)	$\Delta f_j'$ ($MoK\alpha$)	$\Delta f_j''$ ($MoK\alpha$)
Si	0.23	0.36	0.09	0.09
O	0.0	0.1	0.0	0.0

A background noise in the X-ray diffractometer system is obtained by cosmic sources, other nearby equipment, or poor calibration of electronics from the instrument itself. This contribution to the measured X-ray intensity may be determined by running the X-ray tube and electronics under standard operating conditions with the X-ray port closed.

The instrumental background is obtained by extraneous scattering of the X-ray beam; it is raised from air scattering in the neighborhood of the sample and from spurious effects in slits, collimators, etc. This contribution to the measured intensity may be determined by making a complete run under identical operating conditions without the sample. The correction for air scattering was usually important only for the measurements with CuK_α at small angle regions.

Assuming that the observed intensity with the sample removed is from about twice as much irradiated volume as with the sample in position, the total correction for air and background noise[119] can be given by:

$$\text{(VI-4)} \qquad B = R(\text{air}) + R(b) = \frac{1}{2}[\, R(\text{rem}) + R(b) \,]$$

where R(air) is the measured intensity due to air scattering with the sample in position, R(b) is the measured intensity due to background noise when the primary beam is shut off, and R(rem) is the measured intensity with the sample removed.

This was the first correction to the raw intensity data. A background noise was less than a few counts per second. Air scattering was negligible on the MoK_α scans and small beyond the first peak on the CuK_α scans.

Since air scattering dominated the patterns below the first peak on the CuK_α scans, I_{eu}/N was usually extrapolated to zero from $2\theta = 7°$ to $2\theta = 0°$.

C. Correction for Polarization

Although X-rays are scattered in all directions by an electron, the intensity of the scattered beam depends on the angle of scattering. As first worked out by J. J. Thomson[120], the intensity scattered by a single electron at a distance r is given by:

$$I = I_o \frac{K}{r^2} \sin^2\alpha$$

where I_o is the intensity of the incident beam, I is the intensity of the scattered beam, α is the angle between the scattering direction and the direction of acceleration of the electron, and K is the constant.

Suppose the incident beam is traveling in the direction Ox in Figure 10 and line OP is inclined at a scattering angle of 2θ to the incident beam. An unpolarized incident beam has its electric vector **E** in a random direction in the yz plane. Hence, by breaking the electric vector into y and z components,

$$\mathbf{E}^2 = \mathbf{E}^2_y + \mathbf{E}^2_z \quad \text{and} \quad \mathbf{E}^2_y = \mathbf{E}^2_z = \frac{1}{2}\mathbf{E}^2$$

Since the intensity of these two components of the incident beam is proportional to the square of their electric vectors,

$$I_{oy} = I_{oz} = \frac{1}{2} I_o$$

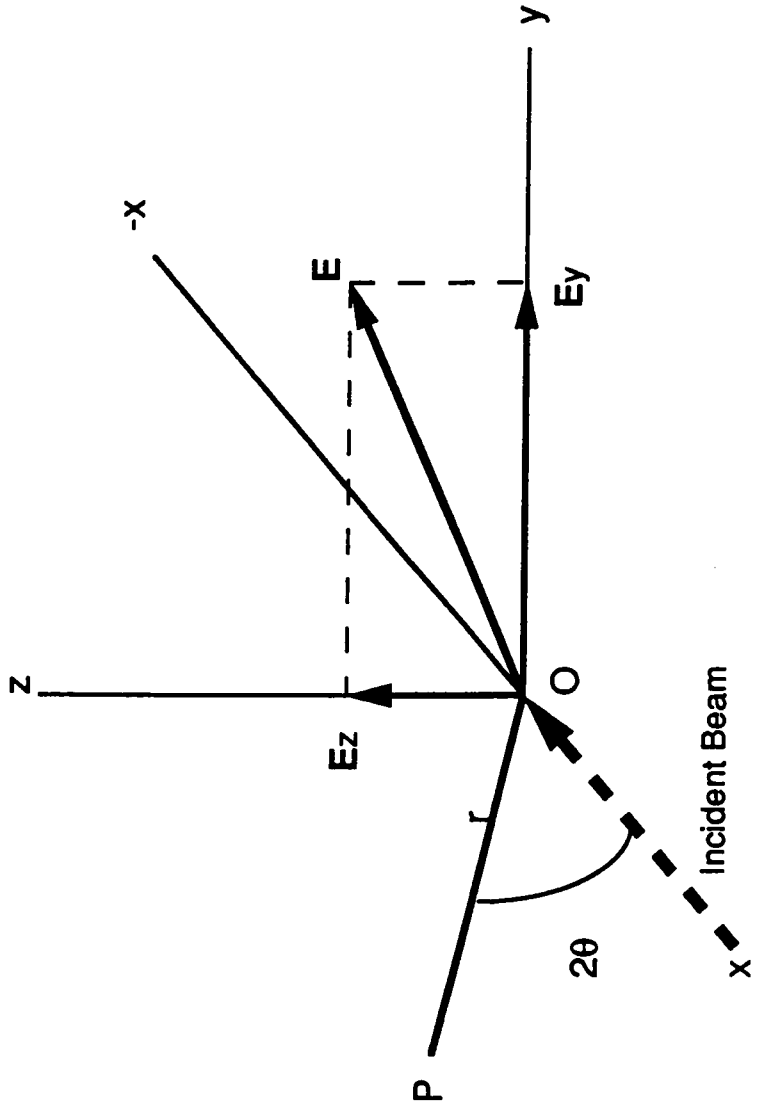

Figure 10. Coherent scattering of incident beams by a single electron.

The total scattered intensity at point P is obtained by summing the intensities of these two scattered components as below:

$$I_p = I_{py} + I_{pz}$$

$$= I_o \frac{K}{r^2} \frac{(1 + \cos^2 2\theta)}{2}$$

Therefore, polarization factor is the last term within the parenthesis:

(VI-5) $$P = \frac{(1 + \cos^2 2\theta)}{2}$$

The correction for this polarization was made by dividing the raw intensity data by the polarization factor as given.

D. Correction for Absorption

Using a highly penetrating radiation (MoK_α) for weakly absorbing material such as silica, the intensities must sometimes be corrected for sample transparency. The standard absorption correction is not adequate in this study because scattering is detected from a fraction of the irradiated volume which varies with angle. This applicable correction was developed by Milberg.[121] The absorption correction as shown in equation (VI-6) was used in this study. The derivation of this equation is discussed in more detail in Appendix II.

(VI-6) $$A = (1 - \frac{1}{\alpha})(1 - e^{-2\mu t \csc\theta}) + \frac{2t \cos\theta}{w} e^{-2\mu t \csc\theta}$$

where $\alpha = 2\mu$ w csc 2θ, w is the width in the cross section of an equivalent parallel incident beam, μ is the absorption coefficient of the sample, t is the sample thickness and θ is the scattering angle. The value of w is determined by the slit and goniometer geometry. The calculated and measured values $\mu = 8.157$ cm^{-1}, t = 0.25 cm and w = 0.32 cm were used in this investigation.

For the CuK_α radiation, the absorption correction was set to 1.0 because of reasons given by Appendix II. For the MoK_α radiation, the absorption correction could be applied. The absorption and polarization corrections were handled together in a single computer program. The corrected intensity was outputted both in analytical and graphical forms.

E. Correction for Instrumental Broadening

Broadening of measured diffraction pattern can result from improper focusing, penetration of the beam in the sample, resolution of the α_1 α_2 doublet at high angles, or use of a wide receiving slit. In principle, α_1 α_2 doublet and the wide receiving slit can lead to a broadening in diffraction peaks. Wicks[93] showed that instrumental broadening could all be handled by a deconvolution procedure in a modification of the Sauder method.[122] By running the standard sample with exactly the same diffraction conditions used with the sample, all broadening factors were handled as a single entity. He took the broadening of the standard peaks as the instrumental broadening of the sample. However, Mozzi[100] reported that the instrumental broadening was found to be negligible for the X-ray pattern of glass materials even though he used the wide receiving slit for RhK_α. Mozzi[100] suggested to use Keating's method[96] to eliminate the α_2

component from the CuK_α pattern of vitreous silica because α_1 α_2 doublet effect was found to be negligible for the amorphous patterns. Therefore, in this investigation the correction for the instrumental broadening was only made by using Keating's method.

F. Correction for Multiple Scattering

For weakly absorbing materials, a non-negligible intensity can result from rays which are scattered two or more times in the sample. To correct measured intensity data for multiple scattering in this study, Warren and Mozzi's method[123] of calculating secondary intensity for reflection geometry using samples of effective infinite thickness was used. Expression (VI-7) shows this relation. The derivation of this relationship is discussed in more detail in Appendix III.

$$\text{(VI-7)} \qquad \frac{I_d}{I_s} = \frac{B^2\, Q(2\theta,q,b)}{J(p) \sum_i A_i \mu_i(m)}$$

$$\text{where } B = \sum_{uc} Z_i^2$$

where I_d / I_s is the ratio of doubly and singly scattered intensity and B is the sum of the square of the total number of electrons present over the unit of composition. A_i and $\mu_i(m)$ are the atomic weight and mass absorption coefficient of the atoms of the unit of composition. J(p), intensity per structural unit in electron units, is calculated from expression (VI-8).

$$\text{(VI-8)} \qquad J(p) = B\left(q + \frac{1-q}{1 + b \sin^2\theta} \right)$$

where q is a function of the scattering angle 2θ. The parameters b and q are necessary to determine Q(2θ,q,b) by an equation relating them to J(p) for the selected structural unit. Values of b and q are selected by a trial and error method, which gives the best fit between the equation (VI-8) and values, which are calculated from the squares of structural factor when incoherent scattering is only counted. After suitable values of b and q are determined, the values of Q(2θ,q,b) can be obtained by interpolation from a table given in Dwiggins' paper.[124] When only unmodified scattering is considered, the best fit is usually obtained with q = 0. When the interest is in both the unmodified and modified intensities, it is necessary to use a value of q other than zero.

When Q(2θ,q,b) is obtained, the intensity ratio of secondary to primary intensity can be determined by using equation (VI-7). With this intensity ratio of secondary to primary intensity, the corrected intensity for multiple scattering is given by:

$$I_{corrected} = I_s - I_s \times \frac{I_d}{I_s} \qquad \text{(VI-9)}$$

Mozzi[100] observed that the intensity ratio (I_d/I_s) for calculated multiple scattering to the measured intensity of CuK_α radiation on vitreous silica was negligible. For RhK_α radiation, Warren and Mozzi[123] obtained for I_d/I_s a value of about 0.08 in the range $2\theta = 90^0$ to $2\theta = 180^0$. For AgK_α radiation, Meek[125] observed that I_d/I_s ranged from 0.09 to 0.11 over the region of k greater than 15. In this investigation, the value of I_d/I_s for CuK_α radiation was detemined to be less than 0.0001 and was then

considered negligible. For MoK_α radiation, the multiple scattering was calculated and I_d/I_s ranged from 0.045 to 0.059 over the entire region of k as shown in Figure 11. Therefore, the measured intensity for multiple scattering was corrected using equation (VI-9).

G. Correction for the Compton Modified Scattering

Slight errors in the subtraction of the contribution of the Compton modified scattering to the measured intensity produce serious errors in the coherent scattering obtained and then in the pair function distribution. Therefore, the correction for the Compton modified scattering was carefully handled for each given radiation as below.

1. Correction in CuK_α Radiation

The intensity of modified scattering, in electron units, can be calculated for any atom by the following formula[118]:

$$(VI\text{-}10) \qquad (I_{eu})_{mod} = \sum^{z} (1 - f_j^2) = Z_j - \sum^{z} f_j^2$$

A more rigorous analysis, including the Pauli exclusion principle, which forbids electronic transitions to already occupied states, leads to

$$(VI\text{-}11) \qquad (I_{eu})_{mod} = Z_j - \sum_{n} f_{nn}^2 - \sum\sum_{m \neq n} |f_{mn}|^2$$

Experimental measurements of the incoherent scattering suggest that the value in above equation is consistently too large by a small factor. Hence,

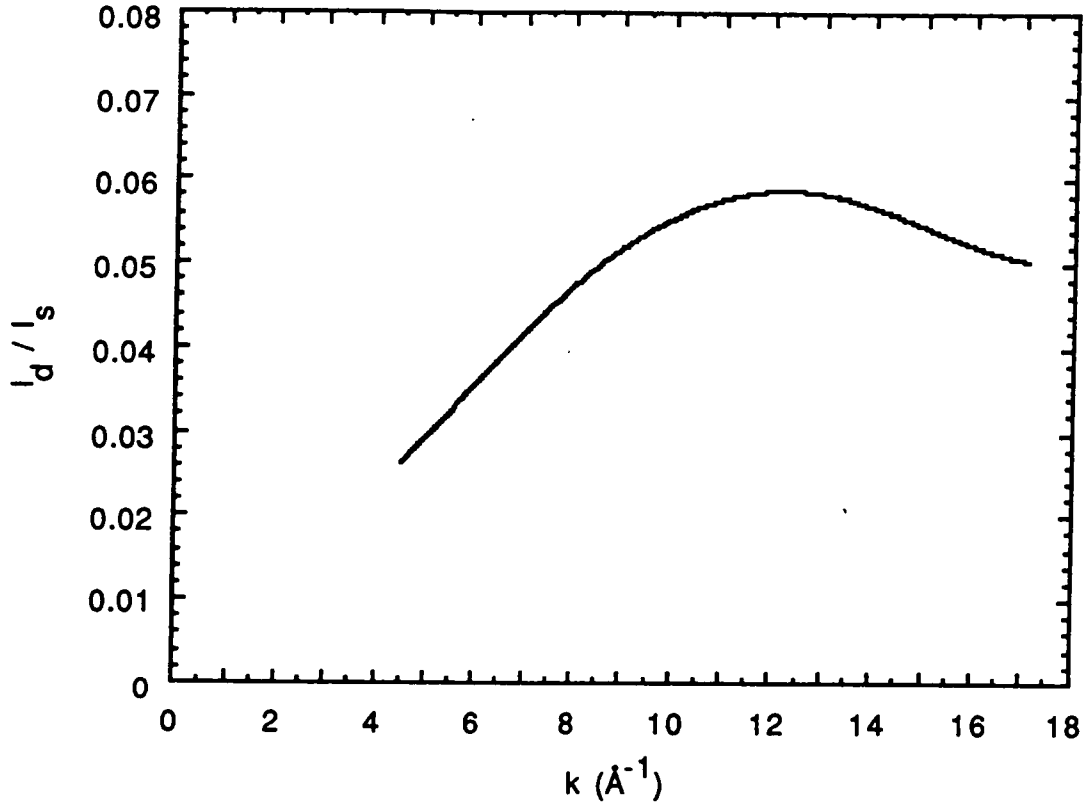

Figure 11. Multiple scattering correction curve in MoK_α radiation.

summing over a unit of composition and applying the Breit-Dirac recoil factor R, the total intensity of the Compton modified scattering is

$$\text{(VI-12)} \qquad C.M. = R \sum_{uc} \{ Z_j - \sum_{n} f_{nn}^2 - \sum_{m \neq n} \sum |f_{mn}|^2 \}$$

where $R = (\lambda / \lambda')^{3.5}$, λ is the unmodified wavelength and λ' is the modified wavelength. R can be derived by an explicit consideration of the recoil electron's velocity or quantum-mechanical considerations. The Breit-Dirac recoil factor and the Compton modified intensity as a function of $\sin \theta / \lambda$ can be obtained from in Volume III of International Tables for X-ray Crystallography.[118] In this study, the Compton modified intensity was subtracted from the previously corrected CuK_α intensity in a computer program that also normalized the intensity data. Therefore, a pair function distribution could be derived only from a Fourier transform of the unmodified intensity scattered from the sample.

2. Correction in MoK_α Radiation

Since the Compton modified scattering is produced overlapping the unmodified scattering, this Compton modified scattering must be subtracted from the measured intensity. However, there is a problem to subtract the Compton modified intensity from the measured intensity in shorter incident wavelengths such as MoK_α radiation because the unmodified intensity is much smaller than the Compton modified intensity at high angle regions. Therefore, it is desirable that the Compton modified scattering is removed as effectively as possible in the experimental procedure.

The scattering of X-rays by the Compton effect is obtained by the collision between an incidient photon of wavelength λ and an electron. The electron is expelled from the atom and the photon has, after the collision, a slightly smaller energy, which is a wavelength λ' slightly larger. The wavelength change is given by

$$\lambda' = \lambda + \frac{h}{mc}(1 - \cos 2\theta) \qquad \text{(VI-13)}$$

with $h / m c = 0.02426$ Å.

The use of balanced filters to produce monochromatization of X-rays was first reported by Ross[126] and various aspects of their use have been described by many researchers.[127-129] This technique requires the use of two filters, one having a K absorption edge above, the other below, the line of interest. It is accomplished by using two filters composed of elements of adjacent atomic number whose thickness have been so adjusted that the transmitted spectra are identical for all wavelengths except those lying within the narrow band between the two K absorption limits. Berman and Ergun[115] proposed the use of rhodium, ruthenium, and technetium as balanced filters to produce monochromatization of AgK_α. For example, Rh and Ru were used to isolate the $K_{\alpha 1}$, Ru and Tc for the $K_{\alpha 2}$, and Rh and Tc were used for the K_α doublet.

Since λ (MoK_α) = 0.71073 Å and λ (Y K_{edge}) = 0.72766 Å, the Compton modified scattering involving shifts larger than the differences between the two wavelengths (0.01693 Å) can be effectively removed by Zr-Y balanced filters. Using this Zr-Y balanced filters in this investigation, the Compton modified scattering became very small at values at k greater than 7.50. Therefore, the Compton modified scattering was experimentally eliminated

in the important high angle region. In actual practice, there could exist a small portion of Compton due to the excessively large tails of the incoherent profile as determined by Eisenberger[130], but this contribution should be on the order of only a few percent.

H. Normalization

Before the corrected data can be analyzed, the corrected intensity must be converted from arbitrary to absolute units.

1. Normalization for CuK_α data

The corrected intensity was normalized by a modified Norman method.[131] The details of the normalization procedure are presented in Appendix IV. The normalizing factor n is determined by

$$n \int_0^{k_m} \frac{k^2 e^{-\alpha^2 k^2}}{f_e^2} \frac{I_m - B}{P} dk = \int_0^{k_m} \frac{k^2 e^{-\alpha^2 k^2}}{f_e^2} [\sum_{uc} f_i^2 + C.M.] dk - 2\pi^2 \rho_e \sum_{uc} Z_j \quad \text{(VI-14)}$$

The normalizing factor n can be evaluated from known quantities and experimental measurements. In this study, k_m was taken as 7.5 $Å^{-1}$. Also, strong convergence factors with $\alpha^2 k_m^2 \approx 4$ were used since the integrands involve k^2. From values of the Compton modified scattering tabulated in Volume III of International Tables for X-ray Crystallography[118], the normalized unmodified-intensity in electron units per unit composition, I_{eu}/N, was determined using equation (AIV-4).

2. Normalization for MoK_α data

The corrected intensity was normalized by a curve matching method.[30] The measured intensity curve could be normalized by allowing it to oscillate above and below the unmodified independent scattering $\sum_{uc} f_j^2$ curve or the total independent scattering curve, $\sum_{uc} f_j^2$ + C.M. + M.S. Since the intensity profile was low and undulations about the total independent scattering curve was small at high k values, this type of normalization method became easier to find a normalization factor in this study.

The MoK_α data were normalized by choosing normalization factor such that the corrected intensity oscillated above and below the unmodified independent scattering curve from $12 \leq k \leq 17.11$. In choosing a normalization factor by fitting the corrected intensity curve to the unmodified independent scattering curve, it was found that the corrected intensity curve fell below the unmodified independent scattering curve for k less than about 12. This was considered to be the Compton modified scattering and multiple scattering. Hence, the MoK_α data from $7.5 < k < 12$ were normalized by the corrected intensity oscillated above and below the total independent scattering curve. The final choice was that one which gave the smallest oscillations in the pair function distribution in the r region below the shortest interatomic spacing.

I. Correction for Error in k i(k) on the Pair Function Distribution

This correction was made on the final pair function distribution by taking the difference between measured curve and calculated curve. The origin of this correction[132] was not clear, but probably arose from the

localized error in k i(k) introduced by compiling the two different radiations.

The measured paid function distribution (PFD) is given:

$$\text{(VI-15)} \qquad PFD = 2\pi^2 r\rho_e \sum_{uc} Z_j + \int_0^{k_m} k\, i(k)\, e^{-\alpha^2 k^2} \sin rk\, dk$$

Therefore, the error in PFD due to an error in k i(k) localized at k_o can be given:

$$\text{(VI-16)} \qquad PFD \Big|_e = \int_0^{k_m} [k_o\, i(k_o)] \Big|_e\, e^{-\alpha^2 k_o^2} \sin rk\, dk$$

Since the error in k i(k) is assumed to be a Gaussian error, $[\, k_o\, i(k_o)\,] \Big|_e$ can be given by:

$$\text{(VI-17)} \qquad [\, k_o\, i(k_o)\,] \Big|_e = A \exp\{-\beta^2 (k - k_o)^2\}$$

With inserting equation (VI-17) into equation (VI-16), the error in PFD can be simplified:

$$\text{(VI-18)} \qquad PFD \Big|_e = A\, e^{-\alpha^2 k_o^2} \int_0^{k_m} \exp\{-\beta^2 (k - k_o)^2\} \sin rk\, dk$$

$$= C \int_0^{k_m} \exp\{-\beta^2 (k - k_o)^2\} \sin rk\, dk$$

where C is a constant because slowly varying quantities have been taken outside the integral and then would be denoted a constant. By letting $\kappa = k - k_o$ and $d\kappa = dk$,

$$\text{(VI-19)} \qquad \text{PFD}\Big|_e = C \int_{-k_m}^{k_m - k_o} \exp\{-\beta^2 \kappa^2\} \sin r(\kappa + k_o)\, d\kappa$$

$$\approx C \int_{-\infty}^{+\infty} \exp\{-\beta^2 \kappa^2\} \sin r(\kappa + k_o)\, d\kappa$$

Now $\sin r(\kappa + k_o) = \sin r\kappa \cos rk_o + \cos r\kappa \sin rk_o$ and the first term is an odd function of κ and will not contribute to the integral so,

$$\text{(VI-20)} \qquad \text{PFD}\Big|_e = C \sin rk_o \int_{-\infty}^{+\infty} \exp\{-\beta^2 \kappa^2\} \cos r\kappa\, d\kappa$$

$$= C \sin rk_o \left[\frac{2\sqrt{\pi} \exp(-r^2/4\beta^2)}{2\beta}\right]$$

$$= D \exp(-r^2/4\beta^2) \sin rk_o$$

where D is a new constant. In this study, extrapolations are made at peak positions in the PFD since the resultant error was a damped sinusoidal term. This localized error resulted in the negligible change of peak position but contributed to the peak area of the first few maxima in the pair function distribution.

Chapter VII.

Results and Discussion

The results of the present investigation are presented and discussed in this chapter. The microwave heating of the silica sand and the pure fused silica is discussed first, and then the analysis of X-ray diffraction patterns and the analysis of pair function distributions (PFD) and distance distribution functions (DDF) are discussed. These analyses will show the structural differences between the conventionally melted pure silica and the microwave melted pure silica. Most of the computations described in this chapter were done by Macintosh II-si computer using programs written by the author. These computer programs written by FORTRAN 77 are listed in Appendix V.

A. Microwave Heating of Vitreous Silica

The microwave heating of the silica samples was divided into two groups: one was that the silica sand was heated without a susceptor, and the other was that the pure fused silica was heated with a susceptor. This microwave heating process could be described as a three-step, namely 1) heating zone, 2) melting zone, and 3) cooling zone.

Figure 12 shows plots of heating time versus surface temperature for the five runs of the silica sand. Figure 13 shows plots of heating time versus surface temperature for the several runs of the pure fused silica. A noticeable phenomenon was the difference of maximum surface temperature. The surface temperature of the silica sand was incorrectly

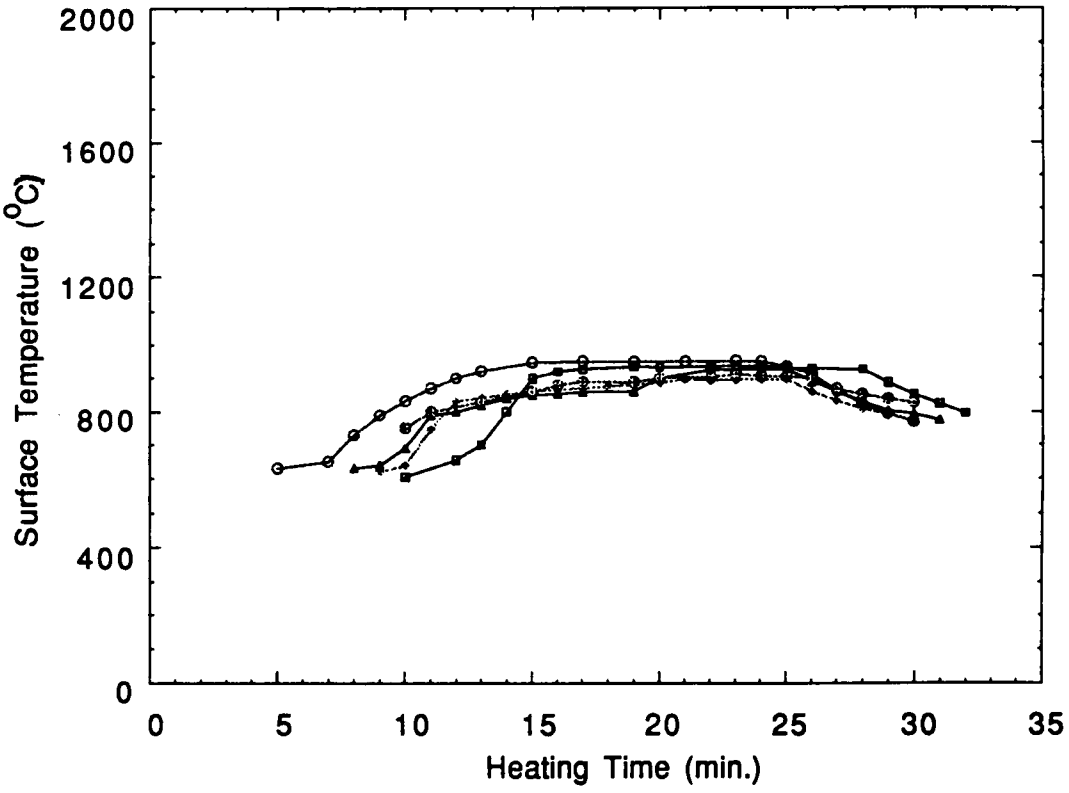

Figure 12. Temperature profile of microwave heating for silica sand.

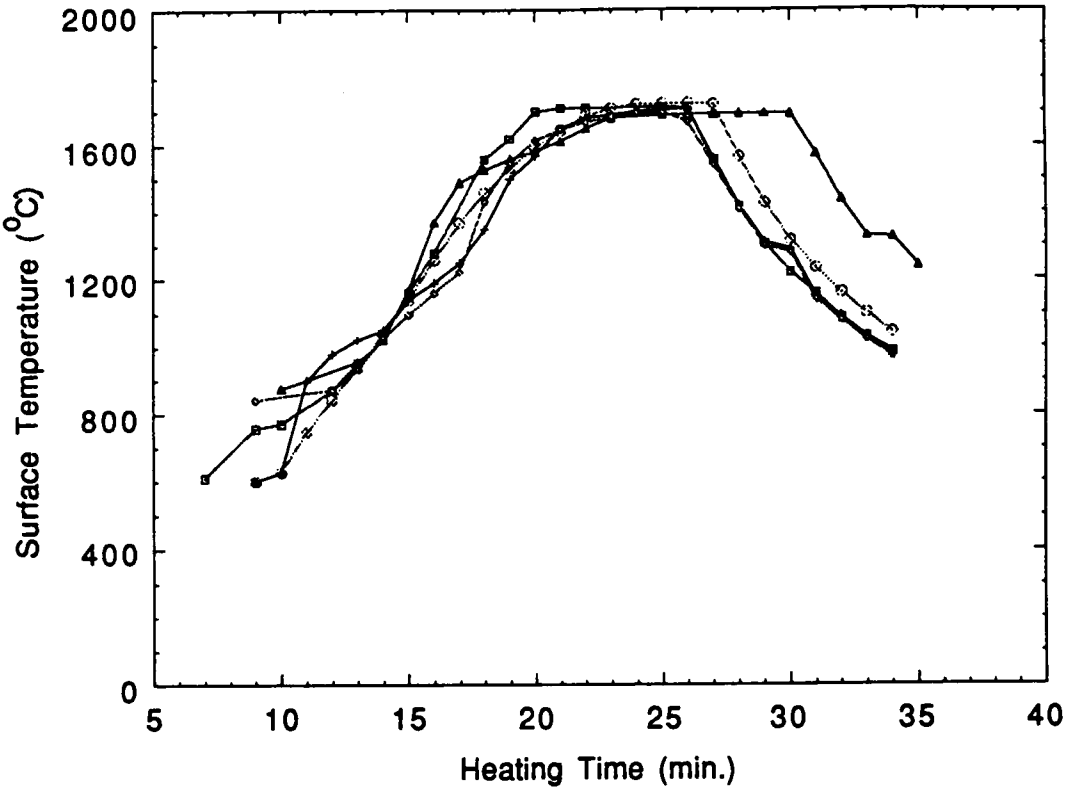

Figure 13. Temperature profile of microwave heating for the pure fused silica.

monitored by IR-pyrometer because the melted region of this sample was covered by unmelted silica on the outside, which was relatively cool.

In the heating zone, the silica sand was coupled effectively with 2.45 GHz microwave radiation. The pure fused silica was not coupled with 2.45 GHz microwave radiation at room temperature, but initially 2.45 GHz microwave radiation coupled with a zirconia susceptor instead of the pure fused silica. After the pure fused silica was heated indirectly to about 1000 °C by a hot susceptor, it began to couple efficiently with microwave radiation because the loss tangent of most ceramic materials increased exponentially with increasing temperature. Hassler and Johansen[60] also reported that the loss factor of quartz was strongly dependent on the temperature below 1000 °C and less dependent above. They preheated quartz to 1000 °C to couple quartz easily with microwave radiation. In this study, above this temperature range, the pure fused silica was heated to its melting temperature and the susceptor coupled much less. As a result, microwave input power was adjusted manually to keep heating rate at a desired value since heating rate was markedly accelerated at constant power.

In the melting zone, the pure fused silica was melted uniformly and thermal runaway did not occur. Stable heating temperature up to 1700 °C could be maintained by applying constant power from 1.8 kW to 2.0 kW. Although temperature of the sample was already up to 1700 °C during the microwave heating, the microwave cavity wall was relatively cool to touch due to the selective heating of microwave radiation. The silica sand was melted partially by applying constant power of 1.0 kW and the unmelted silica sand of outside functioned as an insulation.

In the cooling zone, the melted silica sand and the melted pure fused silica were cooled in air because microwave power was turned off and circulated air was turned on. Hence, a densification of the structure for the samples took place. This fact could be explained by the freezing-in of a high temperature state produced by microwave radiation.

The low absorption of microwave energy by the pure vitreous silica was due to the completely rigid atomic structure. Structurally, it will be understood that the network of vitreous silica is highly symmetric and rigid in a cooperative sense, resulting from the high field strength and from the four-fold valency of the Si^{4+} and the two-fold valency of O^{2-} for the part of the polar binary force, and from the symmetric distribution function of the part of the directed covalent binding force. As shown by Warren[24], this vitreous silica is made of an uninterrupted series of (-Si-O-Si-O-) linkage, each of which comprises a strong bonding of adjacent atoms. Since the total structure of integrally bonded tetrahedra is extremely rigid, microwave waves are transmitted without setting the atoms into motion. Energy absorption is consequently low and dielectric losses are also low.

According to Lal and Thoma[133], even though the microwave power of about 9 watts was applied to single silicon crystal, the microwave field interacted strongly with the electron cloud of the silicon atoms. In this investigation, a possible factor for microwave coupling in the pure fused silica was the polarization of O^{2-} by the strong field of the central cation Si^{4+}. At room temperature, the electronic cloud of oxygen ion O^{2-} may be affected by the electric field of the cation Si^{4+}, causing the pure fused silica not to couple with microwave radiation. When it was heated up to about 1000 ^{o}C by a microwave coupler, the electronic shell of the oxygen ions was

affected improving coupling. This affected electronic shell of the oxygen ions could decrease the field strength of the cation Si^{4+}. With aid of the polarization effect exerted on O^{2-} by infrared active condition, the pure fused silica could couple readily with microwave radiation. When the pure fused silica was heated its melting temperature, the increased amplitude of infrared oscillation and microwave enhanced oscillation could be preferentially accommodated in the void space of the silica structure, and the twisting reorientation of Si-O tetrahedra could also occur. This twisting reorientation in the rigid structure of vitreous silica would be difficult without bond cleavage due to the nature of the random network. This network could be fragmented, and the mobility could become great soon. Therefore, it was assumed that the pure fused silica could couple readily with microwave radiation due to the generation of the non-bridging oxygens and the modification of the random network. The generation of the singly bonded oxygens and the resultant affect on the random network, which resulted in a shift of Si-O-Si bond angle distribution and in broader distance distributions of Si-O, O-O, and Si-O pairs, could be indicative of the dynamics of the processes leading to microwave densification.

While a zirconia susceptor could be used to couple with microwave radiation for the case of the pure fused silica, the silica sand coupled easily with microwave radiation at lower input power without this susceptor. This was because of the greater impurities of the silica sand. From Table 4, it was predicted that the silica sand was easily coupled with microwave radiation due to Na_2O, K_2O, and FeO elements. As shown by Warren et al.[134], alkali oxides produced gaps in the random network of vitreous silica. Some rigid bonds (-Si-O-Si-) were broken and (-Si-O-.....Na^+.....-O-Si-)

Table 4. Chemical composition of silica sand.

Content	Weight fraction
SiO_2	96.8 wt%
Iron	1.70 wt%
Sodium	0.68 wt%
Calcium	0.48 wt%
Magnesium	0.17 wt%
Aluminum	0.16 wt%

linkages could be replaced them. The Na^+....O bond is relatively weak, and the oxygen atoms adjacent to each alkali ion were essentially single bonded. The net effect was that the alkali ions were weakly held in the interstices of the random network of vitreous silica. When the silica sand was heated using microwave radiation, alkali ions in the silica sand were easily set into motion under the influence of microwave enhanced oscillation. Consequently, it absorbed effectively microwave radiation and gave rise to its dielectric losses. Therefore, the greater the alkali content, the more the energy absorbed and the higher the losses.

When the silica sand reached its melting temperature, the increased amplitude of infrared oscillation and microwave enhanced oscillation could be preferentially accommodated in the void space of the silica structure. Consequently, the random network could be broken up and the impurity ions were able to move more freely and then the silica sand easily absorbed more microwave radiation. In terms of the atomic structure, this silica sand could contain larger number of singly bonded oxygen atoms than the microwave melted pure fused silica.

Glass materials under the influence of microwave radiation are able to exhibit high-frequency relaxation mechanisms which will contribute to its loss mechanisms, such as deformation losses, ion migration losses, and conduction losses. The origin of deformation losses[67] is the bending of non-bridging oxygens and the reorientation of the immediate surroundings, the origin of the ion migration losses[66] is the jump relaxation of alkali ions, and the origin of conduction losses[37] is the exponential increase in electrical conductivity with elevated temperature.

In this investigation, the major losses for the pure fused silica could be the deformation losses, which were due to the small modification of the random network with a low activation energy or to the generation of the non-bridging oxygens. The other major losses for the pure fused silica could be the conduction losses, which were predominant losses at high temperature due to the exponential increase in electrical conductivity at about its melting temperature. The major losses for the silica sand could be the deformation losses, the conduction losses, and the ion migration losses due to the alkali impurities.

The formation of glass is favored for those properties of the constituents that hinder the sudden transition from their spatial distribution in the liquid state to the thermodynamically more stable arrangement of the crystal. The inhibition of this transition is associated with the low mobility of the constituents, that is, with relatively high viscosity attained by the liquid at the freezing temperature. When the melted silica is cooled to room temperature, β-crystobalite is metastably retained as a result of the large tensile stresses developed during the quenching.[135]

In this investigation, although the microwave melted silica sand was quenched at slower cooling rate, crystobalite-like structure was not formed. This phenomenon would be explained by different thermal gradient formed due to the internal heating of microwave radiation. When the conventional melted silica sand was quenched from temperature above its melting point, the usual permanent stress distribution was built up by the latter contraction of the interior rather than the exterior part. This produced tension in the temperature range of possible flow in the interior, and a

compressive stress in the exterior part. The thermal gradient of microwave heating within the silica sand would be different from that of the conventional heating due to the internal heating characteristics of microwave radiation. This different thermal gradient could form less tensile stresses in the interior of the microwave melted silica sand. Therefore, the different stress gradient of the microwave melted silica sand could prevent retaining the crystobalite-like structure during the quenching.

B. Analysis of X-ray Diffraction Patterns

The raw intensity curves for CuK_α and MoK_α radiation are listed for the several runs of microwave-melted pure fused silica and silica sand in Appendix VI. Also, the raw intensity curves for CuK_α and MoK_α radiation are listed for the several runs of conventionally melted pure fused silica and silica sand in Appendix VI. The X-ray diffraction patterns of the microwave melted pure fused silica and the conventionally melted pure fused silica were compared only because the experimental pair function distribution was not derived precisely from the X-ray diffraction pattern of the silica sand due to its impurities. The typical X-ray diffraction patterns of these samples, which were produced by combining normalized unmodified intensity data from CuK_α and MoK_α with the appropriate corrections earlier discussed, are given in Figure 14 and 15 for the microwave sample and in Figure 16 and 17 for the conventional sample. Also, Figure 14, 15, 16, and 17 show I_{eu}/N superimposed on $\sum_{uc} f_i^2$ curve, the independent unmodified scattering curve. The discontinuities at $k = 7.5$

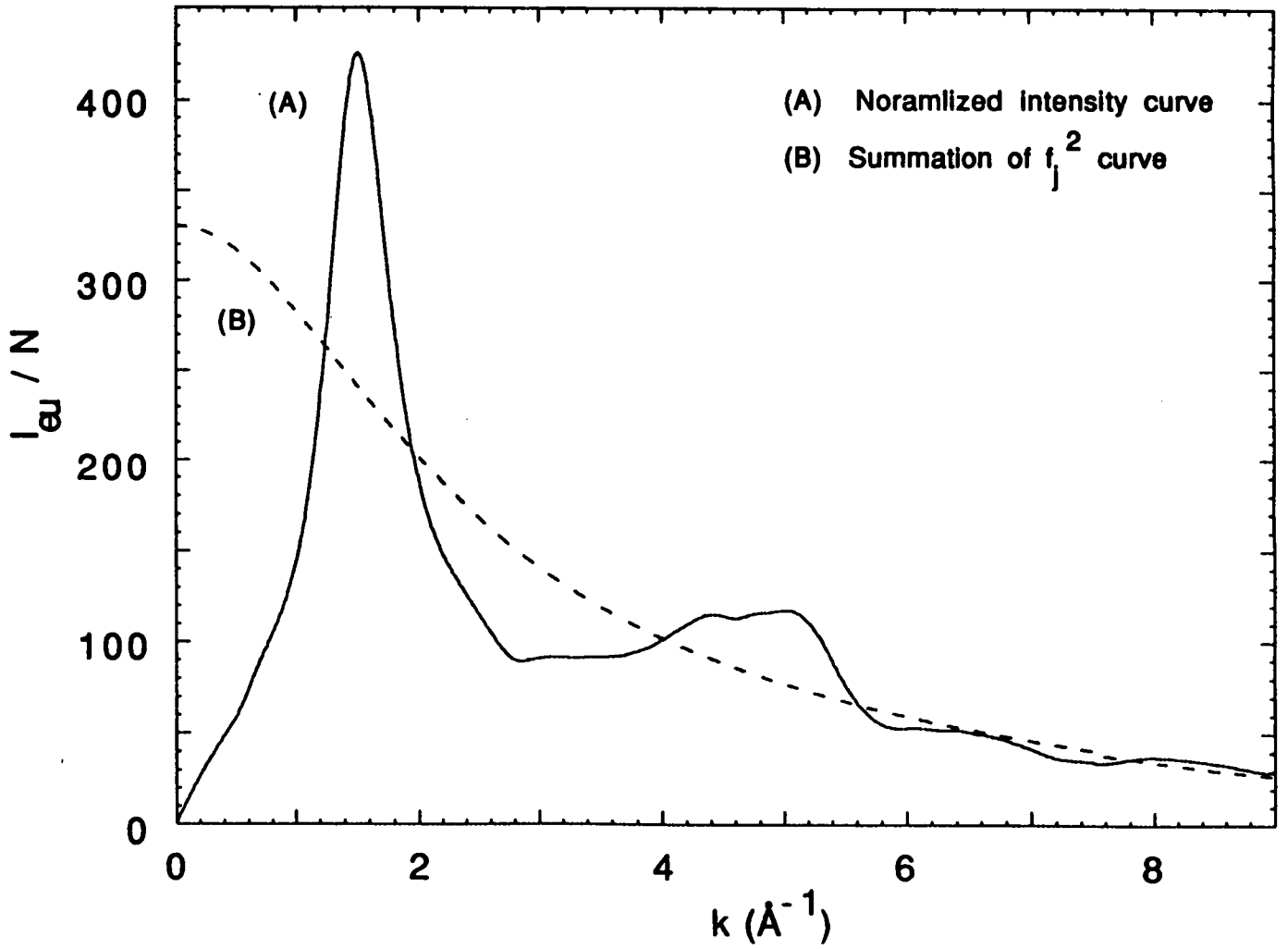

Figure 14. Normalized X-ray diffraction pattern from $0 \leq k \leq 9$ for the microwave sample.

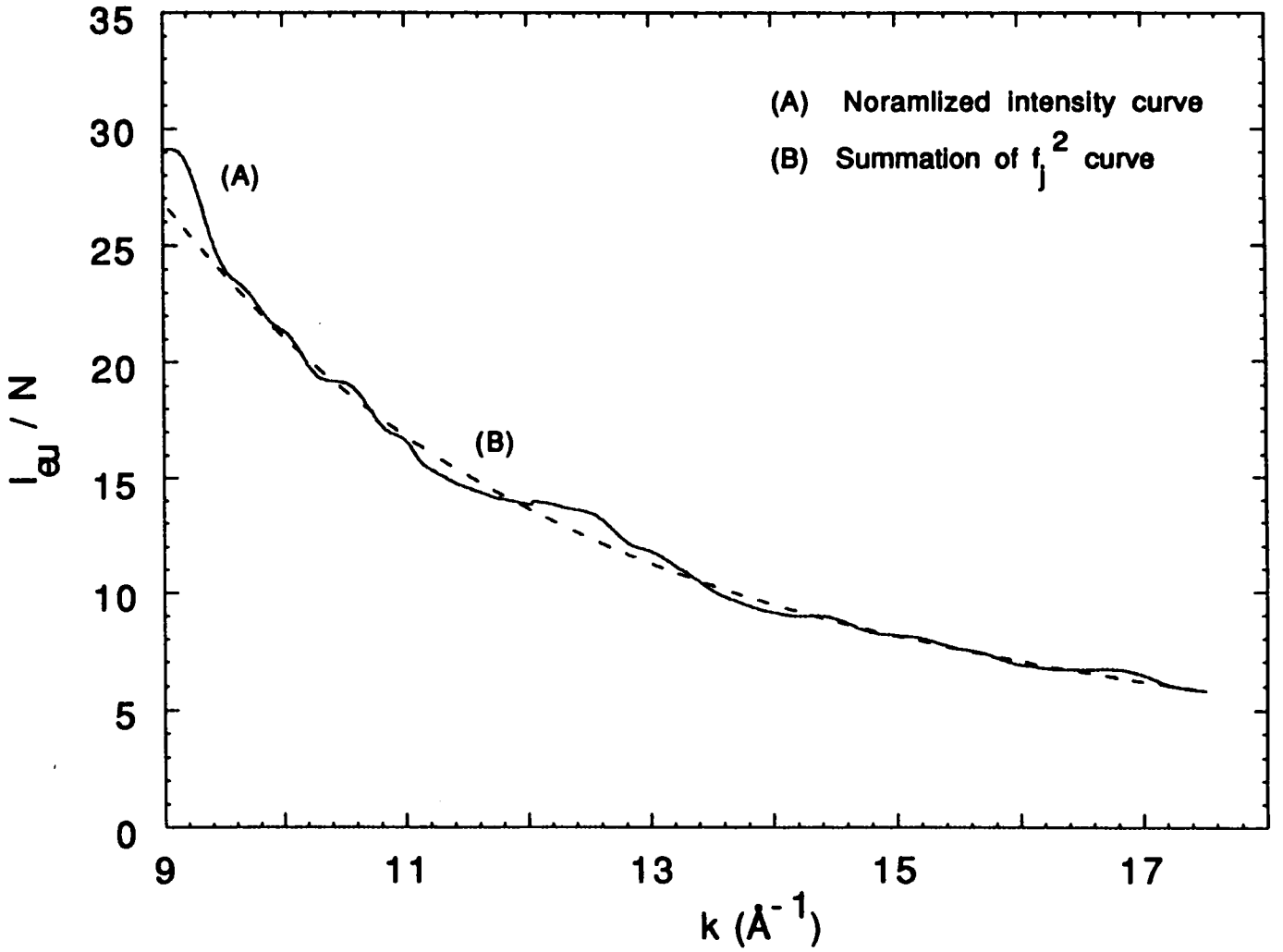

Figure 15. Normalized X-ray diffraction pattern from $9 \leq k \leq 17.5$ for the microwave sample.

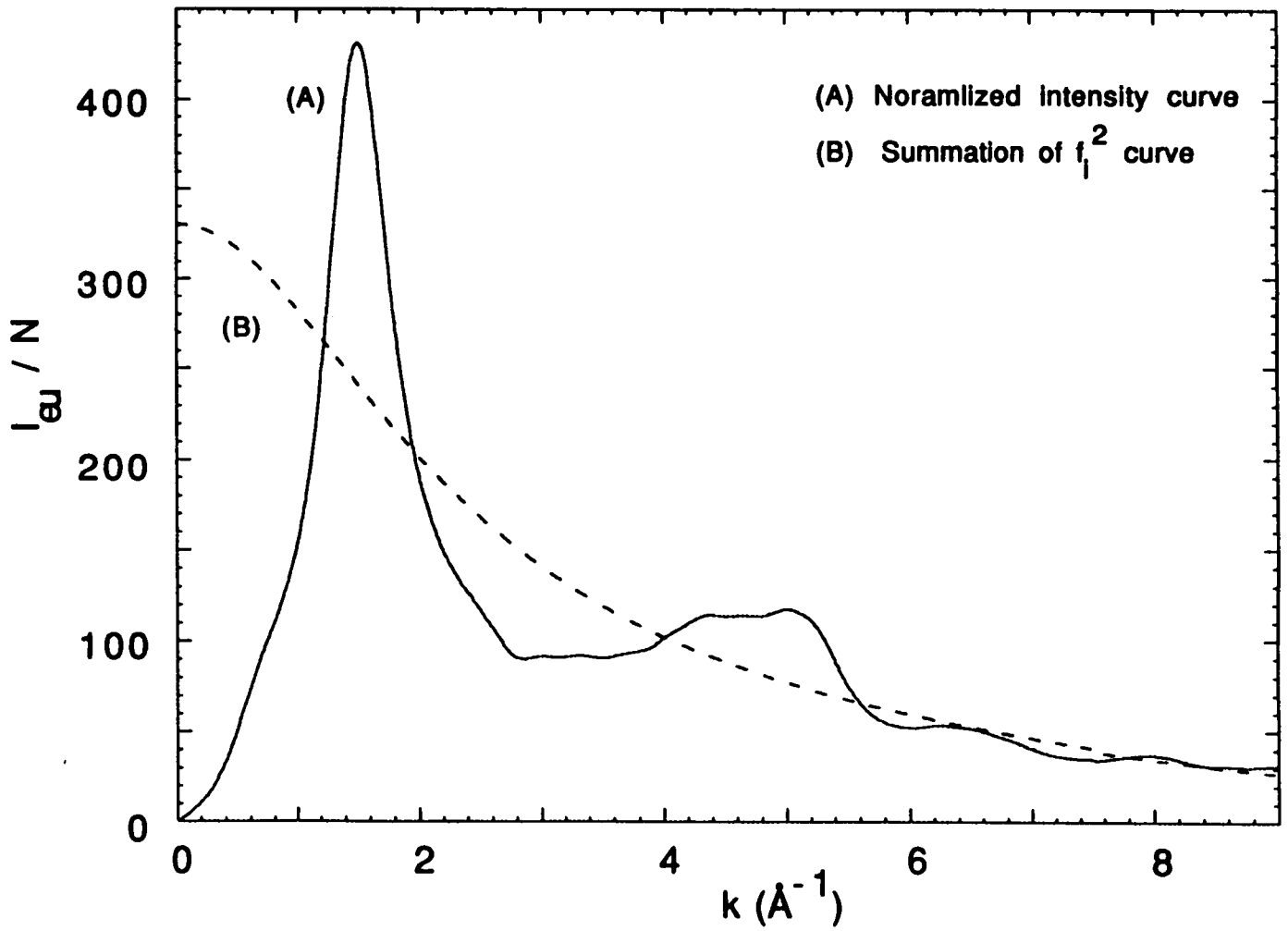

Figure 16. Normalized X-ray diffraction pattern from $0 \leq k \leq 9$ for the conventional sample.

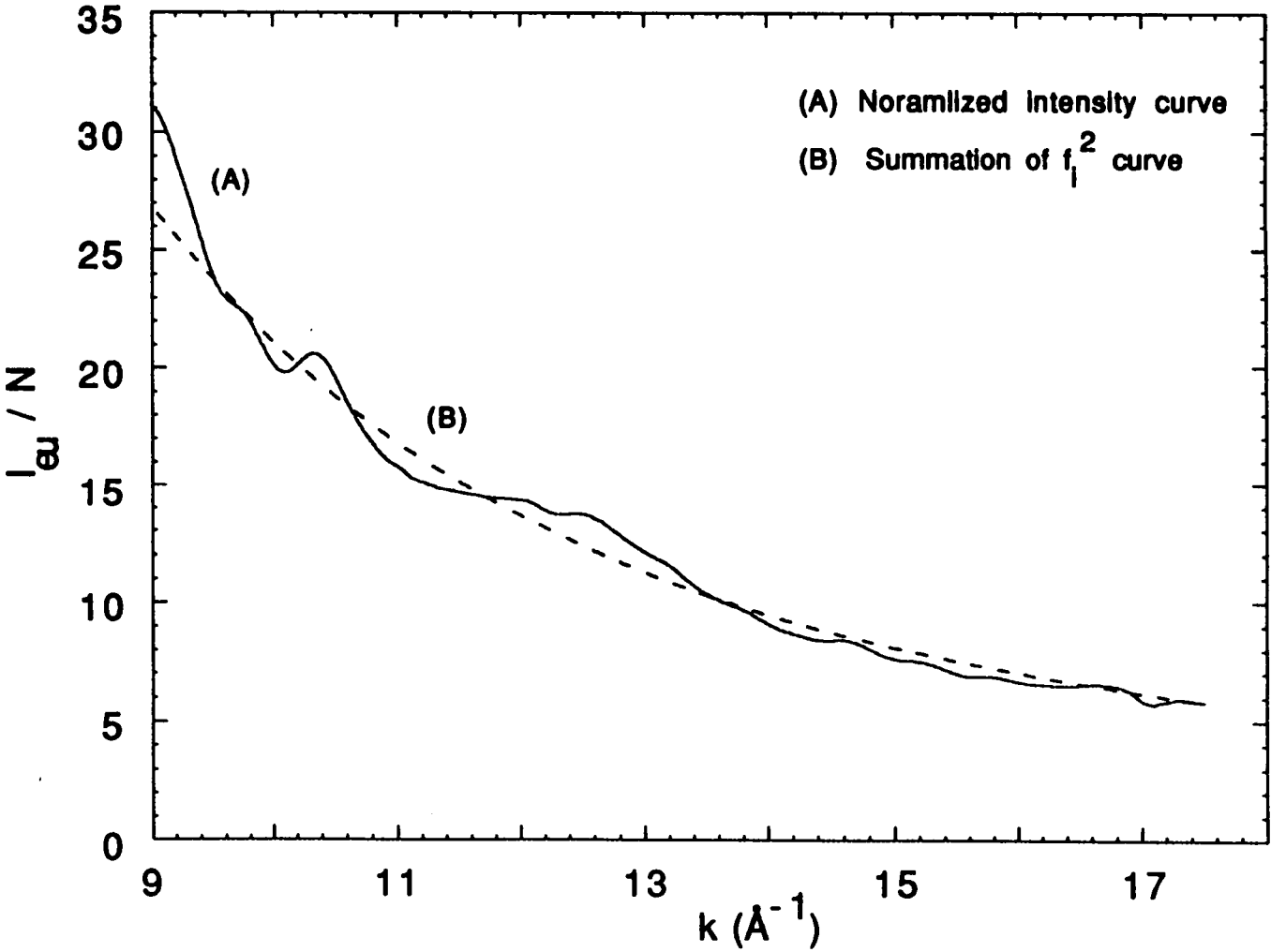

Figure 17. Normalized X-ray diffraction pattern from $9 \leq k \leq 17.5$ for the conventional sample.

were due to the different anomalous dispersion corrections used for CuK_α and MoK_α radiation.

To determine the accuracy of the normalization, the area above and below the independent unmodified scattering curve was calculated using equation (IV-13). Figure 18 for the microwave sample and Figure 19 for the conventional sample show k i(k) $\exp(-\alpha^2k^2)$ curve. The k i(k) was extrapolated from k_m = 17.11 to 17.50 to reduce low frequency oscillations in the experimental PFD curve. A sharpening factor was chosen as f_e, the average scattering factor per electron. Various convergence factors were tried to yield the best normalization of the intensity data and $\exp(-\alpha^2k^2)$ = 0.25 was provided adequate weighting of high k regions without a serious loss of resolution in the pair distribution function.

Lal and Thoma[133] observed an anomalously large change in the intensity of X-ray diffracted beam from the silicon single crystal on the application of the microwave electromagnetic field. They concluded that the observed effect was caused by the strong interaction of the microwave field with electron cloud of silicon atoms. Himmel et al.[136] found that the angular position of the first maximum peak in the X-ray pattern of v-SiO_2 and porous SiO_2 glass produced by chemical extraction was always constant. It would be predicted that changes of short-range order in vitreous silica were independent of the fictive temperature caused by the cooling regime of the sample. Gerber and Himmel[137] showed that the different fictive temperature strongly influenced the X-ray diffraction pattern in the region of the first maximum peak determined chiefly by the middle-range order of network, but that it did not influence the X-ray

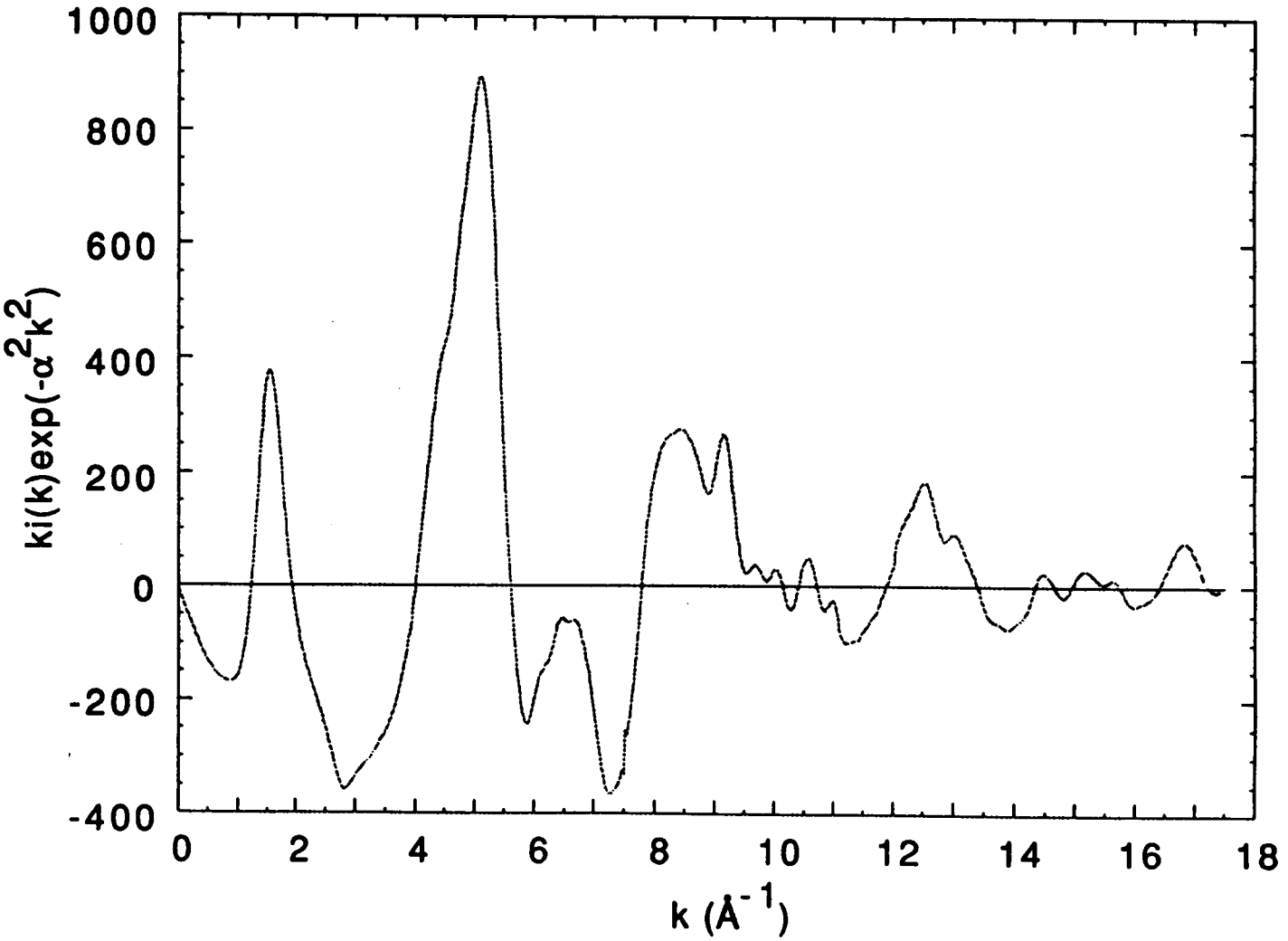

Figure 18. k i(k) exp(-α^2k^2) curve for the microwave sample.

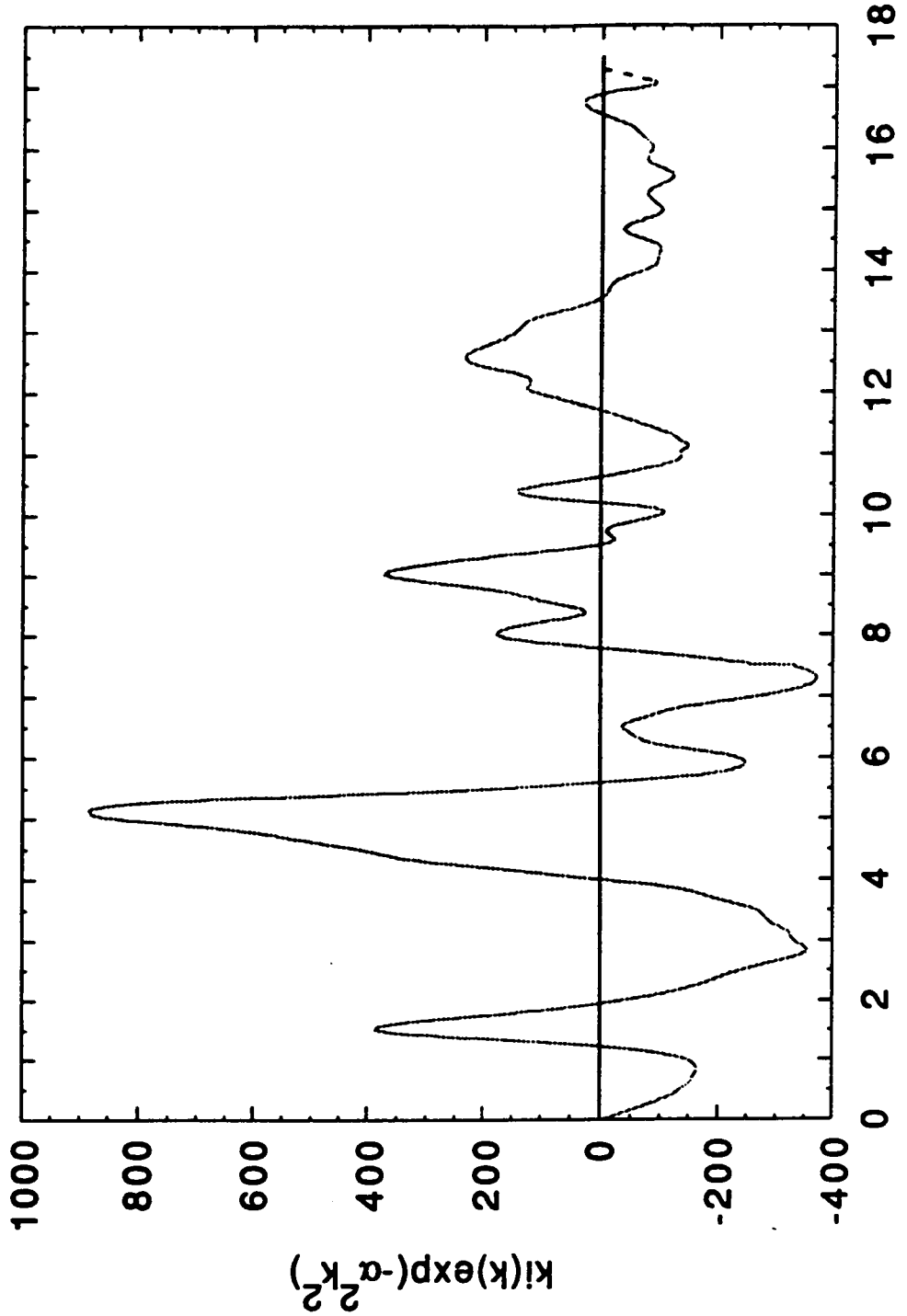

Figure 19. k i(k) exp(-α^2k^2) curve for the conventional sample.

diffraction pattern at higher k regions due to higher viscosity of vitreous silica.

In this investigation, the typical X-ray diffraction patterns of the microwave sample and the conventional sample showed that the first peak positions of two curves were almost same, but the patterns of two curves at the high k regions were considerably different. Therefore, it was concluded that the difference of two X-ray diffraction patterns at high k regions was caused by different heating and coupling mechanisms of microwave radiation, not by the different cooling condition. The structural difference between the microwave sample and the conventional sample will be discussed using an analysis of PFD and DDF in more detail.

C. Analysis of PFD and DDF

The typical pair function distributions (PFD) of the microwave sample and the conventional sample computed using the right-hand side of equation (IV-23) are shown in Figure 20 and 21. Also, the several curves of PFD for the conventional samples and microwave samples are listed in Appendix VII. In the previous Chapter III, the vitreous silica consists of tetrahedral arrangements of oxygen atoms with each oxygen atom shared by two tetrahedra and with a silicon atom at the center of each tetrahedron. In crystalline silicates, a Si-O distance is about 1.62 Å and a O-^{1st} O distance is 2.64 Å. The first three small peaks in Figure in 20 and 21 are not real peaks but are low frequency oscillations due to an error in normalization and also due to errors in correcting for incoherent scattering. Therefore, the first three large peaks in Figure 20 and 21 are arisen from Si-O, O-^{1st} O, and Si-^{1st} Si pairs.

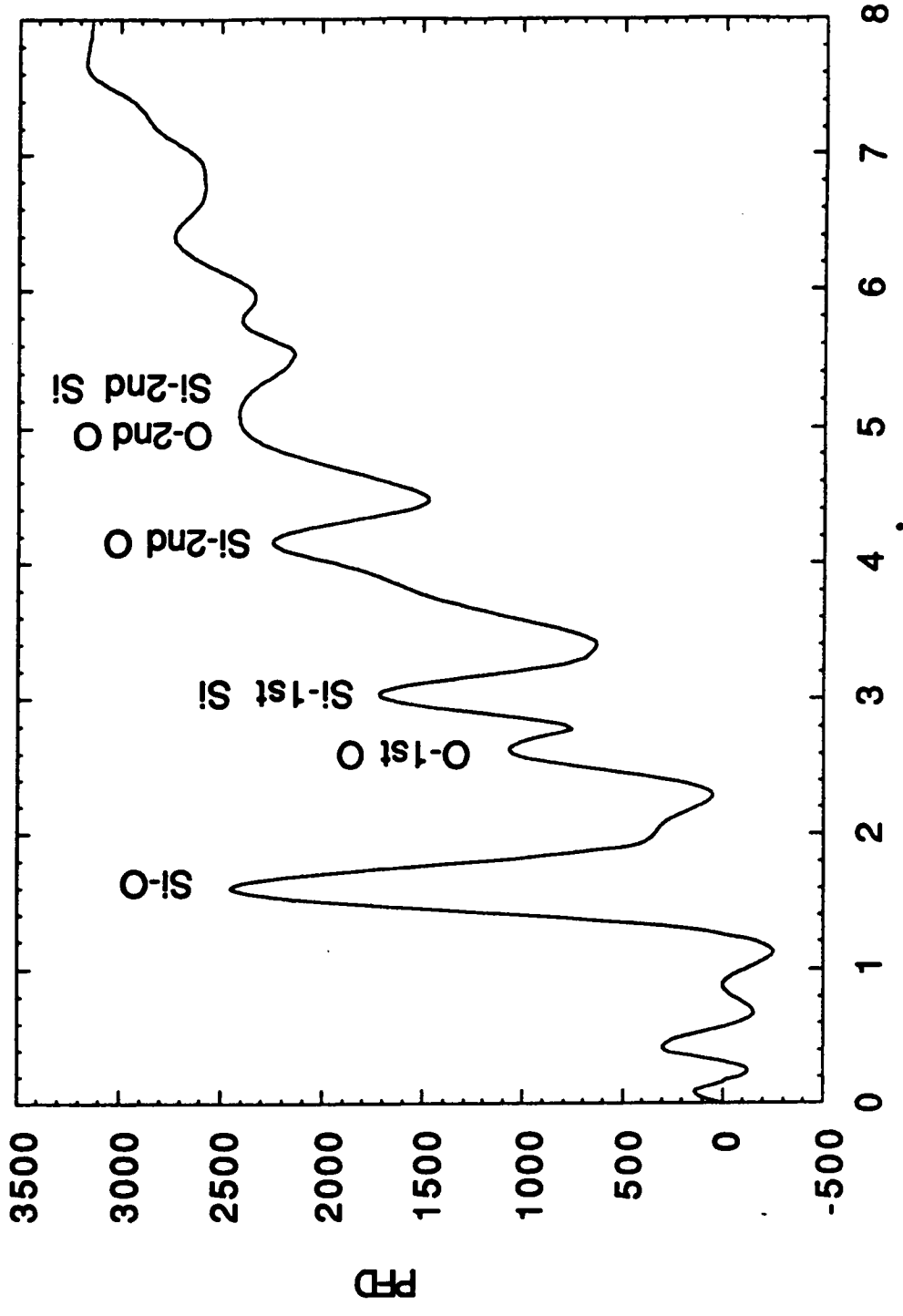

Figure 20. Pair function distribution for the microwave sample.

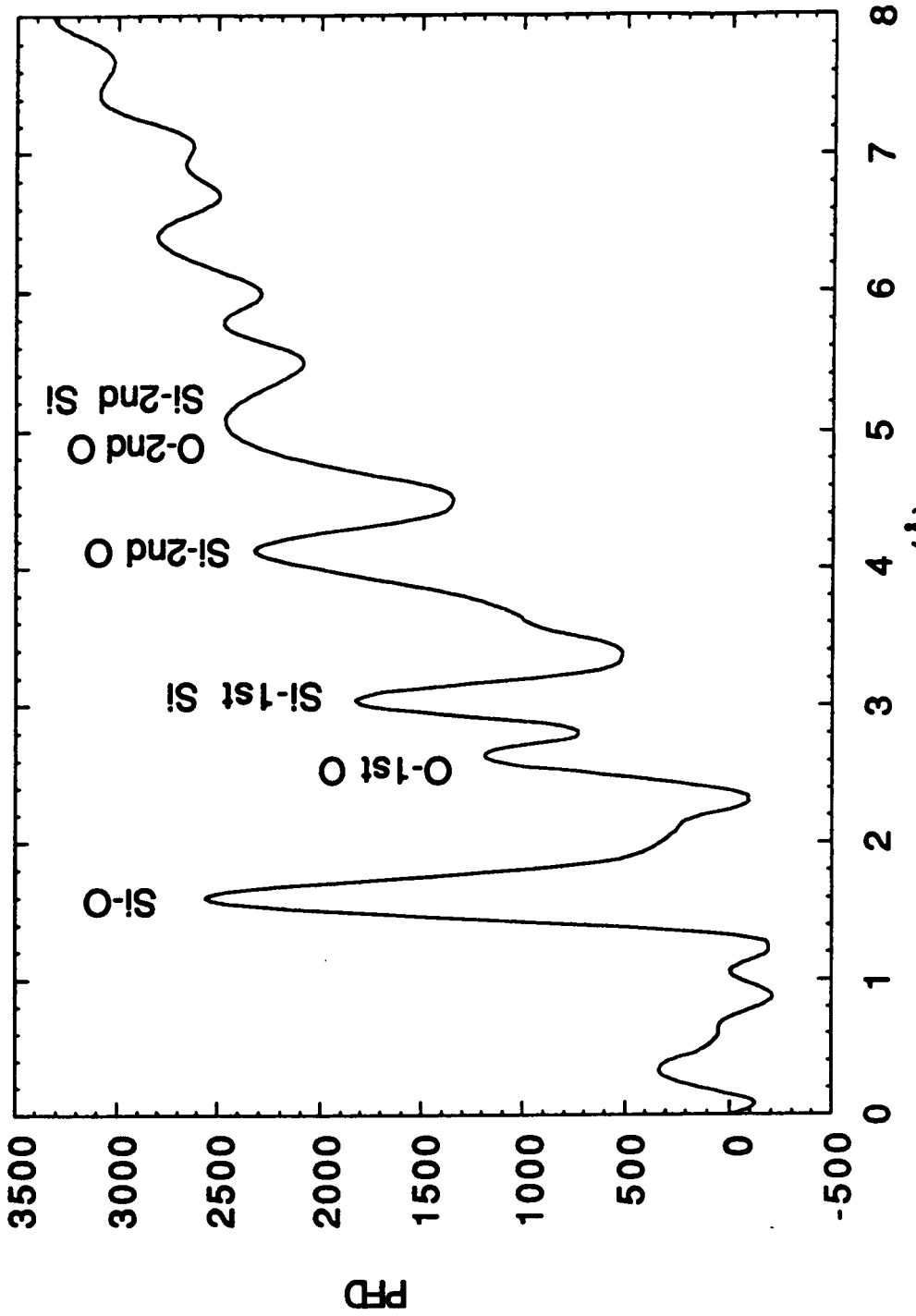

Figure 21. Pair function distribution for the conventional sample.

The primary objective was to obtain a direct comparison between the experimental PFDs of the conventionally melted and the microwave melted samples under equivalent conditions. But, a direct comparison of the PFDs was difficult due to nature of the PFD correction procedure. Therefore, the distance distribution function (DDF) approach offered a more reliable index of structural changes in this investigation. The experimental PFDs were analyzed by the DDF approach.

An attempt was then made to match the experimental PFD curves of the microwave sample and the conventional sample with the theoretical PFD curve on corresponding peaks. The theoretical PFD curve of each peak was determined as a function of distance from the central atom taken as the origin with the aid of auxiliary functions $Q_{ij}(r)$. These Q-functions, assigned by appropriate atom scattering combinations, are shown in Figure 22. The summation of Q-functions was calculated using equation (IV-20). By using the experimentally determined interatomic distances and a trial coordination numbers and by choosing corresponding Q-functions for each peak, the final theoretical PFD was calculated for the best matching with the experimental PFD curve. The experimental PFD curves of the microwave sample and the conventional sample were a little broader than the theoretical PFD curve due to the thermal vibration in the vitreous silica. Therefore, the experimental PFD curve was compared with the modified PFD curve which was convoluted by collecting a suitable set of DDF. The distance distribution function $G(r_{ij})$ and the modified pair function $P'_{ij}(r)$ were introduced as applied by Mozzi and Warren.[30] The modified PFD is given by:

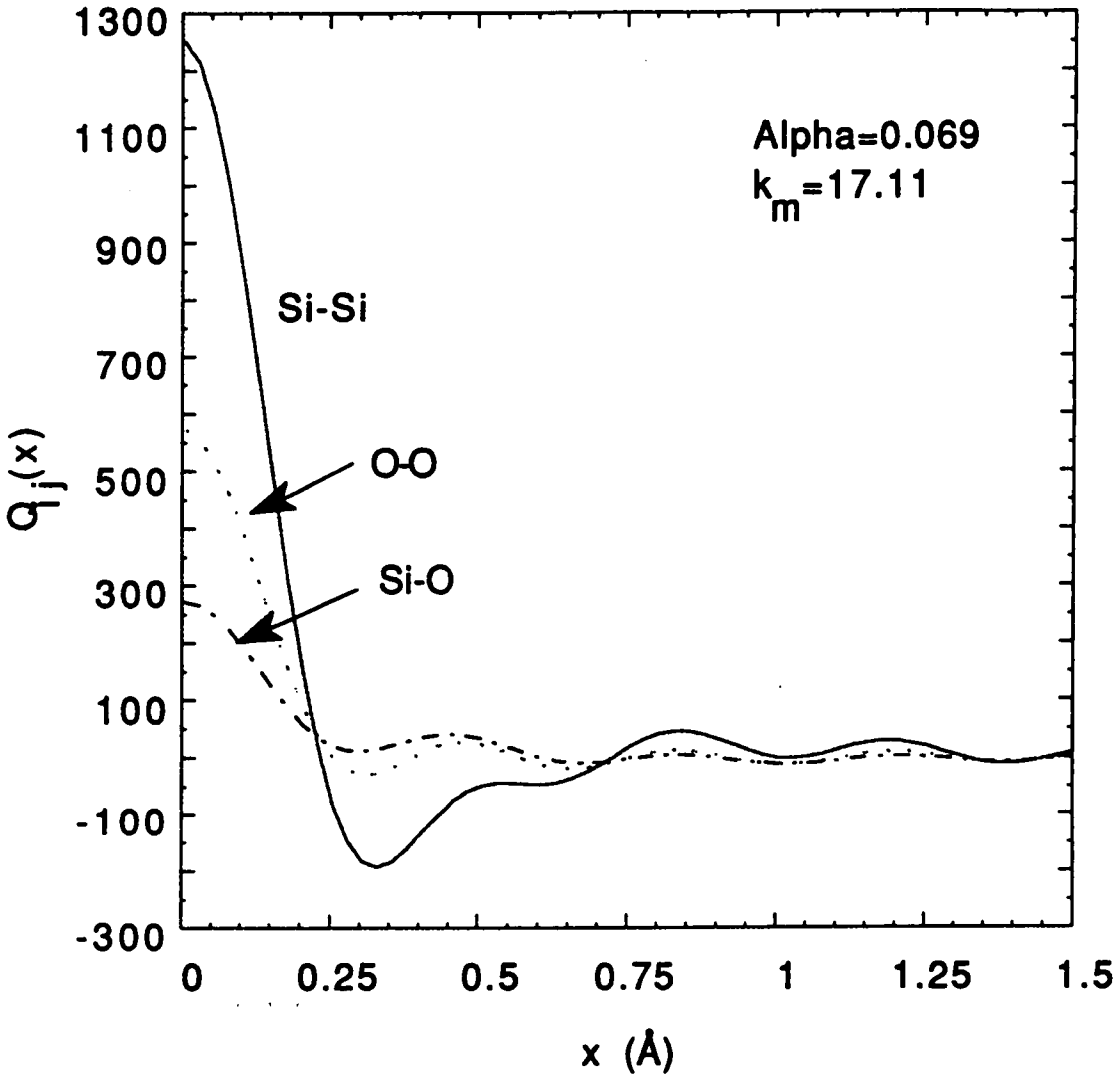

Figure 22. Q-functions for vitreous silica.

(VII-1) $P'_{ij}(r) = \int G(r_{ij})\, Q(r-r_{ij})\, dr_{ij}$

The first peaks of the microwave and the conventional samples each in Figure 20 and 21 had the same peak position at about 1.60 Å, which were attributed to the nearest neighboring Si-O pairs. To improve the fit over the portion of the peak whose height was less than one third of the peak maximum, the DDF was applied. $G(r_{ij})$ was assumed to be $C \exp\{-(r - r_0)^2/2\sigma_{ij}^2)\}$ with the root mean square deviation (σ_{ij}), and $G(r_{ij})$ represented a Gaussian broadening of the near neighbor distances. The accuracy of the derived $G(r_{ij})$ was judged by how well the calculated peak could reproduce the first peak of the experimental PFD curve. For the microwave sample, the satisfactory fit of Si-O peak was obtained by using a DDF over the interval 1.44 Å $\leq r_{ij} \leq$ 1.84 Å using r_0 = 1.60 Å, σ_{ij} = 0.14, and the coordination number $\sum N_{ij}$ = 8.46. For the conventional sample, the satisfactory fit of Si-O peak was obtained by using a DDF over the interval 1.44 Å $\leq r_{ij} \leq$ 1.84 Å using r_0 = 1.60 Å, σ_{ij} = 0.08, and the coordination number $\sum N_{ij}$ = 8.07. These results indicated that the first peak of the microwave sample was broader than that of the conventional sample.

The second peaks of the microwave and conventional samples each in Figure 20 and 21 had the same peak position at about 2.64 Å, which were attributed to the nearest neighboring O-^{1st} O pairs. For the microwave sample, the satisfactory fit of O-^{1st} O peak was obtained by using a DDF over the interval 2.48 Å $\leq r_{ij} \leq$ 2.76 Å using r_0 = 2.64 Å, σ_{ij} = 0.065, and the coordination number $\sum N_{ij}$ = 11.53. For the conventional sample, the satisfactory fit of O-^{1st} O peak was obtained by using a DDF over the interval 2.48 Å $\leq r_{ij} \leq$ 2.76 Å using r_0 = 2.64 Å, σ_{ij} = 0.03, and the coordination number $\sum N_{ij}$ = 12.00. These results indicated that the second peak of the

microwave sample was broader than that of the conventional sample. Also, the distances and coordination numbers of Si-O and O-^{1st} O pairs for the microwave sample and the conventional sample were consistent with regular tetrahedra unit.

The third peaks of the microwave sample and the conventional samples in Figure 20 and 21 were positioned at about 3.02 Å and 3.04 Å, which were attributed to the Si-^{1st} Si pairs. These third peaks were much broader than the theoretical Si-^{1st} Si PFD curve and overlapped with other peaks. Since the thermal vibrations for the first and second peaks were assessed using a Gaussian distribution, this would indicate a negligible variation in Si-O and O-^{1st} O tetrahedral distances beyond those resulting from thermal effects. Additional difficulty was arisen due to the fact that how one could extract the Si-^{1st} Si peak from the experimental PFD curve. The DDF of Si-^{1st} Si pairs in the third peak was derived using the result of Mozzi and Warren[100]:

$$\text{(VII-2)} \qquad G(r_{ij}) = \frac{2}{\pi} \int_0^{k_m} H(k) \sin r_{ij} k \, dk$$

$$\text{and } H(k) = \frac{2}{\pi} \sum_{uc} \sum_{i} \frac{\langle r_{ij} \rangle}{N_{ij}} \frac{f_e^2 \exp(\alpha^2 k^2)}{f_j f_i} \int_0^{\infty} F(r) \sin kr \, dr$$

where F(r) is the observed pair function distribution peak. By using equation (VII-2) and extracting the Si-^{1st} Si peak data from the experimental PFD curve, the DDFs for the microwave sample and conventional sample were determined. The DDF of Si-^{1st} Si pairs, normalized to a peak maximum of 1.0, is shown in Figure 23. This distribution shows a significant difference between the microwave sample

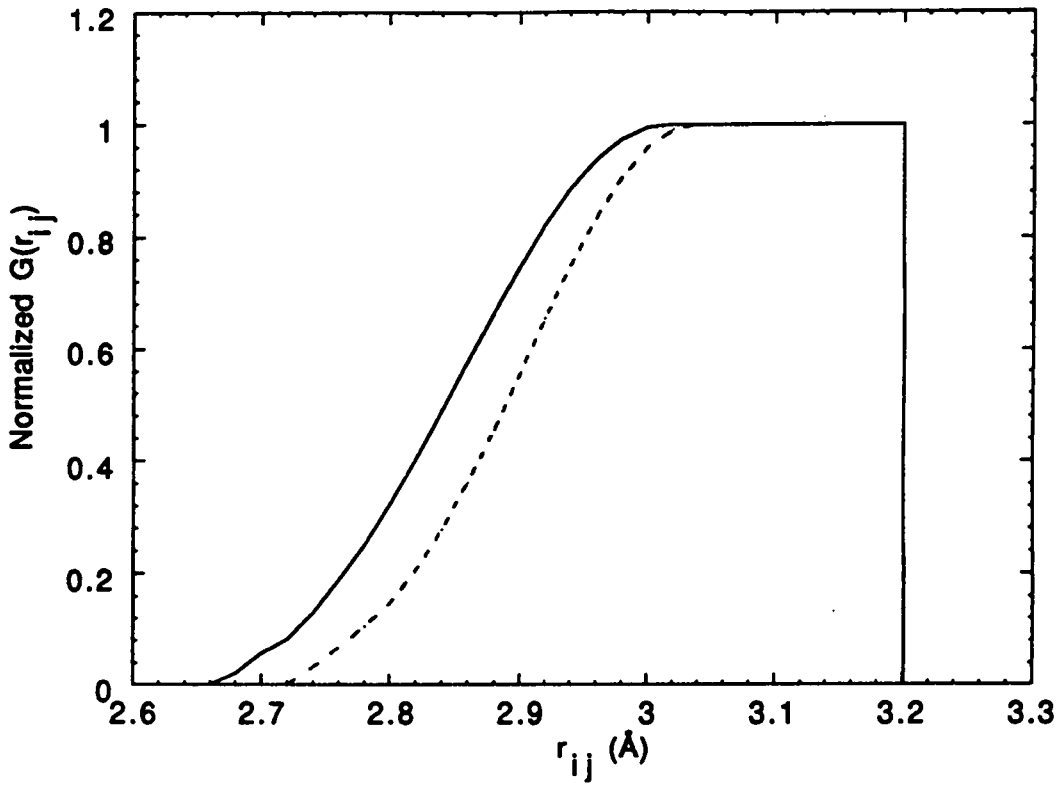

Figure 23. Distance distribution of Si-^{1st} Si for the microwave and conventional sample. The solid line is for the microwave sample. The dashed line is for the conventional sample.

and the conventional sample. The Si-^{1st} Si peak was represented from 2.75 Å ≤ r ≤ 3.24 Å with the derived DDF. The coordination number was chosen about 4.01 for the microwave sample and 4.23 for the conventional sample. The satisfactory fit of Si-^{1st} Si peak was obtained by using this derived DDF and coordination number for the microwave and conventional samples. The distance and coordination number of Si-^{1st} Si pairs for the microwave sample and the conventional sample were consistent with a network of regular tetrahedra with each oxygen atom defining the apex of two adjoining tetrahedra.

The concept of the angular distribution function (ADF) is more convenient than a DDF for the following fourth and fifth peaks. The Si-O-Si bond angle α is represented in Figure 24(a) and the distance of Si-^{1st} Si pairs is related to the angle α by:

(VII-2) $r_{ij} = 3.20 \sin \alpha/2$

Also, the Si-^{1st} Si DDF is related to the distribution V(α) of the Si-O-Si bond angle α by:

(VII-3) $V(\alpha) = G(r_{ij})\ 1.60 \cos \alpha/2$

The angular distribution V(α) calculated from the experimental PFD curve using equation (VII-3) for the microwave sample and the conventional sample is shown in Figure 25. It indicates that the microwave sample and the conventional sample could be characterized by a broad angular distribution, which could provide the first insight into the nature of the

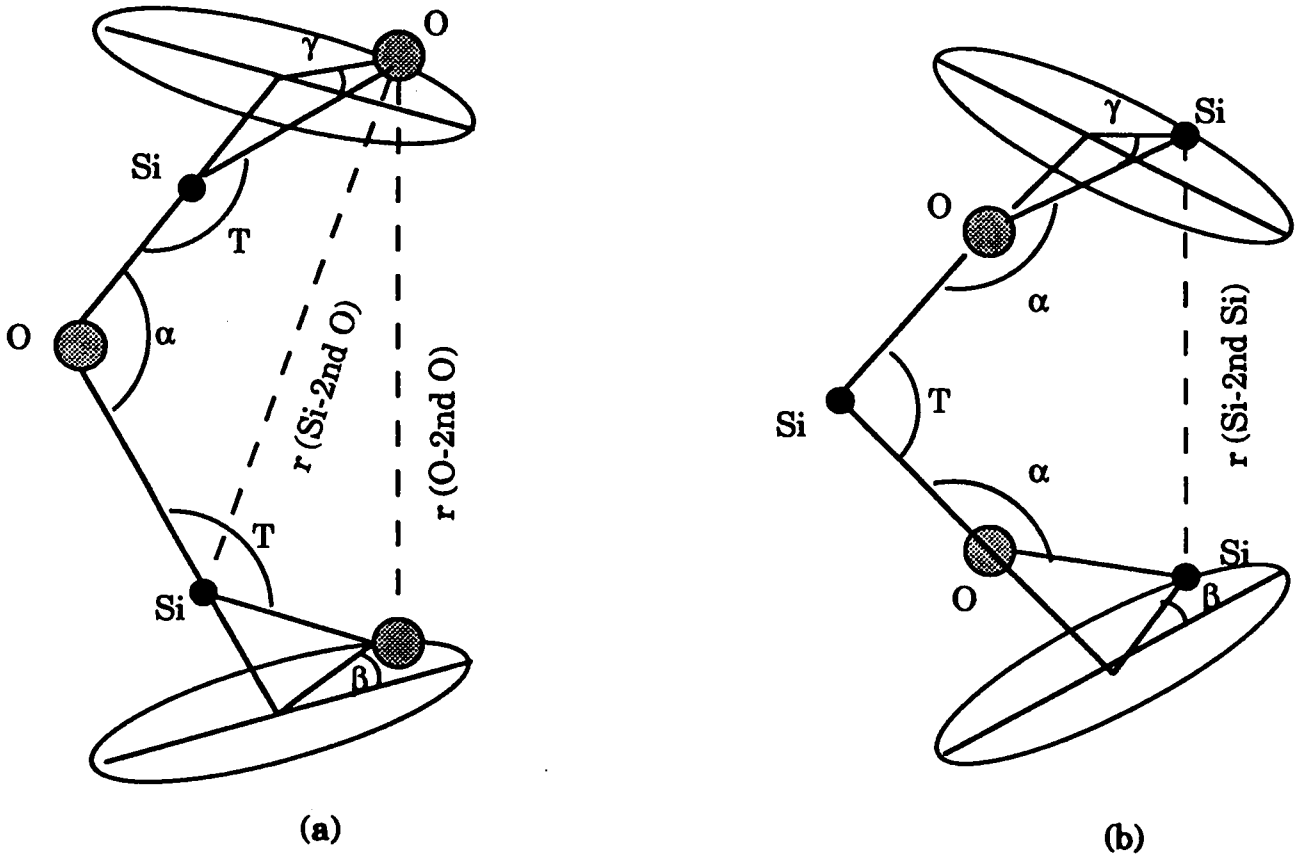

Figure 24. The relations between distances r_{ij} and the angles α, β, γ. (a) Si-^{2nd} O and O-^{2nd} O. (b) Si-^{2nd} Si.

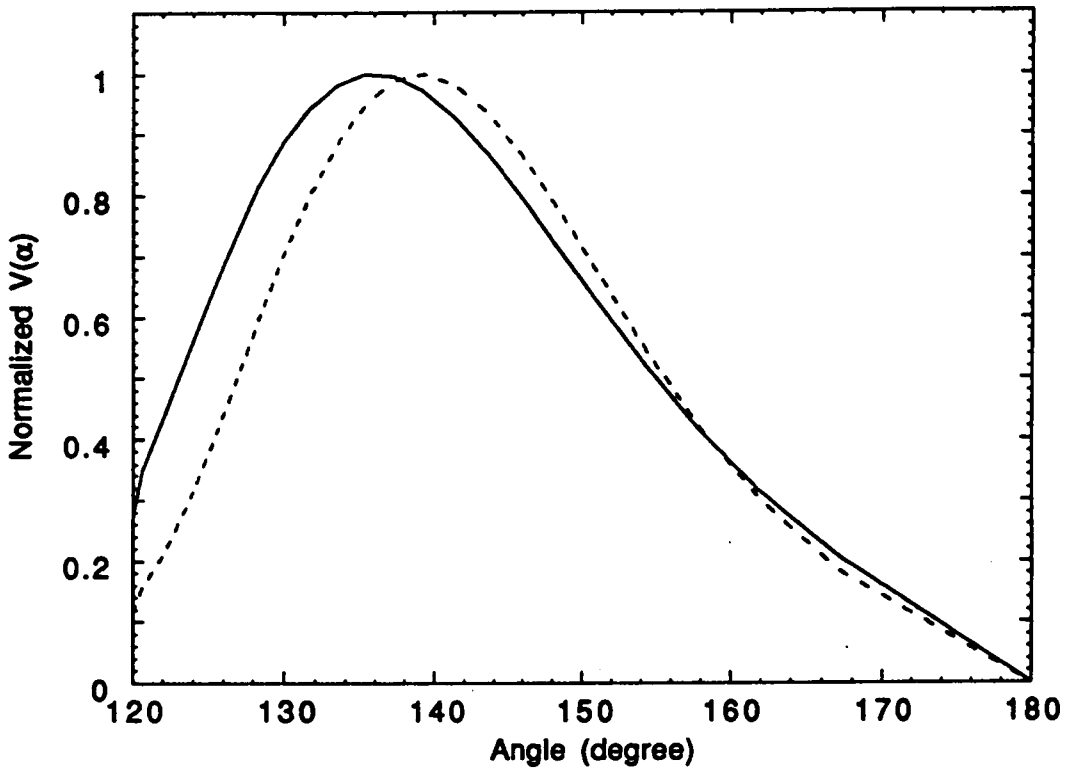

Figure 25. Angular distribution of Si-^{1st} Si for the microwave and conventional sample. The solid line is for the microwave sample. The dashed line is for the conventional sample.

random network for vitreous silica. Comparing the V(α) curve of the microwave sample with that of the conventional sample, the V(α) curve of the microwave sample has shifted to lower values of the angle α with the distribution of angle extending from 130° to 180° than that of the conventional sample. The maximum in the V(α) of the microwave sample occurs at about 136° and that of the conventional sample occurs at about 139°.

The fourth peaks of the microwave sample and the conventional sample in Figure 20 and 21 were positioned at about 4.13 Å and 4.14 Å, which were a consequence of Si-2nd O pairs at distances from the central silicon atom in one tetrahedron to oxygen atoms at the bases of the four adjoining tetrahedra as shown in Figure 24(a). If the adjoining tetrahedra have all possible orientations with equal probability for a given β, the second nearest oxygen neighbors of an average silicon can be considered to be uniformly distributed on circles defined by the three opposite corners of each adjoining tetrahedra. The distribution of Si-^{2nd} O distances can be calculated as a function of β. From Figure 24(a), the distance of Si-^{2nd} O pairs is derived as:

(VII-4) $$r^2_{ij} = 9.65 - 7.0 \cos \alpha - 4.96 \sin \alpha \cos \beta$$

Therefore, the fourth peak can be deconvoluted by the distribution of the Si-O-Si bond angle α and the distribution of the angle β characterizing the mutual distortion around the Si-O-Si bond direction. Mozzi and Warren[30] reported that assumption, that β took with equal probability all values from

0° to 360°, produced the DDF which yielded the modified PFD curve consistent with the experimental PFD curve for vitreous silica.

By solving for r_{ij} using the angle distribution of Si-O-Si V(α), a series of Si-^{2nd} O distances were chosen at 0.05 Å interval from 2.95 Å to 4.25 Å. By varying the value of α between 120° and 180° in 5° step and varying β from 0° to 180° in 5° step, the equation (VII-4) was solved to give corresponding r_{ij} values. The computer program could classify the calculated r_{ij} values into the various 0.05 Å intervals, assigning each r_{ij} value to the weight V(α) of the corresponding value of α. By weighting the probability of occurrence and by assigning the r occurrences in 0.05 Å intervals, a normalized DDFs of Si-^{2nd} O pairs for the microwave sample and the conventional sample were obtained as shown in Figure 26. The DDF for the microwave sample had shifted slightly to lower values of the distance r than that of the conventional sample. The satisfactory fit of Si-^{2nd} O peak was obtained by using this derived DDF allowing β to vary from 0° to 180° with equal probability. Hence, it appeared that the twisting of one tetrahedra with respect to another occurred in a completely random fashion. In addition, this fourth peak for the microwave sample was similar in position to that for the conventional sample, although the Si-O-Si bond angles α for the microwave sample were broader with lower maximum of the V(α) than that for the conventional sample. This was due to the relation among the interatomic distance of Si-^{2nd} O, Si-O-Si bond angle, and the dihedral angles in vitreous silica.

The fifth peaks of the microwave sample and the conventional sample in Figure 20 and 21 were positioned at about 5.06 Å and 5.09 Å, which were the consequence of the superposition of the two contributions O-

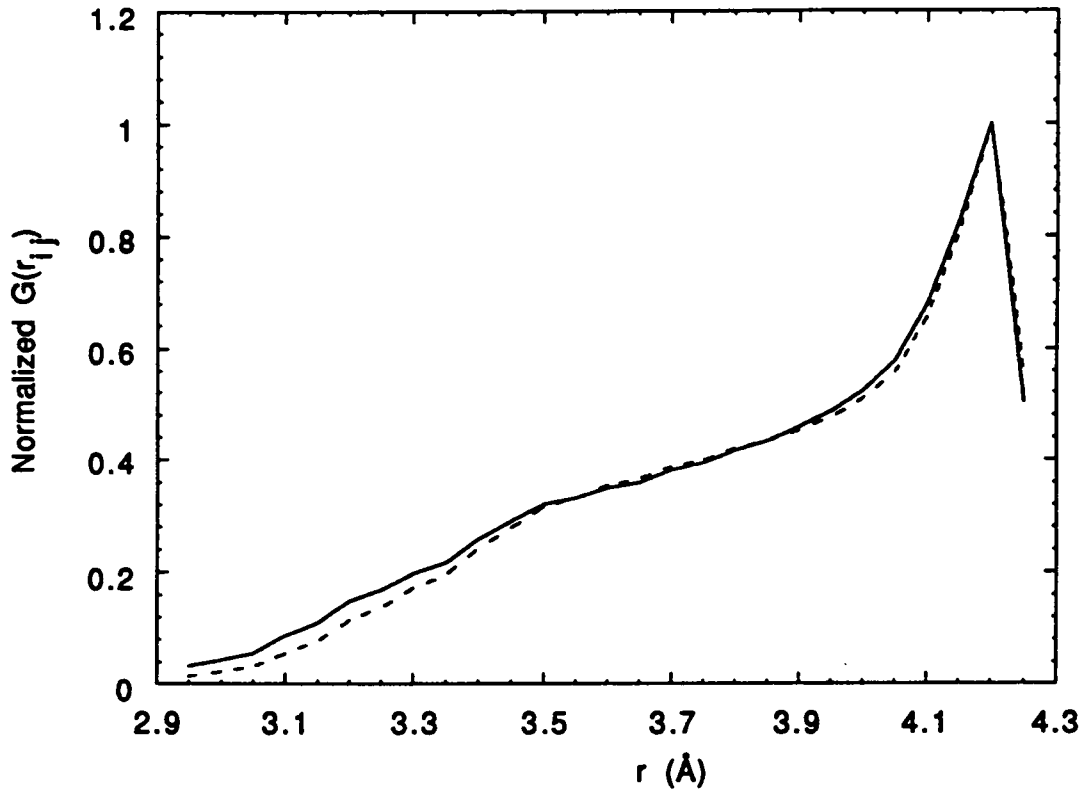

Figure 26. Distance distribution of Si-^{2nd} O for the microwave and conventional sample. The solid line is for the microwave sample. The dashed line is for the conventional sample.

^{2nd} O pairs and Si-^{2nd} Si pairs. The distance of O-^{2nd} O pairs is from one oxygen atom to the other oxygen atom on opposite bases of adjoining tetrahedra as shown in Figure 24(a). The O-^{2nd} O distances is derived as:

$$(VII\text{-}5) \qquad r^2_{ij} = 4.654 (\cos\alpha - \sin\beta \sin\gamma + \cos\alpha \cos\beta \cos\gamma) + 7.015 \{ 2 - 2\cos\alpha - 0.9417 \sin\alpha (\cos\beta + \cos\gamma)\}$$

The distance of Si-^{2nd} Si pairs is from one silicon atom to the other silicon atom on the opposite center of adjoining tetrahedra as shown in Figure 24(b). The Si-^{2nd} Si distance is derived as:

$$(VII\text{-}6) \qquad r^2_{ij} = 10.5 (\sin\alpha/2)^2 \{ 2.673 - 0.9417 \sin\alpha (\cos\beta + \cos\gamma)\} - 5.24 (\sin\alpha)^2 \{ 0.3365 + 0.3365 \cos\beta \cos\gamma + \sin\beta \sin\gamma \}$$

The DDFs of O-^{2nd} O and Si-^{2nd} Si in the fifth peak were calculated in a similar manner to that of the fourth peak, but taking into account the variation of the third angle γ for each of the set of values of α and β. Mozzi and Warren[30] reported that a variation of γ similar to that of β ,which took with equal probability all values from 0° to 360°, gave the best fit to the experimental PFD curve. This means that the SiO_4 tetrahedra in vitreous silica could be assumed to be a random orientation about the plane containing the Si-O-Si bond angle α. The DDFs of O-^{2nd} O pairs and Si-^{2nd} Si pairs for the microwave sample and the conventional sample are shown in Figure 27 and 28. The DDFs of O-^{2nd} O pairs and Si-^{2nd} Si pairs in the microwave sample had slightly shifted to lower values of the distance r than that in the conventional sample. The satisfactory fit of O-^{2nd} O and Si-

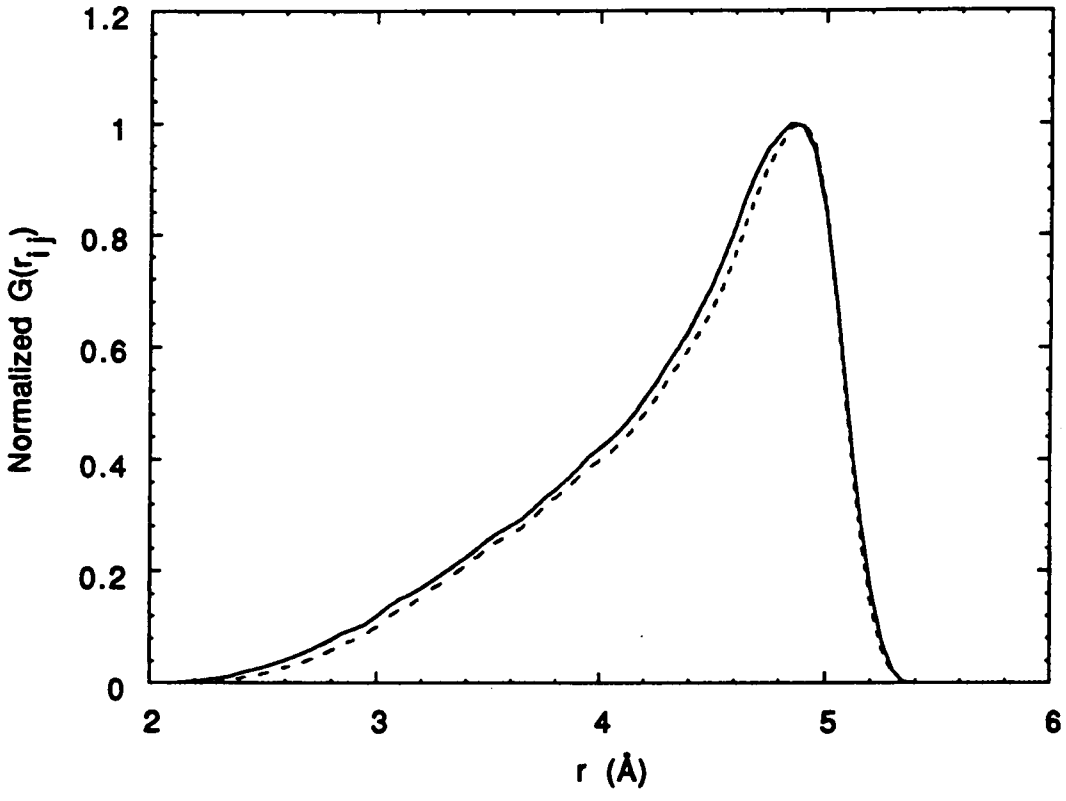

Figure 27. Distance distribution of O-2nd O for the microwave and conventional sample. The solid line is for the microwave sample. The dashed line is for the conventional sample.

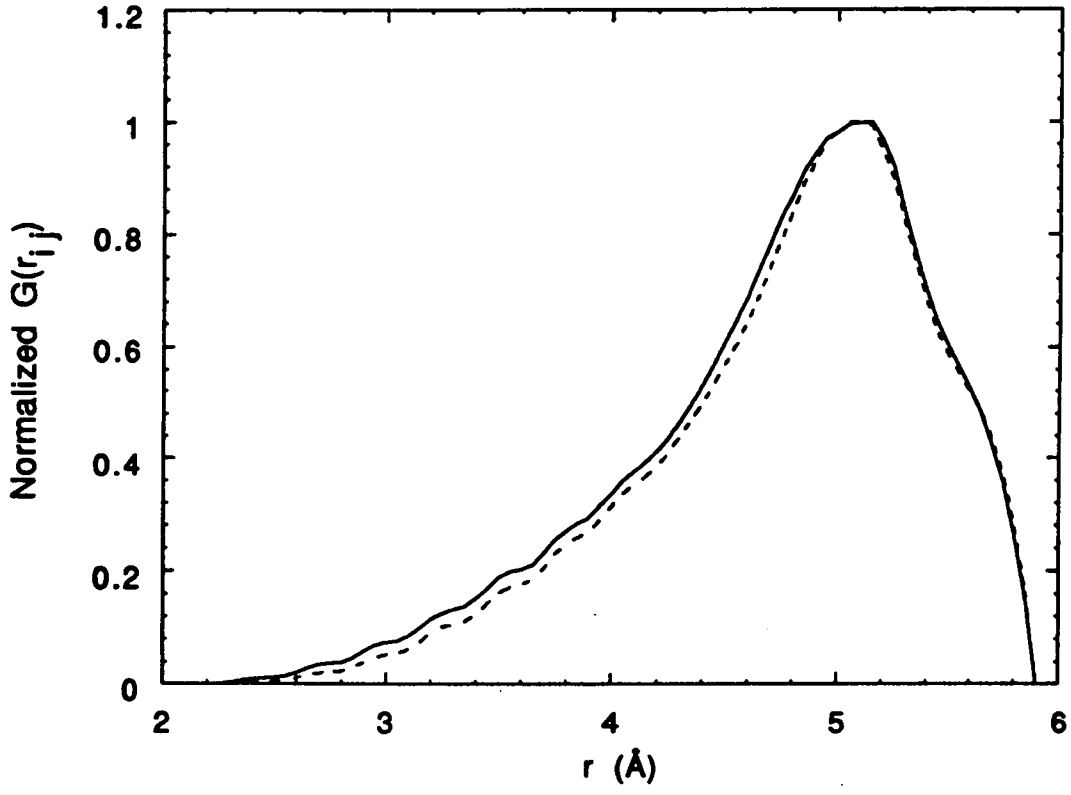

Figure 28. Distance distribution of Si-2nd Si for the microwave and conventional sample. The solid line is for the microwave sample. The dashed line is for the conventional sample.

^{2nd} Si peaks was obtained by using these derived DDFs allowing β to vary from 0° to 180° and γ to vary from 0° to 180° with equal probability.

Attempts were made to match the experimental PFD curve with previously modified PFD curve of several peaks. The modified PFD curve of each peak which was convoluted with the proper DDF was then substituted in the left-hand side of equation (IV-23). The individual calculated peaks for the microwave sample and the conventional sample are shown in Figure 29 and 30. The total PFD curves obtained by adding together the individual contributions are shown in Figure 31 for the microwave sample and in Figure 32 for the conventional sample. It was clear that a fairly good fit was obtained for the first three peaks of the modified PFD curve, but the fit was not so good from the fourth peak on. The Si-^{3rd} O peak should exist at about 6.4 Å as shown by Mozzi and Warren.[30] In this study, the contribution of this Si-^{3rd} O peak as well as subsequent peaks was neglected in the total PFD curve, so the lack of fit from the fourth peak on was due to the fact that contributions from the peaks beyond the fifth peak were not taken into account.

The structural differences between the microwave sample and the conventional sample are tabulated in Table 5. These tabulated data are explored in order to propose a process for the structural modifications induced in vitreous silica by microwave radiation. The coordination number of the Si-O pairs in the microwave sample is larger than that in the conventional sample. The coordination number of the O-^{1st} O and Si-^{1st} Si pairs in the microwave sample is smaller than that in the conventional sample. The summation of the coordination number of the Si-O, O-^{1st} O, and Si-^{1st} Si pairs in the microwave sample is approximately same as that

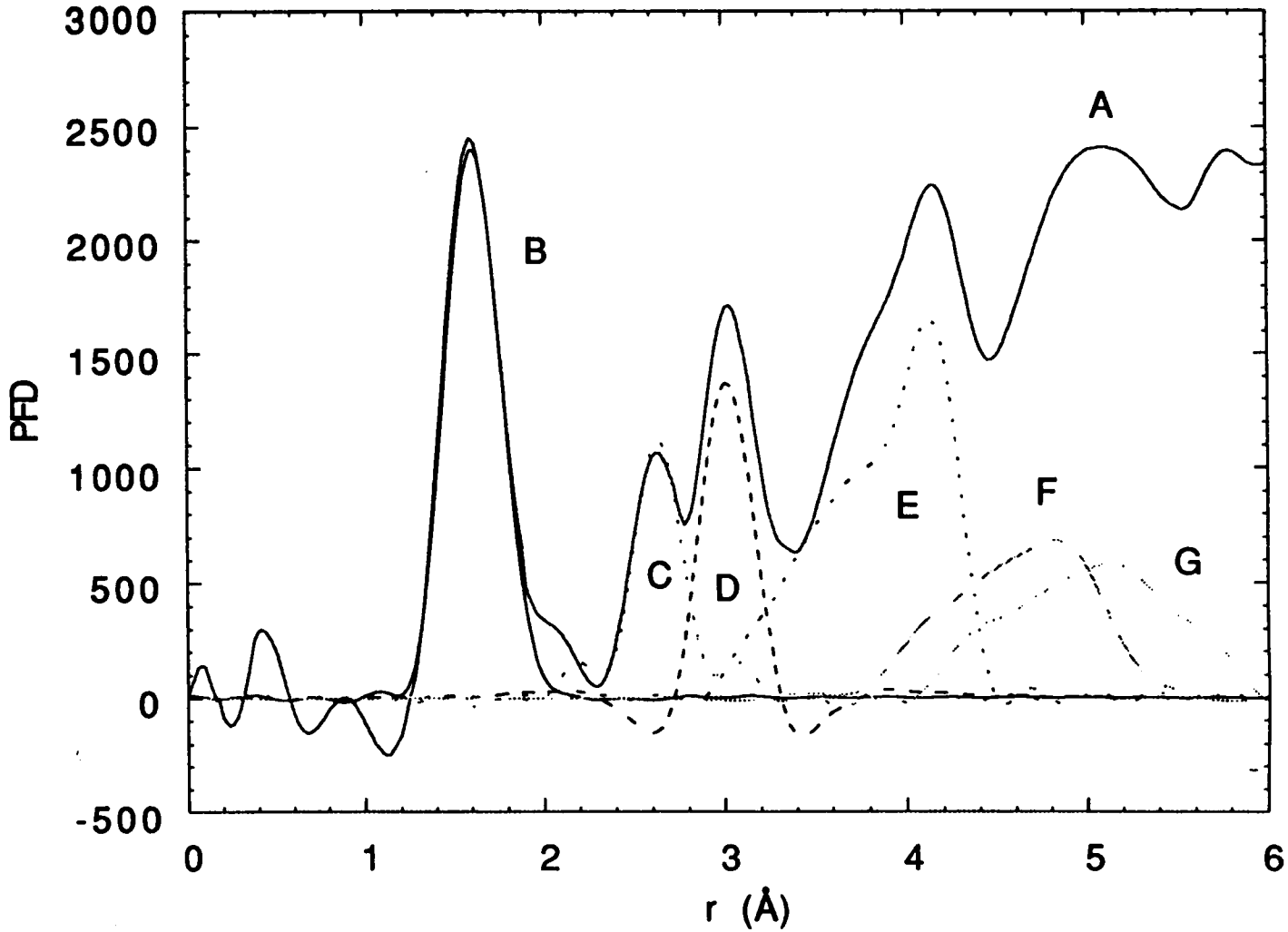

Figure 29. Comparison of the experimental PFD curve for the microwave sample with each calculated contribution. A is the experimental curve. The calculated contributions are given by: B, Si-O; C, O-^{1st} O; D, Si-^{1st} Si; E, Si-^{2nd} O; F, O-^{2nd} O; G, Si-^{2nd} Si.

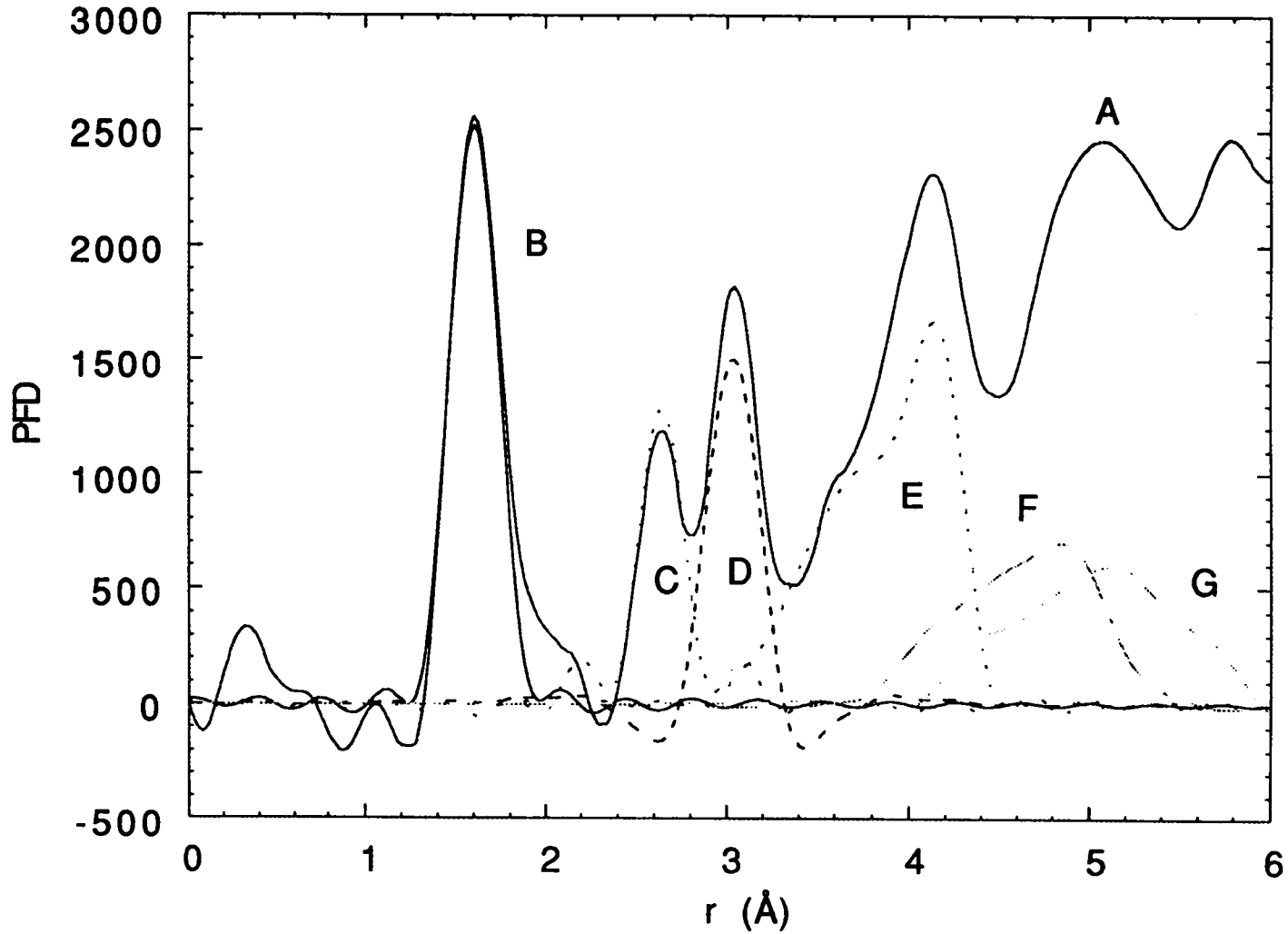

Figure 30. **Comparison of the experimental PFD curve for the conventional sample with each calculated contribution. A is the experimental curve. The calculated contributions are given by: B, Si-O; C, O-^{1st} O; D, Si-^{1st} Si; E, Si-^{2nd} O; F, O-^{2nd} O; G, Si-^{2nd} Si.**

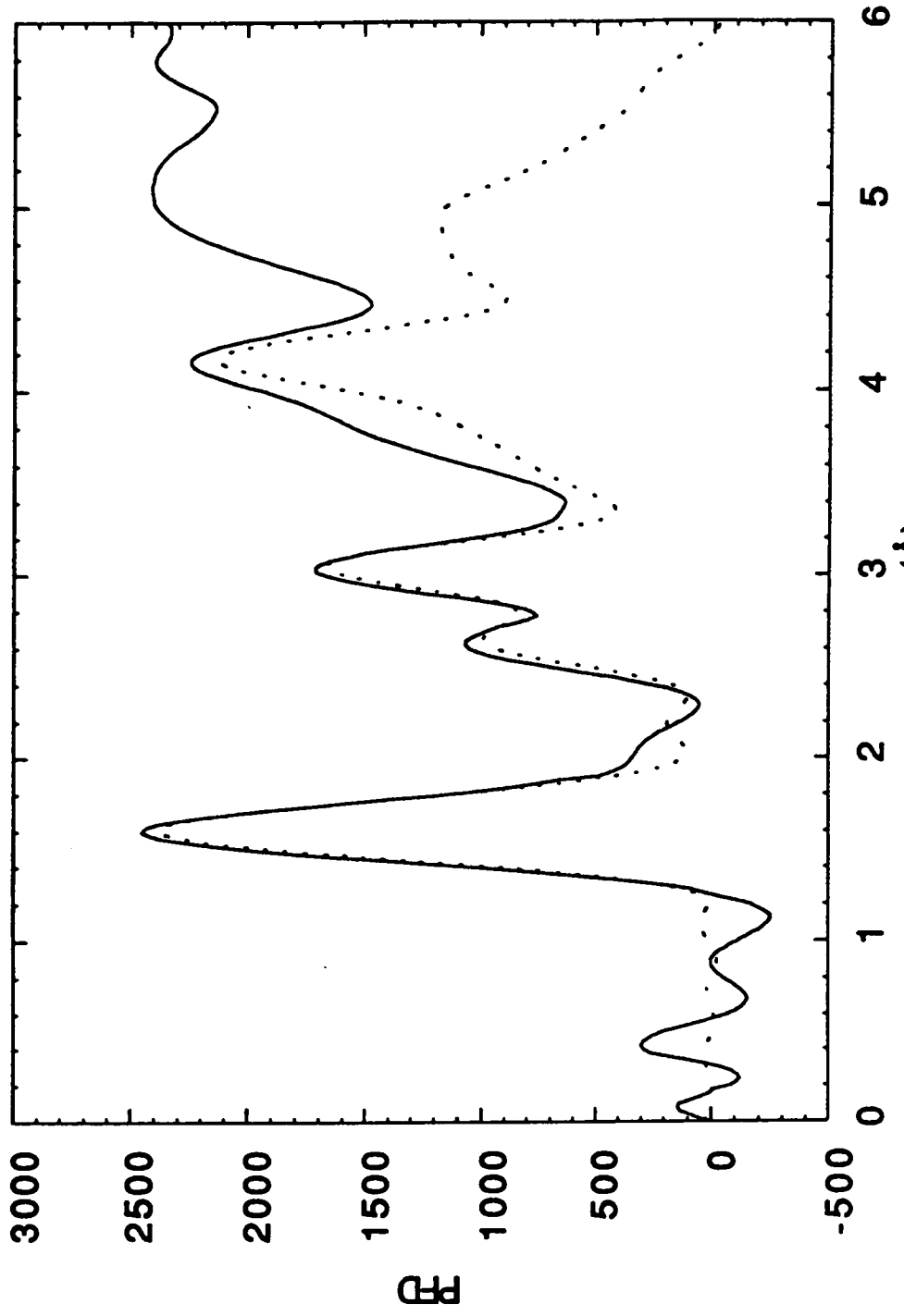

Figure 31. Comparison of the experimental PFD curve for the microwave sample with calculated total PFD curve. The solid line is for the experimental curve. The dashed line is for the calculated curve.

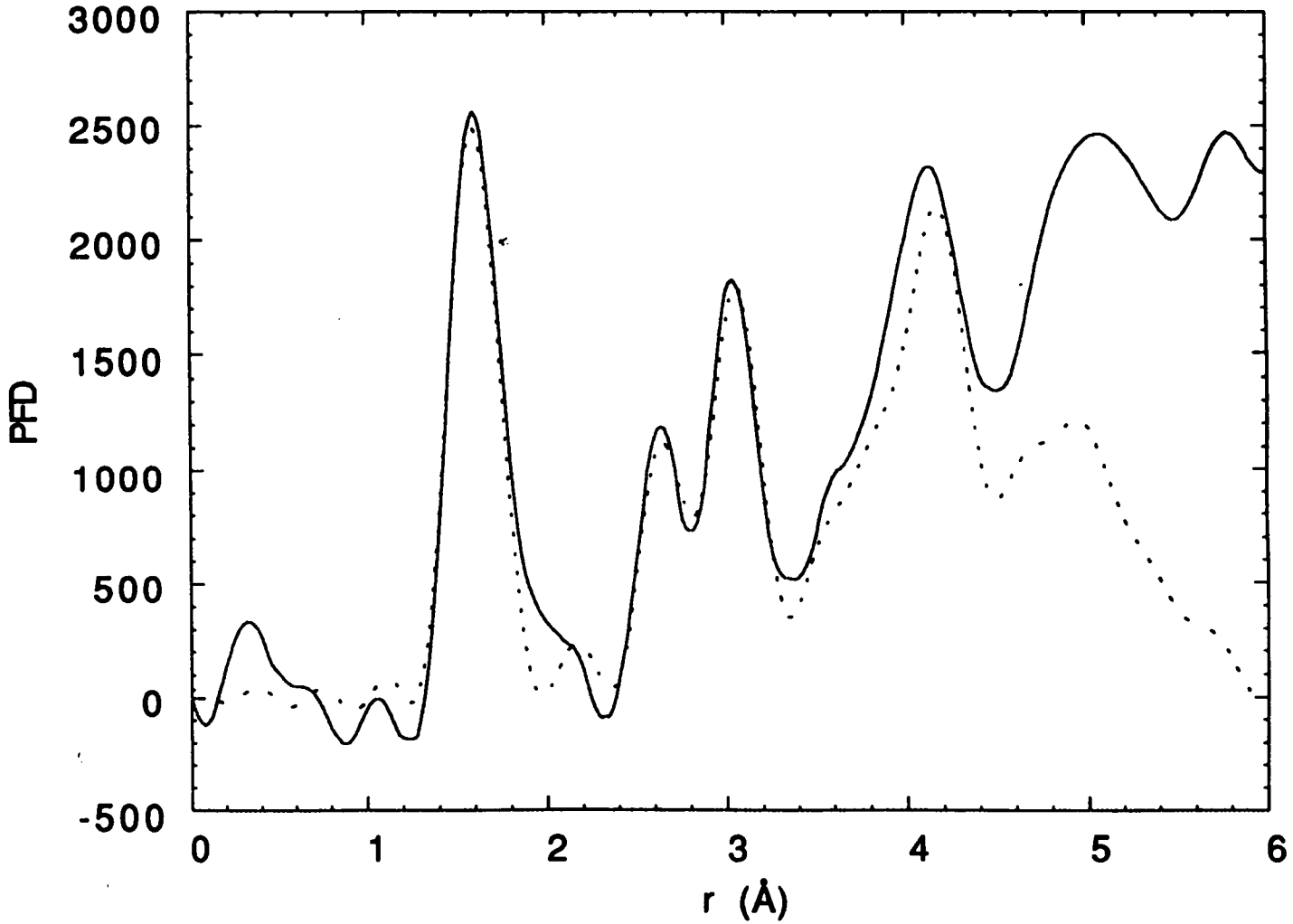

Figure 32. **Comparison of the experimental PFD curve for the conventional sample with calculated total PFD curve. The solid line is for the experimental curve. The dashed line is for the calculated curve.**

Table 5. Summary of PFD and DDF in the microwave and conventional sample.

	Peak Position		Coordination Numbers (N_{ij})		Root Mean Square Deviations (σ_{ij})	
	Microwave	Convention	Microwave	Convention	Microwave	Convention
1st peak (Si-O)	1.60 Å	1.60 Å	8.46	8.07	0.14	0.08
2nd peak (O-^{1st}O)	2.64 Å	2.64 Å	11.53	12.00	0.065	0.03
3rd peak (Si-^{1st}Si)	3.02 Å	3.04 Å	4.01	4.23	α_{max}=136°	α_{max}=139°
4th peak(Si-^{2nd} O)	4.13 Å	4.14 Å				
5th peak (O-^{2nd} O)	5.06 Å	5.09 Å				
5th peak (Si-^{2nd} Si)	5.06 Å	5.09 Å				

in the conventional sample. These indicate that bond cleavages are occurred and the singly bonded oxygens are then generated and bent in the rigid structure of vitreous silica due to microwave radiation. From Figure 25 and Table 5, the V(α) curve of the microwave sample is shifted to lower values of angle α with the angle distribution extending from 120° to 180° than that of the conventional sample. It indicates that the twisting reorientation of SiO_4 tetrahedra or the bending of the non-bridging oxygens will occur. Although the Si-O-Si bond angles α for the microwave sample are shifted lower value of angle with a maximum (136°) of the V(α) than that for with a maximum (139°) of the V(α) for the conventional sample, the Si-^{2nd} O peak for the microwave sample is similar in position to that for the conventional sample. From Figures 23, 26, 27, and 28, the shift difference to lower value r in $G(r_{ij})$ curves for the microwave sample and the conventional sample is decreased in a comparison with the third, fourth, and fifth peaks. It can be explained by the relation among the interatomic distance of Si-^{2nd} O, the Si-O-Si bond angle (α), and the dihedral angles (β and γ) in vitreous silica. The fifth peak, which is attributed to the combination of O-^{2nd} O pairs and Si-^{2nd} Si pairs, for the microwave sample is seen to shift to slightly lower values of r than that of the conventional sample. It indicates that interatomic distances are decreased due to the densification of the microwave sample. This microwave induced affect can be explained by the modification of the random network in vitreous silica.

In this investigation, the experimental PFD curve of the microwave sample was broader than that of the conventional sample. This effect could not be explained as a transient general thermal effect, but it would be explained by a rapid transient effect associated with the local distortion of

the network or energy deposition of microwave radiation. Therefore, the peak broadening of the microwave sample could be the generation of non-bridging oxygens, the bending of the non-bridging oxygens, and the twisting reorientation of SiO_4 tetrahedra.

The structural modification in the microwave sample is mainly in the nature of adjoining tetrahedra being bent or twisted with respect to each other. As suggested by Vucevich,[138] the restoring force constant for the transverse oxygen vibrations in vitreous silica is eleven times smaller than the constant of the longitudinal mode. Since it is easier to bend the Si-O-Si bond angle than to change the Si-O distance, the transverse oxygen mode would lead to decrease in Si-^{1st} Si distance and densification of the random network. In this investigation, the $V(\alpha)$ of the microwave sample was shifted to lower values of α with a maximum at 136° than that of the conventional sample with a maximum at 139°. It could be interpreted as being due to Si-O-Si bond deformation vibrations of those oxygen atoms having alternative positions of equal energies under the influence of microwave radiation.

Wick[93] reported that the formation of singly bonded oxygens by adding K_2O in vitreous silica, which would break up some of the Si-O-Si links in the random network, would cause a greater distribution of intertetrahedral angles. In his study, this could be seen by the increasingly diffuse nature of the peaks in the experimental PFD curve and particularly by the increased distribution of intertetrahedral angles. Himmel et al.[136] reported that the network defects like five-fold or seven-fold rings which could arrange in lines distorted the polyhedra in vitreous silica and resulted finally in a broad distribution of the Si-O-Si bond angle.

In this investigation, the PFD curve of the microwave sample in Figure 20 is much broader than that of the conventional sample in Figure 21 at distances smaller than 5.5 Å and the PFD curve of the microwave sample in Figure 20 has less structure than that of the conventional sample in Figure 21 at distances larger than 5.5 Å. At smaller distances, it could be explained by the generation of singly bonded oxygens, the bending of the non-bridging oxygens, and the twisting of the immediate surrounding. At larger distances, it was assumed that the middle range ordering in the microwave sample came to be more uniformly random than that of the conventional sample. This randomness should be increased by the way in which the six-fold rings would be distorted in the random network. From the possibility of changing the ring distribution statistics, it could be assumed that microwave radiation could produce various size rings in the microwave sample to increase randomness.

The present PFD-DDF results of the structure of the microwave sample and the conventional sample was in qualitative agreement with the results of Mozzi and Warren.[30] The PFD-DDF analysis was much more useful and the present results showed that the generation of the singly bonded oxygen and the modification of the random network, which resulted in a shift of Si-O-Si bond angle distribution and in broader distance distributions of S1-O, O-O, and Si-O pairs, could be indicative of the dynamics of the processes leading to microwave densification. These analyses approved several assumptions of the previous section.

Chapter VIII.

Summary and Conclusions

The results of the present investigation could determine the main details of loss mechanisms for microwave heating of glass materials. It is hoped that this investigation will provide an impetus to further work on the theoretical explanation of loss mechanisms. The random network of vitreous silica appears to be affected by microwave radiation. Because the rigid atomic structures do not oscillate readily under the influence of 2.45 GHz microwave radiation, the dielectric losses are low. When vitreous silica is coupled and melted using a zirconia susceptor, the increased amplitude of infrared oscillation and microwave-enhanced oscillation make its random network deform or twist. As a result, the modification of the nearest neighbor distance distributions and the coordination numbers is obtained. X-ray diffraction method and PFD-DDF analysis provide results about fundamental structural units as well as about their connection to a random network by yielding data on bond distance distributions and bond angle distributions.

The following conclusions can be made from the examination of the results in this investigation.

1. The rigid and continuous networks of vitreous silica are relatively transparent to microwave radiation. Since microwave energy absorption and dielectric losses are low, vitreous silica couples with 2.45 GHz microwave radiation using a zirconia susceptor and it is then heated to its melting temperature. The silica sand, contained small amount of

impurities, yields greater microwave energy absorption owing to the oscillation of the interstitial ions.

2. The thermal gradient of microwave heating within the sample is different from that of conventional heating due to the internal heating characteristics of microwave radiation. The different stress gradient in the microwave sample due to the different thermal gradient prevents freeze-in liquid retaining the crystobalite-like structure during the quenching.

3. X-ray diffraction patterns in the microwave sample and the conventional sample are somewhat different at higher k regions.

4. The distance of the Si-O and O-^{1st} O pairs for the microwave sample is the same as that for the conventional sample. The coordination number of the Si-O pairs for the microwave sample is larger than that for the conventional sample. The coordination number of the O-^{1st} O and Si-^{1st} Si pairs for the microwave sample is smaller than that for the conventional sample. The summation of the coordination number of the Si-O, O-^{1st} O, and Si-^{1st} Si pairs for the microwave sample is approximately same as that for the conventional sample. It indicates that the singly bonded oxygens are generated due to bond cleavages and the non-bridging oxygens are bent in the random network of SiO_4 tetrahedra under the influence of microwave radiation.

5. The distance of Si-^{1st} Si in the microwave sample is somewhat smaller than that in the conventional sample. A distribution of intertetrahedral angles V(α) ranging from 130° to 180° for the microwave sample is shifted to a lower value of angle α than that for the conventional sample. The maximum value of 136° in V(α) is obtained for the microwave sample, and the maximum value of 139° in V(α) is obtained for the

conventional sample. The DDFs of O-^{2nd} O pairs and Si-^{2nd} Si pairs in the microwave sample had slightly shifted to lower values of the distance r than that in the conventional sample. It indicates that the twisting reorientation of SiO_4 tetrahedra or the bending of non-bridging oxygens will occur due to microwave densification.

6. The middle range ordering for the microwave sample is more uniformly random than that for the conventional sample. It indicates that microwave radiation produces various size rings in vitreous silica to increase randomness.

7. The possible major loss mechanisms for vitreous silica are the deformation losses and the conduction losses. The possible major loss mechanisms for silicate glasses are the deformation losses, the conduction losses, and the ion migration losses.

Chapter VIIII.

Suggestions for Future Work

The dielectric constant and the loss tangent for the glass materials should be measured as a function of temperature to predict possible loss mechanisms more precisely in microwave heating of glass materials. Heat transfer and thermal stresses of the microwave sample during heating and cooling should be solved in order to better understand the microwave heating of any specific materials.

Due to the characteristics of the microwave heating, which is to prohibit the formation of cystobalite-like structure, the application of microwave energy for the annealing of glass materials would be particularly appealing.

The loss mechanisms which have been proposed here, indicate that alkali ions should play a very important role in microwave coupling, affecting high energy-loss behavior. Currently, it is the most important area of investigation for microwave heating. Using the improved experimental and theoretical techniques of X-ray diffraction and PFD-DDF, improved data can be obtained on the structure of silicate glasses. It would be interesting to examine other glass-forming system, especially high lossy glass materials, and to investigate the relevant forms of network generation.

In cases where it is not possible to experimentally eliminate Compton, the Compton scattering should be experimentally determined. Improvement should be made to the X-ray diffraction system used in

present investigation. The use of MoK_α radiation in the present investigation limited the range of high k values in which accurate intensity data were available. An experimental set-up using AgK_α radiation with Rh-Ru balanced filters to experimentally eliminate the Compton scattering should be tried to give accurate intensity data out to higher values of k. This would enhance the resolution possible in the PFD-DDF analysis method and make the PFD-DDF analysis more precise.

Infrared and Raman spectroscopy with X-ray diffraction method should be made to give a better picture of the existence of non-bridging oxygens and the distribution of various size rings in microwave melted vitreous silica.

Bibliography

Bibliography

1. W. H. Sutton, "Microwave Processing of Ceramic Materials," Am. Ceram. Soc. Bulletin, Vol. 68, No. 2, pp. 376-86, (1989).

2. D. S. Patil and B. C. Mutsuddy, "Microwave Sintering of Alumina Ceramics in a Single Mode Applicator," Ceramic Transactions, Vol. 21, pp. 301-09, The American Ceramic Society, Inc., Westerville, Ohio, (1991).

3. A. De, I. Ahmad, E. D. Whitney, and D. E. Clark, "Microwave (Hybrid) Heating of Alumina at 2.45 GHz," Ceramic Transactions, Vol. 21, pp. 329-39, The American Ceramic Society, Inc., Westerville, Ohio, (1991).

4. M. C. L. Patterson, R. M. Kimber, and P. S. Apte, "The Properties of Alumina Sintered in a 2.45 GHz Microwave Field," Microwave Processing of Materials II, Vol. 189, pp. 257-66, Materials Research Society, Pittsburgh, PA, (1991).

5. W. B. Harrison, M. R. B. Hanson, and B. G. Koepke, "Microwave Processing and Sintering of PZT and PLZT Ceramics," Microwave Processing of Materials II, Vol. 189, pp. 279-86, Materials Research Society, Pittsburgh, PA, (1991).

6. M. A. Janney, C. L. Calhoun, and H. D. Kimrey, "Microwave Sintering of Zirconia-8 Mol% Yttria," Ceramic Transactions, Vol. 21, pp. 311-18, The American Ceramic Society, Inc., Westerville, Ohio, (1991).

7. S. S. Park and T. T. Meek, "Characterization of ZrO_2-Al_2O_3 Composites Sintered in a 2.45 GHz Electromagnetic Field," J. Mat. Sci., Vol. 26, No. 23, pp. 6309-13, (1991).

8. H. D. Kimrey, J. O. Kiggans, M. A. Janney, and R. L. Beatty, "Microwave Sintering of Zirconia-Toughened Alumina Composites," Microwave Processing of Materials II, Vol. 189, pp. 243-55, Materials Research Society, Pittsburgh, PA, (1991).

9. E. A. Maguire and D. W. Readey, "Microwave-Absorbing Ferrite Composites," J. Am. Ceram. Soc., Vol. 59, No. 9-10, pp. 434-37, (1976).

10. M. K. Krage, "Microwave Sintering of Ferrites," Am. Ceram. Soc. Bulletin, Vol. 60, No. 11, pp. 1232-34, (1981).

11. S. N. Kumar, A. Pant, R. R. Sood, J. Ng-Yelim, and R. T. Holt, "Production of Ultra-Fine Silicon Carbide by Fast Firing in Microwave and Resistance Furnaces," Ceramic Transactions, Vol. 21, pp. 395-410, The American Ceramic Society Inc., Westerville, Ohio, (1991).

12. R. Silberglitt and D. Palaith, "Investigation of Interlayer Materials for the Microwave Joining of SiC," Ceramic Transactions, Vol. 21, pp. 487-95, The American Ceramic Society, Inc., Westerville, Ohio, (1991).

13. Y. H. Kao and J. D. Mackenzie, "Magnetite As a Sintering Aid for Microwave Consolidation of Soda-Lime Glass," Ceramic Transactions, Vol. 21, pp. 341-48, The American Ceramic Society, Inc., Westerville, Ohio, (1991).

14. Z. Fathi, I. Ahmad, J. H. Simmons, and D. E. Clark, "Surface Modification of Sodium Aluminosilicate Glasses Using Microwave Energy," Ceramic Transactions, Vol. 21, pp. 623-29, The American Ceramic Society, Inc., Westerville, Ohio, (1991).

15. E. J. A. Pope, "Microwave Sintering of Sol-Gel Derived Silica Glass," Am. Ceram. Soc. Bulletin, Vol. 70, No. 11, pp. 1777-78, (1991).

16. Y. L. Tian, D. L. Johnson, and M. E. Brodwin, "Ultrafine Microstructure of Al_2O_3 Produced by Microwave Sintering," Ceramic Powder Science, II, pp. 925-32, The American Ceramic Society, Inc., Westerville, Ohio, (1988).

17. S. Das and T. R. Curlee, "Microwave Sintering of Ceramics: Can We Save Energy?" Am. Ceram. Soc. Bulletin, Vol. 66, No. 7, pp. 1093-94, (1987).

18. I. J. Chabinsky and E. E. Eves III, "The Application of Microwave Energy in Drying, Calcining, and Firing of Ceramics," Inter. Ceram., Vol. 6, pp. 30-35, (1986).

19. L. M. Sheppard, "Manufacturing Ceramics with Microwaves: The Potential for Economical Production," Am. Ceram. Soc. Bulletin, Vol. 67, No. 10, pp. 1656-61, (1988).

20. W. R. Tinga, "Fundamentals of Microwave-Material Interactions and Sintering," Microwave Processing of Materials, Vol. 124, pp. 33-44, Materials Research Society, Pittsburgh, PA, (1988).

21. V. K. Varadar, Y. Ma, A. Lakhtakia, and V. V. Varadan, "Microwave Sintering of Ceramics," Microwave Processing of Materials, Vol. 124, pp. 45-47, Materials Research Society, Pittsburgh, PA, (1988).

22. R. E. Newnham, S. L. Jang, Ming Xu, and F. Jones, "Fundamental Interaction Mechanisms Between Microwaves and Matter," Ceramic Transactions, Vol. 21, pp. 51-67, The American Ceramic Society, Inc., Westerville, Ohio, (1991).

23. V. M. Kenkre, "Theory of Microwave Interactions with Ceramic Materials," Ceramic Transactions, Vol. 21, pp. 69-80, The American Ceramic Society, Inc., Westerville, Ohio, (1991).

24. B. E. Warren, "X-ray Determination of the Structure of Glass," J. Am. Ceram. Soc., Vol. 17, pp. 249-54, (1934).

25. R. J. Breen, R. M. Delaney, P. J. Persiani, and A. H. Weber, "Total Neutron Scattering in Vitreous Silica," Phys. Rev., Vol. 105, No. 2, pp. 517-21, (1957).

26. G. O. McClurg, "An Electron Diffraction Study of Some Glasses," J. Chem. Phys., Vol. 20, No. 9, pp. 1398-1400, (1952).

27. B. E. Warren, "X-ray Diffraction of Vitreous Silica," Z. Krist., Vol. 86, pp. 349-58, (1933).

28. J. Waser, "The Fourier Inversion of Diffraction Data," Rev. Mod. Phys., Vol. 25, No. 3, pp. 671-90, (1953).

29. B. E. Warren, X-ray Diffraction, Chap. 10, Addison-Wesley Publishing Co., Inc., Reading, MA, (1969).

30. R. L. Mozzi and B. E. Warren, "The Structure of Vitreous Silica," J. Appl. Cryst., Vol. 2, pp. 164-72, (1969).

31. B. E. Warren and G. Mavel, "Elimination of the Compton Component in Amorphous Scattering," Rev. Sci. Instrum., Vol. 36, No. 2, pp. 196-97, (1965).

32. A. R. Von Hipple, Dielectric Materials and Applications, Technology Press of MIT and John Wiley & Sons, Inc., New York, (1954).

33. W. R. Tinga and S. O. Nelson, "Dielectric Properties of Materials for Microwave Processing-Tabulated," J. Microwave Power, Vol. 8, No. 1, pp. 23-66, (1973).

34. W. R. Tinga and E. M. Edwards, "Dielectric Measurement Using Swept Frequency Techniques," J. Microwave Power, Vol. 3, No. 3, pp. 144-75, (1968).

35. W. A. G. Voss and W. R. Tinga, "Materials Evaluation and

Measurement Techniques," Microwave Power Engineering, Vol. 2, pp. 189-99, Academic Press, New York, (1968).

36. W. R. Tinga, "Interactions of Microwaves with Materials," Proc. of IMPI, Short Course for Users of Microwave Power, pp. 19-29, (1970).

37. A. J. Berteaud and J. C. Badot, "High Temperature Microwave Heating in Refractory Materials," J. Microwave Power, Vol. 11, No. 4, pp. 315-20, (1976).

38. N. W. Schubring, "Microwave Sintering of Alumina Spark Plug Insulators," Tech. Rept. GMR-4471, General Motors Research Laboratory, pp. 1-27, (1983).

39. S. L. McGill, J. W. Walkiewicz, and G. A. Smyres, "The Effects of Power Level on the Microwave Heating of Selected Chemicals and Minerals," Microwave Processing of Materials, Vol. 124, pp. 247-52, Materials Research Society, Pittsburgh, PA, (1988).

40. P. A. Hass, "Heating of Uranium Oxides in a Microwave Oven," J. Am. Ceram. Soc., Vol. 58, No. 9, pp. 873, (1979).

41. C. E. Holcombe, "New Microwave Coupler Material," Am. Ceram. Soc. Bulletin, Vol. 62, No. 12, pp. 1388, (1983).

42. C. E. Holcombe, "Microwave Coupler and Method," United States Patent, No. 455942, (1985).

43. T. T. Meek, R. D. Blake, and T. G. Gregory, "Low Density Foams Fabricated Using Microwaves," Ceram. Eng. Sci. Proc., Vol. 6, pp. 1161-70, (1985).

44. T. T. Meek and R. D. Blake, "Ceramic-Ceramic Seals by Microwave Heating," J. Mat. Sci. Lett., Vol. 5, No. 3, pp. 270-74, (1986).

45. T. T. Meek, M. H. Brooks, R. D. Blake, J. J. Petrovic, H. Jory, and J. V. Milewski, "Microwave Processing of Ceramics," J. Microwave Power, Vol. 21, No. 3, pp. 193-94, (1986).

46. T. T. Meek, R. D. Blake, and J. J. Petrovic, "Microwave Sintering of Al_2O_3 and Al_2O_3-SiC Whisker Composites," Ceram. Eng. Sci. Proc., Vol. 8, No. 7-8, pp. 861-71, (1987).

47. T. T. Meek, R. D. Blake, J. D. Katz, J. R. Bradberry, and M. H. Brooks, "Cation Diffusion in Glass Heated Using 2.45 GHz Radiation," J. Mat. Sci. Lett., Vol. 7, No. 1, pp. 28-31, (1988).

48. R. D. Blake and T. T. Meek, "Microwave Processed Composite

Materials," J. Mat. Sci. Lett., Vol. 5, No. 11, pp. 1097-98, (1986).

49. R. Varma, S. P. Nandi, and J. D. Katz, "Detoxification of Hazardous Waste Streams Using Microwave-Assisted Fluid-Bed Oxidation," Microwave Processing of Materials II, Vol. 189, pp. 67-80, Materials Research Society, Pittsburgh, PA, (1991).

50. D. Palaith, R. Silberglitt, C. C. M. Wu, R. Kleiner, and E. L. Libelo, "Microwave Joining of Ceramics," Microwave Processing of Materials, Vol. 124, pp. 255-66, Materials Research Society, Pittsburgh, PA, (1988).

51. H. Fukushima, T. Yamanka, and M. Matsui, "Microwave Heating of Ceramics and Its Application to Joining," Microwave Processing of Materials, Vol. 124, pp. 267-72, Materials Research Society, Pittsburgh, PA, (1988).

52. X. D. Yu, V. V. Varadan, and V. K. Varadan, "Application of Microwave Processing to Simultaneous Sintering and Joining of Ceramics," Ceramic Transactions, Vol. 21, pp. 375-86, The American Ceramic Society, Inc., Westerville, Ohio, (1991).

53. H. D. Kimrey, T. L. White, T. S. Bigelow, and P. F. Becher, "Initial Results of a High Power Microwave Sintering Experiment at ORNL," J. Microwave Power, Vol. 21, No. 3, pp. 81-82, (1986).

54. H. D. Kimrey and M. A. Janney, "Design Principles for High Frequency Microwave Cavities," Microwave Processing of Materials, Vol. 124, pp. 367-72, Materials Research Society, Pittsburgh, PA, (1988).

55. M. A. Janney and M. D. Kimrey, "Microwave Sintering of Alumina at 28 GHz," Ceramic Transactions, Ceramic Powder Science, II, B, pp. 914-24, The American Ceramic Society, Inc., Westerville, Ohio, (1988).

56. M. A. Janney and H. D. Kimrey, "Diffusion-Controlled Processes in Microwave-Fired Oxide Ceramics," Microwave Processing of Materials II, Vol. 189, pp. 215-27, Materials Research Society, Pittsburgh, PA, (1991).

57. C. E. Holcombe and N. L. Dykes, "Ultra High-Temperature Microwave Sintering," Ceramic Transactions, Vol. 21, pp. 375-86, The American Ceramic Society, Inc., Westerville, Ohio, (1991).

58. T. T. Meek, X. Zhang, and M. Rader, "An Analysis of the Individual Grain Structure of an Oxide Heated Using Microwave Radiation and Heated Conventionally," Ceramic Transactions, Vol. 21, pp. 81-93, The American Ceramic Society, Inc., Westerville, Ohio, (1991).

59. R. Roy, S. Komarneni, and L. J. Yang, "Controlled Microwave Heating and Melting of Gels," J. Am. Ceram. Soc., Vol. 68, No. 7, pp. 392-95, (1985).

60. Y. Hassler and L. Johansen, "Microwave Heating of Fused Quarz to High Temperatures in the Fabrication Process of Optical Fibers," Microwave Processing of Materials, Vol. 124, pp. 273-78, Materials Research Society, Pittsburgh, PA, (1988).

61. T. T. Meek, "Proposed Model for the Sintering of a Dielectric in a Microwave Field," J. Mat. Sci. Lett., Vol. 6, pp. 638-40, (1987).

62. W. H. Hayt Jr., Engineering Electromagnetics, pp. 123-28, McGraw-Hill Book Co., Inc., New York, (1958).

63. X. D. Yu, V. V. Varadan, and V. K. Varadan, "Modeling Microwave Heating of Ceramics," Ceramic Transactions, Vol. 21, pp. 167-76, The American Ceramic Society, Inc., Westerville, Ohio, (1991).

64. E. E. Eves II and R. L. Snider, "Preliminary Thermal Model for the High Temperature Processing Using Microwave Energy," Microwave Processing of Materials II, Vol. 189, pp. 201-06, Materials Research Society, Pittsburgh, PA, (1991).

65. W. D. Kingery, H. K. Bowen, and D. R. Uhlmann, Introduction to Ceramics, 2nd ed., John-Wiley and Sons, Inc., New York, (1976).

66. J. D. Katz and R. D. Blake, "Microwave Enhanced Diffusion," Ceramic Transactions, Vol. 21, pp. 95-105, The American Ceramic Society, Inc., Westerville, Ohio, (1991).

67. J. F. MacDowell, "Microwave Heating of Nepheline Glass-Ceramics," Am. Ceram. Soc. Bulletin, Vol. 63, No. 2, pp. 282-86, (1984).

68. L. Navias and R. L. Green, "Dielectric Properties of Glasses at Ultra-High Frequencies and Their Relation to Composition," J. Am. Ceram. Soc., Vol. 29, No. 10, pp. 267-76, (1946).

69. R. J. Breen, R. M. Delamey, P. J. Persiai, and A. H. Weber, "Total Neutron Scattering in Vitreous Silica," Phys. Rev., Vol. 105, No. 2, pp. 517-21, (1957).

70. G. Carraro, M. Domenici, and T. Zucca, Physics of Non-Crystalline Solids, North Holland Publishing Co., Amsterdam, Holland, (1965).

71. R. M. Delaney and A. H. Weber, Non-Crystalline Solids, John Wiley & Sons, Inc., New York, (1960).

72. E. Lorch, "Neutron Diffraction by Germania, Silica and Radiation-Damaged Silica Glasses," J. Phys. C. Ser. 2, Vol. 2, pp. 229-37, (1969).

73. R. N. Sinclair and A. C. Wright, "Neutron Scattering from Vitreous Silica," J. Non-Cryst. Solids, Vol. 57, pp. 447-64, (1983).

74. G. O. McClurg, "An Electron Diffraction Study of Some Glasses," J. Chem. Phys., Vol. 20, No. 9, pp. 1398-1400, (1952).

75. G. L. Hua et al., "An Electron Diffraction and Lattice-Dynamical Study of the Diffuse Scattering in β-Cristobalite, SiO_2," J. Appl. Cryst., Vol. 21, pp. 458-65, (1988).

76. M. Huffman and P. McMillan, "Infrared and Raman Studies of Chemically Vapor Deposited Amorphous Silica," J. Non-Cryst. Solids, Vol. 76, pp. 369-79, (1985).

77. P. McMillan, B. Piriou, and R. Couty, "A Raman Study of Pressure-Densified Vitreous Silica," J. Chem. Phys., Vol. 81, No. 10, pp. 4234-36, (1984).

78. P. J. Bray, A. E. Geissberger, F. Bucholtz, and I. A. Harris, "Glass Structure," J. Non-Cryst. Solids, Vol. 52, pp. 45-66, (1982).

79. A. C. Wright et al., "A Neutron Diffraction and MAS-NMR Study of the Structure of Fast Neutron Irradiated Vitreous Silica," J. Non-Cryst. Solids, Vol. 150, pp. 69-75, (1992).

80. F. Ordway, "Condensation Model Producing Crystalline or Amorphous Tetrahedral Networks," Science, Vol. 143, pp. 800-01, (1964).

81. D. L. Evans and S. V. King, "Random Network Model of Vitreous Silica," Nature, Vol. 212, pp. 1353-54, (1966).

82. R. J. Bell and P. Dean. "Properties of Vitreous Silica: Analysis of Random Network Models," Nature, Vol. 212, pp. 1354-55, (1966).

83. H. A. Robinson, "On the Structure of Vitreous SiO_2- I. A New Pentagonal Dodecahedral Model," J. Phys. Chem. Solids, Vol. 26, pp. 209-22, (1965).

84. A. C. Wright and A. J. Leadbetter, "Diffraction Studies of Glass Structure," Phys. Chem. Glasses, Vol. 17, No. 5, pp. 122-45, (1976).

85. F. L. Galeener, "A Model for the Distribution of Bond Angles in Vitreous SiO_2," Phil. Mag. B, Vol. 51, No. 1, pp. L1-L6, (1985).

86. P. Debye and P. Scherrer, Nachr. Gesell. Wiss. Instru., Vol. 36, pp.

196, (1965).

87. J. T. Randall, H. P. Rooksby, and B. S. Cooper, "X-ray Diffraction and the Structure of Vitreous Solids," Z. Krist., Vol. 75, pp. 196-214, (1930).

88. N. Valenkov and E. Poray-Koshitz, "X-ray Investigation of the Glassy State," Z. Krist., Vol. 95, pp. 195-229, (1936).

89. W. H. Zachariasen, "The Atomic Arrangement in Glass," J. Am. Chem. Soc., Vol. 54, No. 10, pp. 384-51, (1932).

90. B. E. Warren, "The Basic Principles Involved in the Glass State," J. Appl. Phys., Vol. 13, pp. 602-10, (1942).

91. B. E. Warren, H. Krutter, and O. Morningstar, "Fourier Analysis of X-ray Patterns of Vitreous SiO_2 and B_2O_3," J. Am. Ceram. Soc., Vol. 19, pp. 202-06, (1936).

92. G. Hartlief, Z. Anorg. Allgem. Chem., Vol. 238, pp. 353, (1938).

93. G. G. Wicks, "Structural Studies of Amorphous Materials," PhD. Dissertation, Department of Metallurgy and Materials Science, M.I.T., (1975).

94. P. G. Coombs et al., "The Nature of the Si-O-Si Bond Angle Distribution in Vitreous Silica," Phil. Mag. B, Vol. 51, No. 4, pp. L39-L42, (1985).

95. C. V. Gokularathnam, "X-ray Diffraction Analysis of Structural Changes in Vitreous Silica," PhD. Dissertation, Department of Metallurgy and Materials Engineering, University of Florida, (1971).

96. D. T. Keating, "Elimination of the $\alpha_1\alpha_2$ Doublet in X-ray Patterns," Rev. Sci. Instru., Vol. 30, No. 8, pp. 725-27, (1959).

97. E. H. Henninger, R. C. Buschert, and L. Heaton, "Atomic Structure and Correction in Vitreous Silica by X-ray and Neutron Diffraction," J. Phys. Chem. Solids, Vol. 28, pp. 423-32, (1967).

98. M. A. Short, "Experimental Determination of X-ray Compton Scattering from Carbon Blacks and Other Non-Crystalline Materials," Acta Cryst., Vol. 14, pp. 486-88, (1961).

99. W. Ruland, "The Separation of Coherent and Incoherent Compton X-ray Scattering," Brit. J. Appl. Phys., Vol. 15, pp. 1301-07, (1964).

100. R. L. Mozzi, "An X-ray Diffraction Study of the Structure of Glass," PhD. Dissertation, Department of Physics, M.I.T., (1967).

101. S. L. Strong and R. Kaplow, "Elimination of Incoherent X-rays with Diffracted Beam Monochromators," Rev. Sci. Instru., Vol. 37, No. 11, pp. 1495-96, (1966).

102. S. Ergun, W. Braun, and E. Fitzer, "Elimination of the Compton Component of Diffusely Scattering Substances," Rev. Sci. Instru., Vol. 41, No. 8, pp. 1133-35, (1970).

103. G. Ennas et al., "Diffraction Techniques and Structural Models for Amorphous Materials," J. Non-Cryst. Solids, Vol. 150, pp. 65-68, (1992).

104. M. Shimazu and A. Watanabe, "Effective Elimination of the Compton Component in Amorphous Scattering by Experimental Means," J. Appl. Cryst., Vol. 7, pp. 531-35, (1974).

105. G. R. Mitchell and A. H. Windle, "Experimental Separation of the Coherent Component of X-ray Scattering Prior to RDF Analysis of Non-Crystalline Polymers," J. Appl. Cryst., Vol. 13, pp. 135-40, (1980).

106. I. Yasui, H. Hasegawa, and M. Imaoka, "X-ray Diffraction Study of the Structure of Silicate Glasses," Phys. Chem. Glass, Vol. 24, No. 3, pp. 63-71, (1983).

107. F. Zernike and J. A. Prins, Z. Physik, Vol. 41, pp. 184-94, (1927).

108. P. Debye and H. Menke, Physik. Zeit., Vol. 31, pp. 797-78, (1930).

109. J. Mershon, "Accurate High Temperature Measurements in Microwave Environments," Ceramic Transactions, Vol. 21, pp. 641-46, The American Ceramic Society, Inc., Westerville, Ohio, (1991).

110. M. K. Krage, "Microwave Sintering of Ferrites," Am. Ceram. Soc. Bulletin, Vol. 60, No. 11, pp. 1232-34, (1981).

111. T. T. Meek, S. S. Park, M. A. Nehles, and C. W. Kim, "Temperature Measurement for Microwave Processing of Advanced Ceramics," Materials Research Society Symposium Proceedings, Vol. 155, pp. 267-74, Materials Research Society, Pittsburgh, PA, (1989).

112. S. S. Park, "Characterization of Zirconia-Alumina Composites Heated Using 2.45 GHz Radiation," M. S. Thesis, Department of Materials Science & Engineering, University of Tennessee-Knoxville, (1989).

113. C. E. Holcombe, "New Microwave Coupler Material," Am. Ceram. Soc. Bulletin, Vol. 62, No. 12, pp. 1388, (1983).

114. C. C. Johnson and A. W. Guy, "Non-Ionizing Electromagnetic Wave Effects in Biological Materials and Systems," Proc. of IEEE, Vol. 60, No. 6, pp. 692, (1972).

115. M. Berman and S. Ergun, "Balanced Filters for Silver K_α X-rays," Rev. Sci. Instru., Vol. 41, No. 6, pp. 870-73, (1970).

116. D. T. Cromer and J. T. Weber, "Scattering Factors Computed from Relativistic Dirac-Slate Wave Function," Acta. Cryst., Vol. 18, pp. 104-09, (1965).

117. D. T. Cromer, "Anomalous Dispersion Corrections Computed from Self-Consitent Field Relativistic Dirac-Slater Wave Functions," Acta. Cryst., Vol. 18, pp. 17-23, (1965).

118. International Tables for X-ray Crystallography, Vol. III, The Kynoch Press, Birmingham, England, (1962).

119. B. E. Warren and R. L. Mozzi, "Corrections for Intensities Measurement from Glass Samples," J. Appl. Cryst., Vol. 3, pp. 59-65, (1970).

120. B. D. Cullity, Elements of X-ray Diffraction, 2nd ed., Addition-Wesley Publishing Co., Inc., Reading, MA, (1984).

121. M. E. Milberg, "Transparency Factor for Weakly Absorbing Samples in X-ray Diffractometry," J. Appl. Phys., Vol. 29, No. 1, pp. 64-65, (1958).

122. S. Ergun, "Correction of X-ray Profiles for Instrumental Broadening in Transmission Geometry," J. Appl. Phys., Vol. 40, No.1, pp. 293-96, (1969).

123. B. E. Warren and R. L. Mozzi, "Multiple Scattering of X-rays by Amorphous Samples," Acta Cryst., Vol. 21, pp. 459-61, (1966).

124. C. W. Dwiggings and D. A. Park, "Calculation of the Intensity of Secondary Scattering of X-ray by Non-Crystalline Materials," Acta Cryst., Vol. A27, pp. 264-72, (1971).

125. T. T. Meek, "An Energy Dispersive X-ray Diffraction Study of Vitreous Silica," PhD. Dissertation, Department of Ceramic Engineering, Ohio State University, (1977).

126. P. A. Ross, "A New Method of Spectroscopy for Faint X-radiations," J. Optic. Soc. Am., Vol. 16, pp. 433-37, (1918).

127. P. Kirkpatrick, "On the Theory and Use of Ross Filters," Rev. Sci. Instru., Vol. 10, pp. 186-91, (1939).

128. J. A. Soules, W. L. Gordon, and C. H. Shaw, "Design of Differential X-ray Filters for Low-Intensity Scattering Experiments," Rev. Sci. Instru., Vol. 27, No. 1, pp. 12-14, (1956).

129. W. Bol, "The Use of Balanced Filters in X-ray Diffraction," J. Sci. Instru., Vol. 44, pp. 736-39, (1967).

130. P. Eisenberger, A. Phys. Rev., Vol. 5, No. 2, pp. 628, (1972).

131. N. Norman, "The Fourier Transform Method for Normalizing Intensities," Acta Cryst., Vol. 10, pp. 370-74, (1957).

132. B. E. Warren and R. L. Mozzi, "The Termination Effect for Amorphous Patterns," J. Appl. Cryst., Vol. 8, pp. 674-77, (1975).

133. K. Lal and P. Thoma, "Anomalously Large Changes in Diffracted X-Ray Intensity from Silicon Single Crystals Produced by Microwave Fields," Solid State Commun., Vol. 53, No. 2, pp. 107-10, (1985).

134. B. E. Warren and J. Biscoe, "Fourier Analysis of X-Ray Patterns of Soda-Silica Glass," J. Am. Ceram. Soc., Vol. 21, No. 7, pp. 259-65, (1938).

135. F. F. Wagstaff, "Crystallization Kinetics of Internallly Nucleated Vitreous Silica," J. Am. Ceram. Soc., Vol. 51, No. 8, pp. 449-52, (1968).

136. B. Himmel, Th. Gerber, W. Heyer, and W. Blau, "X-ray Diffraction Analysis of SiO_2 Structure," J. Mat. Sci., Vol. 22, pp. 1374-78, (1987).

137. Th. Gerber and B. Himmel, "The Structure of Silica Glass in Dependence on the Fictive Temperature," J. Non-Cryst. Solids, Vol. 92, pp. 407-17, (1987).

138. M. R. Vukcevich, "A New Interpretation of the Anomalous Properties of Vitreous Silica," J. Non-Cryst. Solids, Vol. 11, pp. 25-63, (1972).

Appendixes

Appendix I.

Scattering By Atomic Aggregates

In order to analyze the intensity scattered by an aggregate of atoms in an amorphous material, it is necessary to consider scattering from an average atom at a given instant of time. The general scattering of the intensity scattered in a direction denoted by **s**, forming an angle 2θ with incident-beam direction denoted by $\mathbf{s}_o$, can be formulated easily by analyzing the diffraction geometry shown in Figure A1. At the instant of time being considered, an average atom is chosen as the origin and the distances between this atom and adjacent atoms can be denoted by $\mathbf{r}_1$, $\mathbf{r}_2$, ..., $\mathbf{r}_m$, $\mathbf{r}_n$, etc. The phase difference between the x-rays scattered by the atom m a distance $\mathbf{r}_m$ from the origin atom can be expressed by $\exp\{(2\pi i / \lambda)(\mathbf{s} - \mathbf{s}_o)\cdot\mathbf{r}_m\}$. Therefore, the total intensity scattered by all the atoms relative to the origin atom is simply the sum of the intensities scattered by each of the atoms:

$$\text{(AI-1)} \qquad \sum_m f_m \, e^{(2\pi i/\lambda)(\mathbf{s} - \mathbf{s}_o)\cdot\mathbf{r}_m}$$

By allowing each atom to be the origin, it is necessary to repeat the above summation procedure for each atoms. This leads to the double summation

$$\text{(AI-2)} \qquad I_{eu} = \sum_m f_m \, e^{(2\pi i/\lambda)(\mathbf{s} - \mathbf{s}_o)\cdot\mathbf{r}_m} \sum_n f_n \, e^{(-2\pi i/\lambda)(\mathbf{s} - \mathbf{s}_o)\cdot\mathbf{r}_n}$$

$$= \sum_m \sum_n f_m \, f_n \, e^{(2\pi i/\lambda)(\mathbf{s} - \mathbf{s}_o)\cdot(\mathbf{r}_m - \mathbf{r}_n)}$$

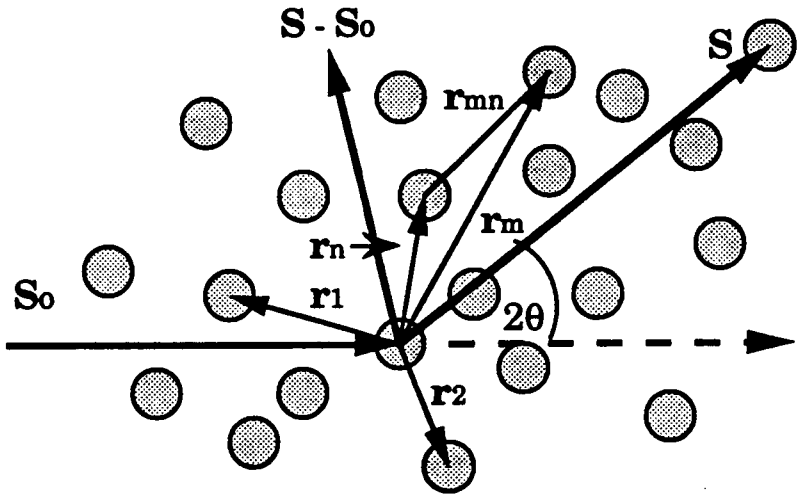

Figure A1. Scattering by an aggregate of atoms.

By letting $\mathbf{r}_{mn} = \mathbf{r}_m - \mathbf{r}_n$, equation (AI-2) can be simplified

$$(AI\text{-}3) \qquad I_{eu} = \sum_m \sum_n f_m f_n e^{(2\pi i/\lambda)(\mathbf{s} - \mathbf{s}_0)\cdot\mathbf{r}_{mn}}$$

where λ is the X-ray wavelength, $\mathbf{s}$ and $\mathbf{s}_0$ are unit vector in the respective the incident and scattered direction, $\mathbf{r}_{mn}$ is the radius vector from atom m to atom n, f_m and f_n are the scattering factor of atom m and atom n. In this investigation, it is known that an electron distribution in the atom can not take on spherical symmetry. It is necessary then to employ a dispersion correction is employed. This correction is expressed by

$$(AI\text{-}4) \qquad f = f_0 + \Delta f' + \Delta f''$$

where f is the corrected scattering factor, f_0 is the uncorrected value, $\Delta f'$ and $\Delta f''$ are the real and imaginary dispersion corrections depending on the X-ray wavelength used.

Since intensity over a finite time interval and not an instant in space is experimentally measured, it is necessary to depict the atomic array in a continuously changing fashion. Also, from assuming a random orientation of the sample, it is allowed to take with equal probability all orientation in space. When $\mathbf{r}_{mn}$ takes all orientations relative to the diffraction vector $\mathbf{s} - \mathbf{s}_0$, the tip of $\mathbf{r}_{mn}$ takes with equal probability all positions on the sphere as shown in Figure A2. The probability that $\mathbf{r}_{mn}$ makes an angle ϕ with $\mathbf{s} - \mathbf{s}_0$ is the ratio of the solid angle $2\pi \sin\phi \, d\phi$ to the total solid angle 4π. For X-rays scattered at an angle 2θ, the magnitude of $\mathbf{s} - \mathbf{s}_0$ is $2 \sin\theta$. Therefore, the exponential term in equation (AI-2) may be replaced by its average value. From Figure A2,

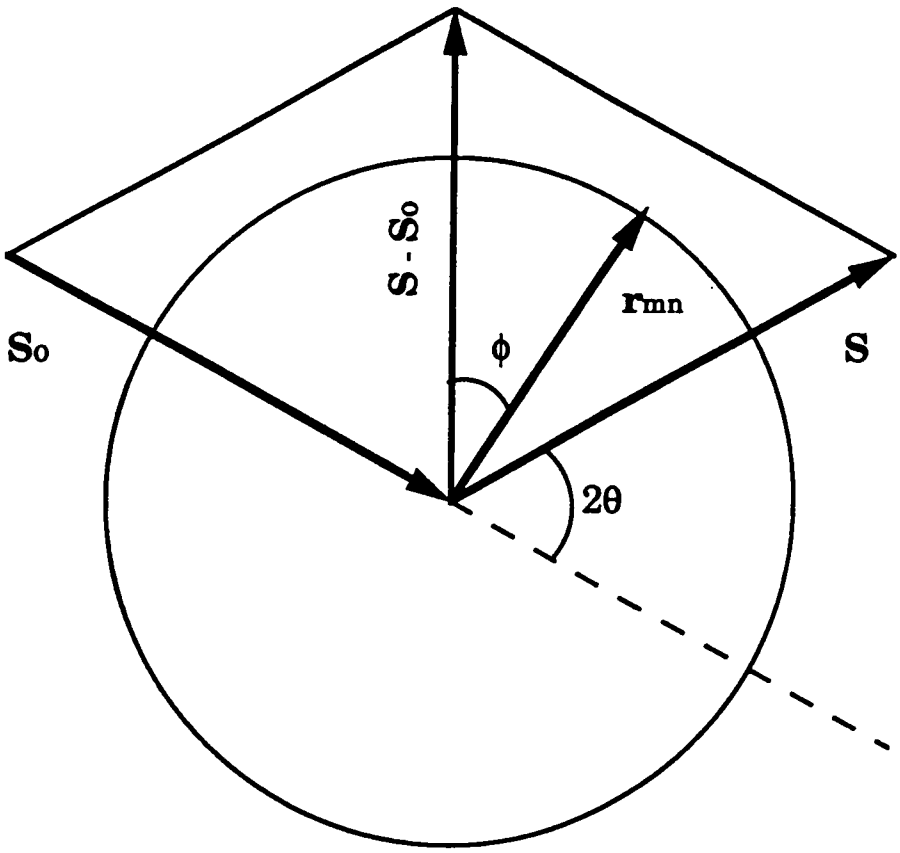

Figure A2. The relation between the unit vectors So and S relative to an interatomic vector rmn take all orientations in space.

(AI-5) $$(\mathbf{s} - \mathbf{s}_0)\cdot\mathbf{r}_{mn} = 2\sin\theta\,(r_{mn}\cos\phi)$$

(AI-6) $$A = 4\pi\, r_{mn}$$

(AI-7) $$dA = 2\pi\,(r_{mn}\sin\phi)\, r\, d\phi = 2\pi\, r_{mn}^2 \sin\phi\, d\phi$$

Letting $k = 4\pi \sin\theta / \lambda$, the average for exponential term of equation (AI-3) is given by:

(AI-8) $$< e^{(2\pi i/\lambda)(\mathbf{s} - \mathbf{s}_0)\cdot \mathbf{r}_{mn}} > = < e^{(4\pi \sin\theta/\lambda)\, i\, r_{mn}\cos\phi} >$$

$$= < e^{\,i\, k r_{mn}\cos\phi} >$$

$$= \frac{1}{4\pi r_{mn}^2} \int_{\phi=0}^{\pi} e^{\,i\, k r_{mn}\cos\phi}\, 2\pi\, r_{mn}^2 \sin\phi\, d\phi$$

$$= \frac{\sin k r_{mn}}{k r_{mn}}$$

With substituting equation (AI-8) in equation (AI-3) for the exponential term,

(AI-9) $$I_{eu} = \sum_m \sum_n f_m f_n \frac{\sin k r_{mn}}{k r_{mn}}$$

Equation (AI-9) is known as the Debye scattering equation. This equation can be used to express scattering from an aggregate of atoms because it is obtained for the average unmodified intensity from an array of atoms which takes all orientations in space.

Appendix II.

Absorption Correction for Weakly Absorbing materials

Consider that the incident and scattered X-ray beams are uniform, parallel and rectangular in cross section, with a height z and widths w and w+2b, respectively. For a flat sample of thickness t, the scattering geometry is represented in Figure A3.

For X-rays scattered from an element of volume dV in a sample of absorption coefficient μ, the intensity scattered is $dI = I_0 \exp(-\mu x)\, dV$. Therefore, the intensity scattered from a volume V is expressed as:

$$\text{(AII-1)} \qquad I = I_0 \int_V e^{-\mu x}\, dV$$

where I_0 is the scattered intensity per unit volume in the absence of absorption and x is a total path length in the sample. The geometry of the irradiated and detected volume is shown in Figure A3 and the intensities scattered in the three regions are given as:

Region I in Figure A3

$$\text{(AII-2)} \qquad I = K\,(\,1 - e^{-\mu t \csc\theta}\,)$$

Region II in Figure A3

$$\text{(AII-3)} \qquad I = K\left[(\,1 - e^{-\mu t \csc\theta}\,) + \left(\frac{2t\cos\theta}{w} - \frac{b}{w} + \frac{1}{\alpha}\right) e^{-\mu t \csc\theta} - \frac{1}{\alpha} e^{-\beta}\right]$$

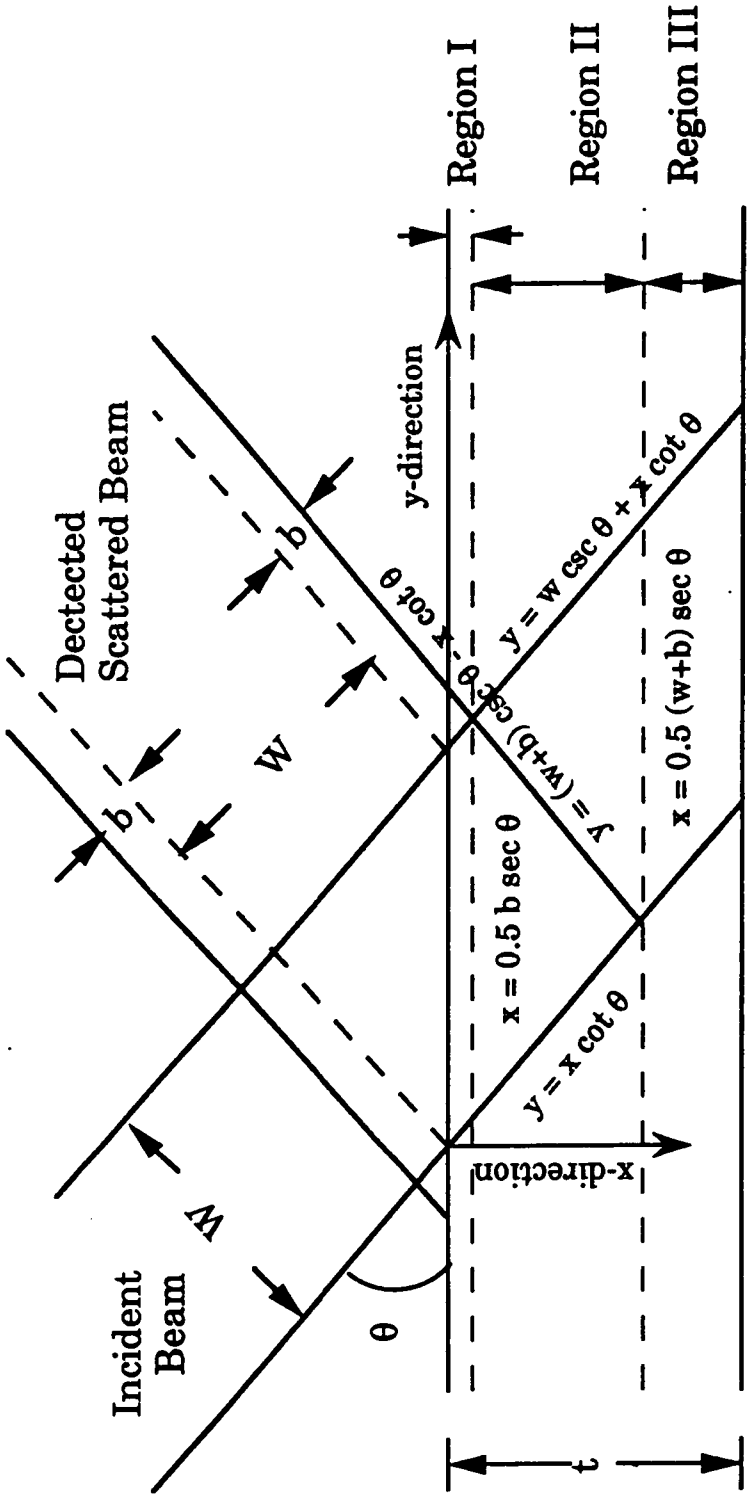

Figure A3. The scattering geometry from weakly absorbing material.

Region III in Figure A3

(AII-4) $$I = K\left[1 - \frac{1}{\alpha}(1 - e^{-\alpha})e^{-\beta}\right]$$

where $K = I_0 w z / 2\mu$

$\alpha = 2\mu w \csc 2\theta$

$\beta = 2\mu b \csc 2\theta$

Assume that the scattered beam is approximately the same width as the incident beam in this study and is allowed in the region II. Since b and β become zero, equation (AII-3) can be simply expressed as:

(AII-5) $$I = K\left[\left(1 - \frac{1}{\alpha}\right)(1 - e^{-2\mu t \csc\theta}) + \frac{2t\cos\theta}{w} e^{-2\mu t \csc\theta}\right]$$

$$= K A$$

In this investigation, A can be used as the absorption correction.

When μ is so high, equation (AII-5) is reduced to

(AII-6) $$I = K = \frac{I_0 w z}{2\mu}$$

which is the usual case of an absorption correction independent of scattering angle. On the other hand, for low μ materials such as silica, a large dependence is predicted between the measured intensity and the scattering angle as shown in equation (AII-5).

Appendix III.

Muliple Scattering Correction

In the study of amorphous solids, it is necessary to correct for multiple scattering. The correction for multiple scattering for reflection geometry using an infinitely thick sample has been treated by Warren and Mozzi.[123]

Consider a flat diffractometer sample as shown in Figure A4 and let n be the number of units of composition per unit volume, and $J(2\theta_1)$ be the first order intensity in electron units per unit composition for scattering at an angle $2\theta_1$. The intensity at r from the volume element dV_1 due to scattering of the primary beam by dV_1 is given by:

$$(AIII\text{-}1) \qquad dI_r = I_o \frac{e^4}{m^2c^4r^2} J(2\theta_1)\, nA_o\, ds$$

As a result of the scattering intensity dI_r by the volume element dV_2, the intensity at R from the sample is given by:

$$(AIII\text{-}2) \qquad dI_m = dI_r \frac{e^4}{m^2c^4r^2} J(2\theta_2)\, n\, dV_2$$

In terms of a small solid angle $d\Omega$ centered on the line r ($d\Omega = \cos\varepsilon\, d\varepsilon\, d\varphi$ and $dV_2 = r^2\, d\Omega\, dr$), the equation (AIII-1) and (AIII-2) can be combined to give

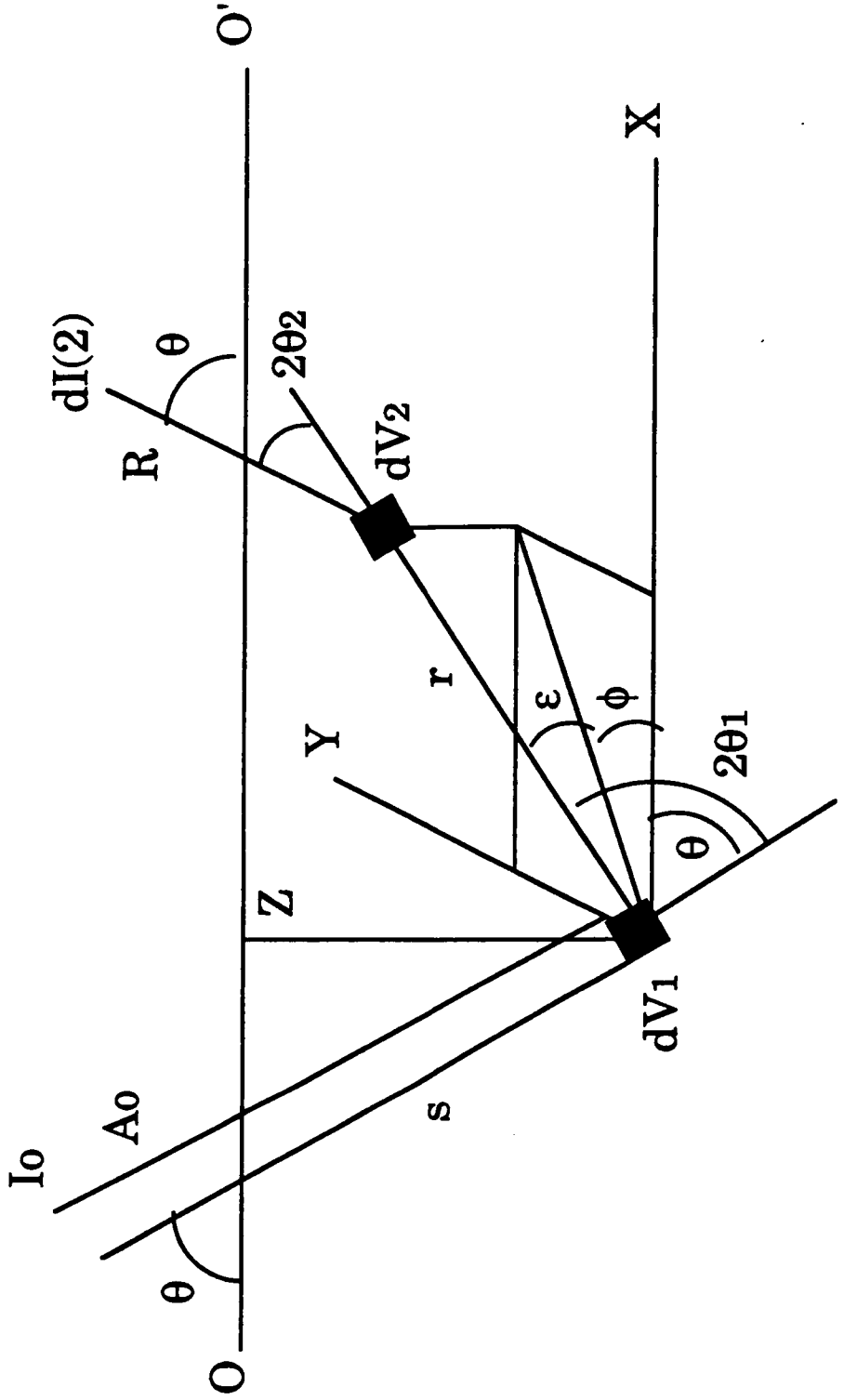

Figure A4. Geometry of the double scattering process.

$$(AIII\text{-}3) \qquad dI_m = P_o \left(\frac{e^4}{m^2c^4r^2}\right)^2 \frac{n^2}{R^2} J(2\theta_1)\, J(2\theta_2) \cos\varepsilon \, d\varepsilon \, d\varphi \, ds \, dr$$

Considering absorption for the sample of thickness t, r goes from zero to s ($\sin\theta / \sin\varepsilon$) and s goes from zero to $t / \sin\theta$ in the integration of equation (AIII-3):

$$(AIII\text{-}4) \qquad \int_{s=0}^{t/\sin\theta} \int_{r=0}^{s(\sin\theta/\sin\varepsilon)} \exp\left[-u\,\{2s + r\,(1-\sin\varepsilon/\sin\theta)\}\right] dr\, ds = \frac{A \sin\theta}{2\mu^2 (\sin\theta + \sin\varepsilon)}$$

$$\text{where} \qquad A = 1 - e^{-2\mu t/\sin\theta} \left(\frac{\sin\theta + \sin\varepsilon - 2\sin\varepsilon\, e^{-\mu t(1/\sin\varepsilon - 1/\sin\theta)}}{\sin\theta - \sin\varepsilon}\right)$$

If an polarized beam is scattered first through an angle $2\theta_1$, and then the scattered beam is scattered through an angle $2\theta_2$, the final direction makes an angle 2θ with the original primary beam. Combining equation (AIII-3) and equation (AIII-4) with adding the polarization factor is given by:

$$(AIII\text{-}5) \qquad I_m = P_o \left(\frac{e^4}{m^2c^4r^2}\right)^2 \frac{n^2}{R^2} \frac{2\sin\theta}{\mu^2}$$

$$\times \int_0^{\pi/2} \int_0^{\pi/2} \frac{[J(p_1)\, J(p_2) + J(-p_1)\, J(-p_2)]}{\sin\theta + \sin\varepsilon} A\,(PF) \cos\varepsilon \, d\varepsilon \, d\varphi$$

$$\text{where} \qquad PF = [\cos^2 2\theta_1 + \cos^2 2\theta_2 + (\cos 2\theta_1 \cos 2\theta_2 - \cos 2\theta)^2] / 2$$

$$n / \mu = N_o / \sum_i A_i \mu_i(m)$$

and N_o is the Avogadro number, A_i is the atomic weight and $\mu_i(m)$ is the mass absorption coefficients of the atoms.

The single scattering intensity for an unpolarized primary beam is given by:

$$(AIII\text{-}6) \qquad I_s = P_o \left(\frac{e^4}{m^2c^4r^2}\right) \frac{1}{R^2} \left(\frac{1 + \cos^2 2\theta}{2}\right) J(2\theta) \frac{n}{2\mu}$$

Dividing equation (AIII-5) by equation (AIII-6), the final equation is given by:

$$(AIII\text{-}7) \qquad \frac{I_m}{I_s} = \left(\frac{e^4}{m^2c^4r^2}\right) \frac{8NC \sin\theta}{(1+\cos^2 2\theta)\, J(2\theta)\, (\sum_i A_i \mu_i(m))\, (1 - e^{-2\mu t/\sin\theta})}$$

$$\text{where} \qquad C = \int_0^{\pi/2} \int_0^{\pi/2} \frac{[J(p_1)\, J(p_2) + J(-p_1)\, J(-p_2)]}{\sin\theta + \sin\varepsilon} A\,(PF) \cos\varepsilon \, d\varepsilon \, d\varphi$$

By means of the $Q(2\theta, q, b)$ function, that is related to the ratio of secondary to primary intensity, equation (AIII-7) is expressed in the simple form:

$$(AIII\text{-}8) \qquad \frac{I_m}{I_s} = \frac{B^2\, Q(2\theta, q, b)}{J(p) \sum_i A_i \mu_i(m)}$$

where $J(p)$ is represented approximately by:

$$J(p) = \sum_i Z_i^2 \left(q + \frac{1-q}{1 + b \sin^2\theta}\right)$$

Appendix IV.

Normalization for CuK_α data

A modified Norman method[30] for standardizing of CuK_α data can be derived from the expression for the pair distribution as below:

$$\text{(AIV-1)} \qquad \sum_{uc}\sum_{i}\frac{N_{ij}}{r_{ij}}\int_0^{k_m}\frac{f_j f_i}{g^2(k)}\,e^{-\alpha^2k^2}\sin kr_{ij}\sin kr\,dk$$

$$= 2\pi^2 r\rho_e\sum_{uc}Z_j + \int_0^{k_m} ki(k)\,e^{-\alpha^2k^2}\sin rk\,dk$$

With dividing both sides of the equation (AIV-1) by r and allowing r to be very small,

$$\text{(AIV-2)} \qquad \sum_{uc}\sum_{i}\frac{N_{ij}}{r_{ij}}\int_0^{k_m}\frac{f_j f_i}{g^2(k)}\,e^{-\alpha^2k^2}\,k\sin kr_{ij}\,dk - 2\pi^2\rho_e\sum_{uc}Z_j =$$

$$\int_0^{k_m} k^2\,i(k)\,e^{-\alpha^2k^2}\,dk$$

Since the first term can be negligible compared to the second term in the left-hand side of equation (AIV-2),

$$\text{(AIV-3)} \qquad -2\pi^2\rho_e\sum_{uc}Z_j = \int_0^{k_m} k^2\,i(k)\,e^{-\alpha^2k^2}\,dk$$

This expression can be used to put the CuK_α data in absolute units and it without the convergence factor has been given by Norman.[131]

Because the multiple scattering intensity for CuK_α intensity data can be negligible, the corrected intensity is

$$(AIV\text{-}4) \qquad \left[\frac{n\,(I_m - B)}{PF}\right] = \frac{I_{eu}}{N} + \sum_{uc} i(M)$$

Now, i(k) is difined previously as:

$$(AIV\text{-}5) \qquad i(k) = \frac{[\,I_{eu}/N\,] - \sum f_j^2}{g(k)^2}$$

By a little rearranging equation (AIV-4) and (AIV-5),

$$(AIV\text{-}6) \qquad i(k) = \frac{n\,[\,(I_m - B)/PF\,] - \sum i(M) - \sum f_j^2}{g(k)^2}$$

With substituting for i(k) from equation (AIV-3),

$$(AIV\text{-}7) \qquad -2\pi^2 \rho_e \sum_{uc} Z_j = \int_0^{k_m} \frac{k^2\, e^{-\alpha^2 k^2}}{g(k)^2} \left[\, n \left\{\frac{(I_m - B)}{PF}\right\} - \sum i(M) - \sum f_j^2\right] dk$$

With rearranging equation (AIV-7),

$$(AIV\text{-}8) \qquad n \int_0^{k_m} \frac{k^2\, e^{-\alpha^2 k^2}}{g(k)^2} \left\{\frac{(I_m - B)}{PF}\right\} dk = \int_0^{k_m} \frac{k^2\, e^{-\alpha^2 k^2}}{g(k)^2} \{\sum i(M) + \sum f_j^2\}\, dk - 2\pi^2 \rho_e \sum_{uc} Z_j$$

where $\sum i(M)$ = C.M. and $g(k) = f_e$.

Appendix V.

Computer Programs Used in Structural Analysis

```
C*****************************************************************C
C
C               PROGRAM CORRECTION WITH ELIMINATION OF DOUBLET
C
C               TO DIGITIZE CORRECTED EXPERIMENTAL INTENSITY DATA
C               FOR POLARIZATION AND COMPTON SCATTERING
C               IT IS USED FOR CU INTENSITY DATA
C
C                               MODIFIED AUGUST 1, 1993
C*****************************************************************C

        PROGRAM DCORRECTION

        CHARACTER*8 TAB,NAME1
        DIMENSION YY(2000),CINT(2000),ZZ(2000),CCINT(2000),
     +  TG(2000),PF(2000),PKA(2000),GIEU(2000)

        COMMON XX(2000),AA(2000)
        TAB=CHAR(9)

        DELTA=0.1
        ANMAX=151.0
C       USE K(ALPHA 1) DUE TO SEPERATE DOUBLET WITH MATH
        ACU=1.540562
        CRYST=1.0
C       DO NOT USE MONOCHROMATOR
C       CRYST=COS(26.57*3.1415927/180.)*COS(26.57*3.1415927/180.)
        ABSOR=1.0
        PKMAX=7.8
        DELPK=0.01

        WRITE(*,*) 'ENTER FILE NAME OF RAW INTENSITY !!!!'
        WRITE(*,*) 'IF USING CU, PLEASE CHECK CMP1.EXP FILE'
        WRITE(*,*) '       FOR CU RAW INTENSITY DATA'
        WRITE(*,*)
        WRITE(*,*) '****************************************'
        READ(*,*) NAME1
        WRITE(*,*)
        WRITE(*,*) 'TO CONTINUE, PUSH RETURN KEY'
        PAUSE

        OPEN(UNIT=5,FILE=NAME1,STATUS='OLD')

C       DUE TO 150.4/0.7 IS NOT INTERGER AND START 7.6 DEGREE
        Q=ANMAX/DELTA+1.001
        N=INT(Q)

        DO I=1,N
        READ(5,100) YY(I),CCINT(I)
        END DO
100     FORMAT(1X,F10.4,1X,F10.4)
        CLOSE(5)
```

```
C       ELIMINATION OF DOUBLET FOR CU RADIATION
        CINT(1)=CCINT(1)
        CINT(2)=1.5*(0.67187*CCINT(2))
        CINT(3)=1.5*(CCINT(3)-0.32813*CCINT(2))
        CINT(4)=1.5*(CCINT(4)-0.5*CCINT(3)+0.17187*CCINT(2))
        CINT(5)=1.5*(CCINT(5)-0.5*CCINT(4)+0.25*CCINT(3)+
     +  -0.07813*CCINT(2))
        CINT(6)=1.5*(CCINT(6)-0.5*CCINT(5)+0.25*CCINT(4)
     +  -0.125*CCINT(3)+0.04687*CCINT(2))

        DO J=7,N

        CINT(J)=1.5*(CCINT(J)-0.5*CCINT(J-1)+0.25*CCINT(J-2)
     +  -0.125*CCINT(J-3)+0.0625*CCINT(J-4)
     +  -0.03125*CCINT(J-5)+0.01562*CCINT(J-6))
        END DO

        QQ=PKMAX/DELPK+1.001
        NN=INT(QQ)

        OPEN(UNIT=7,FILE='CDCO.DAT',STATUS='NEW')
        OPEN(UNIT=10,FILE='CDCO.DIS',STATUS='NEW')
        OPEN(UNIT=11,FILE='CDCO.FIG',STATUS='NEW')

        DO 50 I=1,N
        TG(I)=YY(I)*3.1415927/180.
        XX(I)=4.*3.1415927*SIN(TG(I)/2.)/ACU
        PF(I)=(1.+CRYST*COS(TG(I))*COS(TG(I)))/(1.+CRYST)
        AA(I)=CINT(I)/(ABSOR*PF(I))
50      CONTINUE

        CALL SPLINE(N,NN,DELPK,PKA,GIEU)

        DO 60 I=1,NN
        WRITE(7,200) PKA(I),GIEU(I)
200     FORMAT(1X,F10.4,1X,F10.4)
60      CONTINUE
        CLOSE(7)

        WRITE(10,130) (GIEU(I),I=1,NN)
130     FORMAT(4HGIEU/(10F8.4))
        CLOSE(10)

        DO 80 I=1,NN
        WRITE(11,*) PKA(I),TAB,GIEU(I)
80      CONTINUE
        CLOSE(11)

        STOP
        END
```

```
C*******************************************************************************

      SUBROUTINE SPLINE (N,NN,DELPK,PKA,S)

C     NATURAL CUBIC SPLINE
C     TO CONSTRUCT THE CUBIC SPLINE INTERPOLATE S FOR THE FUNCTION F,
C     DEFINED AT THE NUMBERS X0<X1<...<XN, SATISFY S"(X0)=S"(XN)=0

      DIMENSION H(2000),PL(2000),PM(2000),Z(2000),ALFA(2000),
     +  C(2000),B(2000),D(2000),S(2000),PKA(2000)
      COMMON XX(2000),AA(2000)

      DO 110 I=1,N-1
      H(I)=XX(I+1)-XX(I)
110   CONTINUE

      PL(1)=1.0
      PM(1)=0.0
      Z(1)=0.0

      DO 120 I=2,N-1
      ALFA(I)=3.0*(AA(I+1)*H(I-1)-AA(I)*(XX(I+1)-XX(I-1))
     +  +AA(I-1)*H(I))/(H(I-1)*H(I))
      PL(I)=2.0*(XX(I+1)-XX(I-1))-H(I-1)*PM(I-1)
      PM(I)=H(I)/PL(I)
      Z(I)=(ALFA(I)-H(I-1)*Z(I-1))/PL(I)
120   CONTINUE

      PL(N)=1.0
      Z(N)=0.0
      C(N)=0.0

      DO 130 J=N-1,1,-1
      C(J)=Z(J)-PM(J)*C(J+1)
      B(J)=(AA(J+1)-AA(J))/H(J)-H(J)*(C(J+1)+2.0*C(J))/3.0
      D(J)=(C(J+1)-C(J))/(3.0*H(J))
130   CONTINUE

      DO 140 I=1,NN
      PKA(I)=DELPK*FLOAT(I-1)
      J=1
150   IF(PKA(I).GT.XX(J))THEN
      J=J+1
      GOTO 150
      END IF
      J=J-1
      IF(J.LT.1) J=1
      S(I)=AA(J)+B(J)*(PKA(I)-XX(J))+C(J)*(PKA(I)-XX(J))**2.0
     +  +D(J)*(PKA(I)-XX(J))**3.0
140   CONTINUE

      RETURN
      END
```

```
C*****************************************************************C
C
C               PROGRAM CORRECTION FOR MO
C               TO DIGITIZE CORRECTED EXPERIMENTAL INTENSITY DATA
C               FOR POLARIZATION, ABSORPTION, AND MULIPLE SCATTER
C               IT IS USED FOR MO INTENSITY DATA
C
C                              MODIFIED AUGUST 1, 1993
C*****************************************************************C

        PROGRAM MOCORRECT

        CHARACTER*8 TAB,NAME1,NAME2
        DIMENSION YY(2000),CINT(2000),DX(2000),DY(2000),
     +  TG(2000),PF(2000),ALP(2000),ABSOR(2000),PKA(2000),
     +  GIEU(2000)

        COMMON XX(2000),AA(2000)
        TAB=CHAR(9)

        DELTA=0.7
        ANMAX=150.4
C       USE K(ALPHA AVERAGE) DUE TO DOUBLET
        AMO=0.71073
C       DUE TO NOT USE MONOCHROMATORE
        CRYST=1.0
C       CRYST=COS(12.17*3.1415927/180.)*COS(12.17*3.1415927/180.)
        PKMAX=17.08
        DELPK=0.01

        WRITE(*,*) 'ENTER FILE NAME OF RAW INTENSITY !!!!'
        WRITE(*,*) 'IF USING MO, PLEASE CHECK MMP1.EXP FILE'
        WRITE(*,*) '      FOR MO RAW INTENSITY DATA'
        WRITE(*,*) '****************************************'
        READ(*,*) NAME1
C       WRITE(*,*) 'ENTER FILE NAME OF MULTIPLE SCATTERING !!!'
C       WRITE(*,*) 'IF USING MO, PLEASE CHECK MULT.DAT FILE'
C       WRITE(*,*) '      FOR MO RAW INTENSITY DATA'
C       WRITE(*,*) '****************************************'
C       READ(*,*) NAME2

        OPEN(UNIT=4,FILE=NAME1,STATUS='OLD')
C       DUE TO 150.4/0.3 IS NOT INTERGER AND START 7.7 DEGREE
        Q=ANMAX/DELTA+2.001
        N=INT(Q)

        DO I=1,N
        READ(4,100) YY(I),CINT(I)
        END DO
100     FORMAT(1X,F10.4,1X,F10.4)
        CLOSE(4)

        OPEN(UNIT=5,FILE='MCOR.DAT',STATUS='NEW')
        OPEN(UNIT=6,FILE='MCOR.DIS',STATUS='NEW')
        OPEN(UNIT=7,FILE='MCOR.FIG',STATUS='NEW')

C       U IS THE ABSORPTION COEFFICIENT OF SILICA
C       THICK IS THE THICKNESS OF SAMPLE
C       PF(I) IS POLARIZATION CORRECTION FACTOR
C       ABSOR(I) IS THE CORRECTION FOR ABSORPTION

        U=8.157
        THICK=0.25
        WIDTH=0.162
```

```
      DO 50 I=1,N
      TG(I)=YY(I)*3.1415927/180.
      XX(I)=4.*3.1415927*SIN(TG(I)/2.)/AMO
      PF(I)=(1.+CRYST*COS(TG(I))*COS(TG(I)))/(1.+CRYST)
      ALP(I)=2.*U*WIDTH/SIN(TG(I))
      ABSOR(I)=(1.-1./ALP(I))*(1.-EXP(-2.*U*THICK/SIN(TG(I)/2.)))
     +  +2.*THICK*COS(TG(I)/2.)*EXP(-2.*U*THICK/SIN(TG(I)/2.))/WIDTH
      AA(I)=CINT(I)/(ABSOR(I)*PF(I))
50    CONTINUE

      QQ=PKMAX/DELPK+1.001
      NN=INT(QQ)

      CALL SPLINE(N,NN,DELPK,PKA,GIEU)

      DO 60 I=1,NN
      WRITE(5,100) PKA(I),GIEU(I)
      WRITE(7,*) PKA(I),TAB,GIEU(I)
60    CONTINUE
      CLOSE(5)
      CLOSE(7)

      WRITE(6,130) (GIEU(I),I=1,NN)
130   FORMAT(4HGIEU/(10F10.4))
      CLOSE(6)

      STOP
      END

C*************************************************************************

      SUBROUTINE SPLINE (N,NN,DELPK,PKA,S)

C     NATURAL CUBIC SPLINE
C     TO CONSTRUCT THE CUBIC SPLINE INTERPOLATE S FOR THE FUNCTION F,
C     DEFINED AT THE NUMBERS X0<X1<...<XN, SATISFY S"(X0)=S"(XN)=0

      DIMENSION H(2000),PL(2000),PM(2000),Z(2000),ALFA(2000),
     +  C(2000),B(2000),D(2000),S(2000),PKA(2000)
      COMMON XX(2000),AA(2000)

      DO 110 I=1,N-1
      H(I)=XX(I+1)-XX(I)
110   CONTINUE

      PL(1)=1.0
      PM(1)=0.0
      Z(1)=0.0

      DO 120 I=2,N-1
      ALFA(I)=3.0*(AA(I+1)*H(I-1)-AA(I)*(XX(I+1)-XX(I-1))
     +  +AA(I-1)*H(I))/(H(I-1)*H(I))
      PL(I)=2.0*(XX(I+1)-XX(I-1))-H(I-1)*PM(I-1)
      PM(I)=H(I)/PL(I)
      Z(I)=(ALFA(I)-H(I-1)*Z(I-1))/PL(I)
120   CONTINUE

      PL(N)=1.0
      Z(N)=0.0
      C(N)=0.0

      DO 130 J=N-1,1,-1
      C(J)=Z(J)-PM(J)*C(J+1)
```

```
      B(J)=(AA(J+1)-AA(J))/H(J)-H(J)*(C(J+1)+2.0*C(J))/3.0
      D(J)=(C(J+1)-C(J))/(3.0*H(J))
130   CONTINUE

      DO 140 I=1,NN
      PKA(I)=DELPK*FLOAT(I-1)
      J=1
150   IF(PKA(I).GT.XX(J))THEN
      J=J+1
      GOTO 150
      END IF
      J=J-1
      IF(J.LT.1) J=1
      S(I)=AA(J)+B(J)*(PKA(I)-XX(J))+C(J)*(PKA(I)-XX(J))**2.0
     ++D(J)*(PKA(I)-XX(J))**3.0
140   CONTINUE

      RETURN
      END
```

```
C*************************************************************************C
C*
C*            PROGRAM NORMALIZATION BY USING NORMAN METHOD
C*
C*            NORMALIZING OF CU INTENSITY IN VITEROUS SILICA
C*              ONLY USE MO RADIATION
C*
C*                       MODIFIED BY APRIL 5, 1993
C*
C*************************************************************************C

      PROGRAM NORMALIZATION

      DIMENSION C(5,10),FP(5,4),FPP(5,4),D(5),G(4),PKA(3000),
     +  SCFA(3000),SUMFSQ(3000),FESQ(3000),FEIMSQ(3000),
     +  XX(3000),AA(3000),YY(3000),CMI(3000),XNOR(3000),
     +  ZZ(3000),DOUB(3000)


      CHARACTER*8 TAB,NAME1
      COMMON/INDSCA/ FE(3,3000),FSQ(3,3000),FEIM(3,3000)
      TAB=CHAR(9)

C     DELPK IS INTERVAL OF K VALUE, PKMAX IS MAXIMUM OF K.
C     ROZERO IS THE ELECTRON DENSITY IN APPROXIMATION METHOD.
C     ROEL IS THE ELECTRON DENSITY IN EXACT METHOD
C     ALPHA WAS TAKEN FROM A2Km=1.0

      DELPK=0.01
      PKMAX=7.5
      ROEL=0.6843
      PEAR=2.*3.1415927*3.1415927*ROEL
C     To give strong convergence factor
      ALPHA=0.2667
      ALFSQ=ALPHA*ALPHA

      Q=PKMAX/DELPK+1.001
      N=INT(Q)
      WRITE(*,*) 'ENTER FILE NAME TO BE NORMALIZED !!!'
      WRITE(*,*) 'USUALLY CSMO.DAT'
      READ(*,*) NAME1

      OPEN(5,FILE=NAME1,STATUS='OLD')
      OPEN(6,FILE='MCOM.DAT',STATUS='OLD')
      OPEN(10,FILE='MULT.DAT',STATUS='OLD')
      OPEN(7,FILE='CNOR.FIG',STATUS='NEW')
      OPEN(8,FILE='CNOR.DAT',STATUS='NEW')

C     DIGITIZING THE CU INTENSITY IN e.u. FOR SIO2
      I=0
2     I=I+1
      READ(5,3) XX(I),AA(I)
3     FORMAT(1X,F10.4,1X,F10.4)
      IF(XX(I).LE.17.11) GOTO 2
      L=I-1
      CLOSE(5)

C     DIGITIZING THE MO COMPTON INTENSITY FOR SIO2
      J=0
4     J=J+1
      READ(6,10) YY(J),CMI(J)
10    FORMAT(1X,F8.4,1X,F8.4)
      IF(YY(J).LE.17.11) GOTO 4
```

```
      M=J-1
      CLOSE(6)

C     DIGITIZING THE MULTIPLE SCATTERING FOR SIO2
      K=0
6     K=K+1
      READ(10,15) ZZ(K),DOUB(K)
15    FORMAT(1X,F8.4,1X,F8.4)
      IF(ZZ(K).LE.17.11) GOTO 6
      MM=K-1
      CLOSE(10)

      WRITE(*,*) 'KMAX IN MO DATA IS  ', L
      WRITE(*,*) 'KMAX IN MO COMPTON IS  ',M
      WRITE(*,*) 'KMAX IN MULTIPLE SCATTER IS  ',MM
      WRITE(*,*) 'KMAX IN CALCULATION IS  ', N
      WRITE(*,*) '4 PARAMETERS ARE NOT SAME, PLEASE CHECK!!'
      WRITE(*,*) 'TO CONTINUE, PLEASE TOUCH RETURN KEY'
      PAUSE

      WRITE(*,*) 'HELLOW 1'
C     SUMZ OF SiO2 =30.0, NUMBER OF ELEMENT (2 FOR SiO2)
C     NUMBER OF RADIATION USED IS 2 FOR Cu & MO
      SUMZ=30.0
      NOEL=2
      NORAD=1

C     C(I,J) ARE NINE PARAMETER OF DIRAC-SLATER SCATTERING FACTOR.
C     C(1,J) IS FOR SI AND C(2,J) IS FOR O.
      C(1,1)=6.0755
      C(1,2)=2.3497
      C(1,3)=3.2815
      C(1,4)=29.1900
      C(1,5)=2.1670
      C(1,6)=0.7060
      C(1,7)=1.3197
      C(1,8)=84.8342
      C(1,9)=1.1533
      C(2,1)=2.8604
      C(2,2)=12.7907
      C(2,3)=2.5212
      C(2,4)=5.4279
      C(2,5)=1.5296
      C(2,6)=0.3282
      C(2,7)=0.8135
      C(2,8)=34.9406
      C(2,9)=0.2742

C     ANOMALOUS DISPERSION CORRECTION
C     FP(I,K): CORRECT IN REAL-PART, FPP(I,K): CORRECT IN IMAG-PART.
C     I=1 IS FOR SI & I=2 IS FOR O, K=1 IS FOR CU & K=2 IS FOR MO
      FP(1,1)=0.23
      FP(1,2)=0.09
      FP(2,1)=0.0
      FP(2,2)=0.0
      FPP(1,1)=0.36
      FPP(1,2)=0.09
      FPP(2,1)=0.1
      FPP(2,2)=0.0

C     D(I) ARE NO. OF ATOMS OF EACH ELEMENT IN UNIT CELL OF SiO2
C     D(1) IS FOR SI ATOM, D(2) IS FOR O ATOM
      D(1)=1.0
      D(2)=2.0
```

```
C       G(K) ARE HIGHEST K VALUE IN EACH RADIATION
        G(1)=7.5
        G(2)=17.11

        DO 5 IA=1,N
        PKA(IA)=FLOAT(IA-1)*DELPK
5       CONTINUE
        WRITE(*,*) 'HELLOW 2'

        CALL INDSCA(C,D,FP,FPP,G,SUMZ,PKMAX,DELPK,NOEL,SUMFSQ,FESQ)

        WRITE(*,*) 'NOW PROCESSING???'

C       INTEGRATION OF EQUATION GIVEN

        EX=0.0
        TH=0.0
        DO I=1,N,N-1
        EX=EX+PKA(I)**2.*EXP(-ALFSQ*PKA(I)**2.)*AA(I)/FESQ(I)
        TH=TH+PKA(I)**2.*EXP(-ALFSQ*PKA(I)**2.)*
     +  (SUMFSQ(I)*(1.+DOUB(I))+CMI(I))/FESQ(I)
        END DO

        DO I=2,N-1,N-3
        EX=EX+PKA(I)**2.*EXP(-ALFSQ*PKA(I)**2.)*AA(I)/FESQ(I)
        TH=TH+PKA(I)**2.*EXP(-ALFSQ*PKA(I)**2.)*
     +  (SUMFSQ(I)*(1.+DOUB(I))+CMI(I))/FESQ(I)
        END DO

        DO I=3,N-2,N-5
        EX=EX+PKA(I)**2.*EXP(-ALFSQ*PKA(I)**2.)*AA(I)/FESQ(I)
        TH=TH+PKA(I)**2.*EXP(-ALFSQ*PKA(I)**2.)*
     +  (SUMFSQ(I)*(1.+DOUB(I))+CMI(I))/FESQ(I)
        END DO

        DO I=4,N-3,N-7
        EX=EX+PKA(I)**2.*EXP(-ALFSQ*PKA(I)**2.)*AA(I)/FESQ(I)
        TH=TH+PKA(I)**2.*EXP(-ALFSQ*PKA(I)**2.)*
     +  (SUMFSQ(I)*(1.+DOUB(I))+CMI(I))/FESQ(I)
        END DO

        DO I=5,N-4
        EX=EX+PKA(I)**2.*EXP(-ALFSQ*PKA(I)**2.)*AA(I)/FESQ(I)
        TH=TH+PKA(I)**2.*EXP(-ALFSQ*PKA(I)**2.)*
     +  (SUMFSQ(I)*(1.+DOUB(I))+CMI(I))/FESQ(I)
        END DO

        FACNOR=(TH-PEAR*SUMZ)/EX
        WRITE(*,*)'NORMALIZING FACTOR IS  ',FACNOR
        WRITE(*,*)'AFTER CHECK NORAL FACTOR, PUSH RETURN KEY'
        PAUSE

        DO I=1,N
        XNOR(I)=FACNOR*AA(I)-CMI(I)-SUMFSQ(I)*DOUB(I)
        WRITE(7,*) PKA(I),TAB,SUMFSQ(I),TAB,XNOR(I)
        WRITE(8,10) PKA(I),XNOR(I)
        END DO
        CLOSE(7)
        CLOSE(8)

        STOP
        END
```

```
C*************************************************************************C

C                       SUBROUTINE PROGRAM (INDSCA)

C       C(I, J) CROMER-WABER PARAMETERS, I=ELEMENT NO.,J=PARAMETER
C       FP(I, K) REAL HONL CORR. FOR ELEMENT I, RADIATION NO. K
C       G(K) LAST 4PI SIN THETA/LAMBDA FOR WHICH FP(I, K) AND FPP(I, K)
C       D(I) NO. OF ATOMS OF ELEMENT I IN UNIT COMP. (FLOAT. PT.)
C       ARE USED
C       FPP(I, K) IMAG. HONL CORR. FOR ELEMENT I, RADIATION NO. K
C       SUMZ SUM OF ATOMIC NOS. IN UNIT COMP.
C       NOEL NO. OF DIFFERENT ELEMENTS IN UNIT COMP.
C       NORAD NO. OF X-RADIATIONS
C*************************************************************************C

        SUBROUTINE INDSCA (C,D,FP,FPP,G,SUMZ,PKMAX,DELPK,
     +  NOEL,SUMFSQ,FESQ)

        DIMENSION C(5,10),B(20),G(4),SCFA(3000),FP(5,4),FPP(5,4),
     +  SUMFSQ(3000),FESQ(3000),FEIMSQ(3000),D(5)

        COMMON FE(3,3000),FSQ(3,3000),FEIM(3,3000)

        QQ=G(2)/DELPK+1.001
        NN=INT(QQ)

        DO 10 I=1,NOEL
           DO 15 J=1,9
              B(J)=C(I,J)
15         CONTINUE

        CALL SCATFA (B,PKMAX,DELPK,SCFA)

        DO 30 L=1,NN
                FE(I,L)=SCFA(L)+FP(I,2)
                FSQ(I,L)=FE(I,L)*FE(I,L)
                FSQ(I,L)=FSQ(I,L)+FPP(I,2)*FPP(I,2)
                FEIM(I,L)=FPP(I,2)
30      CONTINUE
10      CONTINUE

        DO 40 L=1,NN
           SUMFSQ(L)=0.
           FESQ(L)=0.
           FEIMSQ(L)=0.

           DO 50 I=1,NOEL
                SUMFSQ(L)=SUMFSQ(L)+FSQ(I,L)*D(I)
                FESQ(L)=FESQ(L)+FE(I,L)*D(I)
                FEIMSQ(L)=FEIMSQ(L)+FEIM(I,L)*D(I)
50         CONTINUE

        FESQ(L)=(FESQ(L)*FESQ(L)+FEIMSQ(L)*FEIMSQ(L))/(SUMZ*SUMZ)

40      CONTINUE

        RETURN
        END

C*************************************************************************C
C
C       SUBROUTINE PROGRAM (SCATFA)
C
```

```
C*********************************************************************C

      SUBROUTINE SCATFA (B,PKMAX,DELPK,SCFA)

      DIMENSION B(20),SCFA(3000)

      Q=PKMAX/DELPK+1.001
      NN=INT(Q)

      DO 10 I=1,NN
         PK=FLOAT(I-1)*DELPK
         S=PK*PK/(4.*3.1415927)**2.
         SCFA(I)=B(9)
              DO 5 J=1,7,2
                 SCFA(I)=SCFA(I)+B(J)*EXP(-B(J+1)*S)
5             CONTINUE
10    CONTINUE

      RETURN
      END
```

```
C*************************************************************************C
C*
C*            PROGRAM MULTIPLE SCATTERING FOR MO RADIATION
C*
C*            Id/Is RATIO AND SUMFSQ CURVE OF VITEROUS SILICA
C*              AFTER DETERMINING J(P) AND Q(2Q,q,b)
C*              ONLY USE SILVER RADIATION
C*
C*                       MODIFIED BY AUGUST 1, 1993
C*
C*************************************************************************C

      PROGRAM MULTIPLE

      DIMENSION C(5,10),FP(5,4),FPP(5,4),D(5),G(4),PKA(3000),
     + SCFA(3000),SUMFSQ(3000),FESQ(3000),FEIMSQ(3000),
     + XJ(3000),XQ(3000),XMS(3000),RMS(3000)

      CHARACTER*8 TAB
      COMMON/INDSCA/ FE(3,3000),FSQ(3,3000),FEIM(3,3000)
      TAB=CHAR(9)

C     DELPK IS INTERVAL OF K VALUE, PKMAX IS MAXIMUM OF K.

      DELPK=0.01
      PKMAX=17.11

      Q=PKMAX/DELPK+1.001
      NN=INT(Q)

C     SUMZ OF SiO2 =30.0, NUMBER OF ELEMENT (2 FOR SiO2)
C     NUMBER OF RADIATION USED I.E.2 FOR Cu & MO
      SUMZ=30.0
      NOEL=2

C     C(I,J) ARE NINE PARAMETER OF DIRAC-SLATER SCATTERING FACTOR.
C     C(1,J) IS FOR SI AND C(2,J) IS FOR O.
      C(1,1)=6.0755
      C(1,2)=2.3497
      C(1,3)=3.2815
      C(1,4)=29.1900
      C(1,5)=2.1670
      C(1,6)=0.7060
      C(1,7)=1.3197
      C(1,8)=84.8342
      C(1,9)=1.1533
      C(2,1)=2.8604
      C(2,2)=12.7907
      C(2,3)=2.5212
      C(2,4)=5.4279
      C(2,5)=1.5296
      C(2,6)=0.3282
      C(2,7)=0.8135
      C(2,8)=34.9406
      C(2,9)=0.2742

C     ANOMALOUS DISPERSION CORRECTION
C     FP(I,K): CORRECT IN REAL-PART, FPP(I,K): CORRECT IN IMAG-PART.
C     I=1 IS FOR SI & I=2 IS FOR O, K=1 IS FOR CU & K=2 IS FOR MO
      FP(1,1)=0.23
      FP(1,2)=0.09
      FP(2,1)=0.0
      FP(2,2)=0.0
```

```
        FPP(1,1)=0.36
        FPP(1,2)=0.09
        FPP(2,1)=0.1
        FPP(2,2)=0.0

C       D(I) ARE NO. OF ATOMS OF EACH ELEMENT IN UNIT CELL OF SiO2
C       D(1) IS FOR SI ATOM, D(2) IS FOR O ATOM
        D(1)=1.0
        D(2)=2.0

C       G(K) ARE HIGHEST K VALUE IN EACH RADIATION
        G(1)=7.5
        G(2)=17.11

        OPEN(UNIT=6, FILE='JOFP.FIG', STATUS='NEW')
        OPEN(UNIT=5,FILE='DOUB.FIG',STATUS='NEW')
        OPEN(UNIT=7,FILE='MULTHEO.DAT',STATUS='NEW')
        OPEN(UNIT=8,FILE='MULTI.DAT',STATUS='NEW')

        XB=14.**2.+2*8.**2.
C       FROM MULJP.FOR, THE BEST FIT IS AT b=45.
        XBB=45.
        AU=28.0855*6.44+2*15.9994*1.31

        CALL SPLINE(NN,PKMAX,DELPK,PKA,XQ)

        DO 5 IA=1,NN
        XJ(IA)=XB/(1+XBB*(0.7093*PKA(IA)/(4*3.1415927))**2.)
        XMS(IA)=XB**2.*XQ(IA)*0.0001/(XJ(IA)*AU)
5       CONTINUE

        WRITE(*,*) 'PLEASE WAIT !!!!'
        CALL INDSCA(C,D,FP,FPP,G,SUMZ,PKMAX,DELPK,NOEL,
     + SUMFSQ,FESQ)

        DO 10 I=1,NN
        WRITE(6,*) PKA(I),TAB,SUMFSQ(I),TAB,XJ(I)
        WRITE(5,*) PKA(I),TAB,XMS(I)
10      CONTINUE
        CLOSE(5)
        CLOSE(6)

        DO 20 I=1,NN
        RMS(I)=XMS(I)*SUMFSQ(I)
        WRITE(7,100) PKA(I),RMS(I)
        WRITE(8,100) PKA(I),XMS(I)
20      CONTINUE
100     FORMAT(1X,F8.4,1X,F8.4)
        CLOSE(7)
        CLOSE(8)

        STOP
        END

C*************************************************************************C
C*
C*              SUBROUTINE SPLINE
C*              TO INTERPOLATE DATA POINTS
C*
C*************************************************************************C

        SUBROUTINE SPLINE (NN,PKMAX,DELPK,PKA,S)

C       NATURAL CUBIC SPLINE
```

```
C       TO CONSTRUCT THE CUBIC SPLINE INTERPOLATE S FOR THE FUNCTION F,
C       DEFINED AT THE NUMBERS X0<X1<...<XN, SATISFY S"(X0)=S"(XN)=0

        DIMENSION H(100),PL(100),PM(100),Z(100),ALFA(100),
     +  SC(100),SB(100),SD(100),S(3000),PKA(3000),XX(10),AA(10)

        XX(1)=0.0
        XX(2)=4.5854
        XX(3)=8.8583
        XX(4)=12.5275
        XX(5)=15.343
        XX(6)=17.1129
        XX(7)=17.7159
        AA(1)=67.17
        AA(2)=45.76
        AA(3)=28.77
        AA(4)=17.17
        AA(5)=10.61
        AA(6)=8.05
        AA(7)=7.42

        N=7
        DO 110 I=1,N-1
        H(I)=XX(I+1)-XX(I)
110     CONTINUE

        PL(1)=1.0
        PM(1)=0.0
        Z(1)=0.0
        DO 120 I=2,N-1
        ALFA(I)=3.0*(AA(I+1)*H(I-1)-AA(I)*(XX(I+1)-XX(I-1))
     +  +AA(I-1)*H(I))/(H(I-1)*H(I))
        PL(I)=2.0*(XX(I+1)-XX(I-1))-H(I-1)*PM(I-1)
        PM(I)=H(I)/PL(I)
        Z(I)=(ALFA(I)-H(I-1)*Z(I-1))/PL(I)
120     CONTINUE

        PL(N)=1.0
        Z(N)=0.0
        SC(N)=0.0
        DO 130 J=N-1,1,-1
        SC(J)=Z(J)-PM(J)*SC(J+1)
        SB(J)=(AA(J+1)-AA(J))/H(J)-H(J)*(SC(J+1)+2.0*SC(J))/3.0
        SD(J)=(SC(J+1)-SC(J))/(3.0*H(J))
130     CONTINUE

        DO 140 I=1,NN
        PKA(I)=DELPK*FLOAT(I-1)
        J=1
150     IF(PKA(I).GT.XX(J))THEN
        J=J+1
        GOTO 150
        END IF
        J=J-1
        IF(J.LT.1) J=1
        S(I)=AA(J)+SB(J)*(PKA(I)-XX(J))+SC(J)*(PKA(I)-XX(J))**2.0
     +  +SD(J)*(PKA(I)-XX(J))**3.0
140     CONTINUE

        RETURN
        END

C*************************************************************************C
C
```

```
C                       SUBROUTINE PROGRAM (INDSCA)
C
C       C(I, J) CROMER-WABER PARAMETERS, I=ELEMENT NO.,J=PARAMETER
C       FP(I, K) REAL HONL CORR. FOR ELEMENT I, RADIATION NO. K
C       G(K) LAST 4PI SIN THETA/LAMBDA FOR WHICH FP(I, K) AND FPP(I, K)
C       D(I) NO. OF ATOMS OF ELEMENT I IN UNIT COMP. (FLOAT. PT.)
C       ARE USED
C       FPP(I, K) IMAG. HONL CORR. FOR ELEMENT I, RADIATION NO. K
C       SUMZ SUM OF ATOMIC NOS. IN UNIT COMP.
C       NOEL NO. OF DIFFERENT ELEMENTS IN UNIT COMP.
C       NORAD NO. OF X-RADIATIONS
C*************************************************************************C

        SUBROUTINE INDSCA (C,D,FP,FPP,G,SUMZ,PKMAX,DELPK,
     + NOEL,SUMFSQ,FESQ)

        DIMENSION C(5,10),B(20),G(4),SCFA(3000),FP(5,4),FPP(5,4),
     + SUMFSQ(3000),FESQ(3000),FEIMSQ(3000),D(5)
        COMMON FE(3,3000),FSQ(3,3000),FEIM(3,3000)

        QQ=G(2)/DELPK+1.001
        NN=INT(QQ)

        DO 10 I=1,NOEL
           DO 15 J=1,9
              B(J)=C(I,J)
15         CONTINUE

           CALL SCATFA (B,PKMAX,DELPK,SCFA)

              DO 30 L=1,NN
                 FE(I,L)=SCFA(L)+FP(I,2)
                 FSQ(I,L)=FE(I,L)*FE(I,L)
                 FSQ(I,L)=FSQ(I,L)+FPP(I,2)*FPP(I,2)
                 FEIM(I,L)=FPP(I,2)
30            CONTINUE
10      CONTINUE

        DO 40 L=1,NN
           SUMFSQ(L)=0.
           FESQ(L)=0.
           FEIMSQ(L)=0.
           DO 50 I=1,NOEL
                SUMFSQ(L)=SUMFSQ(L)+FSQ(I,L)*D(I)
                FESQ(L)=FESQ(L)+FE(I,L)*D(I)
                FEIMSQ(L)=FEIMSQ(L)+FEIM(I,L)*D(I)
50         CONTINUE

        FESQ(L)=(FESQ(L)*FESQ(L)+FEIMSQ(L)*FEIMSQ(L))/(SUMZ*SUMZ)

40      CONTINUE

        RETURN
        END

C*************************************************************************C
C
C       SUBROUTINE PROGRAM (SCATFA)
C
C*************************************************************************C

        SUBROUTINE SCATFA (B,PKMAX,DELPK,SCFA)

        DIMENSION B(20),SCFA(3000)
```

```
      Q=PKMAX/DELPK+1.001
      NN=INT(Q)

      DO 10 I=1,NN
         PK=FLOAT(I-1)*DELPK
         S=PK*PK/(4.*3.1415927)**2.
         SCFA(I)=B(9)
              DO 5 J=1,7,2
                 SCFA(I)=SCFA(I)+B(J)*EXP(-B(J+1)*S)
5             CONTINUE
10    CONTINUE

      RETURN
      END
```

```
C*************************************************************************C
C*
C*            PROGRAM Q*P
C*
C*            THEORETICAL P AND Q-FUNCTION OF VITEROUS SILICA
C*              IN CU & MO RADIATION
C*
C*                       MODIFIED BY AUGUST 1, 1993
C*
C*************************************************************************C

      PROGRAM QP

      DIMENSION C(5,10),FP(5,4),FPP(5,4),D(5),G(4),PKA(3000),
     + SCFA(3000),SUMFSQ(3000),FESQ(3000),
     + FEIMSQ(3000),FSIG(3000),FOG(3000),FSIOG(3000),
     + RIJ(6),UIJ(6),SFA(3000,6),FSIOSQ(3000),FO2SQ(3000),
     + FSI2SQ(3000),R(500),QF(500,6),
     + PAIR(500,6),SIDEL(500),X(500,6)

      CHARACTER*8 TAB
C     COMMON/INDSCA/ FE(3,3000),FSQ(3,3000),FEIM(3,3000)
      TAB=CHAR(9)

C     DELPK IS INTERVAL OF K VALUE, PKMAX IS MAXIMUM OF K.

      DELPK=0.01
      PKMAX=17.11

      Q=PKMAX/DELPK+1.001
      N=INT(Q)
      WRITE(*,*) 'HELLOW 1'
C     SUMZ OF SiO2 =30.0, NUMBER OF ELEMENT (2 FOR SiO2)
C     NUMBER OF RADIATION USED I.E.2 FOR Cu & Mo
      SUMZ=30.0
      NOEL=2
      NORAD=2

C     C(I,J) ARE NINE PARAMETER OF DIRAC-SLATER SCATTERING FACTOR.
C     C(1,J) IS FOR SI AND C(2,J) IS FOR O.
      C(1,1)=6.0755
      C(1,2)=2.3497
      C(1,3)=3.2815
      C(1,4)=29.1900
      C(1,5)=2.1670
      C(1,6)=0.7060
      C(1,7)=1.3197
      C(1,8)=84.8342
      C(1,9)=1.1533
      C(2,1)=2.8604
      C(2,2)=12.7907
      C(2,3)=2.5212
      C(2,4)=5.4279
      C(2,5)=1.5296
      C(2,6)=0.3282
      C(2,7)=0.8135
      C(2,8)=34.9406
      C(2,9)=0.2742

C     ANOMALOUS DISPERSION CORRECTION
C     FP(I,K): CORRECT IN REAL-PART, FPP(I,K): CORRECT IN IMAG-PART.
C     I=1 IS FOR SI & I=2 IS FOR O, K=1 IS FOR CU & K=2 IS FOR MO
      FP(1,1)=0.23
```

```
      FP(1,2)=0.09
      FP(2,1)=0.0
      FP(2,2)=0.0
      FPP(1,1)=0.36
      FPP(1,2)=0.09
      FPP(2,1)=0.1
      FPP(2,2)=0.0

C     D(I) ARE NO. OF ATOMS OF EACH ELEMENT IN UNIT CELL OF SiO2
C     D(1) IS FOR SI ATOM, D(2) IS FOR O ATOM
      D(1)=1.0
      D(2)=2.0

C     G(K) ARE HIGHEST K VALUE IN EACH RADIATION
      G(1)=7.5
      G(2)=17.11

      OPEN(UNIT=2,FILE='SUMFSQ.FIG',STATUS='NEW')
      OPEN(UNIT=3,FILE='FESQ.FIG', STATUS='NEW')
      OPEN(UNIT=4,FILE='FSIO.FIG',STATUS='NEW')

      DO 5 IA=1,N
      PKA(IA)=FLOAT(IA-1)*DELPK
5     CONTINUE
      WRITE(*,*) 'HELLOW 2'

      CALL INDSCA(C,D,FP,FPP,G,SUMZ,PKMAX,DELPK,NOEL,NORAD,
     + SUMFSQ,FESQ,FSIG,FOG,FSIOG,FSIOSQ,FO2SQ,FSI2SQ)

      DO 10 I=1,N
      WRITE(2,*) PKA(I),TAB,SUMFSQ(I)
      WRITE(3,*) PKA(I),TAB,FESQ(I)
      WRITE(4,*) PKA(I),TAB,FSIG(I),TAB,FOG(I),TAB,FSIOG(I)
10    CONTINUE
      CLOSE(2)
      CLOSE(3)
      CLOSE(4)

      OPEN(UNIT=5,FILE='Q.FIG',STATUS='NEW')
      OPEN(UNIT=7,FILE='P.FIG',STATUS='NEW')
      OPEN(UNIT=8,FILE='P.DIS',STATUS='NEW')

      RMAX=10.0
      DELR=0.025
      NOCO=400

C     RIJ(1)=RSIO,R(2)=ROO,R(3)=RSISI,R(4)=RSI2DO,
C     R(5)=RO2DO,R(6)=RSI2DSI
      RIJ(1)=1.62
      RIJ(2)=2.65
      RIJ(3)=3.12
      RIJ(4)=4.15
      RIJ(5)=5.1
      RIJ(6)=5.1

C     UIJ(I) IS THE NUMBER OF NEIGHBOR ATOMS IN THE UNIT CELL
      UIJ(1)=8.0
      UIJ(2)=12.0
      UIJ(3)=4.0
      UIJ(4)=24.0
      UIJ(5)=36.0
      UIJ(6)=12.0

C     ALPHA IS TAKEN FROM EXP(-A2Km2)=0.25 TO GET Q-FUNCTION
```

```
      ALPHA=0.069
      ALFSQ=ALPHA*ALPHA

      DO 20 I=1,N
      SFA(I,1)=FSIOSQ(I)
      SFA(I,2)=FO2SQ(I)
      SFA(I,3)=FSI2SQ(I)
      SFA(I,4)=SFA(I,1)
      SFA(I,5)=SFA(I,2)
      SFA(I,6)=SFA(I,3)
20    CONTINUE

      DO 50 L=1,NOCO+1
      R(L)=FLOAT(L-1)*DELR
      DO 40 M=1,6
      PP=0.0
      DO I=1,N,N-1
      X(L,M)=R(L)-RIJ(M)
      PP=PP+17.0*SFA(I,M)/FESQ(I)*EXP(-ALFSQ*PKA(I)*PKA(I))
     + *COS(X(L,M)*PKA(I))/48.0
      END DO
      DO I=2,N-1,N-3
      X(L,M)=R(L)-RIJ(M)
      PP=PP+17.0*SFA(I,M)/FESQ(I)*EXP(-ALFSQ*PKA(I)*PKA(I))
     + *COS(X(L,M)*PKA(I))/48.0
      END DO
      DO I=3,N-2,N-5
      X(L,M)=R(L)-RIJ(M)
      PP=PP+17.0*SFA(I,M)/FESQ(I)*EXP(-ALFSQ*PKA(I)*PKA(I))
     + *COS(X(L,M)*PKA(I))/48.0
      END DO
      DO I=4,N-3,N-7
      X(L,M)=R(L)-RIJ(M)
      PP=PP+17.0*SFA(I,M)/FESQ(I)*EXP(-ALFSQ*PKA(I)*PKA(I))
     + *COS(X(L,M)*PKA(I))/48.0
      END DO
      DO I=5,N-4
      X(L,M)=R(L)-RIJ(M)
      PP=PP+17.0*SFA(I,M)/FESQ(I)*EXP(-ALFSQ*PKA(I)*PKA(I))
     + *COS(X(L,M)*PKA(I))/48.0
      END DO
      QF(L,M)=DELR*PP/2.0
40    CONTINUE
50    CONTINUE

      DO 60 L=1,NOCO+1
      SIDEL(L)=0.0

      DO 70 M=1,6
      PAIR(L,M)=UIJ(M)/RIJ(M)*QF(L,M)
      SIDEL(L)=SIDEL(L)+PAIR(L,M)
70    CONTINUE
60    CONTINUE

      DO 80 M=1,3
      DO 90 L=1,NOCO+1
      IF(X(L,M).LT.0.0) THEN
      GO TO 90
      ELSE IF(X(L,M).GT.2.0) THEN
      GO TO 90
      ELSE
      WRITE(5,*) X(L,M),TAB,QF(L,M)
      END IF
90    CONTINUE
```

```
80      CONTINUE

        DO 100 L=1,NOCO+1
        WRITE(7,*) R(L),TAB,SIDEL(L),TAB,PAIR(L,1),TAB,PAIR(L,2),
     +  TAB,PAIR(L,3),TAB,PAIR(L,4),TAB,PAIR(L,5),TAB,PAIR(L,6)
        WRITE(8,120) R(L),SIDEL(L),PAIR(L,1),PAIR(L,2),PAIR(L,3),
     +  PAIR(L,4),PAIR(L,5),PAIR(L,6)
120     FORMAT(1X,F10.4,1X,F10.4,1X,F10.4,1X,F10.4,1X,F10.4,
     +  1X,F10.4,1X,F10.4,1X,F10.4)
100     CONTINUE

        CLOSE(5)
        CLOSE(7)
        CLOSE(8)

        STOP
        END

C*************************************************************************C

C                       SUBROUTINE PROGRAM (INDSCA)

C       C(I, J) CROMER-WABER PARAMETERS, I=ELEMENT NO.,J=PARAMETER
C       FP(I, K) REAL HONL CORR. FOR ELEMENT I, RADIATION NO. K
C       G(K) LAST 4PI SIN THETA/LAMBDA FOR WHICH FP(I, K) AND FPP(I, K)
C       D(I) NO. OF ATOMS OF ELEMENT I IN UNIT COMP. (FLOAT. PT.)
C       ARE USED
C       FPP(I, K) IMAG. HONL CORR. FOR ELEMENT I, RADIATION NO. K
C       SUMZ SUM OF ATOMIC NOS. IN UNIT COMP.
C       NOEL NO. OF DIFFERENT ELEMENTS IN UNIT COMP.
C       NORAD NO. OF X-RADIATIONS
C*************************************************************************C

        SUBROUTINE INDSCA (C,D,FP,FPP,G,SUMZ,PKMAX,DELPK,
     + NOEL,NORAD,SUMFSQ,FESQ,FSIG,FOG,FSIOG,FSIOSQ,FO2SQ,FSI2SQ)

        DIMENSION C(5,10),B(20),G(4),SCFA(3000),FP(5,4),FPP(5,4),
     + SUMFSQ(3000),FESQ(3000),FEIMSQ(3000),D(5),
     + FSIG(3000),FOG(3000),FSIOG(3000),FE(3,3000),FSQ(3,3000),
     + FEIM(3,3000),FSIOSQ(3000),FO2SQ(3000),FSI2SQ(3000),FX(3000)

        DO 10 I=1,NOEL
           DO 15 J=1,9
              B(J)=C(I,J)
15         CONTINUE

           MO=0
           CALL SCATFA (B,PKMAX,DELPK,SCFA)

           DO 20 K=1, NORAD
              QQ=G(K)/DELPK+1.001
              NNN=INT(QQ)
              NO=1+MO
              DO 30 L=NO, NNN
                 FE(I,L)=SCFA(L)+FP(I,K)
                 FSQ(I,L)=FE(I,L)*FE(I,L)
                 FSQ(I,L)=FSQ(I,L)+FPP(I,K)*FPP(I,K)
                 FEIM(I,L)=FPP(I,K)
30            CONTINUE
              MO=NNN
20         CONTINUE
10      CONTINUE

        Q=PKMAX/DELPK+1.001
```

```
      NN=INT(Q)
      DO 40 L=1,NN
         SUMFSQ(L)=0.
         FESQ(L)=0.
         FEIMSQ(L)=0.

         DO 50 I=1,NOEL
              SUMFSQ(L)=SUMFSQ(L)+FSQ(I,L)*D(I)
              FESQ(L)=FESQ(L)+FE(I,L)*D(I)
              FEIMSQ(L)=FEIMSQ(L)+FEIM(I,L)*D(I)

50       CONTINUE

      FESQ(L)=(FESQ(L)*FESQ(L)+FEIMSQ(L)*FEIMSQ(L))/(SUMZ*SUMZ)
      FSIG(L)=FSQ(1,L)/FESQ(L)
      FOG(L)=FSQ(2,L)/FESQ(L)
      FSIOG(L)=SQRT((FE(1,L)*FE(2,L))**2.+(FEIM(1,L)
     +*FEIM(2,L))**2.)/FESQ(L)

      FSI2SQ(L)=FSQ(1,L)
      FO2SQ(L)=FSQ(2,L)
      FSIOSQ(L)=SQRT((FE(1,L)*FE(2,L))**2.+(FEIM(1,L)
     +*FEIM(2,L))**2.)

40    CONTINUE

      RETURN
      END

C*********************************************************************C
C
C     SUBROUTINE PROGRAM (SCATFA)
C
C*********************************************************************C

      SUBROUTINE SCATFA (B,PKMAX,DELPK,SCFA)

      DIMENSION B(20),SCFA(3000)
      Q=PKMAX/DELPK+1.001
      NN=INT(Q)

      DO 10 I=1,NN
         PK=FLOAT(I-1)*DELPK
         S=PK*PK/(4.*3.1415927)**2.
         SCFA(I)=B(9)
              DO 5 J=1,7,2
                 SCFA(I)=SCFA(I)+B(J)*EXP(-B(J+1)*S)
5             CONTINUE
10    CONTINUE

      RETURN
      END
```

```
C*****************************************************************************C
C*
C*            PROGRAM PFD
C*
C*            PAIR FUNCTION DISTRIBUTION OF VITEROUS SILICA
C*
C*                        MODIFIED BY AUGUST 1,1993
C*
C*****************************************************************************C

      PROGRAM PFD

      DIMENSION C(5,10),FP(5,4),FPP(5,4),D(5),G(4),PKA(3000),
     +  SCFA(3000),SUMFSQ(3000),FESQ(3000),
     +  FEIMSQ(3000),FSIG(3000),FOG(3000),FSIOG(3000),
     +  RIJ(6),UIJ(6),SFA(3000,6),FSIOSQ(3000),FO2SQ(3000),
     +  FSI2SQ(3000),R(500),QF(500,6),TT(3000),PIEU(3000),
     +  PAIR(500,6),SIDEL(500),X(500,6),WKIK(3000),SIDER(500),
     +  RADIST(500),SINCO(500)

      CHARACTER*8 TAB,NAME1
C     COMMON/INDSCA/ FE(3,3000),FSQ(3,3000),FEIM(3,3000)
      TAB=CHAR(9)

C     DELPK IS INTERVAL OF K VALUE, PKMAX IS MAXIMUM OF K.
C     ROZERO IS THE ELECTRON DENSITYOF THE VITREOUS SILICA.
C     ROEL IS THE ELECTRON DENSITY*SUMZ
      DELPK=0.01
      PKMAX=17.11
      ROZERO=0.6843
      ROEL=0.6843*30.0
      TOP=2./3.1415927
      RHFP=ROZERO*4.*3.1415927
      PEAR=2.*3.1415927*3.1415927*ROEL


      Q=PKMAX/DELPK+1.001
      N=INT(Q)
      WRITE(*,*) 'HELLOW 1'
C     SUMZ OF SiO2 =30.0, NUMBER OF ELEMENT (2 FOR SiO2)
C     NUMBER OF RADIATION USED I.E.2 FOR Cu & Mo
      SUMZ=30.0
      NOEL=2
      NORAD=2

C     C(I,J) ARE NINE PARAMETER OF DIRAC-SLATER SCATTERING FACTOR.
C     C(1,J) IS FOR SI AND C(2,J) IS FOR O.
      C(1,1)=6.0755
      C(1,2)=2.3497
      C(1,3)=3.2815
      C(1,4)=29.1900
      C(1,5)=2.1670
      C(1,6)=0.7060
      C(1,7)=1.3197
      C(1,8)=84.8342
      C(1,9)=1.1533
      C(2,1)=2.8604
      C(2,2)=12.7907
      C(2,3)=2.5212
      C(2,4)=5.4279
      C(2,5)=1.5296
      C(2,6)=0.3282
      C(2,7)=0.8135
```

```
      C(2,8)=34.9406
      C(2,9)=0.2742

C     ANOMALOUS DISPERSION CORRECTION
C     FP(I,K): CORRECT IN REAL-PART, FPP(I,K): CORRECT IN IMAG-PART.
C     I=1 IS FOR SI & I=2 IS FOR O, K=1 IS FOR CU & K=2 IS FOR MO
      FP(1,1)=0.23
      FP(1,2)=0.09
      FP(2,1)=0.0
      FP(2,2)=0.0
      FPP(1,1)=0.36
      FPP(1,2)=0.09
      FPP(2,1)=0.1
      FPP(2,2)=0.0

C     D(I) ARE NO. OF ATOMS OF EACH ELEMENT IN UNIT CELL OF SiO2
C     D(1) IS FOR SI ATOM, D(2) IS FOR O ATOM
      D(1)=1.0
      D(2)=2.0

C     G(K) ARE HIGHEST K VALUE IN EACH RADIATION
      G(1)=7.5
      G(2)=17.11

      WRITE(*,*) 'HELLOW 2'

      CALL INDSCA(C,D,FP,FPP,G,SUMZ,PKMAX,DELPK,NOEL,NORAD,
     + SUMFSQ,FESQ,FSIG,FOG,FSIOG,FSIOSQ,FO2SQ,FSI2SQ)

      OPEN(UNIT=4,FILE='SUMFSQ.TAB',STATUS='NEW')
      WRITE(4,11) (SUMFSQ(I),I=1,N)
      WRITE(4,12) (FESQ(I),I=1,N)
      CLOSE(4)
11    FORMAT(6HSUMFSQ/(10F9.4))
12    FORMAT(4HFESQ/(10F8.4))

      OPEN(UNIT=5,FILE='WKIK.FIG',STATUS='NEW')
      OPEN(UNIT=6,FILE='FINA.FIG',STATUS='NEW')
      OPEN(UNIT=7,FILE='TRYG.FIG',STATUS='NEW')
      OPEN(UNIT=8,FILE='PG.FIG',STATUS='NEW')

      RMAX=10.0
      DELR=0.025
      RRR=RMAX/DELR+1.001
      NOCO=INT(RRR)

C     RIJ(1)=RSIO,R(2)=ROO,R(3)=RSISI,R(4)=RSI2DO,
C     R(5)=RO2DO,R(6)=RSI2DSI
      RIJ(1)=1.62
      RIJ(2)=2.65
      RIJ(3)=3.12
      RIJ(4)=4.15
      RIJ(5)=5.1
      RIJ(6)=5.1

C     UIJ(I) IS THE NUMBER OF NEIGHBOR ATOMS IN THE UNIT CELL
      UIJ(1)=8.0
      UIJ(2)=12.0
      UIJ(3)=4.0
      UIJ(4)=24.0
      UIJ(5)=36.0
      UIJ(6)=12.0

C     ALPHA IS TAKEN FROM EXP(A2Km2)=0.25 TO GET Q-FUNCTION
```

```
      ALPHA=0.0688
      ALFSQ=ALPHA*ALPHA

      DO 20 I=1,N
      SFA(I,1)=FSIOSQ(I)
      SFA(I,2)=FO2SQ(I)
      SFA(I,3)=FSI2SQ(I)
      SFA(I,4)=SFA(I,1)
      SFA(I,5)=SFA(I,2)
      SFA(I,6)=SFA(I,3)
20    CONTINUE

      WRITE(*,*) 'PLEASE ENTER DATA FILE NAME !!!'
      READ(*,*) NAME1
      OPEN(UNIT=10,FILE=NAME1,STATUS='OLD')
      DO I=1,N
      READ(10,21) TT(I),PIEU(I)
21    FORMAT(1X,F8.4,1X,F8.4)
      END DO
      CLOSE(10)

      QP=PKMAX/DELPK+1.001
      NP=INT(QP)

      DO I=1,NP
      PKA(I)=DELPK*FLOAT(I-1)
      END DO

      WKIK(1)=0.0
      DO I=2,NP-1
      WKIK(I)=(PIEU(I)-SUMFSQ(I))/FESQ(I)
      WKIK(I)=PKA(I)*WKIK(I)*EXP(-ALFSQ*PKA(I)*PKA(I))
      END DO
      WKIK(NP)=0.0

      DO I=1,NP
      WRITE(5,*) PKA(I),TAB,WKIK(I)
      END DO
      CLOSE(5)

      DO J=1,NOCO
      R(J)=FLOAT(J-1)*DELR
            SS=0.0
            DO K=1,N,N-1
            SS=SS+WKIK(K)*SIN(R(J)*PKA(K))
            END DO
            DO K=2,N-1,N-3
            SS=SS+WKIK(K)*SIN(R(J)*PKA(K))
            END DO
            DO K=3,N-2,N-5
            SS=SS+WKIK(K)*SIN(R(J)*PKA(K))
            END DO
            DO K=4,N-3,N-7
            SS=SS+WKIK(K)*SIN(R(J)*PKA(K))
            END DO
            DO K=5,N-4
            SS=SS+WKIK(K)*SIN(R(J)*PKA(K))
            END DO

      SINCO(J)=SS*DELR
      RADIST(J)=RHFP*R(J)*R(J)+TOP*R(J)*SINCO(J)
      SIDER(J)=PEAR*R(J)+SINCO(J)
      END DO
```

```
      WRITE(*,111) (SINCO(I),I=1,NOCO)
111   FORMAT(5HSINCO/(5F10.4))

      WRITE(*,*) 'NOW PROCESSING???'

      DO 50 L=1,NOCO
      R(L)=FLOAT(L-1)*DELR
      DO 40 M=1,6

      PP=0.0
      DO I=1,N,N-1
      X(L,M)=R(L)-RIJ(M)
      PP=PP+17.0*SFA(I,M)/FESQ(I)*EXP(-ALFSQ*PKA(I)*PKA(I))
     +  *COS(X(L,M)*PKA(I))/48.0
      END DO

      DO I=2,N-1,N-3
      X(L,M)=R(L)-RIJ(M)
      PP=PP+17.0*SFA(I,M)/FESQ(I)*EXP(-ALFSQ*PKA(I)*PKA(I))
     + *COS(X(L,M)*PKA(I))/48.0
      END DO

      DO I=3,N-2,N-5
      X(L,M)=R(L)-RIJ(M)
      PP=PP+17.0*SFA(I,M)/FESQ(I)*EXP(-ALFSQ*PKA(I)*PKA(I))
     + *COS(X(L,M)*PKA(I))/48.0
      END DO

      DO I=4,N-3,N-7
      X(L,M)=R(L)-RIJ(M)
      PP=PP+17.0*SFA(I,M)/FESQ(I)*EXP(-ALFSQ*PKA(I)*PKA(I))
     + *COS(X(L,M)*PKA(I))/48.0
      END DO

      DO I=5,N-4
      X(L,M)=R(L)-RIJ(M)
      PP=PP+17.0*SFA(I,M)/FESQ(I)*EXP(-ALFSQ*PKA(I)*PKA(I))
     + *COS(X(L,M)*PKA(I))/48.0
      END DO

      QF(L,M)=DELR*PP/2.0
40    CONTINUE
50    CONTINUE

      WRITE(*,*) 'NOW PROCESSING AGAING !!!'

      DO 60 L=1,NOCO

      SIDEL(L)=0.0

      DO 70 M=1,6
      PAIR(L,M)=UIJ(M)/RIJ(M)*QF(L,M)

      SIDEL(L)=SIDEL(L)+PAIR(L,M)
70    CONTINUE
60    CONTINUE

      WRITE(*,*) 'NOW PROCESSING AGAIN TWO !!!'

      DO 100 L=1,NOCO
      WRITE(6,*) R(L),TAB,SIDER(L),TAB,SIDEL(L),TAB,RADIST(L)
      WRITE(7,*) R(L),TAB,SIDER(L),TAB,PAIR(L,1),TAB,PAIR(L,2),
     +  TAB,PAIR(L,3),TAB,PAIR(L,4)
      WRITE(8,*) R(L),TAB,SIDEL(L),TAB,PAIR(L,1),TAB,PAIR(L,2),
```

```
     +   TAB,PAIR(L,3),TAB,PAIR(L,4),TAB,PAIR(L,5),TAB,PAIR(L,6)
100      CONTINUE

         CLOSE(6)
         CLOSE(7)
         CLOSE(8)

         STOP
         END

C*******************************************************************************C

C                        SUBROUTINE PROGRAM (INDSCA)

C        C(I, J) CROMER-WABER PARAMETERS, I=ELEMENT NO.,J=PARAMETER
C        FP(I, K) REAL HONL CORR. FOR ELEMENT I, RADIATION NO. K
C        G(K) LAST 4PI SIN THETA/LAMBDA FOR WHICH FP(I, K) AND FPP(I, K)
C        D(I) NO. OF ATOMS OF ELEMENT I IN UNIT COMP. (FLOAT. PT.)
C        ARE USED
C        FPP(I, K) IMAG. HONL CORR. FOR ELEMENT I, RADIATION NO. K
C        SUMZ SUM OF ATOMIC NOS. IN UNIT COMP.
C        NOEL NO. OF DIFFERENT ELEMENTS IN UNIT COMP.
C        NORAD NO. OF X-RADIATIONS
C*******************************************************************************C

         SUBROUTINE INDSCA (C,D,FP,FPP,G,SUMZ,PKMAX,DELPK,
     + NOEL,NORAD,SUMFSQ,FESQ,FSIG,FOG,FSIOG,FSIOSQ,FO2SQ,FSI2SQ)

         DIMENSION C(5,10),B(20),G(4),SCFA(3000),FP(5,4),FPP(5,4),
     + SUMFSQ(3000),FESQ(3000),FEIMSQ(3000),D(5),
     + FSIG(3000),FOG(3000),FSIOG(3000),FE(3,3000),FSQ(3,3000),
     + FEIM(3,3000),FSIOSQ(3000),FO2SQ(3000),FSI2SQ(3000),FX(3000)

         DO 10 I=1,NOEL
            DO 15 J=1,9
               B(J)=C(I,J)
15          CONTINUE

            MO=0
            CALL SCATFA (B,PKMAX,DELPK,SCFA)

            DO 20 K=1, NORAD
               QQ=G(K)/DELPK+1.001
               NNN=INT(QQ)
               NO=1+MO
               DO 30 L=NO, NNN
                   FE(I,L)=SCFA(L)+FP(I,K)
                   FSQ(I,L)=FE(I,L)*FE(I,L)
                   FSQ(I,L)=FSQ(I,L)+FPP(I,K)*FPP(I,K)
                   FEIM(I,L)=FPP(I,K)
30               CONTINUE
               MO=NNN
20          CONTINUE
10       CONTINUE

         Q=PKMAX/DELPK+1.001
         NN=INT(Q)
         DO 40 L=1,NN
            SUMFSQ(L)=0.
            FESQ(L)=0.
            FEIMSQ(L)=0.

            DO 50 I=1,NOEL
                 SUMFSQ(L)=SUMFSQ(L)+FSQ(I,L)*D(I)
```

```
                FESQ(L)=FESQ(L)+FE(I,L)*D(I)
                FEIMSQ(L)=FEIMSQ(L)+FEIM(I,L)*D(I)

50          CONTINUE

        FESQ(L)=(FESQ(L)*FESQ(L)+FEIMSQ(L)*FEIMSQ(L))/(SUMZ*SUMZ)
        FSIG(L)=FSQ(1,L)/FESQ(L)
        FOG(L)=FSQ(2,L)/FESQ(L)
        FSIOG(L)=SQRT((FE(1,L)*FE(2,L))**2.+(FEIM(1,L)
     +  *FEIM(2,L))**2.)/FESQ(L)

        FSI2SQ(L)=FSQ(1,L)
        FO2SQ(L)=FSQ(2,L)
        FSIOSQ(L)=SQRT((FE(1,L)*FE(2,L))**2.+(FEIM(1,L)
     +  *FEIM(2,L))**2.)

40      CONTINUE

        RETURN
        END

C*************************************************************************C
C
C       SUBROUTINE PROGRAM (SCATFA)
C
C*************************************************************************C

        SUBROUTINE SCATFA (B,PKMAX,DELPK,SCFA)

        DIMENSION B(20),SCFA(3000)
        Q=PKMAX/DELPK+1.001
        NN=INT(Q)

        DO 10 I=1,NN
           PK=FLOAT(I-1)*DELPK
           S=PK*PK/(4.*3.1415927)**2.
           SCFA(I)=B(9)
                DO 5 J=1,7,2
                   SCFA(I)=SCFA(I)+B(J)*EXP(-B(J+1)*S)
5               CONTINUE
10      CONTINUE

        RETURN
        END
```

```
C*************************************************************************C
C*
C*            PROGRAM PEAK1 + GAUSS
C*
C*            THEORETICAL P AND Q-FUNCTION OF VITEROUS SILICA
C*              IN CU & MO RADIATION
C*
C*                       MODIFIED BY AUGUST 1 1993
C*
C*************************************************************************C

      PROGRAM GPEAK1

      CHARACTER*8 NAME1,TAB

      DIMENSION C(5,10),FP(5,4),FPP(5,4),D(5),G(4),PKA(2000),
     +  SCFA(2000),SUMFSQ(2000),FESQ(2000),
     +  FEIMSQ(2000),FSIG(2000),FOG(2000),FSIOG(2000),
     +  RIJ(6),UIJ(6),SFA(2000,6),FSIOSQ(2000),FO2SQ(2000),
     +  FSI2SQ(2000),R(1000),QF(1000,3),
     +  X(1000,15),PEAK1(1000,3),YA(1000),YPR(1000),RV(1000),
     +  XGAU(50,3)

C     COMMON/INDSCA/ FE(3,3000),FSQ(3,3000),FEIM(3,3000)
      TAB=CHAR(9)

C     DELPK IS INTERVAL OF K VALUE, PKMAX IS MAXIMUM OF K.

      DELPK=0.01
      PKMAX=17.11

      Q=PKMAX/DELPK+1.001
      N=INT(Q)
      WRITE(*,*) 'HELLOW 1'
C     SUMZ OF SiO2 =30.0, NUMBER OF ELEMENT (2 FOR SiO2)
C     NUMBER OF RADIATION USED I.E.2 FOR Cu & Mo
      SUMZ=30.0
      NOEL=2
      NORAD=2

C     C(I,J) ARE NINE PARAMETER OF DIRAC-SLATER SCATTERING FACTOR.
C     C(1,J) IS FOR SI AND C(2,J) IS FOR O.
      C(1,1)=6.0755
      C(1,2)=2.3497
      C(1,3)=3.2815
      C(1,4)=29.1900
      C(1,5)=2.1670
      C(1,6)=0.7060
      C(1,7)=1.3197
      C(1,8)=84.8342
      C(1,9)=1.1533
      C(2,1)=2.8604
      C(2,2)=12.7907
      C(2,3)=2.5212
      C(2,4)=5.4279
      C(2,5)=1.5296
      C(2,6)=0.3282
      C(2,7)=0.8135
      C(2,8)=34.9406
      C(2,9)=0.2742

C     ANOMALOUS DISPERSION CORRECTION
C     FP(I,K): CORRECT IN REAL-PART, FPP(I,K): CORRECT IN IMAG-PART.
```

```
C       I=1 IS FOR SI & I=2 IS FOR O, K=1 IS FOR CU & K=2 IS FOR MO
        FP(1,1)=0.23
        FP(1,2)=0.09
        FP(2,1)=0.0
        FP(2,2)=0.0
        FPP(1,1)=0.36
        FPP(1,2)=0.09
        FPP(2,1)=0.1
        FPP(2,2)=0.0

C       D(I) ARE NO. OF ATOMS OF EACH ELEMENT IN UNIT CELL OF SiO2
C       D(1) IS FOR SI ATOM, D(2) IS FOR O ATOM
        D(1)=1.0
        D(2)=2.0

C       G(K) ARE HIGHEST K VALUE IN EACH RADIATION
        G(1)=7.5
        G(2)=17.11

        DO 5 IA=1,N
        PKA(IA)=FLOAT(IA-1)*DELPK
5       CONTINUE
        WRITE(*,*) 'HELLOW 2'

        CALL INDSCA(C,D,FP,FPP,G,SUMZ,PKMAX,DELPK,NOEL,NORAD,
     + SUMFSQ,FESQ,FSIG,FOG,FSIOG,FSIOSQ,FO2SQ,FSI2SQ)

        WRITE(*,*) 'PLEASE ENTER FILE NAME FOR PAIR-DAT'
        READ(*,*) NAME1

        OPEN(UNIT=6,FILE=NAME1,STATUS='OLD')
        OPEN(UNIT=7,FILE='GPK1.DAT',STATUS='NEW')
        OPEN(UNIT=8,FILE='GPK1.CHK',STATUS='NEW')

        RMAX=10.0
        DELR=0.02
        RRR=RMAX/DELR+1.001
        NOCO=INT(RRR)

        DO 15 J=1,NOCO
        READ(6,16) YA(J),YPR(J)
16      FORMAT(1X,F10.4,1X,F10.4)
15      CONTINUE
        CLOSE(6)

        WRITE(*,*) 'HELLOW READ'

C       RIJ(1)=RSIO,R(2)=ROO,R(3)=RSISI,R(4)=RSI2DO,
C       R(5)=RO2DO,R(6)=RSI2DSI
        RIJ(1)=1.60
        RIJ(2)=2.64
        RIJ(3)=3.04
        RIJ(4)=4.16
        RIJ(5)=5.1
        RIJ(6)=5.1

C       UIJ(I) IS THE NUMBER OF NEIGHBOR ATOMS IN THE UNIT CELL
        UIJ(1)=11.0
        UIJ(2)=12.0
        UIJ(3)=4.0
        UIJ(4)=24.0
        UIJ(5)=36.0
        UIJ(6)=12.0
```

```
C       ALPHA IS TAKEN FROM A2Km2=0.025 TO GET Q-FUNCTION
        ALPHA=0.0688
        ALFSQ=ALPHA*ALPHA

        DO 20 I=1,N
        SFA(I,1)=FSIOSQ(I)
        SFA(I,2)=FO2SQ(I)
        SFA(I,3)=FSI2SQ(I)
        SFA(I,4)=SFA(I,1)
        SFA(I,5)=SFA(I,2)
        SFA(I,6)=SFA(I,3)
20      CONTINUE

        WRITE(*,*) 'NOW PROCESSING???'

        M=1
C       TO CHECK: SIGMA VALUE AND INTEVAL TO BROAD CURVE !!!!
        SIG=0.14
        DELV=0.04
        E=1./(SIG*SQRT(2.*3.14159))
        EE=2.*SIG*SIG
        QIT=RIJ(M)/DELR+1.0001-8.0001
        QFT=RIJ(M)/DELR+1.0001+12.0001
        MIT=INT(QIT)
        MFT=INT(QFT)

        DO 50 L=1,NOCO
        R(L)=FLOAT(L-1)*DELR

        VV=0.0

        DO 40 K=MIT,MFT,2
        RV(K)=FLOAT(K-1)*DELR
        X(L,K)=R(L)-RV(K)
        XGAU(K,M)=RV(K)-RIJ(M)
        PP=0.0
        DO I=1,N,N-1
        PP=PP+17.0*SFA(I,M)/FESQ(I)*EXP(-ALFSQ*PKA(I)*PKA(I))
     + *COS(X(L,K)*PKA(I))/48.0
        END DO
        DO I=2,N-1,N-3
        PP=PP+17.0*SFA(I,M)/FESQ(I)*EXP(-ALFSQ*PKA(I)*PKA(I))
     + *COS(X(L,K)*PKA(I))/48.0
        END DO
        DO I=3,N-2,N-5
        PP=PP+17.0*SFA(I,M)/FESQ(I)*EXP(-ALFSQ*PKA(I)*PKA(I))
     + *COS(X(L,K)*PKA(I))/48.0
        END DO
        DO I=4,N-3,N-7
        PP=PP+17.0*SFA(I,M)/FESQ(I)*EXP(-ALFSQ*PKA(I)*PKA(I))
     + *COS(X(L,K)*PKA(I))/48.0
        END DO
        DO I=5,N-4
        PP=PP+17.0*SFA(I,M)/FESQ(I)*EXP(-ALFSQ*PKA(I)*PKA(I))
     + *COS(X(L,K)*PKA(I))/48.0
        END DO
        VV=VV+PP*EXP(-XGAU(K,M)*XGAU(K,M)/EE)
40      CONTINUE

        QF(L,M)=DELR*VV/2.0
50      CONTINUE

C       TO NORMALIZE DUE TO ADD GAUSS
        WW=0.0
```

```
      DO K=MIT,MFT,2
      WW=WW+EXP(-XGAU(K,M)*XGAU(K,M)/EE)
      END DO

      WRITE(*,*) 'NOW PROCESSING AGAING !!!'

      DO 60 L=1,NOCO

      PEAK1(L,M)=UIJ(M)/RIJ(M)*QF(L,M)/WW
60    CONTINUE

      WRITE(*,*) 'NOW PROCESSING AGAIN TWO !!!'

      DO 100 L=1,NOCO
      WRITE(8,*) R(L),TAB,YPR(L),TAB,PEAK1(L,M)
      WRITE(7,88) R(L),PEAK1(L,M)
88    FORMAT(1X,F10.4,1X,F10.4)
100   CONTINUE

      CLOSE(8)
      CLOSE(7)
      STOP
      END


C*************************************************************************C

C                       SUBROUTINE PROGRAM (INDSCA)

C     C(I, J) CROMER-WABER PARAMETERS, I=ELEMENT NO.,J=PARAMETER
C     FP(I, K) REAL HONL CORR. FOR ELEMENT I, RADIATION NO. K
C     G(K) LAST 4PI SIN THETA/LAMBDA FOR WHICH FP(I, K) AND FPP(I, K)
C     D(I) NO. OF ATOMS OF ELEMENT I IN UNIT COMP. (FLOAT. PT.)
C     ARE USED
C     FPP(I, K) IMAG. HONL CORR. FOR ELEMENT I, RADIATION NO. K
C     SUMZ SUM OF ATOMIC NOS. IN UNIT COMP.
C     NOEL NO. OF DIFFERENT ELEMENTS IN UNIT COMP.
C     NORAD NO. OF X-RADIATIONS
C*************************************************************************C

      SUBROUTINE INDSCA (C,D,FP,FPP,G,SUMZ,PKMAX,DELPK,
     + NOEL,NORAD,SUMFSQ,FESQ,FSIG,FOG,FSIOG,FSIOSQ,FO2SQ,FSI2SQ)

      DIMENSION C(5,10),B(20),G(4),SCFA(2000),FP(5,4),FPP(5,4),
     + SUMFSQ(2000),FESQ(2000),FEIMSQ(2000),D(5),
     + FSIG(2000),FOG(2000),FSIOG(2000),FE(3,2000),FSQ(3,2000),
     + FEIM(3,2000),FSIOSQ(2000),FO2SQ(2000),FSI2SQ(2000),FX(2000)

      DO 10 I=1,NOEL
         DO 15 J=1,9
            B(J)=C(I,J)
15       CONTINUE

         MO=0
         CALL SCATFA (B,PKMAX,DELPK,SCFA)

         DO 20 K=1, NORAD
            QQ=G(K)/DELPK+1.001
            NNN=INT(QQ)
            NO=1+MO
            DO 30 L=NO, NNN
                FE(I,L)=SCFA(L)+FP(I,K)
                FSQ(I,L)=FE(I,L)*FE(I,L)
                FSQ(I,L)=FSQ(I,L)+FPP(I,K)*FPP(I,K)
```

```
                  FEIM(I,L)=FPP(I,K)
30                CONTINUE
              MO=NNN
20            CONTINUE
10         CONTINUE

           Q=PKMAX/DELPK+1.001
           NN=INT(Q)
           DO 40 L=1,NN
              SUMFSQ(L)=0.
              FESQ(L)=0.
              FEIMSQ(L)=0.

              DO 50 I=1,NOEL
                   SUMFSQ(L)=SUMFSQ(L)+FSQ(I,L)*D(I)
                   FESQ(L)=FESQ(L)+FE(I,L)*D(I)
                   FEIMSQ(L)=FEIMSQ(L)+FEIM(I,L)*D(I)

50            CONTINUE

           FESQ(L)=(FESQ(L)*FESQ(L)+FEIMSQ(L)*FEIMSQ(L))/(SUMZ*SUMZ)
           FSIG(L)=FSQ(1,L)/FESQ(L)
           FOG(L)=FSQ(2,L)/FESQ(L)
           FSIOG(L)=SQRT((FE(1,L)*FE(2,L))**2.+(FEIM(1,L)
     +     *FEIM(2,L))**2.)/FESQ(L)

           FSI2SQ(L)=FSQ(1,L)
           FO2SQ(L)=FSQ(2,L)
           FSIOSQ(L)=SQRT((FE(1,L)*FE(2,L))**2.+(FEIM(1,L)
     +     *FEIM(2,L))**2.)

40         CONTINUE

           RETURN
           END

C*********************************************************************C
C
C          SUBROUTINE PROGRAM (SCATFA)
C
C*********************************************************************C

           SUBROUTINE SCATFA (B,PKMAX,DELPK,SCFA)

           DIMENSION B(20),SCFA(2000)

           Q=PKMAX/DELPK+1.001
           NN=INT(Q)

           DO 10 I=1,NN
              PK=FLOAT(I-1)*DELPK
              S=PK*PK/(4.*3.1415927)**2.
              SCFA(I)=B(9)
                   DO 5 J=1,7,2
                      SCFA(I)=SCFA(I)+B(J)*EXP(-B(J+1)*S)
5                  CONTINUE
10         CONTINUE

           RETURN
           END
```

```
C*************************************************************************C
C*
C*            PROGRAM PEAK4 + GAUSS+CONV OR MW SAMPLE
C*
C*            THEORETICAL P AND Q-FUNCTION OF VITEROUS SILICA
C*              IN CU & MO RADIATION
C*
C*                       MODIFIED BY AUGUST 1 1993
C*
C*************************************************************************C

      PROGRAM GPEAK4

      CHARACTER*8 NAME1,TAB

      DIMENSION C(5,10),FP(5,4),FPP(5,4),D(5),G(4),PKA(2000),
     +  SCFA(2000),SUMFSQ(2000),FESQ(2000),
     +  FEIMSQ(2000),FSIG(2000),FOG(2000),FSIOG(2000),
     +  RIJ(6),UIJ(6),SFA(2000,6),FSIOSQ(2000),FO2SQ(2000),
     +  FSI2SQ(2000),R(1000),QF(1000,3),
     +  X(1000,30),PEAK4(1000,3),YA(1000),YPR(1000),RV(1000),
     +  V(1000)

C     COMMON/INDSCA/ FE(3,3000),FSQ(3,3000),FEIM(3,3000)
      TAB=CHAR(9)
C     DELPK IS INTERVAL OF K VALUE, PKMAX IS MAXIMUM OF K.

      DELPK=0.01
      PKMAX=17.11
      Q=PKMAX/DELPK+1.001
      N=INT(Q)
      WRITE(*,*) 'HELLOW 1'
C     SUMZ OF SiO2 =30.0, NUMBER OF ELEMENT (2 FOR SiO2)
C     NUMBER OF RADIATION USED I.E.2 FOR Cu & Mo
      SUMZ=30.0
      NOEL=2
      NORAD=2
C     C(I,J) ARE NINE PARAMETER OF DIRAC-SLATER SCATTERING FACTOR.
C     C(1,J) IS FOR SI AND C(2,J) IS FOR O.
      C(1,1)=6.0755
      C(1,2)=2.3497
      C(1,3)=3.2815
      C(1,4)=29.1900
      C(1,5)=2.1670
      C(1,6)=0.7060
      C(1,7)=1.3197
      C(1,8)=84.8342
      C(1,9)=1.1533
      C(2,1)=2.8604
      C(2,2)=12.7907
      C(2,3)=2.5212
      C(2,4)=5.4279
      C(2,5)=1.5296
      C(2,6)=0.3282
      C(2,7)=0.8135
      C(2,8)=34.9406
      C(2,9)=0.2742
C     ANOMALOUS DISPERSION CORRECTION
C     FP(I,K): CORRECT IN REAL-PART, FPP(I,K): CORRECT IN IMAG-PART.
C     I=1 IS FOR SI & I=2 IS FOR O, K=1 IS FOR CU & K=2 IS FOR MO
      FP(1,1)=0.23
      FP(1,2)=0.09
      FP(2,1)=0.0
```

```
      FP(2,2)=0.0
      FPP(1,1)=0.36
      FPP(1,2)=0.09
      FPP(2,1)=0.1
      FPP(2,2)=0.0
C     D(I) ARE NO. OF ATOMS OF EACH ELEMENT IN UNIT CELL OF SiO2
C     D(1) IS FOR SI ATOM, D(2) IS FOR O ATOM
      D(1)=1.0
      D(2)=2.0

C     G(K) ARE HIGHEST K VALUE IN EACH RADIATION
      G(1)=7.5
      G(2)=17.11

      DO 5 IA=1,N
      PKA(IA)=FLOAT(IA-1)*DELPK
5     CONTINUE
      WRITE(*,*) 'HELLOW 2'

      CALL INDSCA(C,D,FP,FPP,G,SUMZ,PKMAX,DELPK,NOEL,NORAD,
     + SUMFSQ,FESQ,FSIG,FOG,FSIOG,FSIOSQ,FO2SQ,FSI2SQ)

      WRITE(*,*) 'PLEASE ENTER FILE NAME FOR PAIR-DAT'
      READ(*,*) NAME1

      OPEN(UNIT=6,FILE=NAME1,STATUS='OLD')
      OPEN(UNIT=7,FILE='CPK4.DA',STATUS='NEW')
      OPEN(UNIT=8,FILE='CPK4.FI',STATUS='NEW')

      RMAX=10.0
      DELR=0.02
      RRR=RMAX/DELR+1.001
      NOCO=INT(RRR)

      DO 15 J=1,NOCO
      READ(6,16) YA(J),YPR(J)
16    FORMAT(1X,F10.4,1X,F10.4)
15    CONTINUE
      CLOSE(6)

C     RIJ(1)=RSIO,R(2)=ROO,R(3)=RSISI,R(4)=RSI2DO,
C     R(5)=RO2DO,R(6)=RSI2DSI
      RIJ(1)=1.60
      RIJ(2)=2.64
      RIJ(3)=3.04
      RIJ(4)=4.16
      RIJ(5)=5.1
      RIJ(6)=5.1

C     UIJ(I) IS THE NUMBER OF NEIGHBOR ATOMS IN THE UNIT CELL
      UIJ(1)=8.8
      UIJ(2)=15.5
      UIJ(3)=5.5
      UIJ(4)=24.0
      UIJ(5)=36.0
      UIJ(6)=12.0

C     ALPHA IS TAKEN FROM A2Km2=0.025 TO GET Q-FUNCTION
      ALPHA=0.0688
      ALFSQ=ALPHA*ALPHA

      DO 20 I=1,N
      SFA(I,1)=FSIOSQ(I)
      SFA(I,2)=FO2SQ(I)
```

```
      SFA(I,3)=FSI2SQ(I)
      SFA(I,4)=SFA(I,1)
      SFA(I,5)=SFA(I,2)
      SFA(I,6)=SFA(I,3)
20    CONTINUE

      M=4

C     TO CHECK: GAUSS VALUE
      DO I=1,149
      V(I)=0.0
      END DO
      V(150)=0.01
      V(151)=0.01
      V(152)=0.01
      V(153)=0.01
      V(154)=0.02
      V(155)=0.02
      V(156)=0.07
      V(157)=0.07
      V(158)=0.07
      V(159)=0.04
      V(160)=0.04
      V(161)=0.15
      V(162)=0.15
      V(163)=0.15
      V(164)=0.11
      V(165)=0.11
      V(166)=0.2
      V(167)=0.2
      V(168)=0.2
      V(169)=0.16
      V(170)=0.16
      V(171)=0.25
      V(172)=0.25
      V(173)=0.25
      V(174)=0.28
      V(175)=0.28
      V(176)=0.36
      V(177)=0.36
      V(178)=0.36
      V(179)=0.29
      V(180)=0.29
      V(181)=0.36
      V(182)=0.36
      V(183)=0.36
      V(184)=0.36
      V(185)=0.36
      V(186)=0.41
      V(187)=0.41
      V(188)=0.41
      V(189)=0.35
      V(190)=0.35
      V(191)=0.46
      V(192)=0.46
      V(193)=0.46
      V(194)=0.44
      V(195)=0.44
      V(196)=0.41
      V(197)=0.41
      V(198)=0.41
      V(199)=0.48
      V(200)=0.48
      V(201)=0.55
```

```
      V(202)=0.55
      V(203)=0.55
      V(204)=0.47
      V(205)=0.47
      V(206)=0.62
      V(207)=0.62
      V(208)=0.62
      V(209)=0.78
      V(210)=0.78
      V(211)=1.0
      V(212)=1.0
      V(213)=1.0
      V(214)=0.55
      V(215)=0.55
      V(216)=0.0

      DO I=217,501
      V(I)=0.0
      END DO

C     TO CHECK INTERVAL TO BROAD CURVE(3.04-4.28)
C     4 POINTS INTERVAL
      QIT=RIJ(M)/DELR+1.0001-56.0
      QFT=RIJ(M)/DELR+1.0001+4.0
      MIT=INT(QIT)
      MFT=INT(QFT)

      DO 50 L=1,NOCO
      R(L)=FLOAT(L-1)*DELR

      VV=0.0

      DO 40 K=MIT,MFT,4
      RV(K)=FLOAT(K-1)*DELR
      X(L,K)=R(L)-RV(K)
      PP=0.0
      DO I=1,N,N-1
      PP=PP+17.0*SFA(I,M)/FESQ(I)*EXP(-ALFSQ*PKA(I)*PKA(I))
     + *COS(X(L,K)*PKA(I))/48.0
      END DO
      DO I=2,N-1,N-3
      PP=PP+17.0*SFA(I,M)/FESQ(I)*EXP(-ALFSQ*PKA(I)*PKA(I))
     + *COS(X(L,K)*PKA(I))/48.0
      END DO
      DO I=3,N-2,N-5
      PP=PP+17.0*SFA(I,M)/FESQ(I)*EXP(-ALFSQ*PKA(I)*PKA(I))
     + *COS(X(L,K)*PKA(I))/48.0
      END DO
      DO I=4,N-3,N-7
      PP=PP+17.0*SFA(I,M)/FESQ(I)*EXP(-ALFSQ*PKA(I)*PKA(I))
     + *COS(X(L,K)*PKA(I))/48.0
      END DO
      DO I=5,N-4
      PP=PP+17.0*SFA(I,M)/FESQ(I)*EXP(-ALFSQ*PKA(I)*PKA(I))
     + *COS(X(L,K)*PKA(I))/48.0
      END DO
      VV=VV+PP*V(K)
40    CONTINUE

      QF(L,M)=DELR*VV/2.0
50    CONTINUE

      WW=0.0
      DO K=MIT,MFT,4
```

```
      WW=WW+V(K)
      END DO

      DO 60 L=1,NOCO
C     PLEASE CHECK DIVIDEND?????
      PEAK4(L,M)=UIJ(M)/RIJ(M)*QF(L,M)/WW
60    CONTINUE

      DO 100 L=1,NOCO
      WRITE(8,*) R(L),TAB,YPR(L),TAB,PEAK4(L,M)
      WRITE(7,88) R(L),PEAK4(L,M)
88    FORMAT(1X,F10.4,1X,F10.4)
100   CONTINUE

      CLOSE(8)
      CLOSE(7)
      STOP
      END

C*************************************************************************C

C                     SUBROUTINE PROGRAM (INDSCA)

C     C(I, J) CROMER-WABER PARAMETERS, I=ELEMENT NO.,J=PARAMETER
C     FP(I, K) REAL HONL CORR. FOR ELEMENT I, RADIATION NO. K
C     G(K) LAST 4PI SIN THETA/LAMBDA FOR WHICH FP(I, K) AND FPP(I, K)
C     D(I) NO. OF ATOMS OF ELEMENT I IN UNIT COMP. (FLOAT. PT.)
C     ARE USED
C     FPP(I, K) IMAG. HONL CORR. FOR ELEMENT I, RADIATION NO. K
C     SUMZ SUM OF ATOMIC NOS. IN UNIT COMP.
C     NOEL NO. OF DIFFERENT ELEMENTS IN UNIT COMP.
C     NORAD NO. OF X-RADIATIONS
C*************************************************************************C

      SUBROUTINE INDSCA (C,D,FP,FPP,G,SUMZ,PKMAX,DELPK,
     + NOEL,NORAD,SUMFSQ,FESQ,FSIG,FOG,FSIOG,FSIOSQ,FO2SQ,FSI2SQ)

      DIMENSION C(5,10),B(20),G(4),SCFA(2000),FP(5,4),FPP(5,4),
     + SUMFSQ(2000),FESQ(2000),FEIMSQ(2000),D(5),
     + FSIG(2000),FOG(2000),FSIOG(2000),FE(3,2000),FSQ(3,2000),
     + FEIM(3,2000),FSIOSQ(2000),FO2SQ(2000),FSI2SQ(2000),FX(2000)

      DO 10 I=1,NOEL
         DO 15 J=1,9
            B(J)=C(I,J)
15       CONTINUE

         MO=0
         CALL SCATFA (B,PKMAX,DELPK,SCFA)

         DO 20 K=1, NORAD
            QQ=G(K)/DELPK+1.001
            NNN=INT(QQ)
            NO=1+MO
            DO 30 L=NO, NNN
               FE(I,L)=SCFA(L)+FP(I,K)
               FSQ(I,L)=FE(I,L)*FE(I,L)
               FSQ(I,L)=FSQ(I,L)+FPP(I,K)*FPP(I,K)
               FEIM(I,L)=FPP(I,K)
30          CONTINUE
         MO=NNN
20       CONTINUE
10    CONTINUE
```

```
      Q=PKMAX/DELPK+1.001
      NN=INT(Q)
      DO 40 L=1,NN
         SUMFSQ(L)=0.
         FESQ(L)=0.
         FEIMSQ(L)=0.

         DO 50 I=1,NOEL
              SUMFSQ(L)=SUMFSQ(L)+FSQ(I,L)*D(I)
              FESQ(L)=FESQ(L)+FE(I,L)*D(I)
              FEIMSQ(L)=FEIMSQ(L)+FEIM(I,L)*D(I)

50       CONTINUE

      FESQ(L)=(FESQ(L)*FESQ(L)+FEIMSQ(L)*FEIMSQ(L))/(SUMZ*SUMZ)
      FSIG(L)=FSQ(1,L)/FESQ(L)
      FOG(L)=FSQ(2,L)/FESQ(L)
      FSIOG(L)=SQRT((FE(1,L)*FE(2,L))**2.+(FEIM(1,L)
     +*FEIM(2,L))**2.)/FESQ(L)

      FSI2SQ(L)=FSQ(1,L)
      FO2SQ(L)=FSQ(2,L)
      FSIOSQ(L)=SQRT((FE(1,L)*FE(2,L))**2.+(FEIM(1,L)
     +*FEIM(2,L))**2.)

40    CONTINUE
      RETURN
      END

C*********************************************************************C
C
C     SUBROUTINE PROGRAM (SCATFA)
C
C*********************************************************************C

      SUBROUTINE SCATFA (B,PKMAX,DELPK,SCFA)

      DIMENSION B(20),SCFA(2000)
      Q=PKMAX/DELPK+1.001
      NN=INT(Q)

      DO 10 I=1,NN
         PK=FLOAT(I-1)*DELPK
         S=PK*PK/(4.*3.1415927)**2.
         SCFA(I)=B(9)
              DO 5 J=1,7,2
                 SCFA(I)=SCFA(I)+B(J)*EXP(-B(J+1)*S)
5             CONTINUE
10    CONTINUE
      RETURN
      END
```

```
C*************************************************************************C
C*
C*            PROGRAM PEAK4 + GAUSS+CONV OR MW SAMPLE
C*
C*            TO COLLECT DISTANCE DISTRIBUTION FOR PEAK4
C*              IN CU & MO RADIATION
C*
C*                       MODIFIED BY AUGUST 1, 1993
C*
C*************************************************************************C

      PROGRAM GPEAK4M

      CHARACTER*8 TAB
      DIMENSION TA(50),ALFA(50),BETA(50),DIS(50,50),
     +  W(50),R(50),V(50)

      REAL*8 VALMAX,VALMIN,VALINT,IDEG(50)
      INTEGER MINDEG,INTDEG,NUMDEG
      PARAMETER(NUMDEG=13)
      DATA (W(I),I=1,13)/0.28,0.62,0.89,0.99,0.96,0.82,0.67,
     +  0.51,0.33,0.24,0.16,0.08,0.0/
      TAB=CHAR(9)


      OPEN(UNIT=6,FILE='VK4M.DAT',STATUS='NEW')

      ANMAX=180.
      DELAN=5.
      Q=ANMAX/DELAN+1.001
      N=INT(Q)

      ALMIN=120.
      QQ=ALMIN/DELAN+1.001
      NN=INT(QQ)

      DO I=1,N
      TA(I)=DELAN*FLOAT(I-1)
      ALFA(I)=TA(I)*3.1415927/180.
      BETA(I)=TA(I)*3.1415927/180.
      END DO

      VALMAX=4.30
      VALMIN=2.95
      VALINT=0.05
      MINDEG=120
      INTDEG=5

      DO I=1,NUMDEG
      IDEG(I)=120+(I-1)*5
      END DO

      NRANGE=INT((VALMAX-VALMIN)/VALINT)
      DO I=1,NRANGE
      R(I)=VALMIN+VALINT*(I-1)
      V(I)=0.0
      END DO

      DO 20 J=1,N
      DO 10 I=NN,N
      DIS(I,J)=SQRT(9.65-7.00*COS(ALFA(I))-4.96
     +  *SIN(ALFA(I))*COS(BETA(J)))
      KK=INT((DIS(I,J)-VALMIN)/VALINT+1.0001)
      K=I-NN+1
```

```
          V(KK)=V(KK)+W(K)
10        CONTINUE
20        CONTINUE

          DO KKK=1,NRANGE
          WRITE(6,100) R(KKK),V(KKK)
100       FORMAT(1X,F10.4,1X,F10.4)
          END DO

          CLOSE(6)

          STOP
          END
```

Appendix VI.

Raw Intensity Curves

The raw intensity curves of CuK_α and MoK_α radiation in the conventionally melted silica sand are shown in Figure A5 and A6. The raw intensity curves of CuK_α and MoK_α radiation in the microwave melted silica sand are shown in Figure A7 and A8. Also, the raw intensity curves of CuK_α and MoK_α radiation in the conventionally melted pure fused silica are shown in Figure A9, A10, A11, A12, A17, A18, A19, A20, A21, and A22. The raw intensity curves of CuK_α and MoK_α radiation in the microwave melted pure fused silica are shown in Figure A13, A14, A15, A16, A23, A24, A25, A26, A27, and A28.

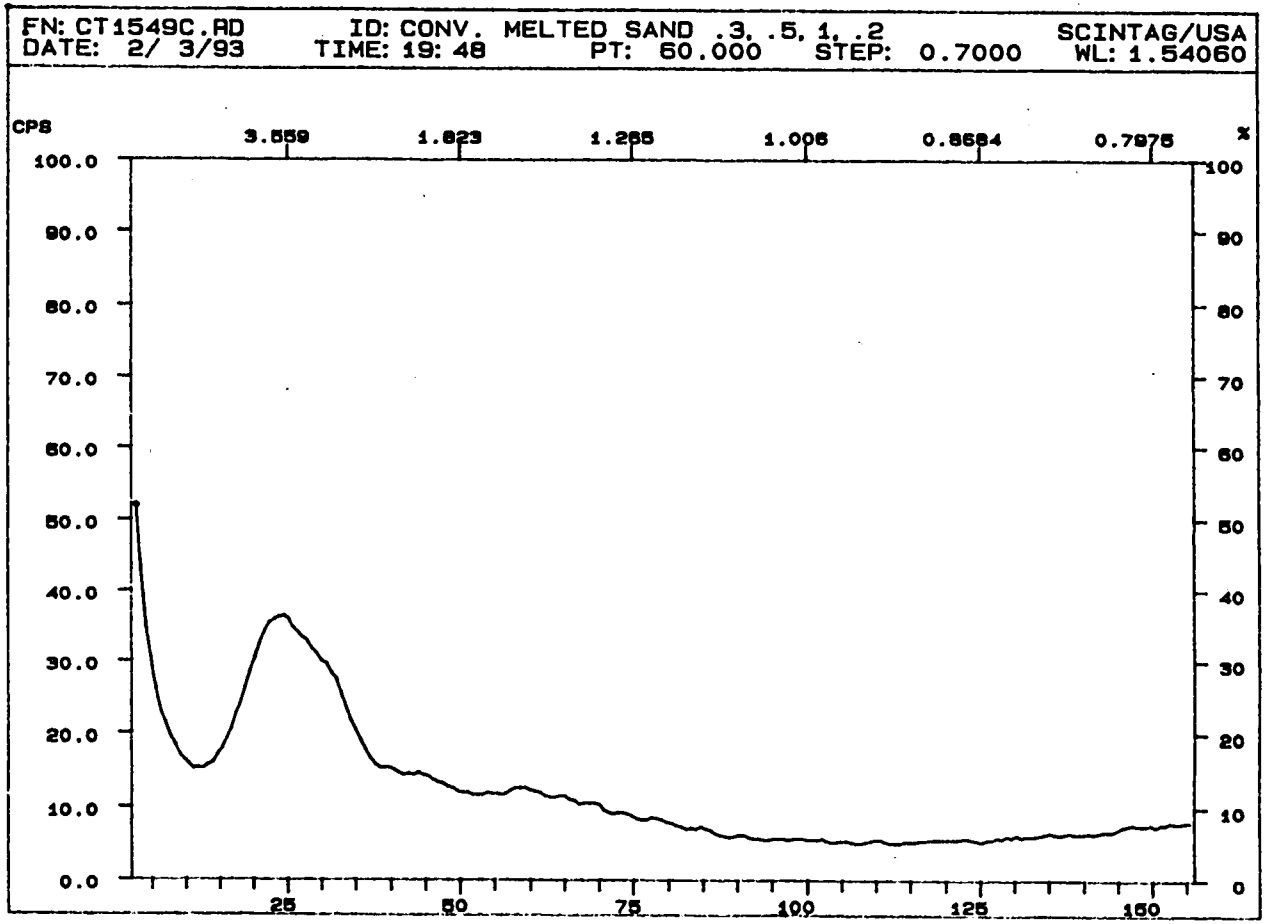

Figure A5. Run using CuK_α radiation in the conventionally melted silica sand.

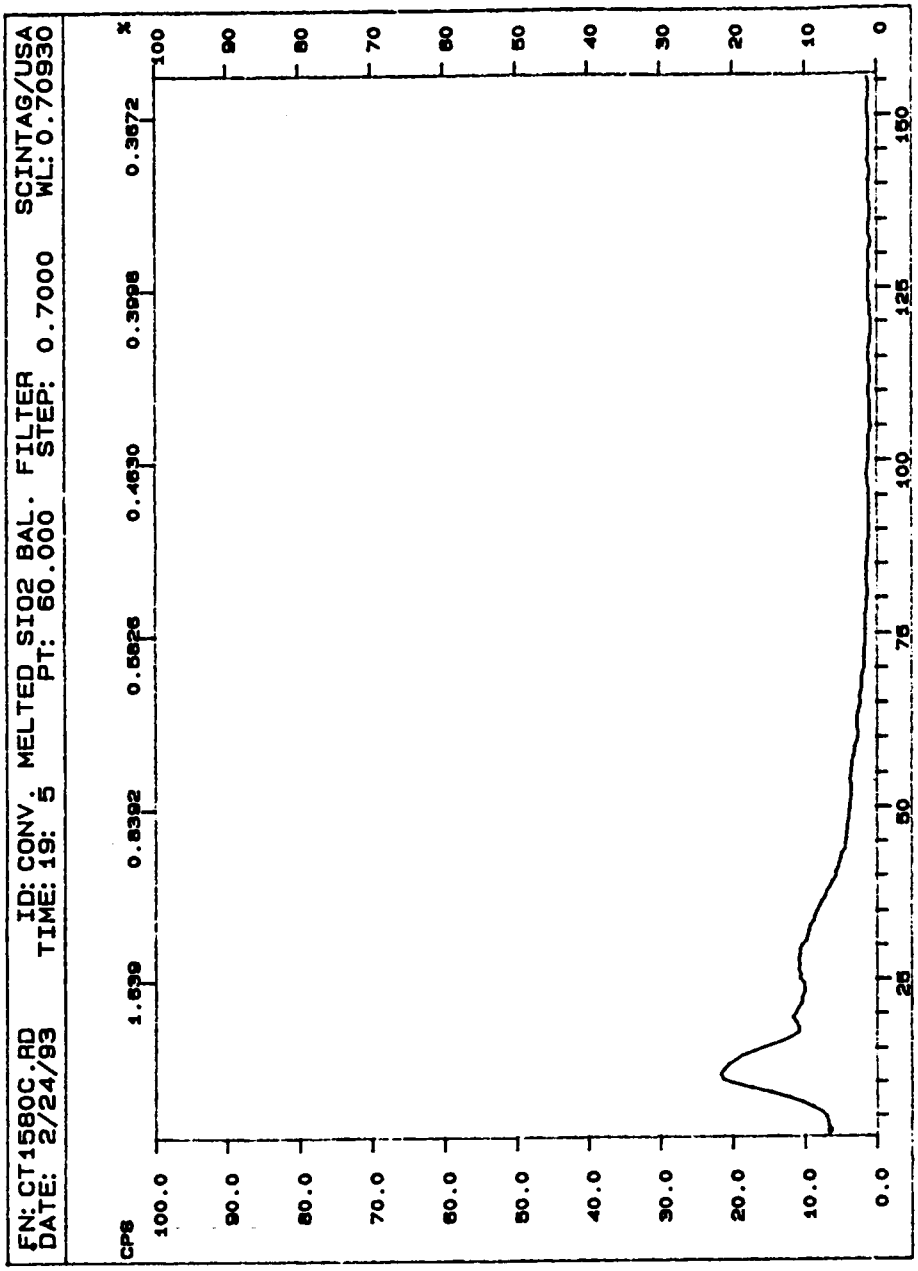

Figure A6. Run using MoK_{α} radiation in the conventionally melted silica sand.

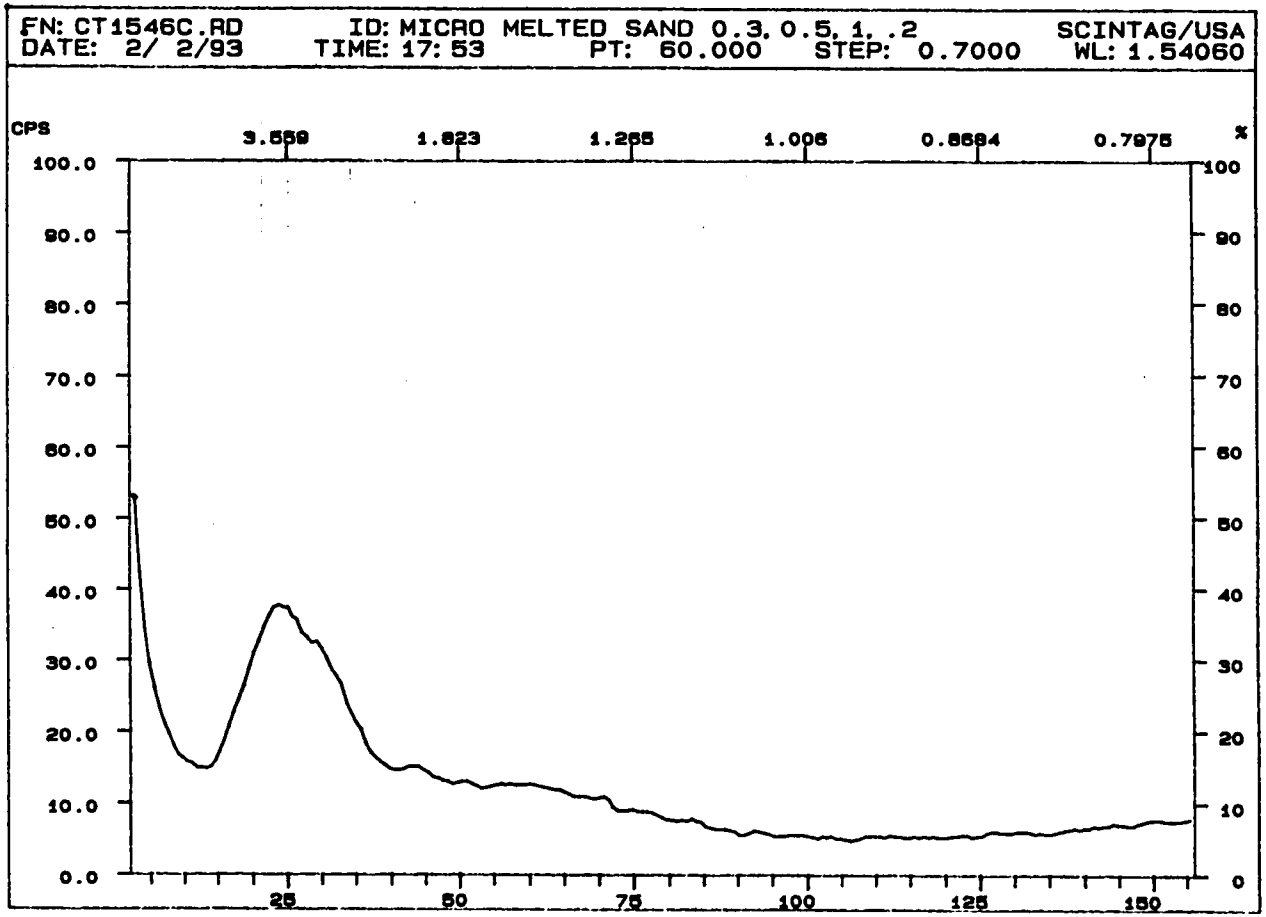

Figure A7. Run using CuK_α radiation in the microwave melted silica sand.

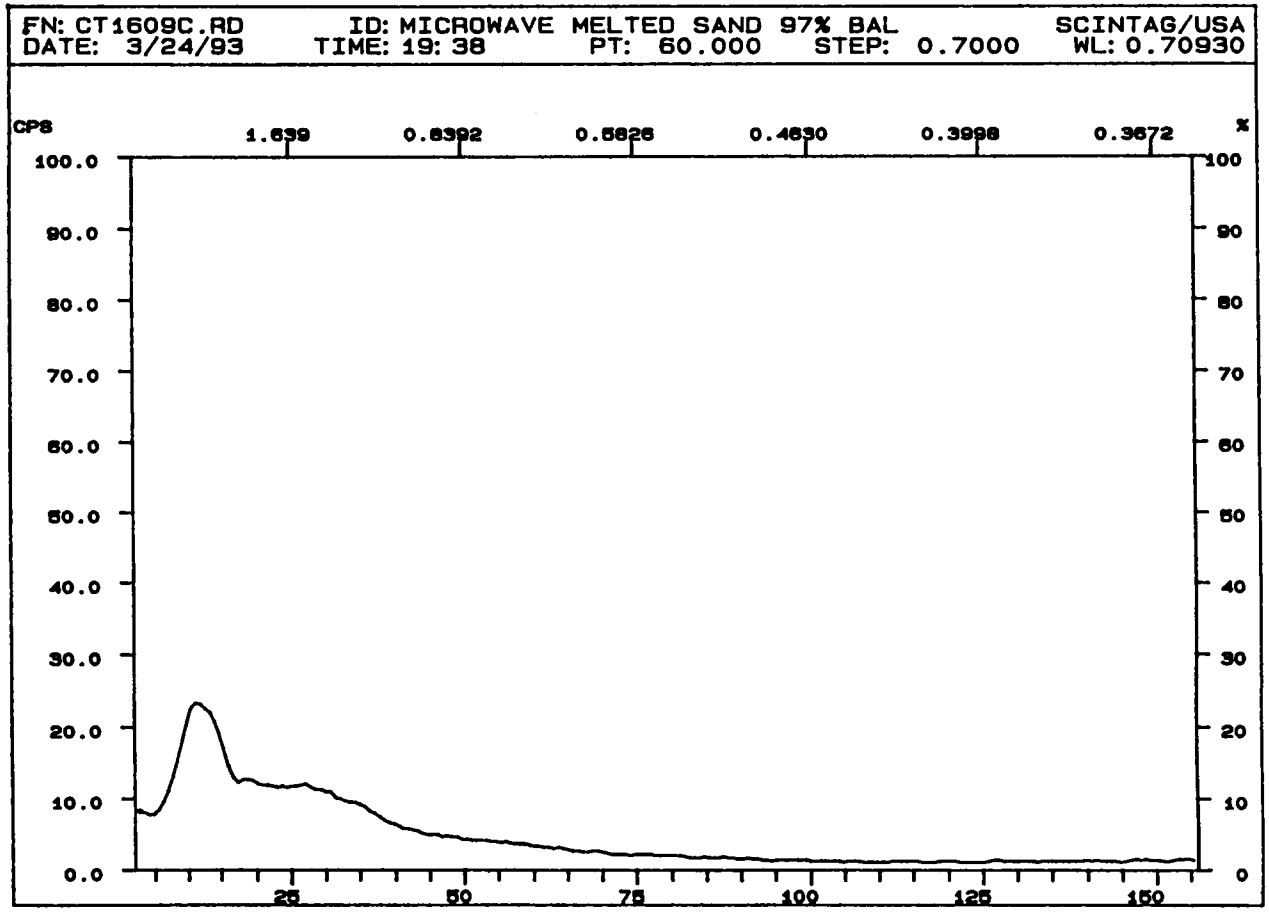

Figure A8. Run using MoK_α radiation in the microwave melted silica sand.

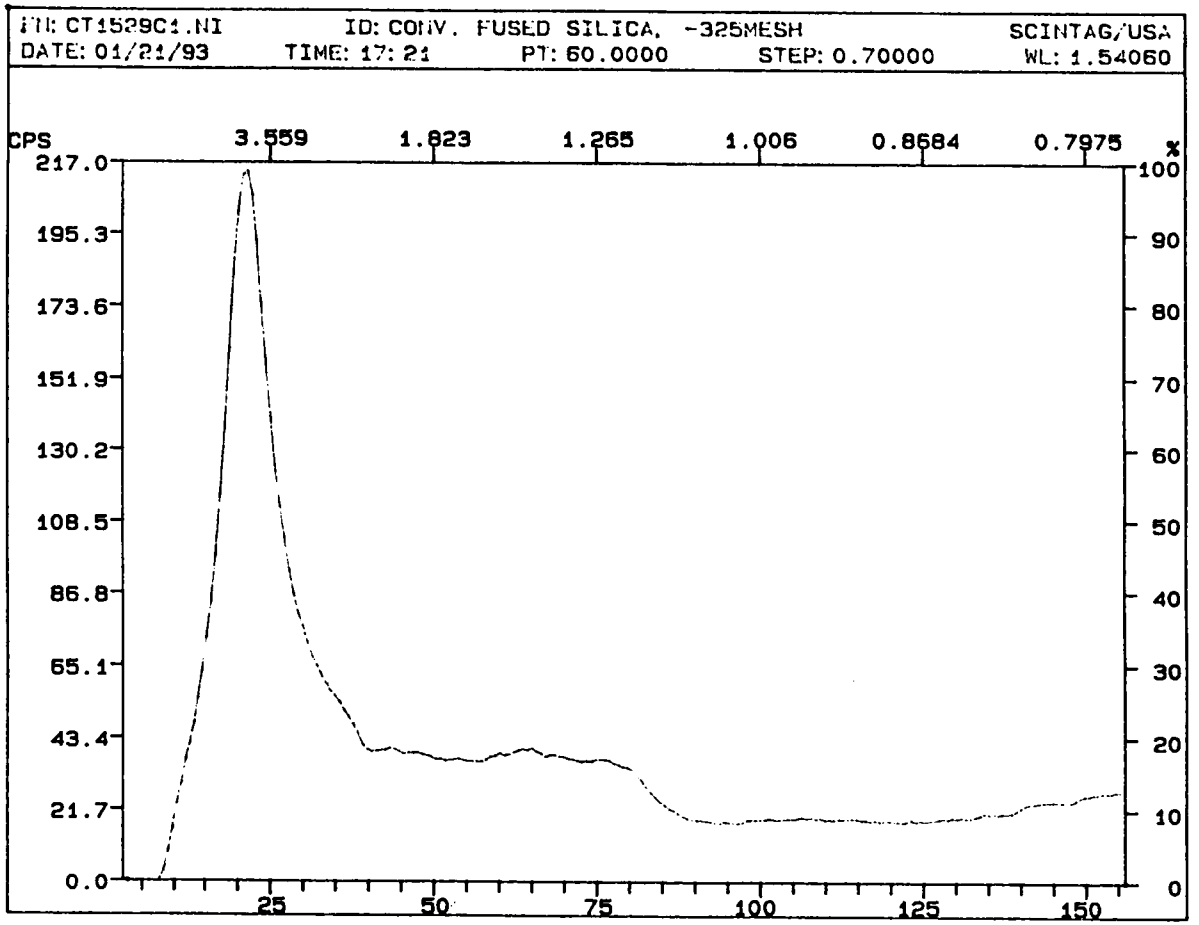

Figure A9. Run using CuK_α radiation in the conventionally melted pure fused silica.

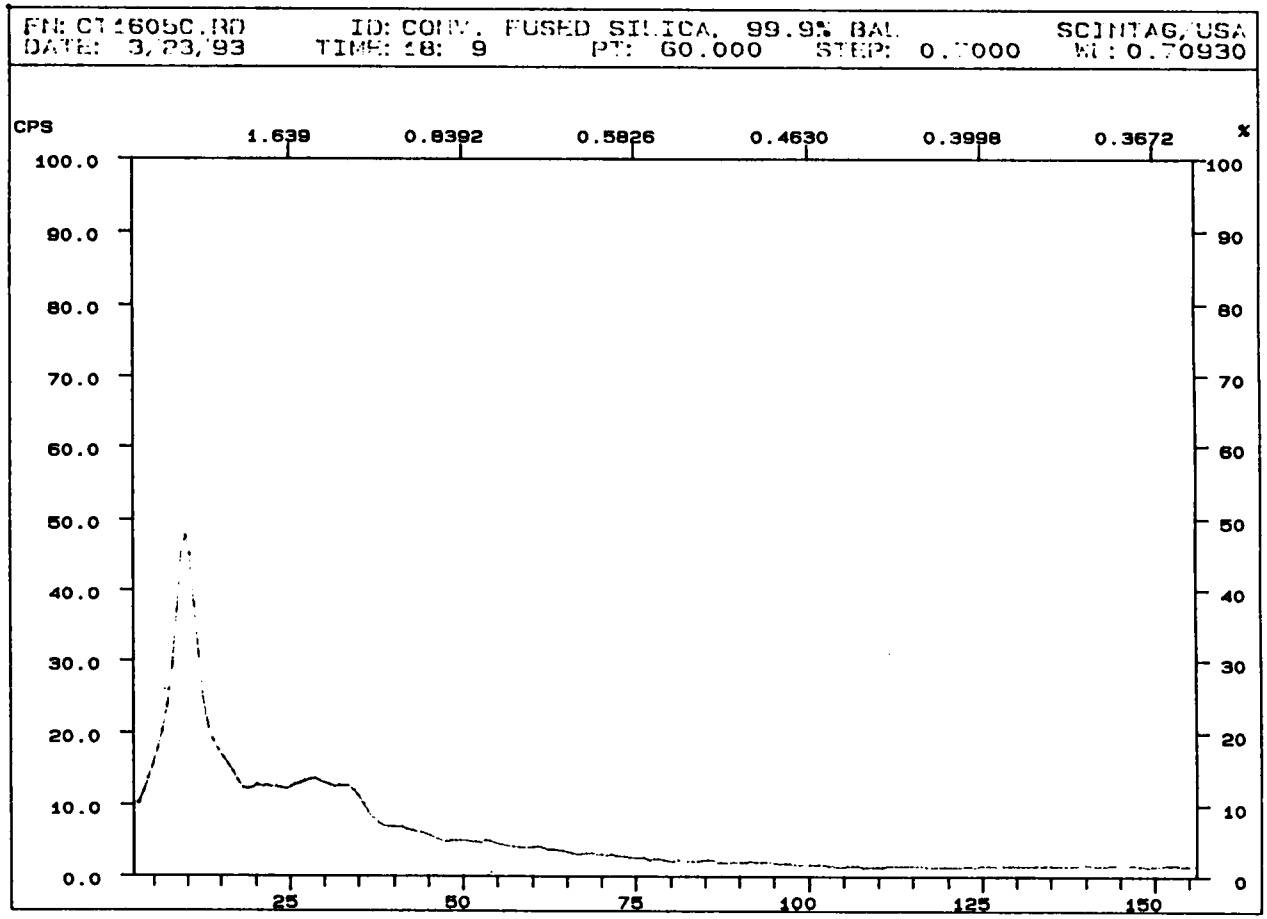

Figure A10. Run #1 using MoK_α radiation in the conventionally melted pure fused silica.

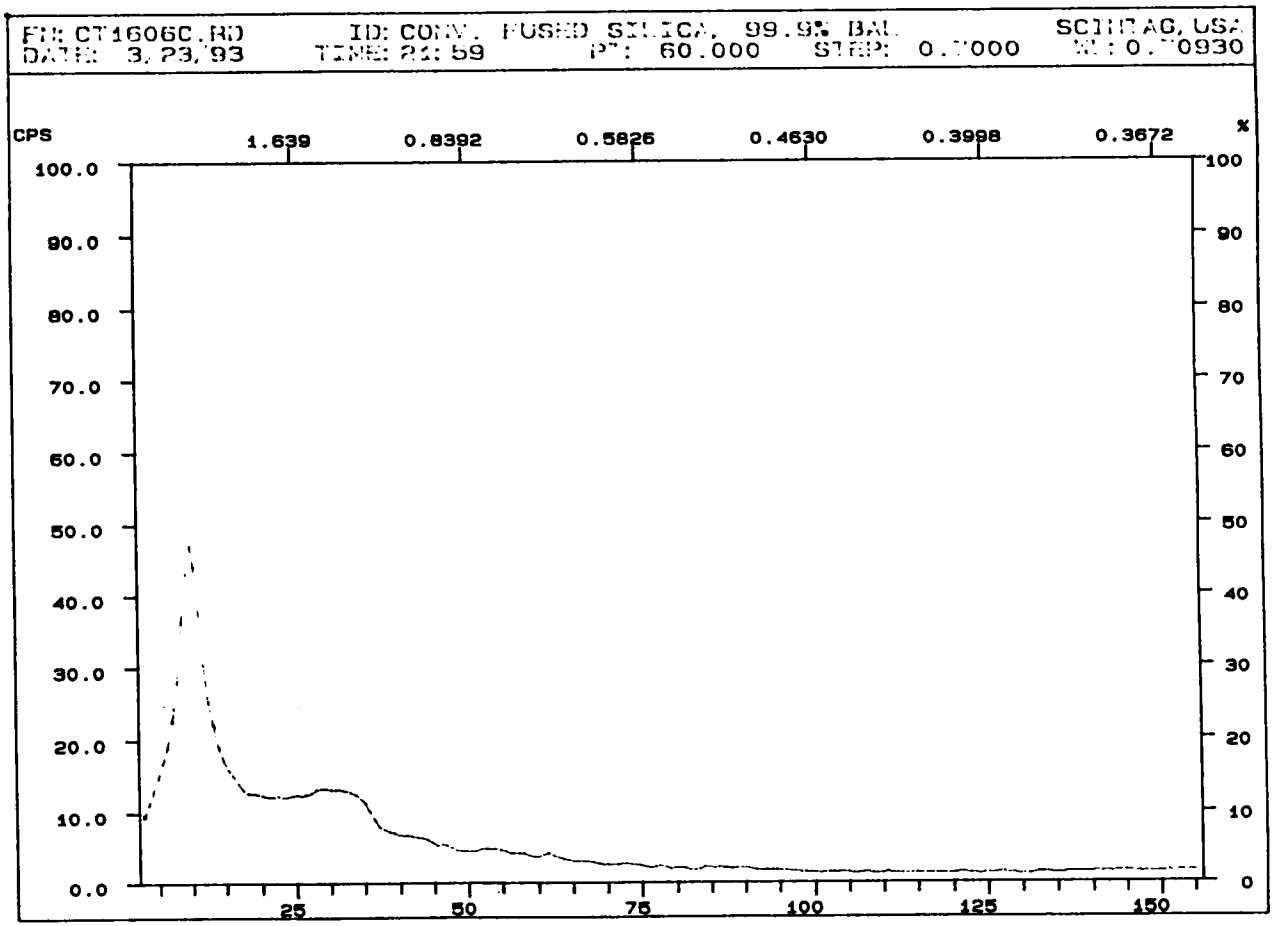

Figure A11. Run #2 using MoK$_\alpha$ radiation in the conventionally melted pure fused silica.

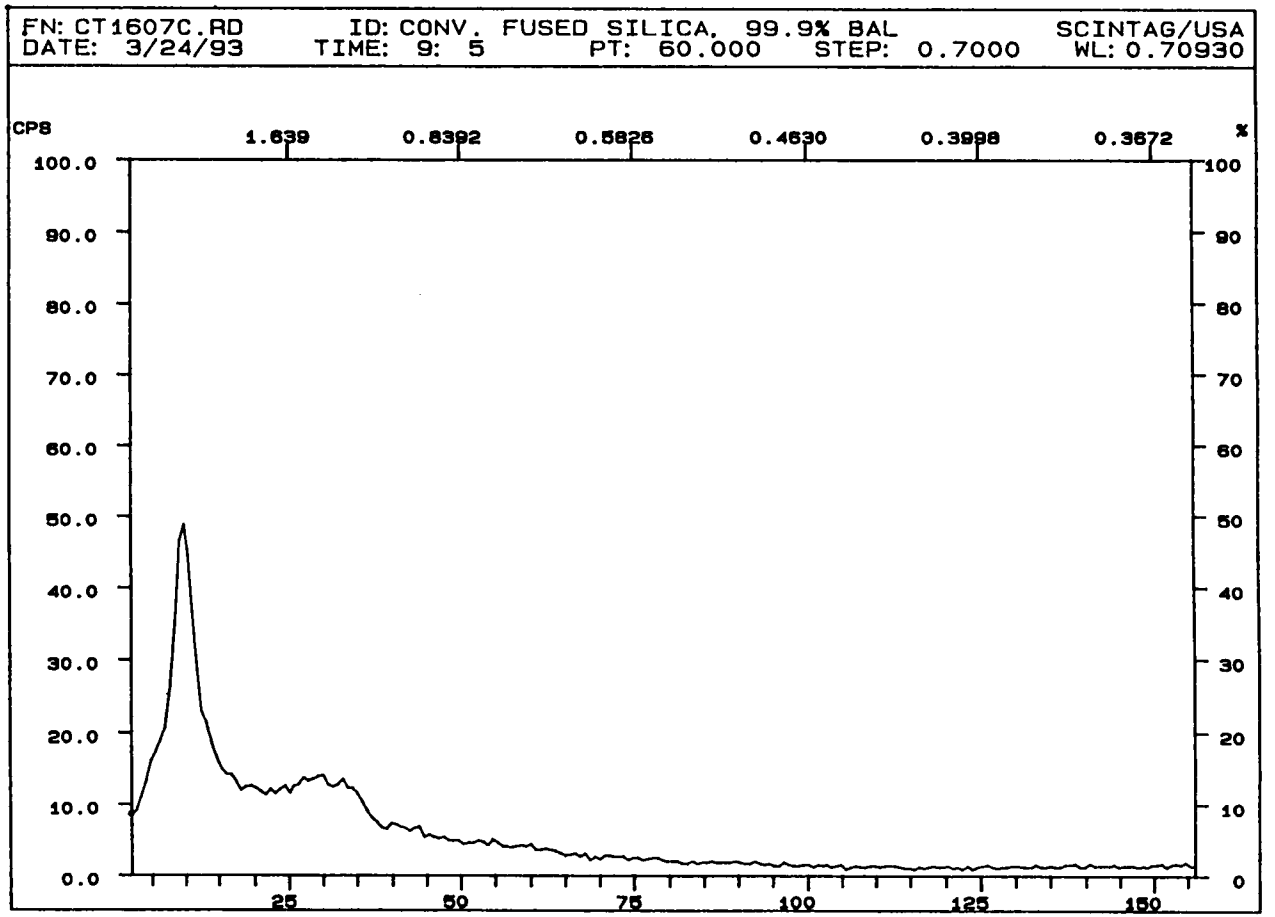

Figure A12. Run #3 using MoK_α radiation in the conventionally melted pure fused silica.

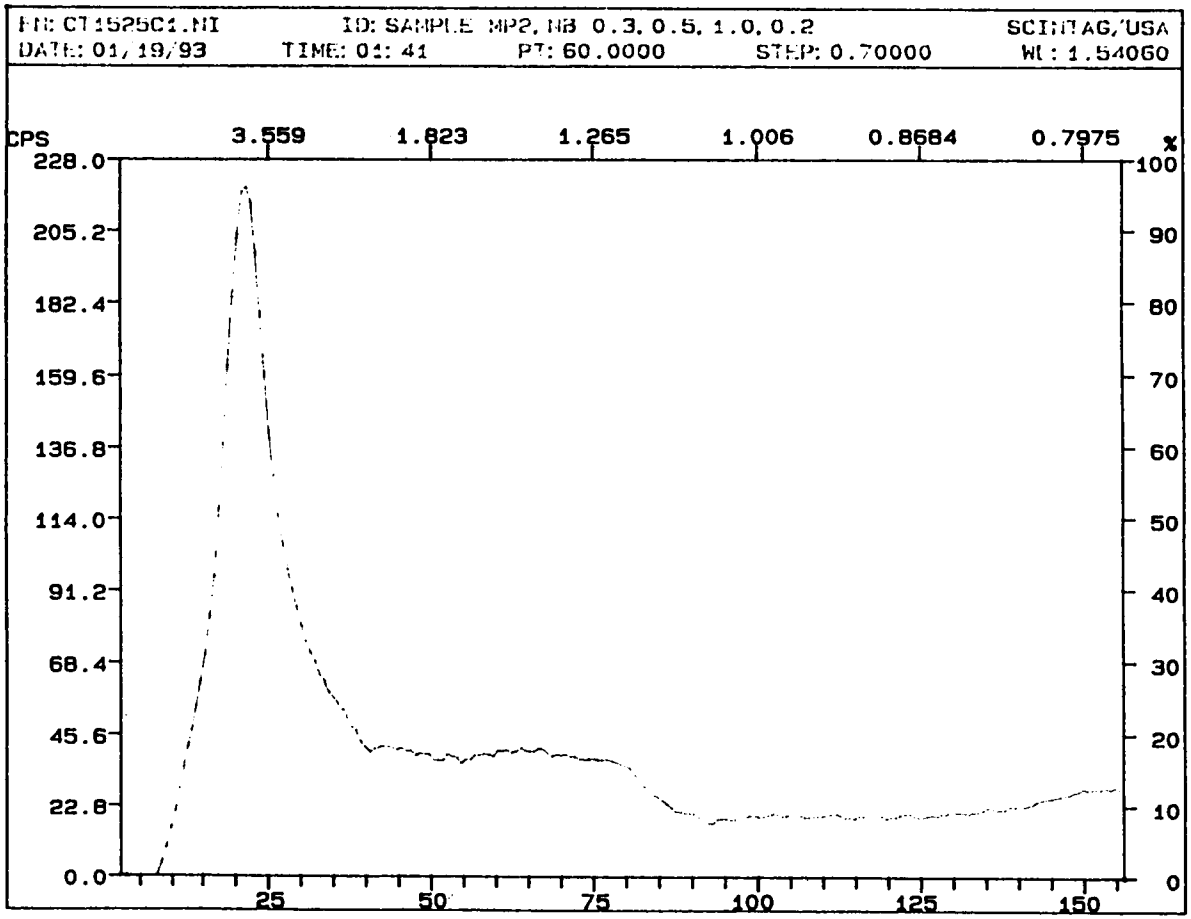

Figure A13. Run using CuK_{α} radiation in the microwave melted pure fused silica.

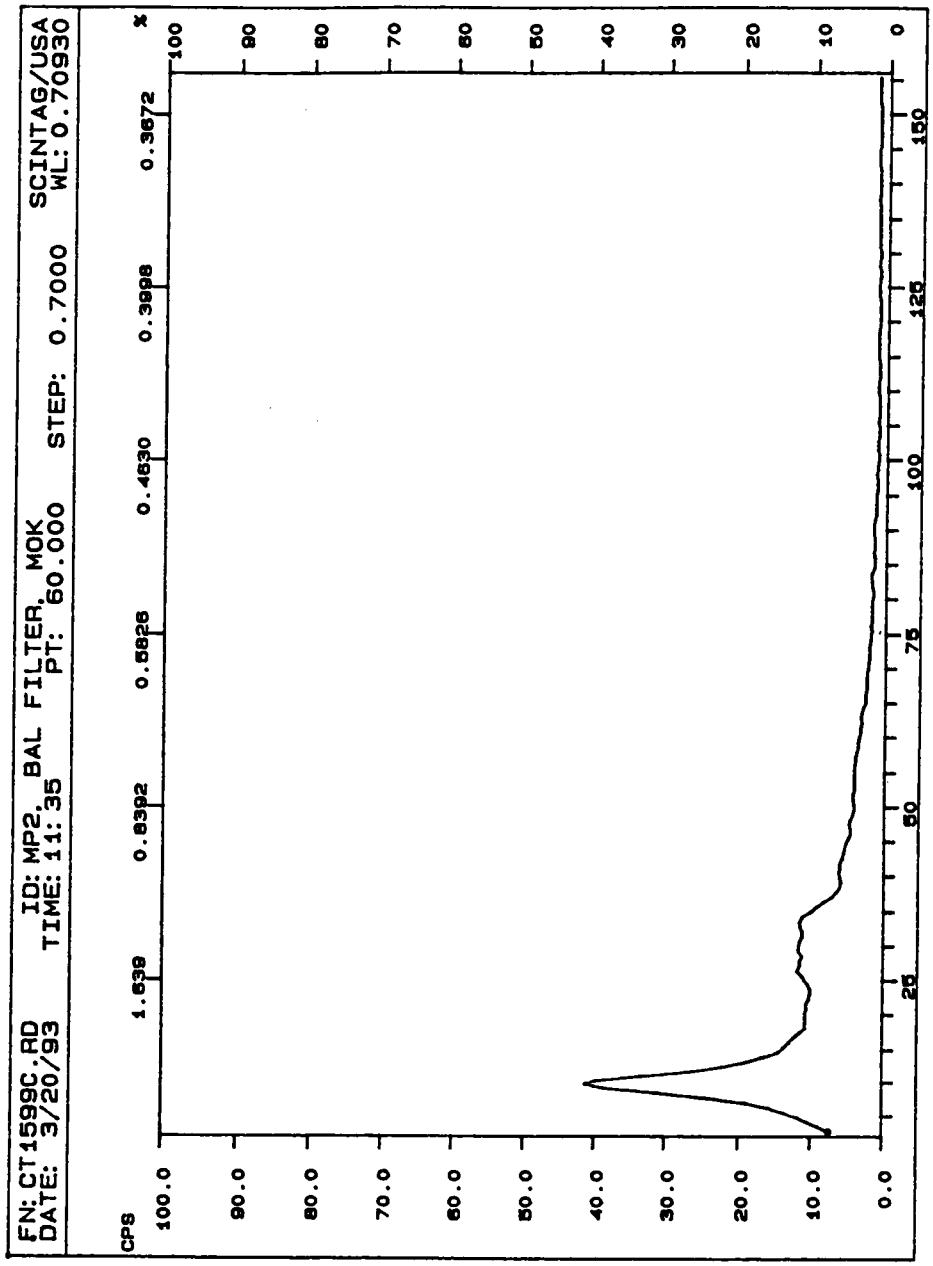

Figure A14. Run #1 using MoK_{α} radiation in the microwave melted pure fused silica.

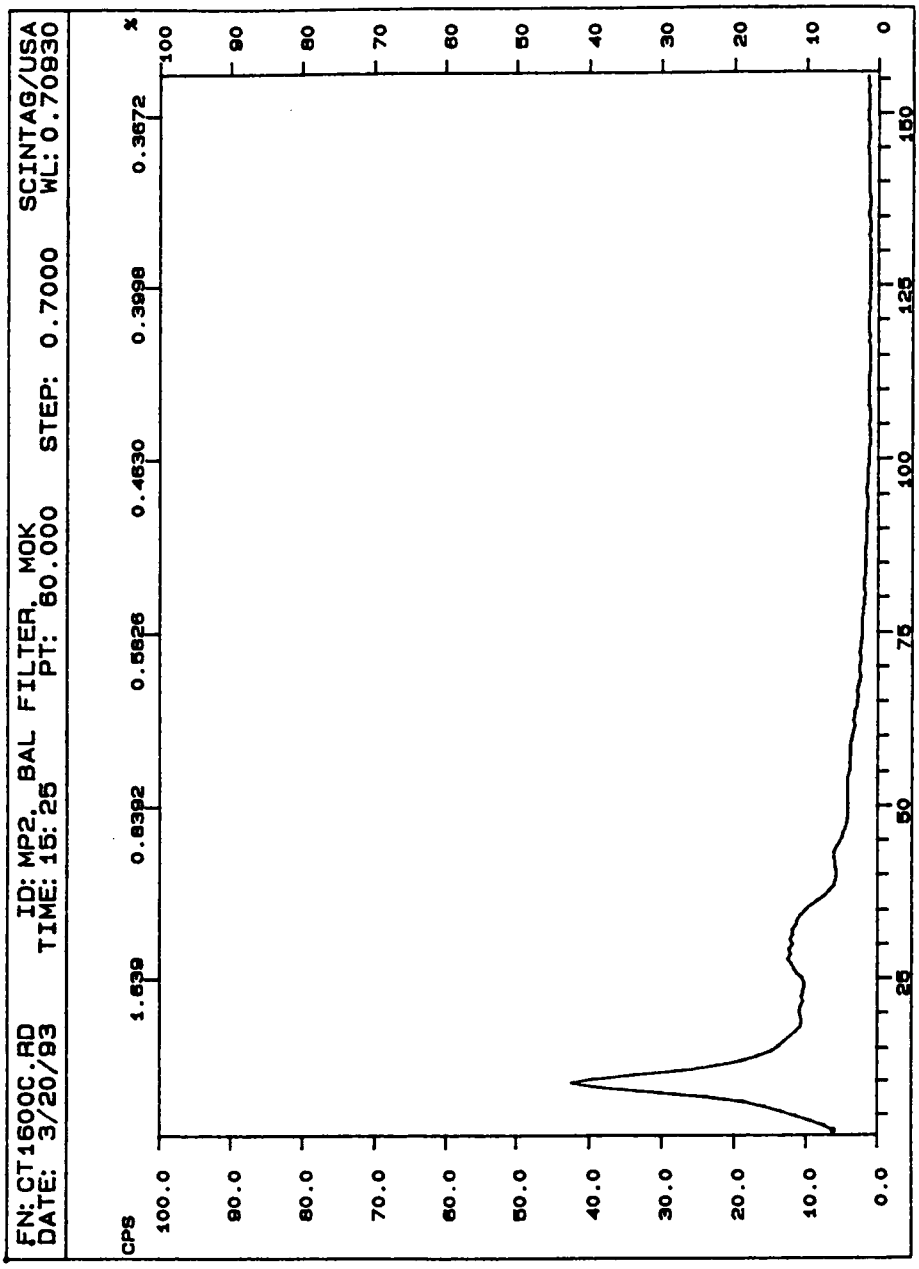

Figure A15. Run #2 using MoK_{α} radiation in the microwave melted pure fused silica.

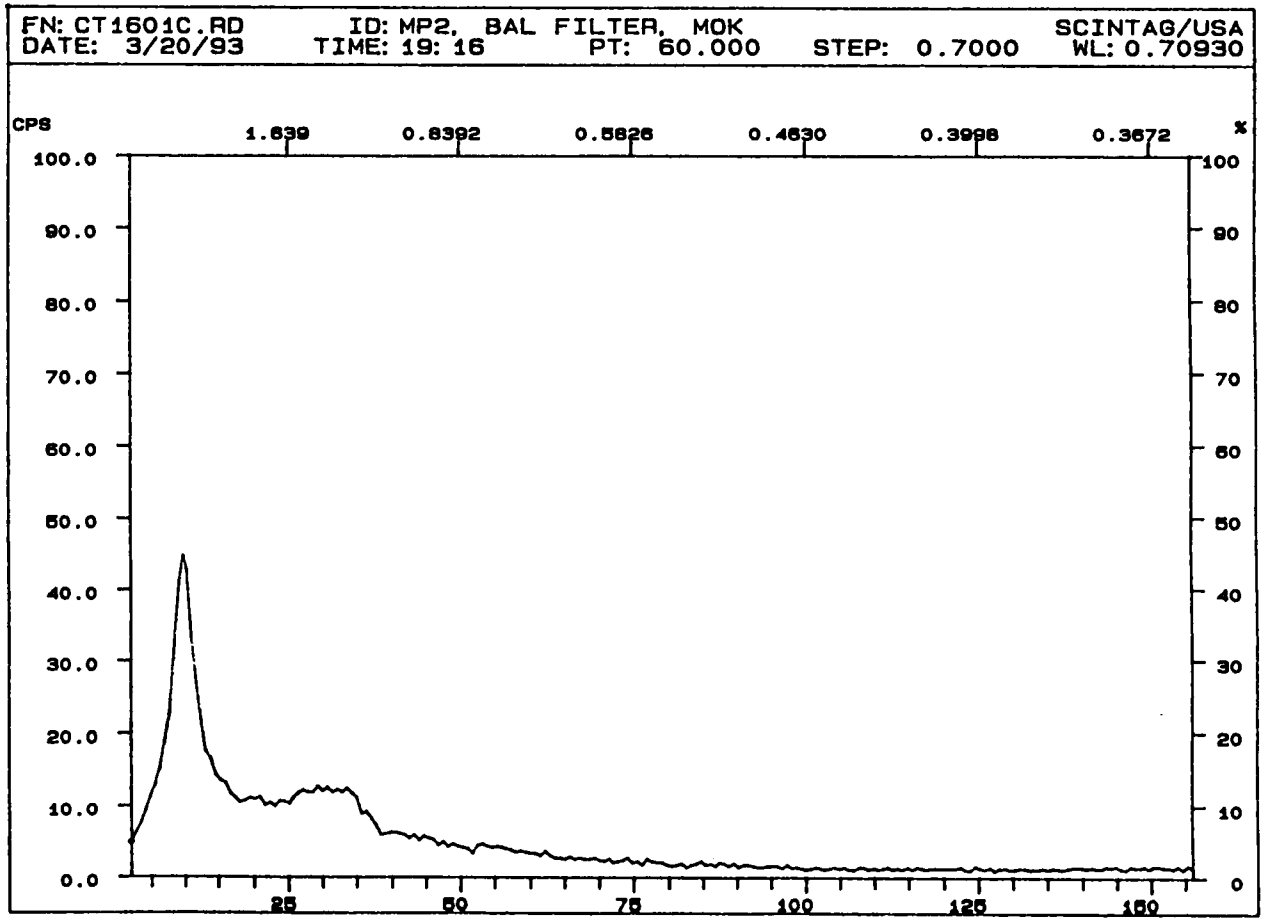

Figure A16. Run #3 using MoK$_\alpha$ radiation in the microwave melted pure fused silica.

Figure A17. Run using CuKα in the conventional sample #1.

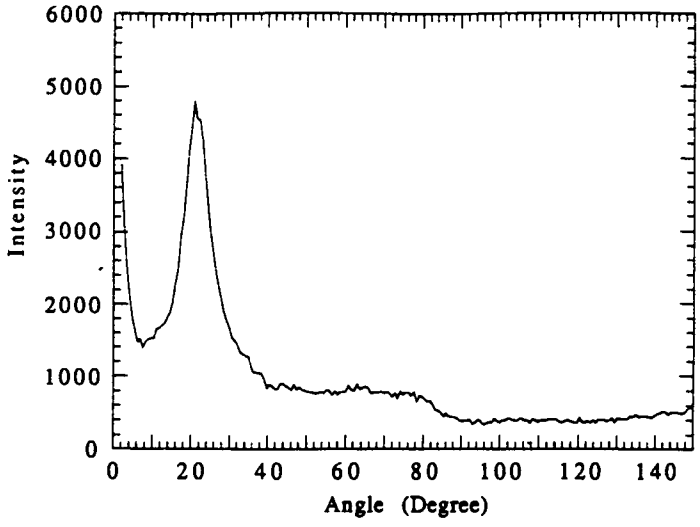

Figure A18. Run using CuKα in the conventional sample #2.

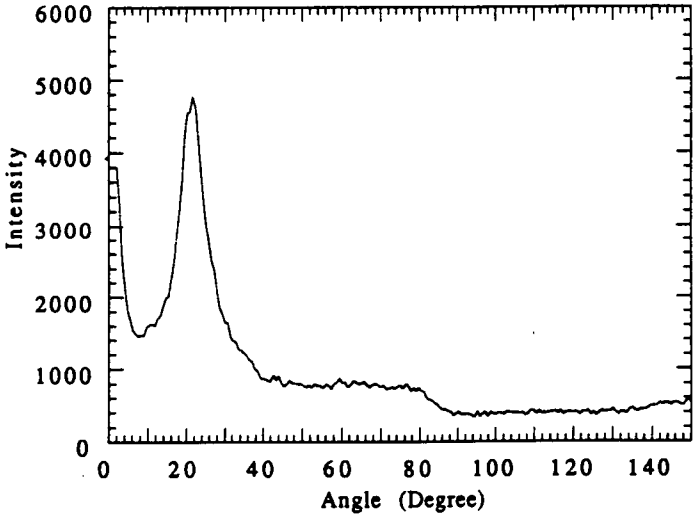

Figure A19. Run using CuKα in the conventional sample #3.

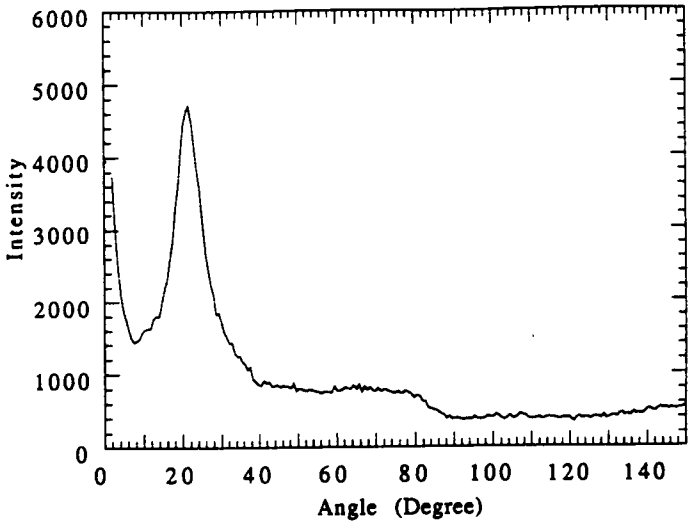

Figure A20. Run using MoKα in the conventional sample #1.

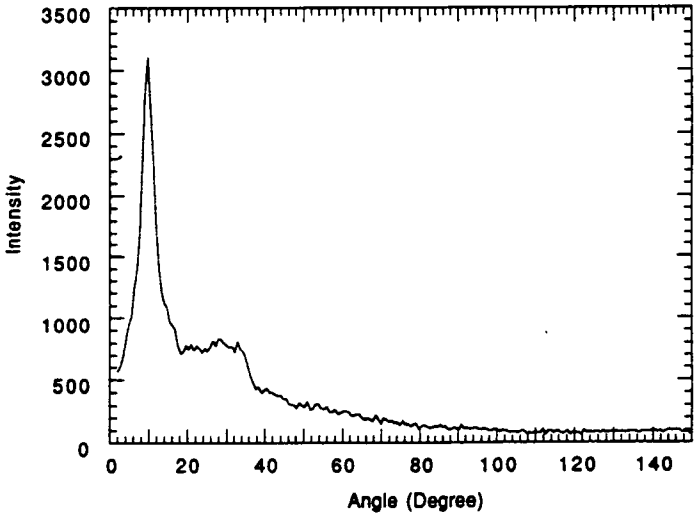

Figure A21. Run using MoKα in the conventional sample #2.

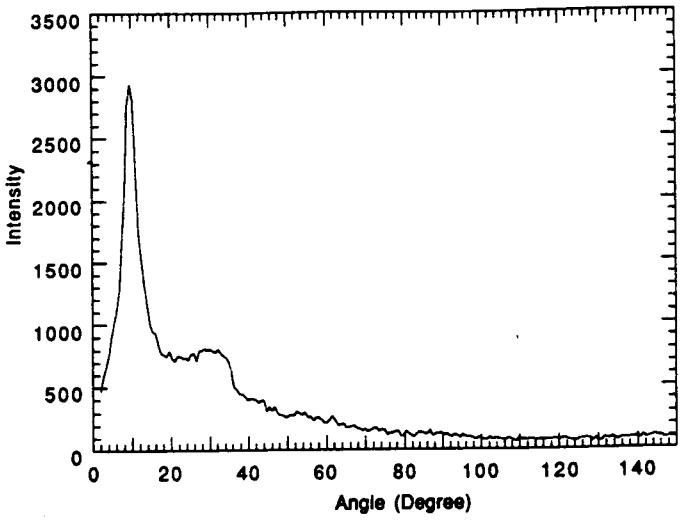

Figure 22. Run using MoKα in the conventional sample #3.

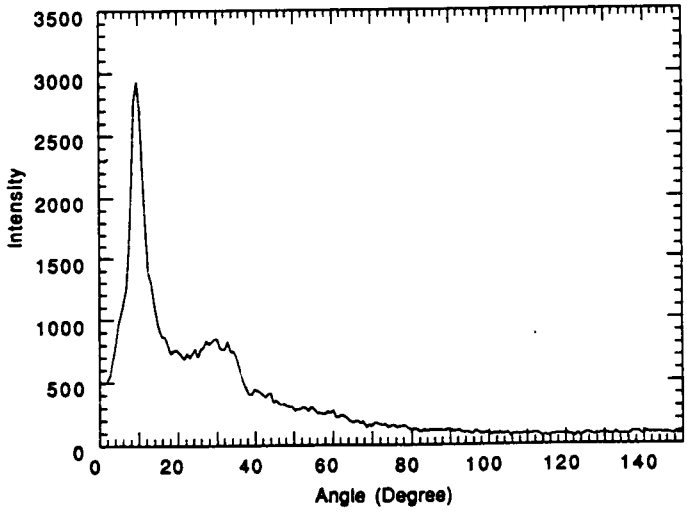

Figure A23. Run using CuKα in the microwave sample #1.

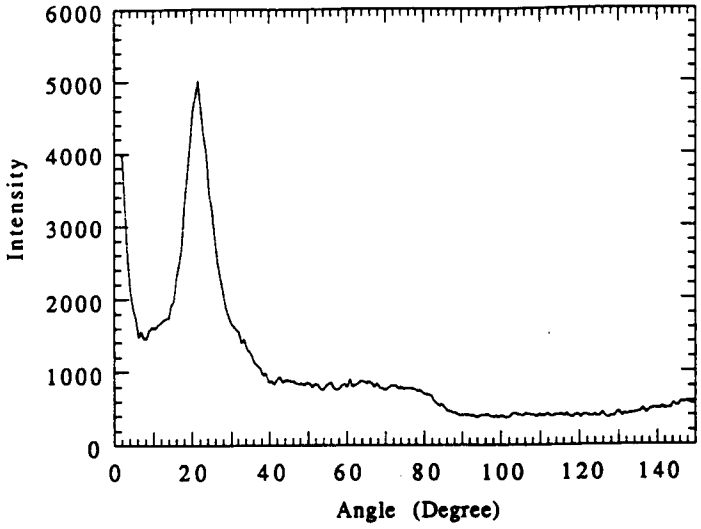

Figure A24. Run using CuKα in the microwave sample #2.

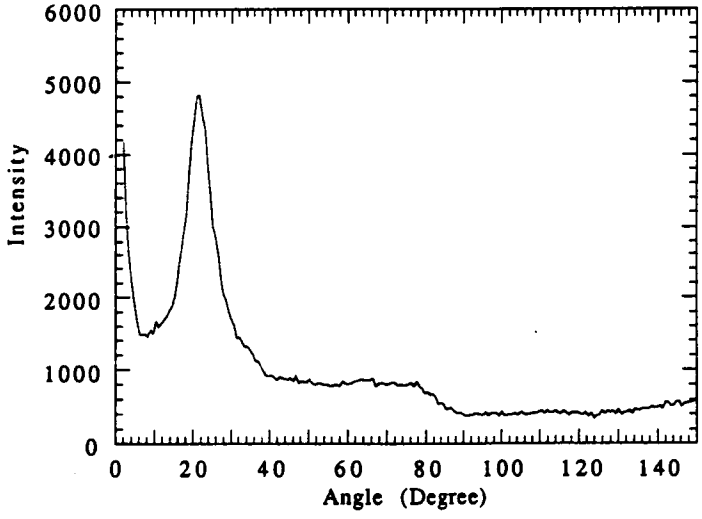

Figure A25. Run using CuKα in the microwave sample #3.

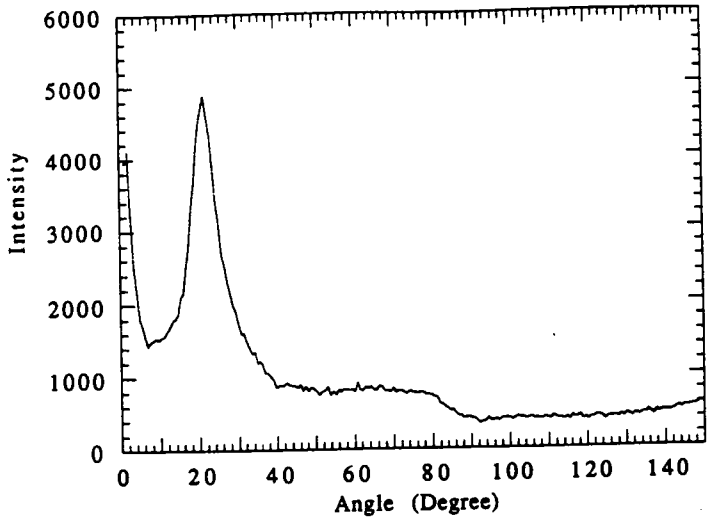

Figure A26. Run using MoKα in the microwave sample #1.

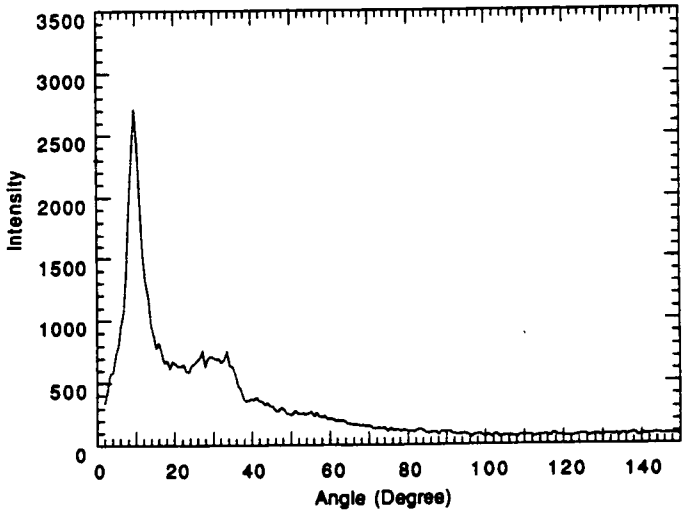

Figure A27. Run using MoKα in the microwave sample #2.

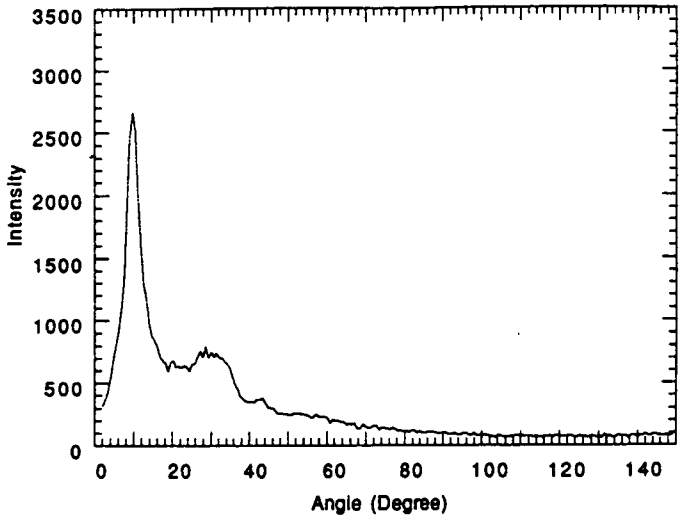

Figure A28. Run using MoKα in the microwave sample #3.

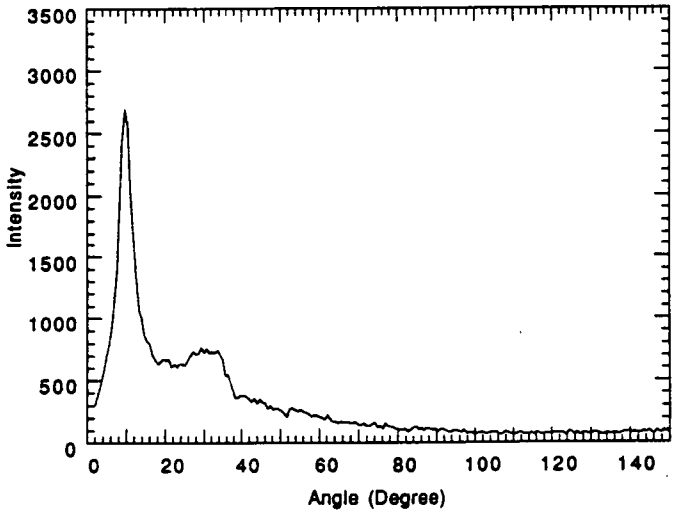

Appendix VII.

PFD Curves

The PFD curves of the conventionally melted pure fused silica are shown in Figure A29, A30, and A31. The PFD curves of the microwave melted pure fused silica are shown in Figure A32, A33, and A34.

Figure A29. The PFD curve of the conventional sample #1.

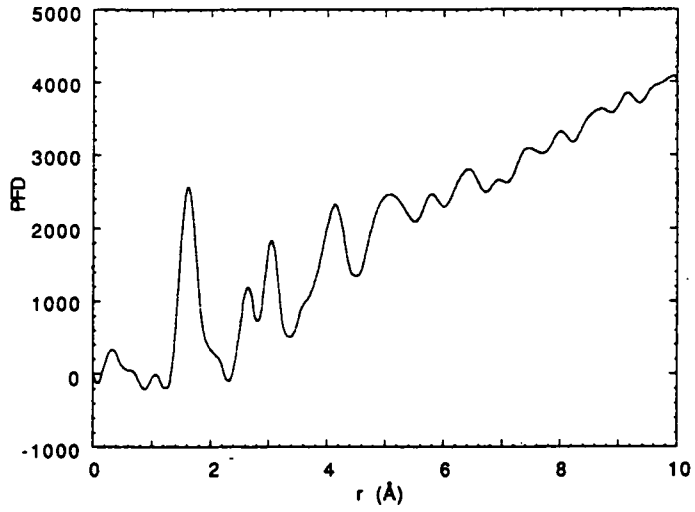

Figure A30. The PFD curve of the conventional sample #2.

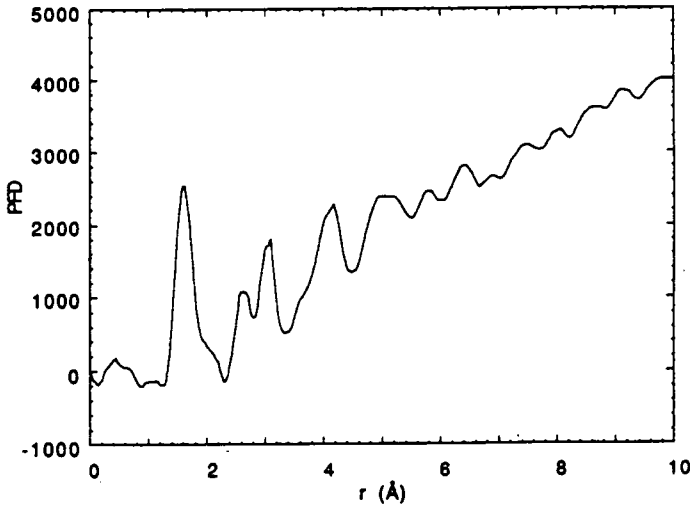

Figure A31. The PFD curve of the conventional sample #3.

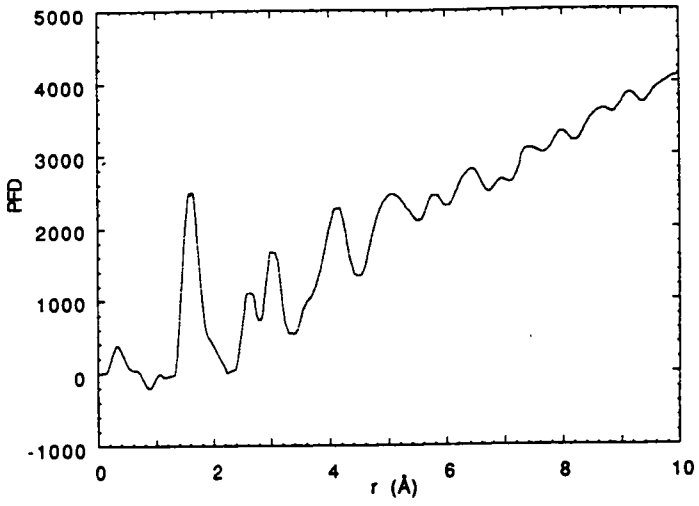

Figure A32. The PFD curve of the microwave sample #1.

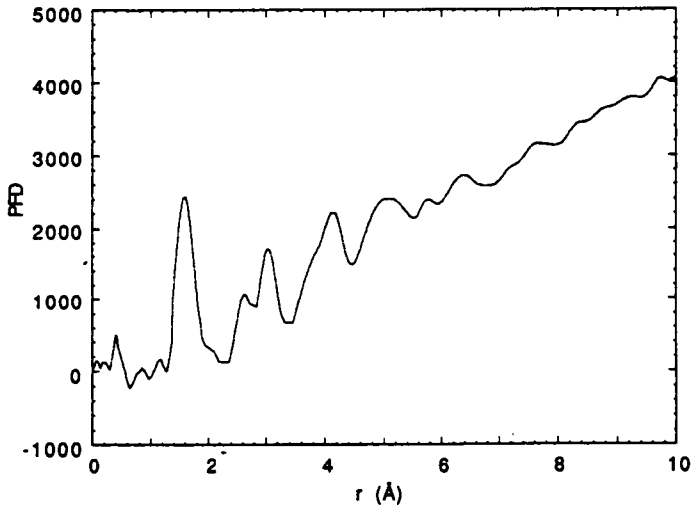

Figure A33. The PFD curve of the microwave sample #2.

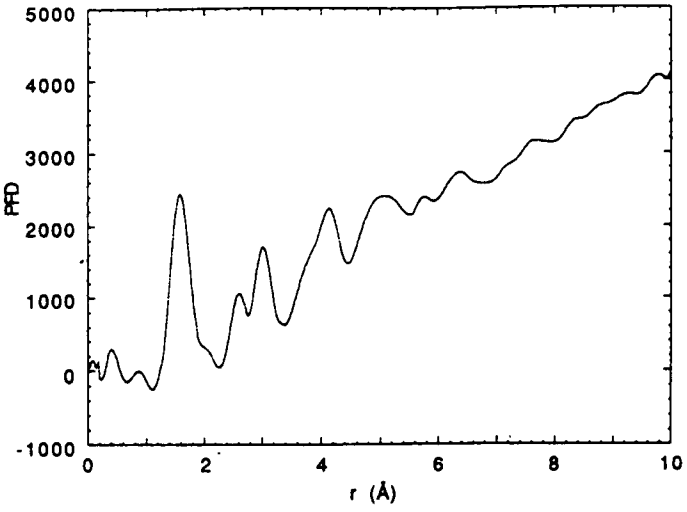

Figure A34. The PFD curve of the microwave sample #3.

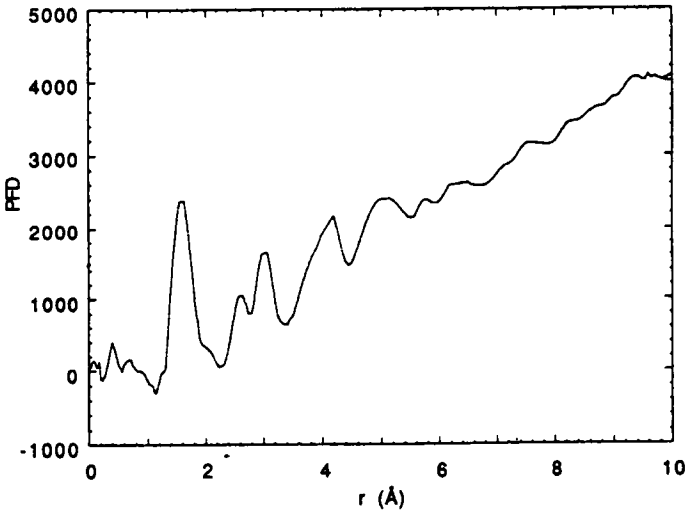

Vita

Seong Soo Park was born in Pusan, Korea, on January 21, 1956. The son of Jeong Soon Kim and Jin Do Park, he graduated from Dongrae High School in Pusan in February 1974. The following March he entered Pusan National University in Pusan. He received both a B. A. in Material Engineering in February 1978. The following March he entered Chemical Engineering in the Graduate School of the Pusan National University. After graduating Graduate School in February 1980. He joined military service. From 1980 to 1982 he served in military as a soldier for 27 months. From June 1982 to November 1982 he worked at Beik-San Paint Corporation. He also worked at R&D center of the International Group from December 1982 to May 1985.

In 1986 he entered the master's program in Materials Science and Engineering at The University of Tennessee. From May 1987 to August 1989 he worked as a research associate and received his Master's degree in August 1989. He is now a candidate for the doctor of philosophy degree in the department of Materials Science and Engineering at The University of Tennessee, where he was a research associate from 1989 to 1992 and a teaching associate from 1992 to present. He is a member of American Ceramic Society and American Society for Metals.